SUMMARIES OF VKI'S DOCTORAL CANDIDATE RESEARCH

2009 - 2010



von Karman Institute for
Fluid Dynamics

©2010 by the von Karman Institute for Fluid Dynamics

ISBN 978-2-87516-011-9

D/2009/0238/574, T. Magin, Editor-in-Chief

The contents of this book are the property of the von Karman Institute for Fluid Dynamics. No part of this book may be reproduced or distributed in any form of by any means, or stored in a database or retrieval system, without the prior written permission from the Publisher.

EDITORIAL NOTES

Please find herewith the proceedings of the first Symposium of the "VKI PhD's research" that took place at the Institute from 1 to 3 March 2010.

This event, allowing interaction among the students and invited guests combined with publishing their (partial) results through proceedings are of high importance for the VKI research.
In fact, up to now, such an event was really missing.
It has to be remarked that the doctoral candidate students of the VKI play a key role in strengthening the expertise in experimental and numerical/physical modeling of the Institute; their research deployed at the Institute forms the basis for further developments and in many cases finds real life industrial applications.

We truly hope that this first volume will be followed by many more and that the reputation of this event will spread quickly in the different research communities. The symposium is free of charge so as to attract as many people that the VKI can host.

The first week of March will always be dedicated to this event.

These proceedings aim at giving a snapshot of the research done at the time of the Symposium. Its content is not reviewed by an editorial board and is the property and responsibility of the candidates and their supervisory teams. The idea is to encourage all candidates to write papers on their research even if this research is still under development or if the associated results are only partial. The goal is to train on communication at the best level possible and to offer a yearly compilation of the research accomplished at the Phd level.

The present proceeding is registered under an ISBN number and may be referred to in any further publication.

In addition to the presentations of the PhD candidates we had this year the pleasure of guest Keynote lecturers:

- Dr Nagi Mansour from NASA for a keynote lecture on "Turbulent Convection and Oscillations in the Solar Interior"
- Raul Vasquez Diaz from Industria de Turbo Propulsores S.A. ITP as a keynote lecturer on "Low Pressure Turbine technology in the last decade and future challenges"
- Dr Gregoire Casalis from ONERA for a keynote lecture on "Instabilities and ONERA research"

Finally we also gave the opportunity to the first year Phd students to present a poster of their planned research.

We truly hope that this first volume will have the attention it deserves.

Jan Michalek Fabio Pinna Phd Representatives And Symposium Co-chairman	Patrick Rambaud Symposium Chairman	Jean Muylaert VKI Director

The contribution of all VKI members who helped on this event is deeply acknowledged (present PhD representatives Davide Masutti and Sergio Lavagnoli, faculty, library, printing office & secretariat).

TABLE OF CONTENTS

Editorial notes i

Table of contents iii

Plasma Flows

Panerai, Francesco 3
Plasma Testing for Thermal Protection System Characterization

Lopes, Silvânia 11
Modelling of Inductively Coupled Plasma Reactor and Nanoparticles Formation

Krassilchikoff, Hyun Woo 25
Plasma Tests Development for Thermal Protection System Design in Real Flight Conditions

Turbine Flows

Lavagnoli, Sergio 33
Interaction of an Innovative LP Stator Vane with a Transonic HP Turbine Stage

Michálek, Jan 47
On Steady and Unsteady Aerodynamic Performance of two Very-High-Lift Low Pressure Turbine Blades

Saracoğlu, Bayındır H (Confidential)
Turbine Base Pressure Active Control through Trailing Edge Blowing

Vass, Peter 61
Numerical Investigation of Squealer Blade Tip Leakage Flows in High Pressure Turbines

Multiphase Flows

Kourakos, Vasilios 71
Two-Phase Flow through Singular Geometries and Safety Valves

Skuza, Pawel 85
Microscale Bubble Simulation in Electrochemical Processes

Myrillas, Konstantinos (Confidential)
Experimental and Numerical Investigation of Gas Jet and Liquid film Interaction

Engine and Compressor Flows

Farkas, Balázs 93
Numerical Investigation of the Secondary Flows in Low Pressure Axial Compressor Stage for Contra-Rotating Turbofan Architectures

Fernández Villacé, Víctor 101
Numerical Simulation of the SABRE Rocket Based Combined Cycle Engine

Şahin, Fatma Ceyhun 109
Boundary Layer Separation Control on a Compressor Blade

Aero-Acoustical Flows

Koloszár, Lilla 119
Numerical Simulation of Noise Production and Propagation

Mueller, Anna 129
Numerical Investigation of Aerodynamic Noise Generation in Confined Flows

Marinus, Benoît G. 137
Current Satus of Propeller Blade Multidisciplinary Optimization

Residual Distribution Scheme Development for Flows

D'Angelo, Stefano 149
Development of H- and P- Solution-adaptive Techniques for Residual Distribution Schemes in Compressible Flow

Vymazal, Martin 161
High–order *RDS* and p–multigrid Solution Algorithms for Compressible Flow

Transitional Flows

Bottini, Henny 169
Analysis of Transition to Turbulence of a Supersonic Flow over a Rigid Surface

Masutti, Davide 177
Characterization of Hypersonic Boundary Layer Transition Induced by Isolated Roughness

Pinna, Fabio 195
Numerical Study of Roughness Induced Transition from Low to High Mach Number

Heat Transfer in Flows

Cukurel, Beni 205
Experimental Conjugate Heat Transfer Assessment in a Smooth Cooling Channel

Villafañe, Laura 213
Aerodynamic Research on Surface Heat Exchangers in the Engine Bypass Flow

Bensassi, Khalil 225
Numerical Simulation of Hypersonic Flow in VKI-Longshot Contoured Nozzle

Hazards in Flows

Horváth, István 243
Determination of Concentration and Velocity Fields by Means of MIE Scattering and Digital Image Post-processing

Laboureur, Delphine 249
Experimental Characterization and Modeling of Hazards: BLEVE and Boilover

First year Doctoral Summaries

Babajee, Jayson 259
Modeling and Analysis of the Laminar to Turbulent Transition in a Low-Pressure Turbine

Bonanni, Antonino 260
Micro-scale Assessment and Prediction of Wind Resources for Wind Farms Based on Numerical Modeling and Simulation

Delmas, Anthony 261
Distorsion and Temperature Measurement on High-Temperature Object by near Infrared Camera

Joly, Michael 262
Multi-Disciplinary Optimization For Concurrent Design of Turbomachinery Blades

Le Quang, Damien 264
High Enthalpy CO_2 Plasma Jet Characterization by means of Optical Emission Spectroscopy Diagnostics

Munafó, Alessandro 266
Multiscale Models and Computational Methods for Aerothermodynamics

Conan, Boris 270
Assessment of Wind Resource in Complex Terrain by Physical Modeling

Garicano Mena, Jesús 272
Residual Distribution Methods for Atmospheric Entry Aerothermodynamics

Lema, Marcos 273
Multiphase Fluid Hammer: Modeling, Experiments and Simulations

Muñoz Esparza, Domingo 274
High-resolution Mesoscale and Microscale Numerical Modeling of Wind over Complex Terrains

Sanna, Alessandro 275
Numerical Algorithms For Multiphysics Coupling Applications

Bacharoudis, Evangelos 277
Experimental Study of Droplet Ejections from Wall Surfaces Due to an External Turbulent Flow Field – Application to Wiper System

Torres, Erik 278
Simulation of Rarefied Gas Flows for Aerospace Applications

PLASMA FLOWS

Doctoral Project Summary

Plasma Testing for Thermal Protection System Characterization

Francesco Panerai*

Supervisor: Chazot Olivier†

von Karman Institute for Fluid Dynamics, Rhode-Saint-Genèse, 1640, Belgium

Promoter: Gianluca Rossi‡

Università degli Studi di Perugia, Perugia, 06125, Italy

Abstract

This work focuses on the study of catalysis phenomena in the von Karman Institute for Fluid Dynamics Plasmatron facility. Thermal protection materials are investigated under conditions that reproduce the atmospheric reentry flight of a spacecraft. Relevant properties, like catalycity and emissivities, are determined by means of experimental and numerical data. Effects of catalycity transition due to thermal protection system discontinuities are also observed.

1 Introduction

Space vehicles reentering the atmosphere undergo extreme conditions that require suitable protections. The phenomena occurring during the flight over a Thermal Protection System (TPS) need to be predicted through ground experiments and numerical simulations during the design phase. Wind tunnel testing and CFD, together with in-flight data, represent the base triangle for the aerothermodynamic research.

Depending on flight environmental conditions (e.g. pressure and temperature), the dissociated species composing the atmosphere surrounding a reentry vehicle could undergo recombination reactions, enhanced or inhibited by the catalytic properties of the materials. The determination of catalycity is a major issue in TPS design [1, 2], since a considerable part of the heat flux is transferred into the spacecraft by recombination reactions. A fully catalytic wall could increase more than 30% the heat flux with respect to a low catalytic wall [3, 4]. Additional phenomena, like catalycity discontinuities could also occur: passing from a low catalytic TPS to a high catalytic one, the heat flux could sharply increase exceeding the design limits.

Catalysis phenomena are investigated in this project though ground experiments that allow the reproduction of real flight conditions. Despite the extensive literature

*PhD Candidate, Aeronautics and Aerospace Department, Chaussée de Waterloo 72, panerai@vki.ac.be.

†Associate Professor, Aeronautics and Aerospace Department, Chaussée de Waterloo 72, chazot@vki.ac.be.

‡Professor, Dipartimento di Ingegneria Industriale, Via Duranti 67, gianluca@unipg.it.

that can be referred about catalycity studies, many questions still remain without an answer and solid databases for vehicle design need to be built.

2 Experimental Setup and Methodology

The experimental activity has been performed in the Plasmatron facility at VKI [5, 6]. This is a high enthalpy wind tunnel able to produce, by electromagnetic induction, an air plasma jet inside a test chamber, kept under atmospheric pressure. The Plasmatron operates under a subsonic flow regime and, as inductively-coupled-plasma (ICP) facility, it is able to create a plasma flow free of contaminations.

Several thermal protection system specimens, ceramic (C/SiC) and metallic (PM1000), have been used for plasma testing. C/SiC and PM1000 are relevant material as they compose the TPS of the EXPERT vehicle [7, 8, 9] from the European Space Agency (ESA). The samples are mounted in opportune probe holders and are investigated by means of optical techniques (IR thermography, pyrometry, radiometry). A probe model mounting a copper calorimeter, able to measure heat flux and dynamic pressure at the stagnation point is used for the calibration of plasma flow conditions.

The reproduction of flight conditions in the Plasmatron facility relies on the Local Heat Transfer Simulation (LHTS) concept. The methodology, developed at the Institute for Problems in Mechanics of Moscow (IPM) [10] and adopted at the VKI [11], is a derivation of the theory of stagnation-point heat transfer in chemically reacting flows developed by Fay and Riddell, Goulard et al. [12, 13, 14, 15] in the late fifties. It has been shown that a complete duplication of the real hypersonic flight can be achieved in a ground subsonic facility if the flight total enthalpy H_f, the total pressure P_f and the velocity gradient dv_f/dr are locally matched on the test sample. Based on LHTS, the process of catalycity prediction by Plasmatron testing in stagnation point configuration exploits test measurements of heat flux, pressure and temperature together with CFD data. Local Thermochemical Equilibrium (LTE) simulations of the Plasmatron flowfield are performed by means of the VKI ICP Code [16, 17, 18]. The reacting boundary layer is solved by the VKI Boundary Layer Code [19, 11], under the Chemical Non-EQuilibrium (CNEQ), in order to obtain the stagnation point heat flux as a function of wall temperature T_w and catalycity γ (see Fig. 1). Additional details on the prediction of catalycity by Plasmatron testing are provided in [2, 20, 21].

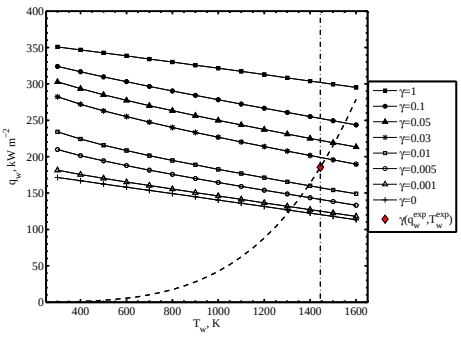

Figure 1: Abacus for catalycity determination.

3 Results

PM1000 and C/SiC emissivities were estimated by spectral reflectivity room-temperature measurements on samples prior to and post plasma exposure, by means of two spectrometers working from the ultraviolet to the medium infrared waveband (0.25 to 40 μm). The knowledge of emissivity for a TPM is fundamental to solve the heat balance at the wall and, consequently, to predict catalycity. Correcting the measured reflectivity by Kirchhoff's law and weighting by the Planck's radiation distribution function $E(\lambda, T)$ the total emissivity as a function of the wall temperature, was determined as:

$$\varepsilon(T) = \frac{\int_{0.25\mu m}^{40\mu m} (1 - r(\lambda)) E(\lambda, T)\, d\lambda}{\int_{0.25\mu m}^{40\mu m} E(\lambda, T)\, d\lambda} \tag{1}$$

The results are shown in Fig. 2(a) for PM1000 and Fig. 2(b) for C/SiC, together with data extracted from literature[22, 22, 23, 24, 25].

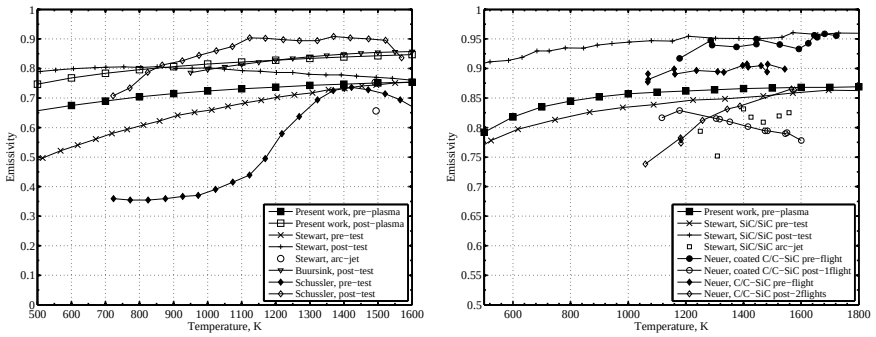

(a) PM1000 emissivity

(b) C/SiC emissivity

Figure 2: Total hemispherical emissivity of the TPM and comparison with literature data.

Pre-plasma PM1000 emissivity rises from $\sim$0.65 to $\sim$0.75 as we go higher in temperature. In the temperature range of interest (from 1300 to 1500 K) the emissivity does not show any significant variation remaining between 0.74 and 0.75. The same behavior is shown by post-plasma measurements that range between 0.83 and 0.84. The measurements accurately agree with data from Buursink [23] and Stewart [26] (post test measurements show a different trend, probably due to the different conditions at which the samples where tested). Measurements on C/SiC samples prior to plasma exposure show an emissivity of about 0.85 in the interesting range, in good agreement with literature values.

Fig. 3 shows the prediction of air recombination coefficients for PM1000 and C/SiC samples as a function of the stagnation point wall temperature. As expected the metallic samples resulted to be higher catalytic than the ceramic at the same conditions. PM1000 catalycity is around 0.01 and remains constant at the three target temperatures. C/SiC catalycity shows a decrease from about 0.005 to about 0.001 as we go

higher in temperature. The margins on the recombination coefficients were determined following the approach proposed in [21], assuming $\pm 10\%$ uncertainty on cold wall heat flux measurements, ± 10 K uncertainty on temperature measurements, and emissivity bounds given by pre- and post-test estimated values. The reduction of the margins, here around one and a half order of magnitude, represents the main challenge in future TPS testing.

In Fig. 3 a survey of literature recombination coefficients, for both PM1000 (a) [21, 2, 20, 26, 24] and C/SiC (b) [27, 28, 29, 22, 30], is proposed. It can be noticed how the dispersion of data is considerable, between different authors. This is mainly due the fact that catalycity, as global identification parameter for gas-surface interaction processes, is strictly connected to the environment under which it is determined.

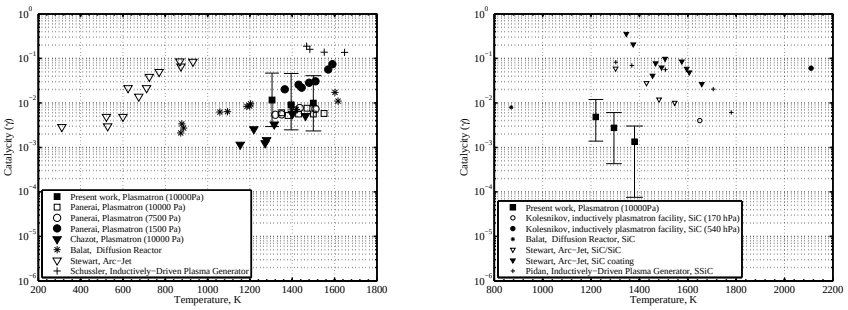

(a) PM1000 (b) C/SiC

Figure 3: Catalycity of the TPM and comparison with literature data.

In order to provide an experimental evidence of the catalycity transition due to TPM discontinuity a probe model consisting of a central sample of C/SiC surrounded by a PM1000 ring was tested in the Plasmatron and analyzed by means of IR thermography (Fig. 4). This configuration was as well compared with two full disks, one of C/SiC and one of PM1000, tested as the same conditions using a heat flux probe as reference.

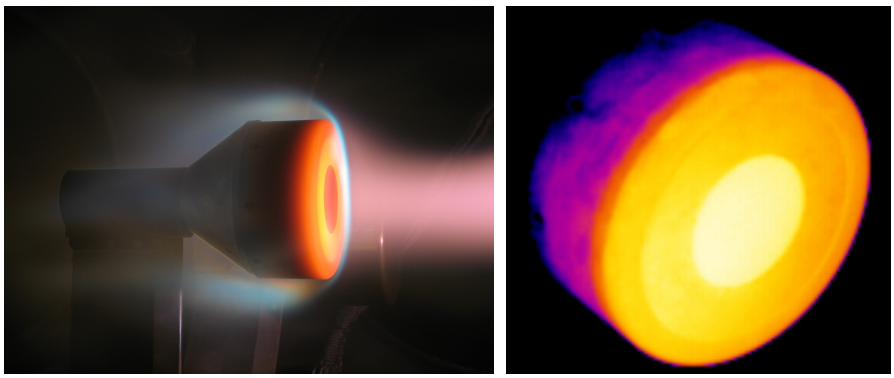

(a) (b)

Figure 4: Test of a low-high catalytic model. (a) Probe exposed to the plasma stream, (b) Infrared snap-shot.

The results are presented in Fig. 5 where the distribution of the wall temperature T_w

along the radius is shown (the junction is at $r = 0.025$ m). As expected, the two materials model shows a temperature jump (~ 160 K) immediately downstream the junction between the silicon carbide disk and the surrounding metal ring, as consequence of the catalycity discontinuity over the surface.

Comparing the two full disks we can note that the stagnation point temperature for the C/SiC is lower with respect to the PM1000 ($\Delta T_{sp,\text{PM1000-C/SiC}} \sim 120$ K). The radiative equilibrium at the wall states the equivalence between the radiative term to the sum of the conductive and diffusive term [31]:

$$-k\frac{\partial T}{\partial y} + \sum_{i=1}^{n} h_i J_{iy} = \sigma \varepsilon T_w^4 \tag{2}$$

Wall temperature and emissivity measurements performed yield a radiative flux that is higher for PM1000, than for C/SiC, $q_{r,\text{PM1000}} > q_{r,\text{C/SiC}}$. The conduction term, that is proportional to the temperature gradient at the wall, is lower for PM1000 than for C/SiC, $q_{c,\text{PM1000}} < q_{c,\text{C/SiC}}$, since the outer edge temperature T_e is the same and $T_{w,\text{C/SiC}} < T_{w,\text{PM1000}}$. As a consequence the diffusive term, that depends on catalycity [31], is higher for PM1000 than for C/SiC, $q_{d,\text{PM1000}} > q_{d,\text{C/SiC}}$. We can conclude that the temperature effect observed ($T_{w,\text{C/SiC}} < T_{w,\text{PM1000}}$) is an effect of the higher recombination of atomic species (read catalycity) promoted by PM1000 than by C/SiC.

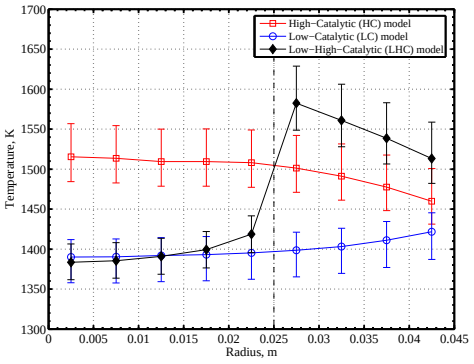

Figure 5: Radial distribution of the wall temperature for the three model configurations

Focusing on the PM1000 in the fully high catalytic and in the combined probe, an overshoot of ~ 70 K for the ring with respect to the full disk can be noticed. Because of the presence of the silicon carbide sample the recombination of the oxygen and nitrogen atoms starts at the stagnation point of the combined model with a lower rate as for the full disk one. The amount of atoms available to recombine at the junction in the combined configuration is higher than in the disk at the same position, resulting in an overall higher temperature.

4 Conclusions

An experimental study on PM1000 and C/SiC samples performed in the Plasmatron facility has been presented. As selected materials the EXPERT capsule Thermal Protection System these components need to be carefully characterized under typical flight conditions. Air recombination coefficients have been determined in order to predict the

portion of heat flux received by the heat shield by chemical activity during the reentry. C/SiC resulted about one order of magnitude less catalytic than PM1000 at similar conditions. A review of catalycity predictions available in literature showed a quite important dispersion of data, mainly due to different facilities and gas mixtures.

The testing of three different models (a full high catalytic disk, a full low catalytic disk and combined configuration composed by a high catalytic ring surrounding a low catalytic central disk) allowed to investigate the behavior of the catalycity discontinuity, occurring where a ceramic and a metal are joined together. Temperature distributions obtained by infrared measurements provided an evidence of the the catalytic transition observing that:

1. A temperature jump was experienced at the junction between C/SiC and PM1000 in the low-high-catalytic configuration.

2. An higher temperature was experienced at the stagnation point of the full high-catalytic model with respect to the full low-catalytic one.

3. An overshoot of temperature was observed on the PM1000 ring in the low-high-catalytic model with respect to the PM1000 disk on the high-catalytic one.

References

[1] M. Schüssler, M. Auweter-Kurtz, G. Herdrich, and S. Lein. Surface Characterization of Metallic and Ceramic TPS-Materials for Reusable Space Vehicles. In *IAC-06-C2.6.09*, 2006.

[2] O. Chazot, H. W. Krassilchikoff, and J. Thoemel. TPS Ground Testing in Plasma Wind Tunnel for Catalytic Properties Determination. In 46th *AIAA Aerospace Science Meeting and Exhibit*, AIAA 2008-1252, Reno, Nevada, January 2008.

[3] J. D. Anderson. *Hypersonic and High Temperature Gas Dynamics*. McGraw Hill, New York, 1989.

[4] A. F. Kolesnikov. Combined Measurements and Computations of High Enthalpy and Plasma Flows for Determination of TPM Surface Catalycity. RTO AVT/VKI Special Course on Measurement Techniques for High Enthalpy Plasma Flows RTO EN-1, Von Karman Institute for Fluid Dynamics, Rhode-Saint-Genese, Belgium, October 1999.

[5] B. Bottin, M. Carbonaro, S. Zemsch, and G. Degrez. Aerothermodynamic Design of an Inductively Coupled Plasma Wind Tunnel. In 32nd *Thermophysics Conference*, AIAA 97-2498, Atlanta, USA, June 1997.

[6] B. Bottin, S. Paris, V. Van Der Haegen, and M. Carbonaro. Experimental and Computational Determination of the VKI Plasmatron Operating Envelope. In 30th *Plasmadynamics and Lasers Conference*, AIAA 99-3607, Norfolk, VA, June-July 1999.

[7] J M. Muylaert, H. Ottens, L. Walpot, F. Cipollini, G. Tumino, M. Caporicci, G. Saccoccia, L Basile, A. Schettino, A. Mohammed, and J. Bonnet. Flight Measurement Technique Development for EXPERT, the ESA In Flight Aerothermodynamic Research Programme. In 55th *International Astronautical Congress*, Vancouver, Canada, 2004.

[8] F. Cipollini and J. M. Muylaert. European Activities on Advanced Flight Measurement Techniques for Hypersonic Space Vehicles. In 5th *AIAA Aerodynamic Measurement Technology and Ground Testing Conference*, San Francisco, California, 2006.

[9] J. Thoemel, S. Tirtey, D. Fletcher, O. Chazot, and S. Birjmohan. Development of an In-Flight Catalysis Experiment within the EXPERT Program. In 2nd *European Conference for Aero-Space Sciences*, Brussels, Belgium, 2007.

[10] A. F. Kolesnikov. Conditions of Simulation of Stagnation Point Heat Transfer from a High-enthalpy Flow. *Fluid Dynamics*, 28(1):131–137, January 1993.

[11] P. F. Barbante and O. Chazot. Flight Extrapolation of Plasma Wind Tunnel Stagnation Region Flowfield. *Journal of Thermophysics and Heat Transfer*, 20(3):493–499, July-September 2006.

[12] J. A. Fay and F. R. Riddell. Theory of Stagnation Point Heat Transfer in Dissociated Air. *Journal of Aeronautical Science*, 25(2):73–85, February 1958.

[13] R. Goulard. On Catalytic Recombination Rates in Hypersonic Stagnation Heat Transfer. *Jet Propulsion*, 28(11):737–745, November 1958.

[14] L. Lees. Laminar Heat Transfer Over Blunt-Nosed Bodies at Hypersonic Flight Speeds. *Jet Propulsion*, 26(4):259–269, 274, 1956.

[15] P. H. Rose and W. I. Stark. Stagnation Point Heat Transfer Measurements in Dissociated Air. *Journal of Aeronautical Science*, 25(2):86–97, February 1958.

[16] T. Magin, D. P. Vanden Abeele, and G. Degrez. An Implicit Multiblock Solver for Inductive Plasma Flows. In *Fluids 2000 Conference and Exhibit*, AIAA 2000-2480, Denver, CO, June 2000.

[17] D. P. Vanden Abeele and G. Degrez. Numerical Model of High-Pressure Air Inductive Plasma Under Thermal and chemical Non-Equilibrium. In *Fluids 2000 Conference and Exhibit*, number AIAA-2000-2416, Denver, CO, June 2000.

[18] G. Degrez, D. P. Vanden Abeele, P. F. Barbante, and B. Bottin. Numerical Simulation of Inductively Coupled Plasma Flows under Chemical Non-equilibrium. *International Journal of Numerical Methods for Heat & Fluid Flow*, 14(4):538–558, 2004.

[19] P. F. Barbante, G. Degrez, and G. S. R. Sarma. Computation of Nonequilibrium High Temperature Axisymmetric Boundary-Layer Flows. *Journal of Thermophysics and Heat Transfer*, 16(4):490–497, 2002.

[20] O. Chazot, J. Thoemel, and M. Balat-Pichelin. Air Catalycity Determination in Plasma Wind Tunnels and Diffusion Reactors. In *Sixth European Symposium on Aerothermodynamics for Space Vehicles*, Versailles, November 2008. ESA.

[21] F. Panerai, J. Thoemel, and O. Chazot. Thermal Protection Material Characterization in Ground Plasma Testing. In 41st *AIAA Thermophysics Conference*, AIAA 2009-4094, San Antonio, TX, USA, June 2009.

[22] D. A. Stewart. Surface Catalysis and Characterization of Proposed Candidate TPS for Access-to-Space Vehicles. Technical Memorandum 112206, NASA Ames Reasearch Center, Moffett Field, California, July 1997.

[23] J. Buursink. *On the Development of a Cooled Metallic Thermal Protection System for Spacecraft*. PhD thesis, TU-Delft, 2005.

[24] M. Schüssler, M. Auweter-Kurtz, G. Herdrich, and S. Lein. Surface Characterization of Metallic and Ceramic TPS-Materials for Reusable Space Vehicles. *Acta Astronautica*, 65(5-6):676–686, September-October 2006.

[25] G Neuer and G Jaroma-Weiland. Spectral and Total Emissivity of High-Temperature Materials. *International Journal of Thermophysics*, 19(3):917–929, 1998.

[26] D. A. Stewart and S. Bouslog. Surface Characterization of Candidate Metallic TPS for RLV. In 33rd *Thermophysics Conference*, AIAA-99-3458, Norfolk, VA, USA, 1999.

[27] A. F. Kolesnikov, A. N. Gordeev, and S. A. Vasil'evsky. Simulation of Stagnation Point Heating and Predicting Surface Catalyisty for the EXPERT Re-Entry Conditions. In *The* 6th *European Symposium on Aerothermodynamics for Space Vehicles*, ESA SP-659, Versailles, France, November 2008.

[28] M. J. H. Balat, M. Czerniak, and J. M. Badie. Ceramics Catalysis Evaluation at High Temperature Using Thermal and CHemical Approaches. *Journal of Spacecraft and Rockets*, 36(2):273–279, March-April 1999.

[29] D. A. Stewart. Determination of Surface Catalytic Efficiency for Thermal Protection Materials - Room Temperature to Their Upper Use Limit. In 31st *AIAA Thermophysics Conference*, AIAA 96-1863, New Orleans, LA,USA, June 1996.

[30] S. Pidan, M. Auweter-Kurtz, G. Herdrich, and M. Fertig. Recombination Coefficients and Spectral Emissivity of Silicon-Carbide-Based Thermal Protection Materials. *Journal of Thermophysics and Heat Transfer*, 19(4):566–571, October-December 2005.

[31] P. F. Barbante. *Accurate and Efficient Modelling of High Temperature Nonequilibrium Air Flows*. PhD thesis, Université Libre de Bruxelles/Von Karman Institute for Fluid Dynamics, 2001.

Doctoral Project Summary

Modelling of inductively coupled plasma reactor and nanoparticles formation

Silvânia Lopes*

Supervisor: Prof. Rambaud Patrick†

von Karman Institute for Fluid Dynamics, Rhode-Saint-Genèse, 1640, Belgium

Promoter: Prof. Proulx Pierre‡

University of Sherbrooke, Sherbrooke (QC), Canada J1K 2R1

Abstract

The general purpose of this thesis is to model the synthesis of nanoparticle in inductively coupled plasma (ICP) reactor with a supersonic nozzle quench configuration.
In the present report, a mathematical model has been developed for simulating the behavior of ICP torches, using an open source code OpenFoam. Preliminary experimental characterization of ICP has been also performed, using the VKI plasma minitorch.

1 Introduction

Nanotechnologies, especially nanopaticles related applications, have recently received tremendous interest due the numerous innovative potential they offer.
Nanomaterials are usually produced by compaction of a powder of nanoparticles. They are characterized by a large number of grain boundary interfaces in which the local atomic arrangements are different from those of the crystal lattice [1]. The small size of the nanoparticles is responsible for many changes in the thermo-physical properties compared with the bulk materials, which makes them suitable for novel applications. Exemples of these new properties include lower melting temperature, improved hardness and ductility, high self-diffusion coeficient, catalytic activity, and intriguing optical and electronic properties. However, the processes used for generating the nanoparticles play an important role in terms of controlling the size, morphology, crystalline phase, and composition, which ultimately determine the properties of the nanostructure material.

* PhD Candidate, Aeronautics and Aerospace department, Chaussée de Waterloo 72,lopes@vki.ac.be

† Associate Professor, AR and AE Department at VKI, Chaussée de Waterloo 72, Rambaud@vki.ac.be

‡ Professor, Chemical Engineering Department at University of Sherbrook, Sherbrooke (QC), Canada J1K 2R1 pierre.proulx@usherbrooke.ca

Inductively couples thermal plasma (ICTP), and in general thermal plasma processing present several distinctive advantages over other synthesis routes for nanoparticles, due mainly to their high temperature and energy density, large plasma volume and long residence/reaction time by virtue of its low velocity. Additionally, an ICTP is inherently contamination-free because it is generated without any internal electrodes and it offers the possibility to work under a controlled atmosphere [2]. In such a field of plasma, a large amount of raw material, even that with a high melting/boiling point, is vaporized. Subsequently, the vapour is transported to the tail of an ICTP and the nanoparticles is formed in the zone of the plasma reactor where gases have cooled considerably and the vapour have fallen into a highly supersaturated state and can condense, via homogeneous nucleation. Althoug several methods have been developed to produce nanoparticles, neither the precise control of the particle size nor mass production has been successful in practice. The final particle size and distributions, chemical compositions, shape and phase of the synthesized nanoparticles, are heavily influenced by the thermal history of the formed particles.

To master and optimize the thermal plasma technologies is it necessary to understant not only the mechanisms of generation, growth, and deposition of nanoparticles, but also the fundamental nature of the transport phenomena occuring in the plasma during the synthesis. Modeling studies can play an important role in the development and improvement of the nanoparticle synthesis process, providing an insight into the phenomena involved and helping to identify the right process operations to employ. In most of the investigation, the plasma generated vapors have been quenched through mixing with cold gas [3] [4]. Although very high quench rate can be achived this way, the quench process is rather uncontrolled, leading to nonuniformities in the quench region, consequently variation in particle nucleation and size distribution. Thus, the overall purpose of this thesis is to develop a plasma process for efficient producing of high-purity nanoparticles with narrow size distribution, controlled composition and morphology by expanding the plasma containing the precursor vapour through a supersonic nozzle. This configuration provides better mixing leading to high uniformity of the quench rate and much higher quenching rate. Control over the quenching condition is noticeably superior to most convectional plasma method in which cold gas is added to the mixture, thus a better control on nanoparticles formation [5].

A full theoretical description of the aerosol dynamics in plasma processing, within actual industrial environment is very complex. A complete model of such a system requires the solution of the coupled system of the fluid mechanical equations of continuity, momentum, and energy, and the vector potential formulation of the Maxwell's equations, that are used to describe the generation of the plasma. The description of the micrometer particles injected in the plasma as a precursor and the equation describing the aerosol dynamics are added to the plasma model. Beside the complexity related to the modelling of such production, the calculation of the transport properties and the effects of the plasma and quenching parameters, including torch design and nozzle configuration, on the flow and on the formation of the nanoparticles are of enormous importance. The investigated is carried out in both computational and experimental way, in order to better understand the physical mechanism of this process.

In the present report, an extended-field model for simulating the behavior of inductively coupled plasma torches (ICPTS) has been developed using a Computational Fluid Dynamic (CFD) open source code, OpenFOAM. One of the key advantages of OpenFOAM is its extensibility: the source code is accessible, and the architecture of OpenFoam makes it relatively easy to write new solvers for new

applications. Therefore, this code can be at some point optimized and adapted for complete prediction of nanoparticles formation, i.e. starting from heat and mass transfer between plasma and particles(particle evaporation) to nucleation and condensation(growth of nano scale particle) . Visualisations of smoke in a cold model of the ICP torch and particle emission in the plasma, in the VKI Minitoch facility have been also performed for the characterization of the plasma-particle flow interaction.

2 Modelling of ICP torch in OpenFoam

The ICP torch modelling using OpenFoam is done by extending the calculating domain of the electromagnetic (EM) field, induced by the induction coil, well outside of the plasma discharge region. The model consists of two systems of equations: the Navier-Stokes equations (completed with Joule heat source term and Lorentz force source term) and the induction equation (consisting of an equation for vector potential). The coupling between these two systems of equations is realized bythe Lorentz force acting on the charged particles, Joule dissipation which heats up the plasma and through the dependence of electrical conductivity on temperature and pressure. Although the geometry of the inductively plasma torch allows to use cylindrical coordinates, in the concrete implementation of the physical model in OpenFoam the equations are transformed to Cartesian coordinates. The boundary conditions of the vector potential are replaced by simpler far field boundary conditions. The current carrying ring (coil) in this case is not assumed to be infinitely thin and the diameter of the rings is taken to be 6mm, which is typical of a coil diameter normally used for inductively plasma generation.

2.1 Hypothesis

The basic assumptions used in the present work are the follow:

- Steady state, axisymetric and laminar pure argon plasma flow at atmospheric pressure.
- Two dimensional electromagnetic, velocity and temperature field
- Local thermodynamic equilibrium conditions (LTE).
- Radiative heat transfer based on the net emission coefficient approach.
- Negligible displacement current
- In the energy equation the viscous dissipation and the pressure work are neglected.

2.2 Governing Equations

Using LTE plasma at atmospheric pressure as a flow interacting with electromagnetic fields is described by continuity, momentum balance, energy balance and electromagnetic field equations.

A. Continuity equation

$$\nabla\cdot(\rho\mathbf{u})=0 \tag{1}$$

B. Momentum

$$\rho \mathbf{u} \cdot \nabla(\mathbf{u}) = -\nabla p + \mu \nabla^2 \mathbf{u} + \mathbf{F_{lz}} \tag{2}$$

C. Energy

$$\rho C_p \mathbf{u} \cdot \nabla(T) - k \nabla^2 T = P + R \tag{3}$$

Where ρ, μ, p and $\mathbf{u}$, are the density, the viscosity, the pressure and the vector velocity respectively. $\mathbf{F_{lz}}$ is the time average Lorentz force induced by the RF discharge inside the ICP torch, which is determined from the electromagnetic field equations. k, C_p are the thermal conductivity and the specific heat at constant pressure respectively. T is the temperature, P is the time-average Joule heating generates RF discharge and R the radiation loss.

D. Vector potential formulation

The EM field in all calculating domains is governed by the Maxwell equations which can be written as:

$$\nabla \times \mathbf{H} = \mathbf{J} \tag{4}$$

$$\nabla \times \mathbf{E} = -\mu_0 \frac{\partial H}{\partial t} \tag{5}$$

and

$$\nabla \bullet \mathbf{H} = 0 \tag{6}$$

Here $\mathbf{E}$ and $\mathbf{H}$ are the magnetic and electric field intensities respectively, μ_0 is the permeability of the free space and $\mathbf{J}$ the total current density.
In order to simplify the solution of the electromagnetic equations, the vector potential formulation is used, derived from Eqs.4-6 [6]:

$$\nabla^2 \mathbf{A} = -\mu_0 (\mathbf{J}_{coil} + \mathbf{J}_{ind}) \tag{7}$$

For the standard induction plasma torch, if the coil is assumed to be composed of parallel rings, the vector has only an azimuthal component $\mathbf{A} = (0, A_\theta, 0)$. A_θ is a phasor quantity, do it has a real and an imaginary parte like:

$$A_\theta = A_{\theta R} + i A_{\theta I} \tag{8}$$

The Eq.7 has various forms according to each zone of the torch. In the plasma zone the current developed in the plasma and the coil by induced electric field is $\mathbf{J}_{ind} = -i\omega\sigma A_\theta$ and the current density induced in the coil by the voltage applied to

the ends of the coil, $\mathbf{J}_{coil} = 0$. In the zone outside the plasma and in the coil zone the electrical conductivity is assumed to be zero, therefore the plasma- induced field outside the torch is zero .
After solve the vector potential equation, the electric and magnetic fields, the Lorentz forces and the Joule heat source are determined from:

$$E_\theta = -i\omega A_\theta \tag{9}$$

$$\mathbf{H} = -\frac{1}{\mu_0}\nabla \times A_\theta \tag{10}$$

$$F_{lz} = -\frac{1}{2}\mu_0 \sigma \omega \,\mathrm{Re}\left[\mathbf{A} \times \mathbf{H}\right] \tag{11}$$

$$P = \frac{1}{2}\sigma \,\mathrm{Re}\left[E_\theta E_\theta^*\right]. \tag{12}$$

2.3 Computational Methodology

In OpenFOAM as in any other CFD code, the flow equations are described by a system of linked partial differential equations. The code itself is a collection of object-oriented routines developed for the manipulation of the tensor fields found in fluid mechanics equations. Coupling between equations is treated in OpenFoam using a segregated approach, in which equations are formulated for each dependent variable and solve sequentially, with the possibility of iteration over the system of equation until convergence is achieved. The approach used in OpenFoam lead to the creation of the FOAM C++ class of library foe computational fluid dynamics. The intention is to develop a C++ class library that makes it possible to implement complicated mathematical and physical models as high-level mathematical expressions.

2.3.1 Grid Structure

OpenFOAM has been designed from the start for 3-dimensional space and defines all geometrical grids or meshes as such. However, two dimensional and axi-symmetric problems can be simulated in OpenFOAM by generating a mesh in 3 dimensions and applying special boundary conditions on any patch in the plane normal to direction of interest. More especially for axi-symmetric problems, the geometry is specified as a wedge of 5 degree angle and one cell thick running along the plane of symmetry, straddling one of the coordinate planes. The mesh id generated by the blockMesh utility supplied with OpenFoam.
The induction torch is based on the commercial Tekna PL35 torch and details of computational grid are given in Figure 1.

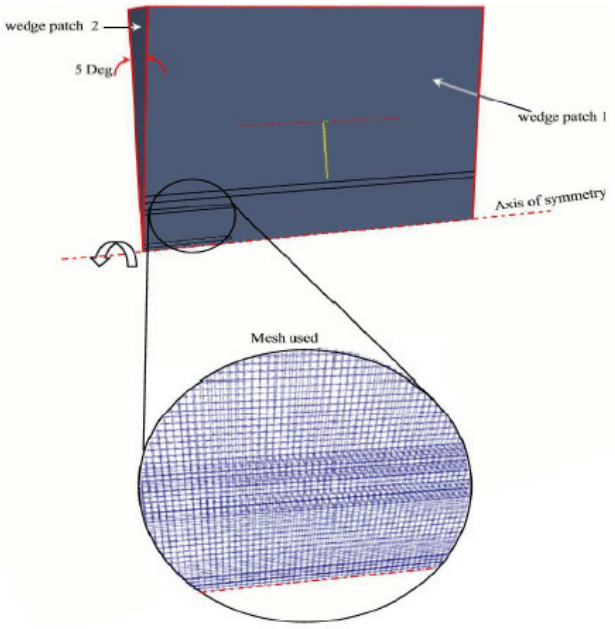

Figure 1: Axisymetric geometry using the wedge patch type and mesh used in OpenFoam (M. Morsli el al., USherbrooke)

2.3.2 Boundary conditions

For the outer boundary conditions, because of the distance from the current carrying coil, are set:

$$A_{\theta R} = A_{\theta l} = 0. \tag{13}$$

At the interfaces between the zones is assumed continuity of the vector potential cross the interfaces with jumping. That is done by creating foe each wall an adjacent wall separated by an arbitrary small distance (1 µm not meshed). The mass flux is described at the inlets and from it is computed the inlet velocity. Zero gradient of the variables are used for the outlet boundary condition and no-slip wall condition for the walls.

2.4 Results and discussion

Figure **2** gives the details of the torch geometry, its characteristic dimension and operating conditions are given in table Table **1**. The geometry used is Tekna model PL-50 with 50mm ID plasma confinement tube. The plasma gas is argon at atmospheric pressure, the oscillator frequency is 3.0 MHz and the net energy dissipated into the plasma is 5.0kW. The coil current is set to 161 A, the current needed to dissipate 5kW in an argon plasma with the flow rate of 31slpm.

Table 1: Torch dimension and operating condition

L0=20mm	L1=40mm	L2=90mm	Lt=136mm

Ro=25mm	Rc=33mm	Rt=125mm	F=3Mhz
$\delta m = 2mm$	$\delta t = 2.2mm$	$\delta w = 3mm$	Pohmic=5kW
dc=6mm	r2=18.8	r2=4mm	Tin=300K
Q1=1.0slpm	Q2=3.0slpm	Q3=31.0slpm	

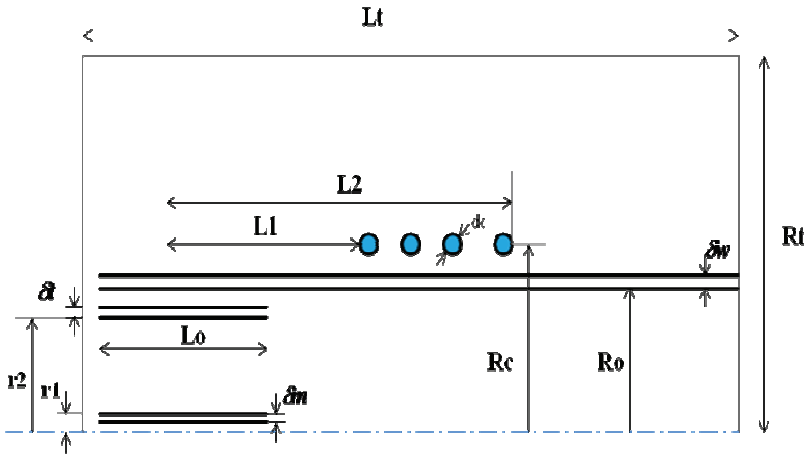

Figure 2: Torch geometry

Solution of the induction equation using openFoam for the real and the imaginary parts of the vector potential are shown in Figure 3 and Figure 4, respectively. Both give realistic distribution of the vector potential and in good agreement with the model developed by [6].

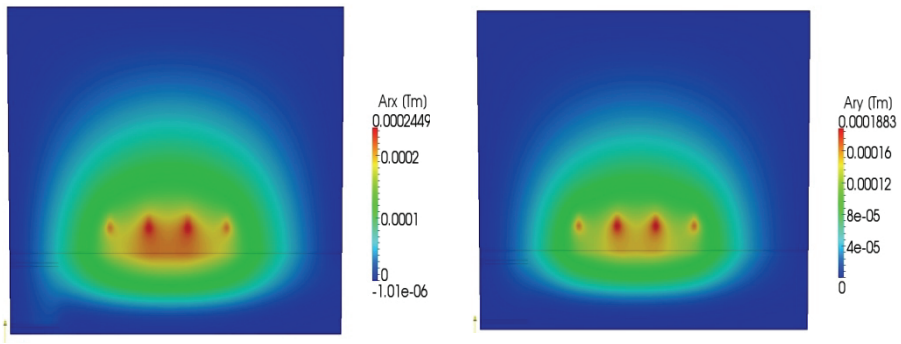

(a) (b)

Figure 3: Isocontours of the real part of the vector potential: (a) x-component, (b) y-component.

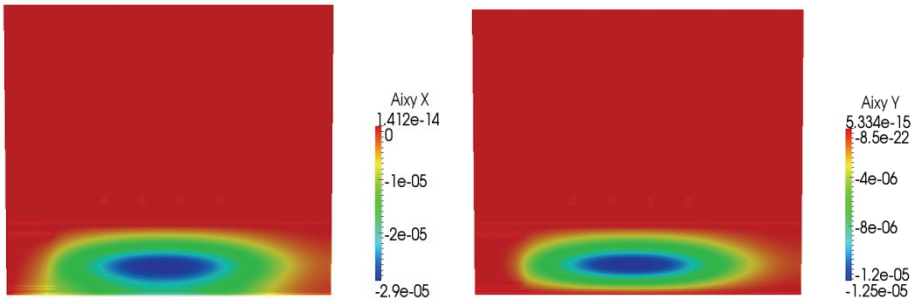

(a) (b)

Figure 4: Isocontours of the imaginary part of the vector potential: (a) x-component, (b) y-component.

Contours of the radial and axial components of the Lorentz Force and the Joule heat are presented in Figure 5Figure 6Figure 7 . Again, good agreement is achieved compared with the solution of [6]. Only the results close to the inlet are affected due to the condition used for the electrical conductivity.

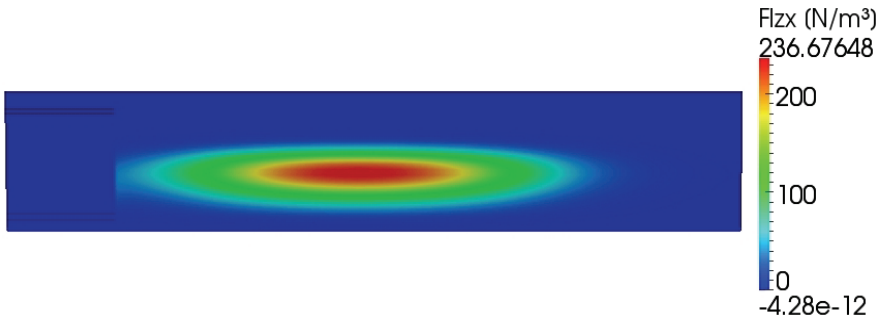

Figure 5: Isocontour of the axial component of the Lorentz force Fx.

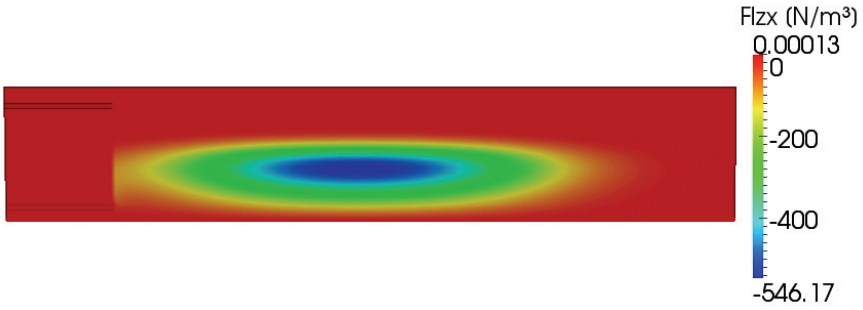

Figure 6: Isocontour of the radial component of the Lorentz force Fy.

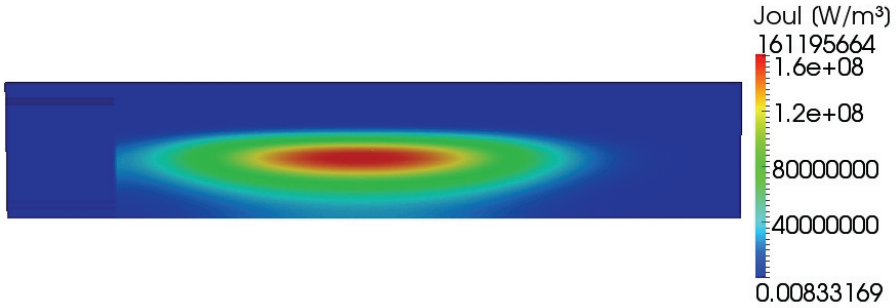

Figure 7: Isocontour of the Joule heat source P [W/m^3]

Predictions of the openFoam code, carried out using the vector potential formulation combined with the continuity, momentum and energy conservation equation, for the plasma flow are obtained. Figure 8 and Figure 9 show the temperature contours and the axial and radial profiles.

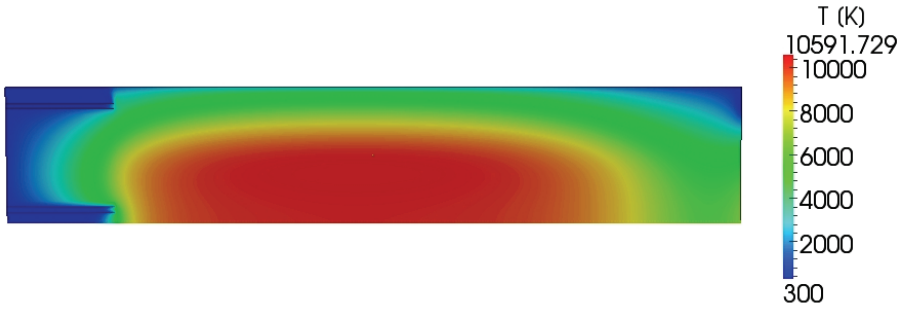

Figure 8: isocontour of the temperature T [K]

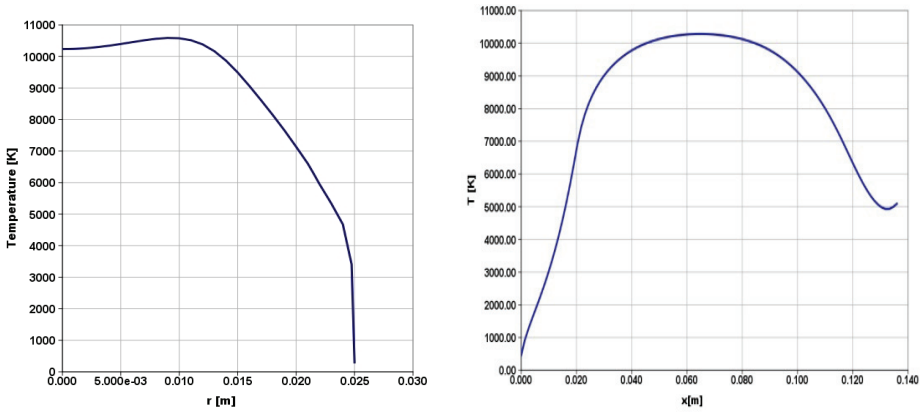

(a) (b)

Figure 9: (a) radial temperature profile at x=0.68m, (b) axial temperature profile at r=0.0mm

Figure 10 shows the results obtain for the axial velocity with the influence of the of Lorentz force. As can be seen the flow presents an unexpected large recirculation zone close to the wall of the torch, which is not present in case the Lorentz force is assumed negligible. This effect of the of Lorentz force, which is prominent at high pressure flow as refereed by [7], needs to be investigated for future optimization of the code.

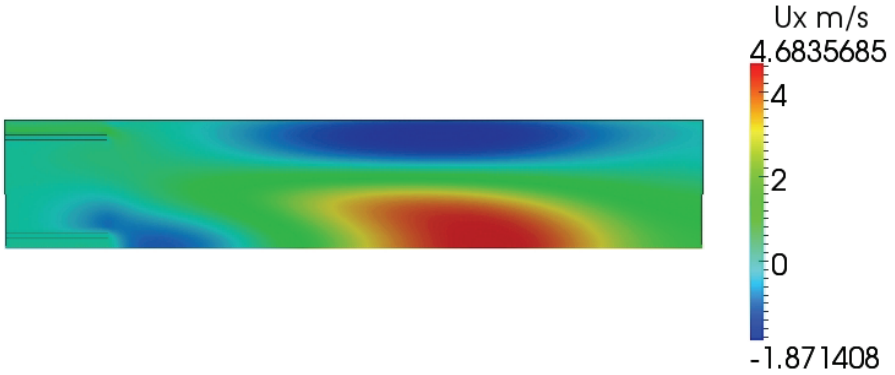

Figure 10: Contours Axial velocity [m/s]

3 Experimental

Currently experimental investigations are being carried out to propose a diagnostic methodology to characterize the behaviour of the plasma flow and the injected particles in the ICP torch for different configurations. The aim is to verify experimentally these behaviours, beside the numerical simulation predictions, to guide on the optimization of torch design more suitable for nanoparticles production applications. These experiments carried out using the VKI minitorch facility will be also a useful support for the real validation of the numerical simulations.

The first stage has been completed with the examination of the ICP torch design and the investigation of flow patterns in the discharge by means of flow visualization on the cold model of the ICP torch.

Smoke was used to visualize the detailed flow pattern of the recirculation zone depending on the range of the Reynolds number. As can be observed in Figure **11**, the annular vortexes are clearly identified and distinct flow patterns are present and associated, in this case with the Reynolds number. Figure **11**(a) shows the typical two annular vortex caused by the flow separation. In Figure **11** (c) it is already notice an inverted zone between the annular vortex, where the axial velocity its positive and Figure **11** (d) the vortex cells became symmetric.

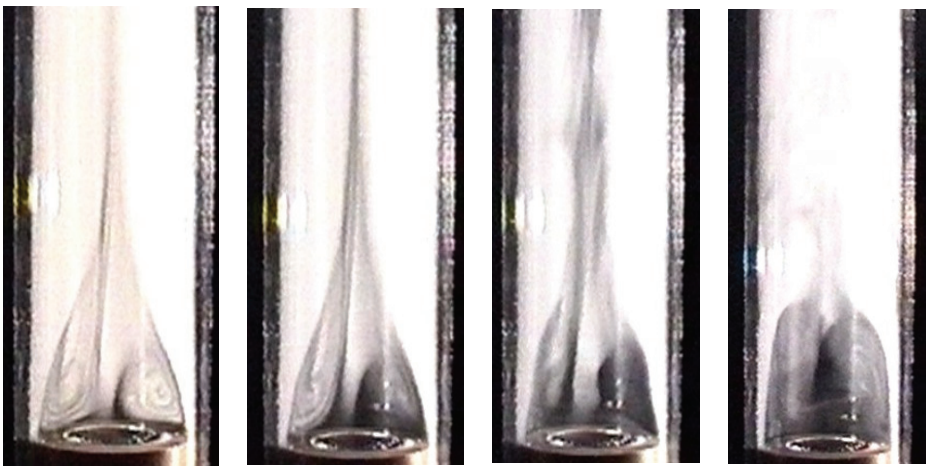

(a) Re≈180 (b) Re≈200 (c) Re≈210 (d) Re≈230

Figure 11: Photograph of the recirculation zone for annular flow injection without swirling

The recirculation zone inside the plasma flow is used as a manner to stabilize the plasma discharge in confined tube. After this visualization it was pointed out that this recirculation zone in some cases is very small or unstable (for example, large distance between the coil and the inner block; bigger than half diameter of the tube), which makes difficult to ignite the plasma and to keep it on stable. To injection overcome this problem a swirling generator with an angle of 60º has been adapted to the actual injection configuration of the Minitorch. With this configuration the swirling motion inside the torch has been improved and plasma discharge could be stabilized even with the distance between the coil and the inner block bigger than two times the diameter of the torch. It can be also realised that with a good swirling flow the inner block could possibly be removed, which can be convenient for some particles injection application.

With the new torch configuration the flow visualization have been performed by injecting some SiO2 particle with the flow and using a high speed camera to follow the particles due to their radiation. The significance of the radiative losses depends on the operating pressure and the nature of the particles. The effect is particularly important at high pressure. Therefore, by operating in relatively high pressure (500mb) the emission of the heated particles inside the plasma in higher than the emission of the plasma, then by filtering the plasma emission it has been possible to follow the particles as can be seen in Figure 12. It is observed that there are particles (with d≈50 μm) with positive velocity going up (red circle) and particles that are going in the reverse way, which means that they are capture by the recirculation zone (black circle), as was expected. Figure 13 and 14 show a cloud of vapour increasing around the particle, identified by the increase on the emission just before they disappear. In the Fig.14, where the particle are much bigger (d≈150 μm), it is observed also that most of the particles do not have enough momentum to follow the flow or to evaporate and a large accumulation is observed at bottom of the inner block (indentified by the intensity of the light emission in this region).

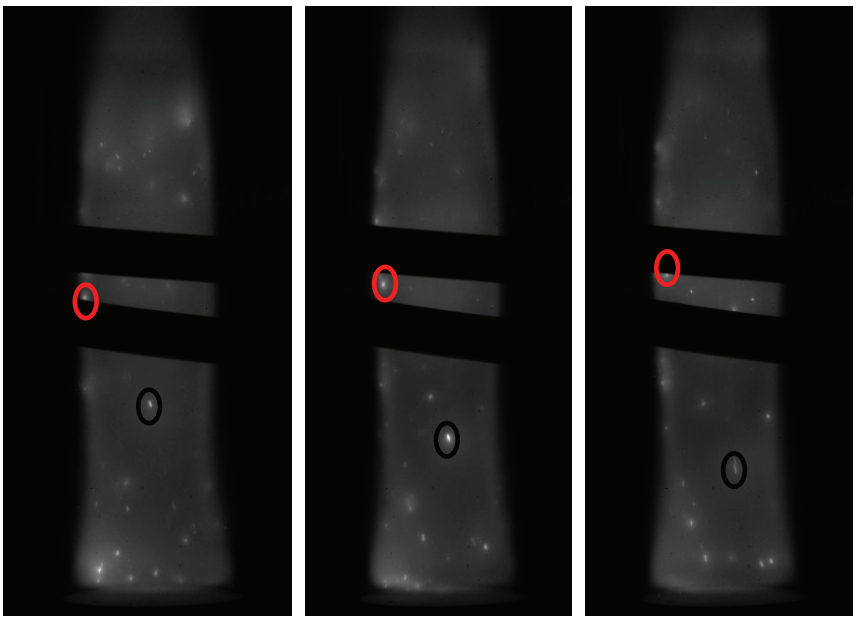

Figure 12: Visualization of the SiO2 particle (d≈50 µm) inside the air plasma of 0.6g/s, 3.5kW

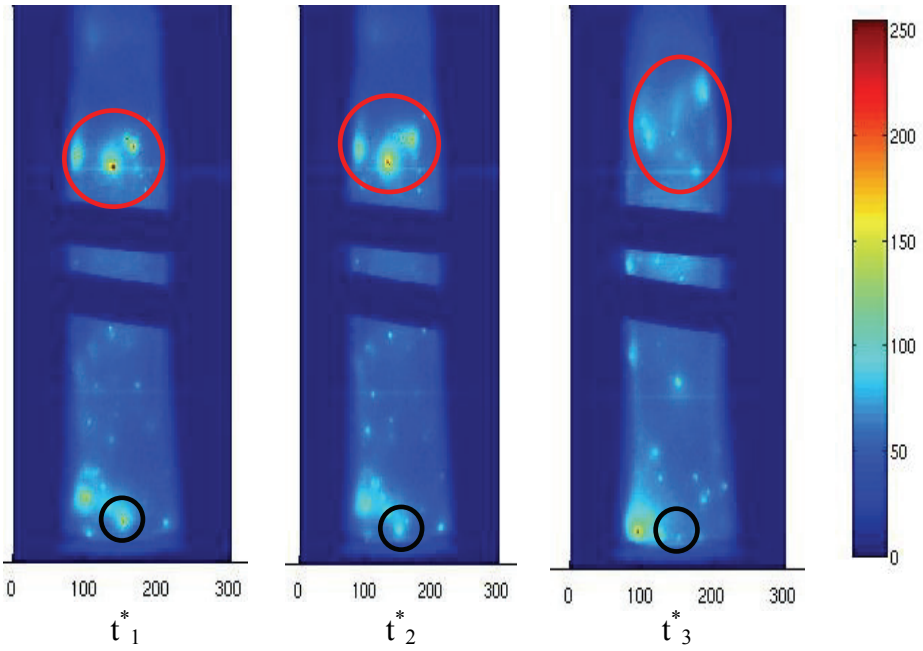

Figure 13: Emission (light intensity) of the SiO2 particle (d≈50 µm) inside the air plasma of 0.6g/s, 3.5kW

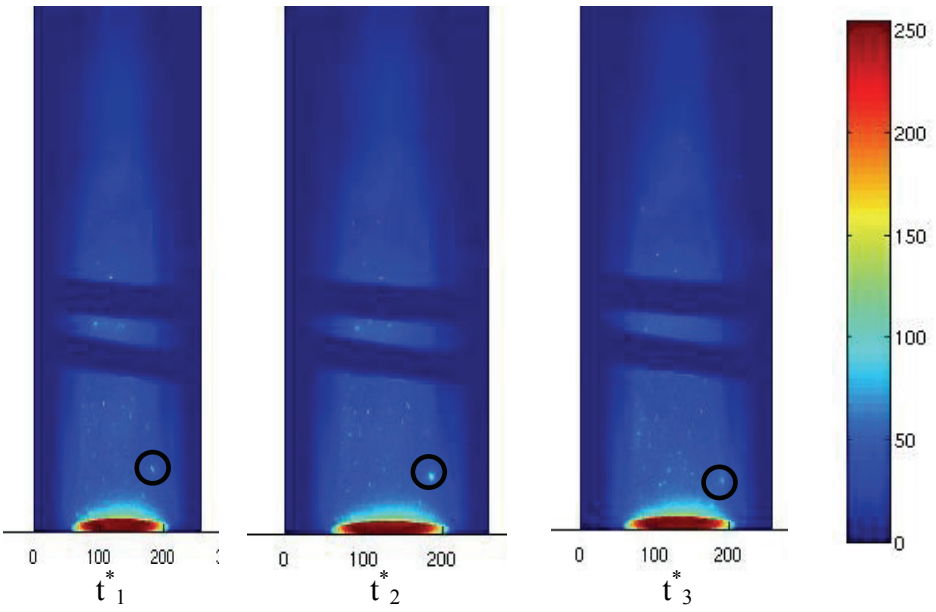

Figure 14: Emission (light intensity) of the SiO2 particle (d≈150 μm) inside the air plasma of 0.6g/s, 3.5kW

4 Conclusion

The model for inductively coupled plasma developed with the open source code, OpenFoam seems to provide solutions that are very much similar to the ones found at literature, using the industrial standard Fluent. On the other hand, the thermodynamic and transport properties of high temperature gases being so important in the prediction of the plasma fields and that could affect the calculations, are easily formulated in OpenFoam and in much more flexible manner. For the future the code is going to be optimized and adapted to nanoparticles formation in inductively coupled plasma.

Concerning to the experimental investigation, although the results obtained at the moment are only qualitative, they already provide some information on the flow topology and how the particles are diffusing in the plasma.

Further experimental techniques namely LDV and spectroscopy measurement are pretended o be used to have better description of the flow and temperature field of the plasma flow, so significant on quality of the finale nanoparicle product.

Acknowledgments

I would like to thank my supervisor Patrick Rambaud and co-supervisor Oliver Chazot and Professor Pierre Proulx and research group at the University of Sherbrooke for all their help and support on this project.

References

[1] S.L.Girshick et al. "Thermal Plasma synthesis of ultrafine iron particles." (Journal of Aerosol science) 24, no. 3 (1993).

[2] Brushan, ed. *Springer Handbook of Nanotechnology.* Springer, 2007.

[3] N.Y. Mendonza-Gonzalez, B. M. Goortani and P. Proulx. "Numerical simulation of silica nanoparticles production in an RF plasma reactor: Effect of quench." (Material science engineering C) 27 (2006).

[4] Watanabe, Masaya Shigeta and Takayuki. "Numerical investigation of cooling effect on platium nanoparticle formation in inductively coupled thermal plasma." (Journal of Applied Physics) 103, no. 074903 (2008).

[5] N.Rao et al. "Nanoparticle formation using a plasma expasion process." (Plasma Chemistry and Plasma processing) 15, no. 4 (1995).

[6] S. Xue, P. Proulx, and M. I. Boulos. "Extented-field electromagnetic model for inductively coupled plasma." (Journal of physics D: Applied physics) 34 (2001).

[7] D. P. Vanden Abeele and G. Degrez. Numerical Model of High-Pressure Air Inductive Plasma Under Thermal and chemical Non-Equilibrium. In Fluids 2000 Conference and Exhibit, Denver, CO, June 2000. AIAA 2000-1453.

Doctoral Project Summary

Plasma tests development for thermal protection system design in real flight conditions

Hyun Woo Krassilchikoff*

Supervisor: Olivier Chazot†

von Karman Institute for Fluid Dynamics, Rhode-Saint-Genèse, 1640, Belgium

Promoter: Miltiadis Papalexandris‡

Université catholique de Louvain, Louvain-la-Neuve, 1348, Belgium

Abstract

In the framework of planetary entry of space vehicles, the Thermal Protection System (TPS) design remains a crucial issue. It must be thick enough to ensure safety yet light to maximize the payload. The design can be studied at the VKI by means of a facility such as the Plasmatron. The purpose of this PhD is to develop an accurate experimental procedure to duplicate a given real flight environment in order to test TPS.

1 Introduction

The final goal of this project is to develop an experimental procedure to test thermal protection material in given flight conditions. The study was achieved for the VKI plasmatron facility, a 1.2 MW inductively coupled plasma generator. A description of the facility can be found in [1]. Briefly, a gas is heated by Joules effect in a torch. The temperature rises up to about 10000 K, which is enough to create dissociations and ionisation of the gas component. When these reactions are sufficiently important to make the gas conductive, the gas is then called plasma.

The structure of the fully subsonic jet in the plasmatron is actually very different from the hypersonic flow encountered in real flight and a theory sometimes known as Local Heat Transfer Simulation (LHTS) in the literature was already developed to make the bridge between real flight and subsonic plasma jet environment [2]. It is important to understand that this bridge is only made locally in the stagnation region. Hence, the experimental procedure developed in this project aims at duplicating the stagnation region of a given real flight situation in the plasmatron.

*PhD Candidate, Aeronautics and Aerospace Department, Chaussée de Waterloo 72, krassilc@vki.ac.be.

†Associate Professor, Aeronautics and Aerospace Department, Chaussée de Waterloo 72, chazot@vki.ac.be.

‡Associate Professor, Département de Mécanique, Unité de Thermodynamique, Place du Levant, 2, miltos@uclouvain.be.

In theory, once the stagnation region can be described with enough accuracy, the theory of LHTS explains how to translate ground facility data into real flight data. Practically, an accurate description of a stagnation region is a difficult task because it requires the quantification of stagnation heat flux, pressure and temperature, the free stream enthalpy and velocity gradient as well as the wall catalycity, which is a wall effect on the chemical recombinations occurring inside the stagnation region. It also requires an accurate boundary layer theory for this specific problem since the Reynolds number is typically low and does not allow the use of classical boundary layer theory. The novelties brought by this project are the experimental quantification of the free stream enthalpy by means of a calorimetric probe, a better understanding of the wall catalycity as well as a correlation of catalycity for cold copper, a consistent flight extrapolation that takes into account any modifications in the boundary layer formulations and a new experimental procedure for TPS design

2 Experimental tools

The experimental setup is illustrated in Fig. 1. A 50 mm of overall diameter probe support is placed at the center of the plasma jet. Several probes can be flush mounted at the center of the probe support. Several probes can be successively injected in the same plasma jet, ensuring that several complementary measurements were taken under the same experimental conditions. This paper will only review the enthalpy measurement,

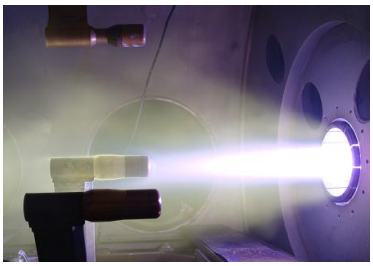

Figure 1: test chamber of the VKI plasmatron

the quantification of the other boundary layer parameters, i.e. pressure, heat flux and velocity gradient, was done according to the state-of-the art. The interested reader will find all the necessary information in [3, 4, 5]. It must be noticed that all the measurements were taken with water cooled probes, hence, the surface temperature can be reasonably estimated at 350 K without making a significant error on the heat flux.

The enthalpy was measured by means of a double jacketed calorimetric probe [6, 7, 8, 9]. Basically, this probe continuously collects a measured quantity of plasma. The enthalpy is transfered from the sampled plasma to the probe by means of a heat exchanger. From energy conservation, the free stream enthalpy H_{g1} is given by eq. 1, provided that all and only the streamlines exchanging heat with the probe are sampled.

$$H_{g1} = H_{g2} + \frac{\dot{m}_w}{\dot{m}_g} c_p \left(T_{w2} - T_{w1}\right) \tag{1}$$

where H is the enthalpy, T is the temperature, $\dot{m}$ is the mass flow rate, subscripts 1 and 2 refers respectively to the inlet and the outlet, subscripts w and g refers respectively to water and gas.

This particular sampling mass flow rate is qualified balanced. If the mass flow rate is higher, some of the sampled streamlines will exchange energy with the insulating jacket, resulting in a lower measurement of the specific enthalpy. If the mass flow rate lower, some not sampled streamlines will exchange energy with the probe, resulting in a higher measurement of the specific enthalpy 2. Bearing this in mind, it can be understood that the enthalpy probe will give a response of the type eq. 2.

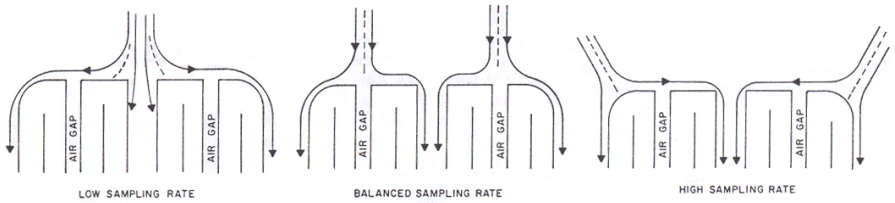

Figure 2: Three schematics of flow patterns sampled by the enthalpy probe. The insulating jacket is outside, the sensitive device is the heat exchanger at the center.

$$H_{read} = A\frac{1}{\dot{m}_g} + B \tag{2}$$

This response was measured in the plasmatron with a 16 g/s air plasma jet at several test conditions ranging from 10000 to 20000 pa and 130 to 210 kW. Eq. 3, i.e. an expression of the sampled mass flow rate assuming that the enthalpy is constant all the over the stagnation ring, is the missing equation to close the system and provide the enthalpy solution. All the results are presented in the next section.

$$\dot{m}_g = \rho_{(H_{read})} V S = \rho_{(H_{read})} \sqrt{\frac{2p_{dyn}}{\rho_{(H_{read})} k_p}} \pi R^2 \tag{3}$$

Where V is the free stream velocity, S is the surface inside the stagnation ring, R is the radius of the calorimetric probe and k_p is the Barker correction coefficient required at low Reynolds number [10], p_{dyn} is the dynamic pressure.

3 Catalycity

Strong temperature gradients take place in the boundary layer, due to the important difference of temperature between the wall and the free stream. As a consequence, the dissociated particles tend to recombine closer to the wall. It must be noticed that the reactions that occur are detrimental to the vehicle since they are exothermic and hence, significantly increase the heat load. Yet, for typical atmospheric entry problems, the recombination process is actually often too long to take place when reaching the cold wall. Consequently, the flow is often in local non-equilibrium in the stagnation region. In this recombination process however, the wall can act as a catalyst of these detrimental recombination reactions and a material with low catalycity must therefore be carefully chosen.

A simplified catalycity, or recombination efficiency, model such as the one used by Goulard [11] was chosen. It is defined as the ratio of the number of atoms recombining on the surface per unit area per unit time over the total number of atoms striking the wall

per unit area per unit time. The enthalpy can be computed numerically as a function of catalycity when wall temperature, heat flux, pressure, and velocity gradient are given. The result is a typical curve with two plateaus, as shown in Fig. 3 for cold copper (350 K). The superimposition of the experimentally measured enthalpy gives a value for wall catalycity. More details about this method can be found in [12]. This procedure was repeated for all the measurements taken in section 2 and all the results are plotted in Fig. 3. No trend can be observed with respect to the static pressure but with respect to the

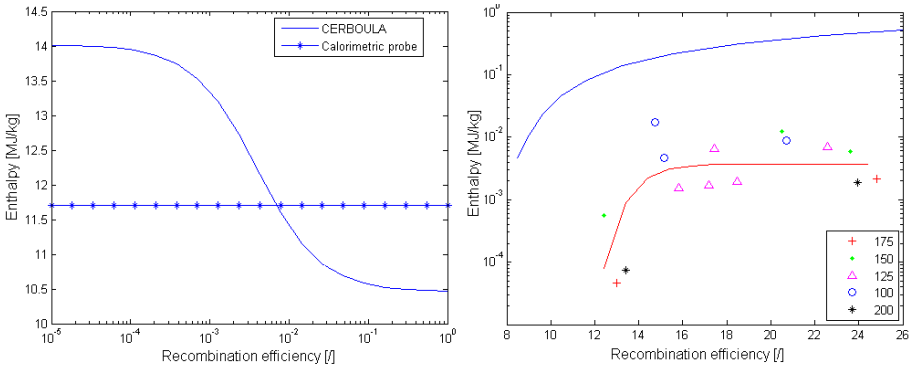

Figure 3: Left: Catalycity result taken from [6] - Rigth: Catalycity results for cold copper as function of free stream enthalpy. The upper curve is the concentration of recombinable species, the lower curve is a correlation (eq. 4)

enthalpy, catalycity of copper seems to increase and reach a plateau of $\gamma = 3.73\ 10^{-3}$ around 16 MJ/kg. Eq. 4 is a correlation of the data (H in MJ/kg).

$$\gamma = 0.00373\ 10^{-414670.exp(-H)} \tag{4}$$

It is interesting to superimpose the ratio of the numbers of recombinable and total particles of the plasma. This curve does not vary significantly for the range of pressure of this study. This can explain why cold copper catalycity is not influenced by the pressure. This figure also shows that both trends are similar. This figure seems to tell that for a given material and velocity gradient, it makes more sense to analyse catalycity as a function of recombinable species instead of the BL parameters such as temperature and pressure.

4 Flight extrapolation and experimental procedure for TPS testing

An inverse method was proposed for this project in order to address the different BL formulations that can be considered for a low Reynolds boundary layer. At a typical value of 100, the BL is so thick that classical BL theory cannot be applied anymore. And since the BL thickness must be taken into account, a particular BL solver will closely depends on the considered definition of BL thickness [13, 14, 15, 16]. The idea of the suggested method is to find the size of the non-catalytic sphere in hypersonic flow that will experience the non-catalytic heat flux determined from experiments under conditions of enthalpy and pressure also measured experimentally. The interested reader will find more details about this method and its implementation in [13].

The previous chapters reviewed a complete method to characterize the stagnation region, i.e. wall heat flux, temperature, pressure and catalycity as well as free stream enthalpy and velocity gradient, in the VKI plasmatron. Kolesnikov [17] explained how to link vehicle speed and altitude to total enthalpy and pressure in ground facility. Now the last remaining problem is to determine the geometry of the probe that can be matched with the one of the vehicle. This can be done by using the same inverse method the other way around.

Practically, the analysis of a given real flight heat environment in the stagnation region can be achieved following these four steps:

1. a CFD simulation of a non-catalytic sphere in hypersonic flow in flight conditions will provide the non-catalytic heat flux that must be aimed by the calorimeter in the test chamber.

2. the altitude-speed trajectory will provide the enthalpy and static pressure that must be created inside the plasmatron test chamber.

3. the analysis of three stagnation regions created before three probes with different radii but exposed to the free stream conditions computed in the previous step will provide the probe radius. This is done by matching the non-catalytic heat fluxes with the one computed in step 1.

4. a TPS sample can be then flush mounted on a probe support of a radius determined in step 3 and tested in conditions of enthalpy and static pressure determined in step 2.

5 Conclusion

Several new tools and procedures were developed in order to analyse the environment created inside the VKI plasmatron facility. The calorimetric probe for enthalpy measurement was reviewed and an original procedure was proposed in order to achieve balanced sampling rate. On the other hand, the cold copper catalycity identification was improved and it was then possible to obtain a data base of enthalpy and catalycity of copper. It was also shown that static pressure does not have a significant impact on the value of catalycity while the enthalpy seems to play a major role below $16\ MJ/kg$. All these dependencies can be explained by the availability of recombinable particles. A correlation of catalycity of copper was proposed as function of enthalpy. These new tools together with other existing probes and method (for pressure, heat flux and velocity gradient) are enough to fully characterize a stagnation region created in the plasmatron test chamber.

An inverse method was also proposed for flight extrapolation. This method has the major advantage of being applicable for any definition of low Reynolds boundary layer thickness. It can also be applied the other way around to determine the setup that must be used in order the duplicate the real flight conditions in a ground test facility.

References

[1] B. Bottin, O. Chazot, M. Carbonaro, V. Van Der Haegen and S. Paris, The VKI plasmatron characteristics and performance RTO-EN8, art.6

[2] A.F. Kolesnikov, An efficient modeling stagnation point heat transfer for subsonic aerothermal test conditions, VKI Technical Note 200, Jan. 2001

[3] ASTM E 457-96, Standard test method for measuring heat-transfer rate using a thermal capacitance (slug) calorimeter.

[4] ASTM E 422-99, Standard test method for measuring heat flux using a water-cooled calorimeter

[5] H. Krassilchikoff, O. Chazot and J. Thmel, Procedure for the determination of cold copper recombination efficiency. 2nd EUCASS conf., Bruxelles, July 2007

[6] H. Krassilchikoff, O. Chazot, Enthalpy determination for ground testing conditions in plasma wind tunnel. ESA congrex, Versailles 2008

[7] J. Grey, P.F. Jacobs and M.P. Sherman, Calorimetric probe for the measurement of extremely high temperatures, The review of scientific instruments, Vol 33 No 7, pp 738-741, Jul 1962

[8] A.A. Ovsyannikov, M.F. Zhukov, Plasma diagnostics, Cambridge international science publishing, 2000

[9] S. Katta, J.A. Lewis and W.H. Gauvin, A plasma calorimetric probe, Rev. Sci. Instrum., Vol 44, No 10, pp 1519-1523, Oct 1973

[10] M. Barker, On the use of very small Pitot tubes for measuring wind velocity, Proc. Roy. Soc., London, AIOI, 1922, pp 435-445

[11] R. Goulard, On catalytic recombination rates in hypersonic stagnation heat transfer, AIAA, Vol. 25, No. 11, pp. 737-745, Nov. 1958

[12] H. Krassilchikoff and O. Chazot, Characterization of plasma environment in the VKI plasmatron facility. 2nd NEPCAP conf., Sochi, Ocotber 2009

[13] H. Krassilchikoff, K. Bensassi, A. Lani, M. Panesi and O. Chazot, Flight extrapolation at low Reynolds number. 3rd EUCASS conf., Versailles, July 2009

[14] G. Tirskii, Continuum models in problems of the hypersonic flow of a rarified gas around blunt bodies, J. Appl. Maths Mechs, Vol. 61, No. 6, 1997, pp 875-900

[15] P. Barbante, Accurate and efficient modeling of high temperature nonequilibrium air flows, VKI PhD Thesis, 2001

[16] M. Van Dyke, Second-order compressible boundary layer theory with application to blunt bodies in supersonic flow, Jet prop., Vol. 28, No. 11, Nov 1958, pp 737-745

[17] A.F.Kolesnikov, Extrapolation from high enthalpy tests to flight based on the concept of the local heat transfer simulation, RTO EN-8, Course on measurement techniques for high enthalpy and plasma flow, Belgium, Oct 1999

TURBINE FLOWS

Doctoral Project Summary

Interaction of an Innovative LP Stator Vane with a Transonic HP Turbine Stage

Sergio Lavagnoli*

Supervisor: Prof. Guillermo Paniagua†

von Karman for Fluid Dynamics, Rhode-Saint-Genèse, 1640, Belgium

Promoter: Prof. Francisco Payri González‡

Universidad Politécnica de Valencia, Valencia, 46022, Spain

Abstract

Increasing fuel costs and environmental restrictions force aero-engine designers towards high bypass ratio engines. Such architecture requires a decrease in the fan rotational speed, and therefore a reduction in the low pressure turbine (LPT) peripheral speed in conventional designs. This paper analyzes the aerodynamics of an innovative splitter guide vane configuration mounted in a swan-neck diffuser. The swan-neck diffuser allows preserving the LPT peripheral speed as well as the turbine loading, while keeping the engine length. The aerodynamic performance of such configuration is studied using numerical and experimental resources at engine representative conditions. The results are presented considering the steady and unsteady performance of the new concept.

1 Introduction

The quest for higher performances and durability for modern aero-engines requires the understanding of the complex flow field experienced by the gas turbine stages. Ultra-high bypass ratio aero-engines with increased fan diameters demand a reduction of rotational speed to maintain an acceptable tip velocity. Hence, the LP turbine radius must be increased in order to keep an acceptable level of efficiency [1]. Furthermore, to reduce the axial length of the whole machine, a swan-neck diffuser is adopted to link the HP turbine to the LP guide vane. Usually such transition ducts are equipped with big struts that are used to support the engine shaft and to route service pipes. Their large size represents an effective obstacle for the flow coming from the HP turbine and causes higher losses. Many investigations report on the aerodynamic flow field in s-shaped duct. Among them a wide research has been carried out by Dominy et al. [2].

* PhD Candidate, Turbomachinery and Propulsion department, Chaussée de Waterloo 72, lavagnoli@vki.ac.be

† Associate Professor, Turbomachinery and Propulsion department, Chaussée de Waterloo 72, paniagua@vki.ac.be

‡ Professor, Departamento de Máquinas y Motores Térmicos, Camino de Vera s/n, fpayri@mot.upv.es

The performance of a compact engine is highly affected by the blade row interactions. The periodic convection of wakes coming from the upstream stage and the unsteadiness introduced by the trailing edge shock system have a strong influence on the flow field of the next blade row. An intense research activity has been carried out by different research groups on the characterization of the flow field of a single stage turbine. Among them Giles [3], Hilditch et al. [4], Dénos et al. [5], Miller et al. [6], Paniagua et al. [7]. Less work has been done on the effect of the HP turbine on the components downstream and their mutual interaction. Billiard et al. [8] investigated the effect of clocking on the aero-thermal performance of one and a half turbine stage. They report the positive effect of the vane-vane interaction in dumping the rotor shock wave if the LP vane leading edge is clocked with the incoming wake avenue. An explanation for this phenomenon was proposed by Hummel [9] by means of a numerical investigation on a transonic HPT. Hummel suggests that the interaction between the first vane avenue and the rotor wake with the rotor trailing edge shock waves can reduce the shock strength of 50% for optimum clocking positions and axial blade row spacing. Schennach et al. [10] observed the weakening of the rotor shock waves when the next vane row is at an optimum clocking position. They also reported that the impingement of the first stator wake on the second vane leading edge lowered the pressure fluctuations in this region. Reinmöller et al. [11] found that the shift of the first vane wake avenue due to the clocking alters the turbulence and the velocity distribution at the second vane outlet.

Li and He [12] performed numerical computations to study the influence of blade count on the unsteady flow field of a three blade row turbine. The results show that a blade count difference between the first and the second stator vane produces a relevant circumferential unsteady blade force variation with a periodicity imposed by the blade count difference itself. Additionally, the stator vanes may experience periodic distortions due to the NGV vane wake avenues and the rotor passage at the same frequency. The phasing between these occurrences is only determined by the NGV-stator clocking position. Miller et al. [13], [14] reported time-resolved pressure measurements and computational predictions on a rotor blade of a high-pressure turbine coupled with a vane located in a swan-necked diffuser. The results inferred that the second stator potential field has a great influence on the rotor throat region and strongly interacts with the trailing edge shock system of the first vane. The interaction frequency depends on the blade row counting. Davis et al. [15] carried out experimental and numerical research on a similar turbine architecture. The authors concluded that the interaction between the rotor and the second vane increased the unsteadiness in both rows but slightly affected the overall aerodynamic losses. The shock patterns emanated from the rotor trailing edge can be either swept forward inside the vane passage or reflected by the duct both towards the second vane and backwards to the rotor. Analogous results were reported by Haldeman et al. [16] for an experimental investigation on the clocking effect in one and a half turbine stage. They suggested that the unsteadiness created by the reflections from the transition duct and the LP vane can be modified by the clocking position.

In the frame of new engine architectures, an innovative stator for the LP turbine is proposed with a multi-splitter configuration. The struts have been re-designed from an aerodynamic point of view and included in the LP vane together with small aero-vanes. The LP vane is placed inside the S-shaped transition duct to further reduce the engine dimensions. Little public research has been carried out on this subject before and the aerodynamics of a non-uniform vane row has not previously been studied. One of the pioneer works on splitter vanes has been provided by Zhou et al. [17], [18]. The airfoil design, blade placement and number of splitter vanes to be used for

such configuration were explained for the case of impulse steam turbines. The authors proposed to maintain the same mass flow to pass in every vane passage, i.e. the pitch must be the same for each blade-to-blade channel. Numerical calculations provided velocity distributions and profile losses for three vane configurations with one, two and three smaller aero-vanes. Kodama et al. [19] studied a non-uniform spaced vane row to control and improve the performance of the strut-stator system. They focused on the noise production due to the potential field interaction at different stator stagger angles. Similar numerical studies on a rotor-stator-strut configuration were presented by Cerri et al. [20], [21] and Parry et al. [22]. The authors suggest that blade row interactions can be reduced by using non-uniform re-staggering the airfoils along the circumferential direction. Ro et al. [23] proposed to control the horse shoe vortex generation by applying cut splittered vanes at the endwalls in between the blade passage. The local improvement by the horseshoe vortex control was counterbalanced by the negative effect of wake generation downstream the splitter vanes.
In the current study the flow field of an innovative LPT stator located downstream of a high pressure turbine is investigated experimentally. The testing is carried out for three operating conditions. The performance of each airfoil type is measured by pressure transducers at mid-span for each case. The characterization of the unsteady rotor–LP stator interaction is conducted for flight conditions. The present investigation aims to provide an experimental database to improve future civil aero-engine design and CFD simulations.

2 Experimental Methodology

The model turbine is a combination of a single stage high pressure turbine (HPT) and a LP guide vane located in a swan-neck diffuser. The HPT consists of 43 cylindrical stator vanes and 64 3D rotor blades. The LP stator is composed of 16 big aerodynamic struts and 48 smaller airfoils (aero-vanes), arranged in a multi-splitter configuration. Three small aero-vanes are located in every large structural vane pitch, the resulting four passages are identical in an attempt to maintain the same massflow distribution. The big aerodynamic struts and the aerovanes have the same rear profile to ensure a uniform outlet gas flow. The airfoil configuration and the meridional view of the model turbine are depicted in Figure 1. The low aspect ratio and the large maximum blade thickness for the strut vanes are imposed by the design objectives. The axial gap between the struts and the rotor is 1.15 of the rotor axial chord while the axial gap between the rotor and the upstream stator is 0.41 of the rotor axial chord. Additional information on the blade rows geometry is reported in Table 1. For the transition duct, a mean slope of 30 deg. has been selected. This is a good compromise between the diffusion rate that takes place in the duct and the constraint to avoid boundary layer separation in particular at tip section.

The turbine is tested in von Karman Institute compression tube facility. This short duration facility is able to simulate the aero-thermal performance of highly loaded high pressure turbines in a larger scale. It reproduces independently temperature ratios, Reynolds and Mach numbers of the actual engine conditions. The facility consists of two volumes separated by a fast opening valve (Figure 2). In the compression tube, the air is compressed by a free piston. The isentropically compressed air is discharged to the test section and dump tank. The schematic of the facility and the change of operating conditions during a typical test are plotted in Figure 2. Further details on the operation cycle are provided by Dénos and Paniagua [24].

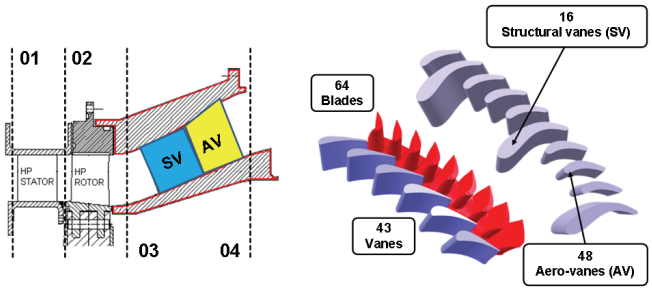

Figure 1: Meridional view of the test section (left), HP turbine and LP vane 3D view (right).

	HPT		LPV	
	Stator	Rotor	Strut	Aerovane
Blades	43	64	16	48
g/C	0.75	0.75	1.43	0.73
H/C	0.70	1.05	0.52	1.10
$C_{ax}/C_{ax,r}$	1.03	1.00	2.58	1.14

Table 1: Summary of the blade row geometries at mid-span.

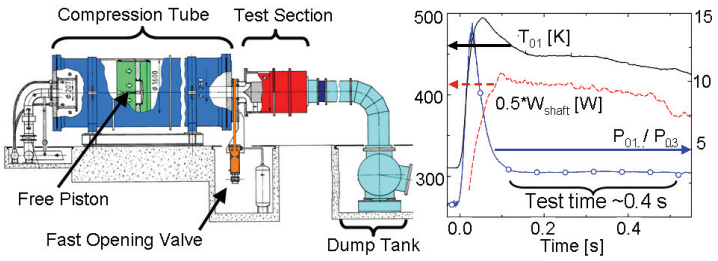

Figure 2: Compression tube facility overview (left), change of conditions in a typical test (right).

Four measurement planes are located in the facility in axial direction (Figure 1-left), namely turbine inlet (1), stator exit (2), rotor exit (3) and LP vane exit (4). Additionally, one sector composed of three aero-vanes and one structural vane is housing the instrumented blades. In plane 1, 3 and 4 reference probes located at 50% of the channel height are used to check the operating conditions. 19 pneumatic taps and 17 piezo-resistive pressure transducers are distributed around 2 aero-vanes (Figure 3). A structural vane is equipped with 27 pneumatic taps and a second one is instrumented with 25 piezo-resistive transducers. All instrumentation is located at mid-span of the airfoils. Figure 3 shows the distribution of the measurement locations around the blades. The mean values are acquired with a sampling rate of 1.5 kHz. The unsteady data are high-pass filtered at 100 Hz and amplified by 10 then, sampled at 300 kHz. The steady results are time averaged for duration of 40 ms. The Phase-Lock-Averaging (PLA) is applied for three rotor revolutions (192 blade passing) to the unsteady raw signal to distinguish the deterministic variation from the random ones.

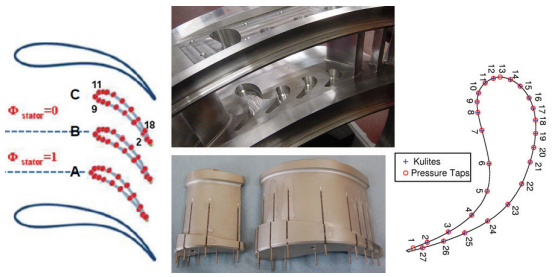

Figure 3: Location of the instrumentation around both LP vanes

3 Numerical tools

Three-dimensional computations have been carried out by ONERA with its in-house CFD software *elsA*. This software is capable of solving compressible three-dimensional Reynolds averaged Navier-Stokes equations in the relative frame of reference. The *elsA* solver uses a multi-domain approach on structured meshes and a cell-centered finite volume scheme. The time integration is accomplished with a backward-Euler scheme coupled to an LU implicit phase technique. The calculations presented in this paper have been achieved with the one equation Spalart-Allmaras turbulence model.

In the present case, the unsteady computations have been performed with a blade count reduction: the computational domain is composed of 3 HP stators, 4 rotors, one structural vane and 3 aero-vanes. The computational grid is meshed with a 63 blocks structured grid including 20×10^6 points. "O-blocks" are used around the blades, and "H-blocks" fill the rest of the passage. The rotor tip clearance gap is also taken into account. The values of the normalized distance of first wall cell (y+) at the blade wall is between 1~2.

Boundary conditions based on the characteristics method are prescribed at the stage inlet and outlet. The stage pressure ratio is specified at the hub outlet, and then radial equilibrium is applied. Walls are treated applying a non-slip condition associated with a uniform temperature distribution ($T_w = 291.5$ K). The unsteadiness induced by the blade passing is taken into account through the use of the reduce blade count approach [25] with a stage reduction matching conditions at the interface between adjacent blade rows.

4 Results

4.1 Operating conditions

The investigation has been carried out for 3 operating conditions. The stage pressure ratio (P_{01}/P_3) of 2.92 and a rotational speed of 6790 RPM that represent the fly condition of an engine is chosen as nominal condition (Nom-Nom). At this condition, the LP vane is choked and limits the stage pressure ratio. The effect of pressure ratio is studied by reducing the stage pressure ratio down to 1.92 while keeping the rotational speed constant (Low-Nom). At the off-design condition, the inlet flow angle for the LP vane changes drastically. To avoid this large flow angle variation, a

third test condition is selected for the same low pressure ratio by reducing the rotational speed down to 4500 RPM (Low-Low). The measured test conditions for three cases are listed in Table 2. A Non-ISentropic Radial Equilibrium (NISRE) calculation is also performed for a single HP stage to get detailed information about the stage exit flow properties (Table 3).

	Rotational Speed	P_{01}/P_3	P_{01}/P_4	$M_{2is,hub}$
Nom-Nom	6785	2.92	3.76	1.09
Low-Nom	6788	1.92	2.05	0.90
Low-Low	4520	1.93	2.07	0.97

Table 2: Summary of the test conditions

	$M_{2,hub}$	M_{3r}	M_3	α_3
Nom-Nom	1.15	0.89	0.42	12.5
Low-Nom	0.92	0.59	0.31	-25.3
Low-Low	0.96	0.60	0.30	14.2

Table 3: Results of NISRE calculation

4.2 Steady pressure field of the LP stator

4.2.1 Structural vane aerodynamics

Measurements of surface pressure around the structural vane at the mid-span section are shown in Figure 4 for the three test conditions. Pressure side and suction side pressure envelopes are plotted in separated graphs. The non-dimensional measured static pressure at each gauge location is plotted as a function of the non-dimensional curvilinear abscissa. Three regions can be recognized in the strut pressure distribution for design condition. In the front part a steep acceleration occurs for both suction and pressure side promoted by the large curvature of the strut leading edge and the positive flow incidence. The flow decelerates between S/S_{max} ~10 % up to S/S_{max} ~50 %. The increase of area in the transition channel is not counter-balanced by the low curvature of the strut profile in that zone resulting in diffusion. In the rear part, flow is well guided by both the strut and small aero-vane profiles. The turning imposed by the blades is enough to oppose the diffusion generated by the interturbine channel and accelerates the flow up to the geometric throat. The same considerations can be extended to the pressure field measured at *Low-Low* off-design condition.
When the turbine operates at *Low-Nom* regime, the rotor outlet flow angle changes significantly. The flow impinges on the strut with a large negative incidence (-25 deg.). The detrimental effect on the aerodynamics is clearly visible on the pressure profile. The stagnation point moves to the suction side (S/S_{max}= 7 %). The flow abruptly accelerates on the pressure side leading edge region. At S/S_{max} ~20% the boundary layer detaches because of the strong adverse pressure gradient that closely follows the velocity peak. The separated region extends along most part of the strut pressure side. It is also enhanced by the diffusion imposed by the transition duct at that axial position. The detached flow region evidently affects the pressure field of the

adjacent small vane (aero-vane C). On the suction surface, the flow remains attached and smoothly accelerates up to the throat region.

4.2.2 Aero-vane aerodynamics

The steady pressure fields around three small aerofoils are displayed in Figure 4-bottom. The presence of the large structural vane alters sensibly the aerodynamic flow field of the small vanes in the front part. The outlet rotor flow structures are disturbed as the flow enters the low aspect-ratio vane. The struts cause an evident blockage effect and worsen the circumferential non-uniformity of the aero-vane inlet flow field. Hence, the flow field in the aero-vanes' leading edge region is distorted. The surfaces adjacent to the strut profiles (pressure side of vane A and suction side of vane C) are the most affected. The experimental results show large velocity peaks for aero-vane A on the pressure side measurements. This can be explained by directed inlet flow. The flow accelerates and turns as it follows the profile of the strut. Thus, it impinges to the vane A with a negative incidence. Moving from vane A to vane C, the peak is reduced in size as the flow incidence reduces but still an important difference exists between two adjacent airfoils. On the suction surface, three aero-vanes present similar trends when the incidence angle is positive. As it can be expected, the vane load at *Low-Low* condition is different but smooth flow acceleration is preserved.
At *Low-Nom* case the rotor absolute exit flow angle is drastically modified (-25 deg.) and flow separates on the strut pressure side. The suction side of vane C is substantially affected by the flow structure distortion imposed by the structural vane.

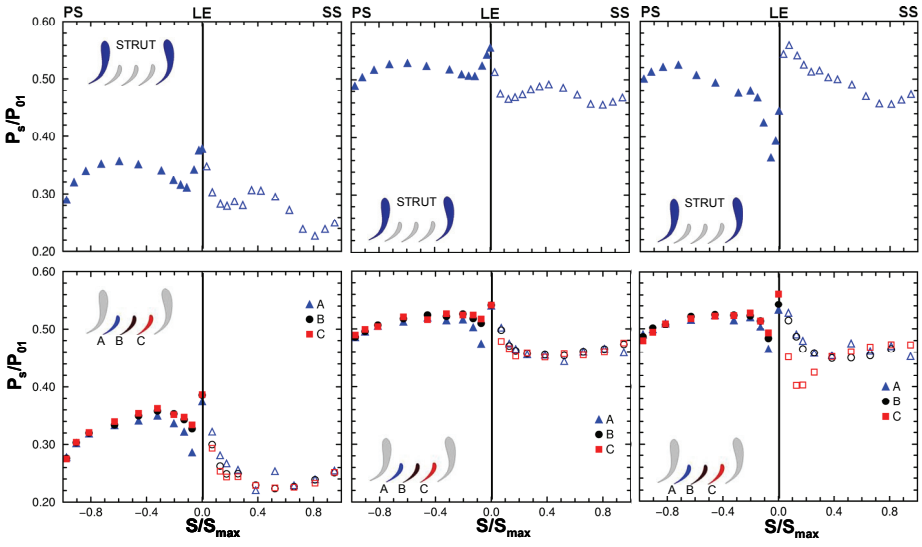

Figure 4: Steady static pressure distribution on stator strut (top) and aerovanes (bottom) at three operating conditions: Nom-Nom (left), Low-Low (center) and Low-Nom (right).

The resulting velocity profile is dominated by a large velocity peak in the leading edge neighbourhood.
The low-speed recirculation structure obstructs a wide portion of the vane passage as it is clearly showed by the CFD snapshot in Figure 7. The flow steeply accelerates on the vane C suction surface due to this blockage effect. However, the flow still attacks the three aero-vanes with a negative incidence. Thus, the velocity peak on the vane C pressure side is larger than what has been measured for the positive incidence turbine regimes. The negative flow incidence strengthens the velocity peaks on the pressure side of vane A and B compared to the case of *Low–Low* condition.
At the rear part of the airfoils, the pressure levels are very similar and they merge after S/S_{max} =0.40-0.50. This characteristic is present for all conditions.

4.2.3 Unsteady pressure field of Aero-vanes

The interaction between the rotor and the aero-vane is presented only for the design conditions (*Nom-Nom*) focusing on the effect of the vane position. Additionally, the separated flow region (at *Low-Nom*) between the aero-vane C and structural vane is discussed. The measured time-resolved surface pressure is shown in Figure 5 at several gauge locations together with the frequency analysis. The pressure fluctuations are presented normalized by the rotor outlet total pressure (P_{03}). The phase-locked average is plotted as a function of the rotor phase Φ_r which is a normalization of a rotor blade pitch. The zero phase corresponds to the time when the rotor blade leading edge is aligned with the leading edge of the aerovane. Because of the large amount of data (18 gauges x 3 aerovane positions), only few representative gauges have been considered for the present flow analysis.
At airfoil leading edge (gauges 10), the 3rd harmonic of the blade passing frequency appears as the dominant frequency for all three positions. At position B, the pressure variation is stronger than the other positions by 20 % of P_{03}. The relatively high spectrum amplitude in a wide low frequency band (<1 kHz) is likely to be caused by the rotor blade signature effect which is most sensed by the exposed leading edge gauge.
At gauge 14, the unsteadiness is dominated by the rotor passing frequency for all vanes. The level of variations differs depending on the position mainly due to the presence of the structural vanes. Two local pressure drops are recognized for vane C. The first one (around phase 0.2) is caused by the rotor wake which hits the vane C and moves towards the suction side. The impact of the spot is rather small being 2%. The second region starts around phase 0.35 and ends up at phase 1.05. In this period, the pressure decreases by 5% due to the sweeping of the rotor unsteadiness to the pressure side of the structural vane. The rotor non-uniform flow field hits the vane B earlier than the vane C at phase 0.05. The impingement occurs early because the structural vane passage changes the flow direction as well as the aero-vane inlet flow angle. Due to the sweeping of the unsteadiness, the pressure is lower by 8% of P_{03}. Vane A experiences the rotor unsteadiness probably around phase 0.25 that varies the pressure by 5% of P_{03}.

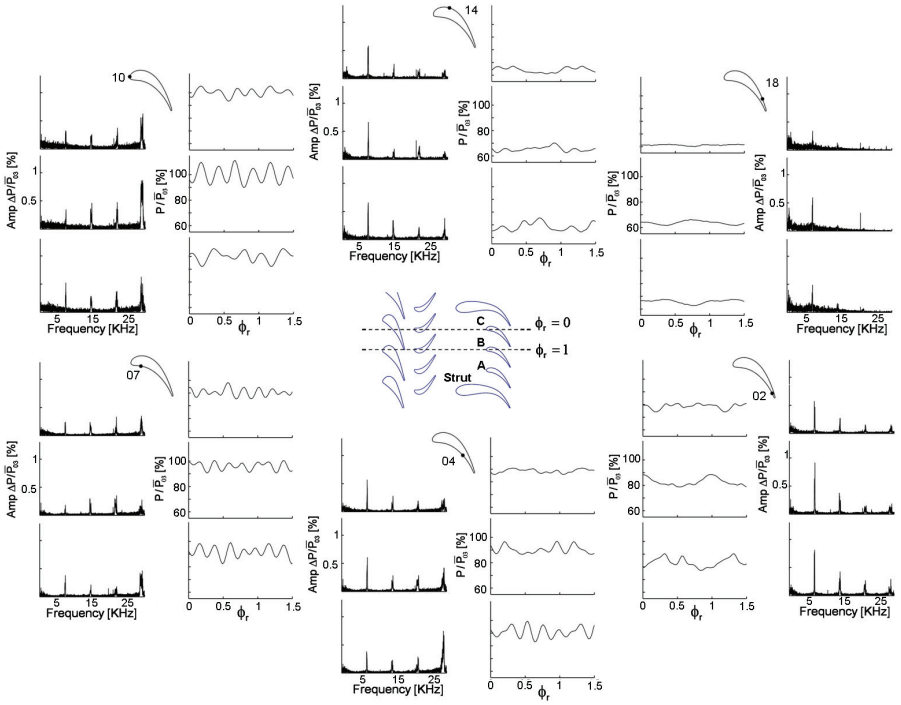

Figure 5: Phase-resolved and frequency content surface pressure of fast response sensors for aero-vane A, B and C. Test at nominal PR – 6790 RPM

A second region that causes a pressure reduction by 9% of P_{03} appears around phase 0.75, which can be attributed to the blockage effect of the strut. At the pressure side gauge 7, the pressure oscillations look similar to the one at the stagnation point. For gauge 4, the rotor passing frequency becomes dominant for vane B and C whereas the 3rd harmonic still has the maximum amplitude at vane A. The pressure variation is slightly lower (about 4%) at position C. However, the variation becomes 10% of P_{03} at vane B. At this position, two pressure deficits are presented. The complex rotor outlet flow fits the vane B leading edge. By the movement of the rotor, it sweeps pressure side towards the trailing edge. This phenomenon results in a pressure drop in a wide range starting from phase 0.23 to 0.95. Then, a second sudden pressure change occurs around phase 1.1 due to the presence of the adjacent vane. The rotor unsteadiness hitting the vane A front suction side is responsible from the sudden pressure drop. Both phenomena affect the pressure value equally. At rear pressure side, close to the trailing edge (gauge 2), rotor blade passing has a strong influence on the pressure variations. At vane C, a pressure deficit (5% of P_{03}) is amplified in comparison to the one at gauge 4. It covers only 26% of the period. Since the strong pressure variation appears only for a short period, the pressure deficit is probably generated by the rotor unsteadiness which hits the vane B crown. The rotor wake sweeping the vane C pressure side by the rotor movement is not recognized. At vane B, two pressure deficits are not distinguished anymore. A single low pressure region remains for 90% of the blade passing period. The variation of 8% is slightly higher than the variation of vane C. Two low pressure regions exist clearly close to the strut suction side. At the phase 0.46, the rotor unsteadiness that impinges on

vane A and sweeps towards the pressure side affects the pressure measurements and causes a pressure drop of 9%. Then, a second low pressure zone is detected at a phase between 0.6 and 1.25. This area is generated by the rotor unsteadiness impinging on the strut and moving towards the suction side. It varies the pressure by 12% of P_{03}.

The Fourier analysis is performed for all gauges around the blade at three positions. The frequency content of all signals and changes of their magnitudes are plotted inFigure 6. For all gauges, the blade passing frequency and its harmonics are well captured. Additionally, the low frequency components appear to increase in magnitude towards to trailing edge at the rear suction side at all positions. It is mainly due to the unguided behaviour of the flow. The peak frequency differs depending on the position. At vane A, the peak appears around 400 Hz whereas the peak frequency increases to 600 Hz and 1000 Hz at vane B and C, respectively. The 3rd harmonic is the dominant frequency around the leading edge region at all locations. Its effect is maintained especially at vane A the front pressure side and at vane C crown. It also shows that its magnitude is linked with the presence of the structural vane. The magnitude of blade passing frequency is amplified all along the pressure side whereas it is constant up to the throat in the suction side and then it starts to diminish for all positions.

The unsteady flow field changes significantly depending on the aerovane position. The aerovane inlet flow is spatially non-periodic from one vane passage to another along the pitchwise direction if one full strut pitch is considered. The presence of the strut certainly modifies the transport and mixing out processes of the unsteady flow structures generated by the upstream stage when the rotor passes in the proximity of the strut leading edge. Additionally, rotor traversing in the strut leading edge region alters locally the rotor exit static pressure field. Because of the relative long axial distance between rotor and aerovanes, it is unlikely that the rotor outlet pressure field is affected by the aerovane potential field in the middle strut passage. Each aerovane is at a different clocking position with respect to the HP vane due to the blade count ratio between the two stators (43/64). This also enhances the non-uniformities found in the unsteady flow field sensed by the three aerovanes. In fact, in regions where the effect of struts is expected to be less strong, i.e. on the vane surfaces not adjacent to the struts, the measured unsteady pressure traces varies depending on the vane location. This is true for gauge 14 and 18 on the suction side of aerovane A and B as shown in Figure 5. The same is found to occur for gauge 2, 4 and 7 on the pressure side of aerovane B and C.

The steady measurements show a separation region at the structural vane and high acceleration rate at vane C when the pressure ratio is decreased at the nominal rotational speed. The separated flow is further investigated by using numerical solvers. Figure 7 shows the results of the frequency analysis performed on the vane C suction side (based on experimental data) and comparison of the flow features at two operating conditions at different time steps (based on the calculations). The low frequency components (<1 kHz) become significant towards the crown and the vane throat region. The amplitudes of the perturbations are even higher than the one at blade passing frequency. A big separation region is detected in the numerical computations. Due to the high negative incidence of the structural vane, the flow generates a big separated flow region at the rear pressure side. The size of the zone varies by the rotor movement. It detaches periodically from the strut surface and is released in the downstream flow field. It also creates a blockage increasing the acceleration rate on the aero-vane C.

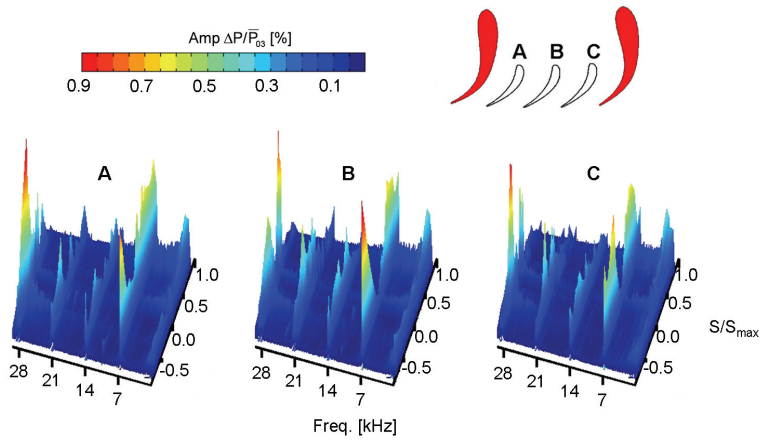

Figure 6: Frequency content of all the gauges on three aero-vanes for Nom-Nom condition.

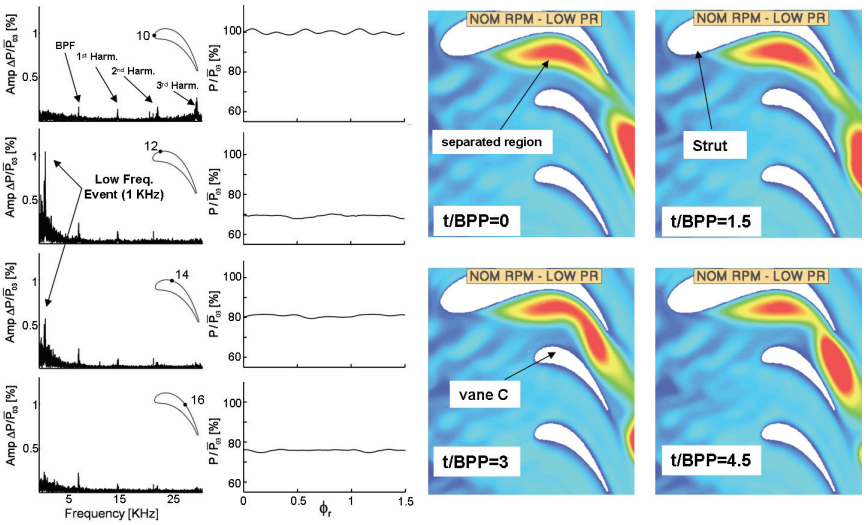

Figure 7: Phase-resolved and frequency content surface pressure of fast response sensors for aerovane C (left) and CFD contours of turbulent to laminar viscosity ratio at different blade passing periods (right) at low PR – 6790 RPM.

5 Conclusions

The performance of an innovative splitter vane configuration has been tested at design and two off-design conditions. The aero-vane outlet flow is independent from the position for both the design and off-design conditions. On the other hand, the acceleration rate at the front part of the aero-vane pressure side is slightly affected by the vane location. The structural vane is sensitive to the negative incidence. The flow separates at strut pressure side when the incidence is -25 deg. In contrast, the flow is

able to follow the aero-vanes profile for all flow angles. The pressure field of the aero-vane C suffers from the flow separation on the strut pressure side. Due to the blockage of the separated region, the acceleration rate is higher at the front suction side of the vane. For all cases, the blade passing frequency and its 3 harmonics are well captured. At leading edge region, the 3rd harmonic of the BPF is dominant. The variation of the magnitude of the 3rd harmonic depends on the vane position. Low frequency components become significant at the suction side where the flow is unguided. However, the peak frequency also differs at each vane position. The position has a strong influence on the unsteady pressure variation on the blade surface. The separated flow zone is also well captured by time resolved data and the numerical simulations. The frequency of the separation is around 1 kHz. The size of the region changes by the rotor movement. It detaches from the strut and is transferred to the downstream flow field.

Nomenclature

C	Chord [m]
M	Mach number
g	Pitch [m]
H	Blade height [m]
P	Pressure [Pa]
S	Curvilinear length [m]
t	Time [s]
W	Work [W]
α	Absolute flow angle [deg.]
Φ	Phase
BPP	Blade passing period [s]
BPF	Blade passing frequency [Hz]
LE	Leading edge
PS	Pressure side
SS	Suction side
Subscripts	
0	Free-stream
1	Stator inlet
2	Stator-rotor interface
4	LP vane outlet
3	Rotor outlet
ax	Axial
is	Isentropic
r	Rotor; Relative frame of reference
s	Stator; Static conditions

Acknowledgments

The author addresses a special thanks to Tolga Yasa for the great and constant support during all the period of his research activity. The author would like also to thank to Simone Duni and Francesco Giannattasio for their assistance on testing and data processing. The author also wishes to acknowledge the financial support of the European Commission and European manufacturers that are participating in the Project TATEF2 “Turbine Aero-Thermal External Flows 2”.

References

[1] de la Calzada, P., 2008 “Aerothermodynamic Design of Low Pressure Turbines” von Karman Institute Lecture series on “Aero-Engine Design: from State of the Art Turbofans towards Innovative Architectures” 2008-03. ISBN: 978-2-930389-83-4. Rhode-Saint-Genèse, Belgium.

[2] Dominy, R.G., Kirkham, D.A., Smith, A.D., 1998 “Flow Development through Inter-Turbine Diffusers”, ASME Journal of Turbomachinery, Vol. 120, No. 2, pp. 298-304.

[3] Giles, M.B., 1990 “Stator/Rotor Interaction in a Transonic Turbine” AIAA Journal of Propulsion and Power, Vol. 6, No. 5, pp. 621-627.

[4] Hilditch, M.A., Smith, G.C., Singh, U.K., 1998 “Unsteady Flow in a Single Stage Turbine” ASME Paper 98-GT-531.

[5] Denos, R., Arts, T., Paniagua, G., Michelassi, V., Martelli, F., 2001 “Investigation of the Unsteady Rotor Aerodynamics in a Transonic Turbine Stage” ASME Journal of Turbomachinery, Vol. 123, No. 1, pp. 81-89.

[6] Miller, R.J., Moss, R.W., Ainsworth, R.W., Horwood, C.K. 2003 “Time-Resolved Vane-Rotor Interaction in a High-Pressure Turbine Stage” ASME Journal of Turbomachinery, Vol. 125, No. 1, pp. 1-13.

[7] Paniagua G., Yasa T., de la Loma A., Castillon L., Coton T., 2008, “Unsteady Strong Shocks Interactions in a Transonic Turbine: Experimental and Numerical Analysis”. Journal of Propulsion and Power. Vol. 24, No. 4, pp 722-731.

[8] Billiard N., Paniagua G., Dénos R., 2008, “Impact of Clocking on the Aero-Thermodynamics of a Second Stator Tested in a One and a Half Stage HP Turbine”. *Journal of Thermal Science,* Vol. 17, No. 2, pp 97-110.]

[9] Hummel, F., 2002. “Wake-Wake Interaction and Its Potential for Clocking in a Transonic High-Pressure Turbine” ASME Journal of Turbomachinery, Vol. 124, pp. 69-76.

[10] Schennach, O., Pecnik, R., Paradiso, B., Göttlich, E., Marn, A., Woisetschläger, J., 2008 “The Effect of Vane Clocking on the Unsteady Flow Field in a One-and-a-Half Stage Transonic Turbine” ASME Journal of Turbomachinery, Vol. 130.

[11] Reinmöller, U., Stephan, B., Schmidt, S., Niehuis, R., 2002 “Clocking Effects in a 1.5 Stage Axial Turbine – Steady and Unsteady Experimental Investigations Supported by Numerical Simulations” ASME Journal of Turbomachinery, Vol. 124, pp. 52-60.

[12] Li, H.D., He, H.D., 2003 “Blade Count and Clocking Effects on Three-Blade-Row Interaction in a Transonic Turbine” ASME Journal of Turbomachinery, Vol.125, pp. 632-640.

[13] Miller, R.J., Moss, R.W., Ainsworth, R.W., Harvey, N.W., 2003 “Wake, Shock, and Potential Field Interactions in a 1.5 Stage Turbine-Part I: Vane-Rotor and Rotor-Vane Interaction” ASME Journal of Turbomachinery, Vol. 125, pp. 33-39.

[14] Miller, R.J., Moss, R.W., Ainsworth, R.W., Harvey, N.W., 2003 “Wake, Shock, and Potential Field Interactions in a 1.5 Stage Turbine-Part II: Vane-Vane Interaction and Discussion of Results” ASME Journal of Turbomachinery, Vol. 125, pp. 40-47.

[15] Davis, R. L., Yao, J., Clark J.P., Stetson, G., Alonso, J.J., Jameson, A., Haldeman C.W., Dunn M.G., “Unsteady interaction between a transonic turbine stage and downstream components” International Journal of Rotating Machinery , Vol. 10, pp. 495-506.

[16] Haldeman, C.W., Krumanaker, M.L., Dunn, M.G., 2003 “Influence of Clocking and Vane/Blade Spacing on the Unsteady Surface pressure Loading for a Modern Stage and One-Half Transonic Turbine” ASME Journal of Turbomachinery, Vol. 125, pp. 743-753.

[17] Zhou, D. M., Zhang, Z. G., Li, Y. S., 1993. “Numerical Prediction of Profile and Endwall Losses for Multi-Splitter Turbine Cascades” ASME paper 93-GT-255.

[18] Zhou, D. M., Zhang, Z. G., Li, Y. S., 1993. “Design and Calculation for Splittered Axial Turbine Cascade” ASME 93-GT-311.

[19] Kodama, H., Nagano, S., 1989. “Potential Pressure Field by Stator/Strut Interaction” ASME Journal of Turbomachinery, Vol. 111, pp. 197-203.

[20] Cerri, G., O’Brien, W.F., 1989, “Sensitivity Analysis and Optimum Design Method for Reduced Rotor-Stator-Strut Flow Interaction” ASME Journal of Turbomachinery, Vol. 111, pp. 401-408.

[21] Cerri, G., Boatto, C., O’Brien, W.F., Sorrenti, A. 1994. “Optimization of Rotor-Stator-Strut Potential Flow Interaction Including Rotor Feedback Effects” ASME 94-GT-274.

[22] Parry, A.B., Bailey, R.H., 1997 “The Use Of Cyclic Variations In Strut Stagger To Reduce Coupled Blade-Vane-Strut-Pylon Interaction And System Losses" ASME 97-GT-470.

[23] Ro, M. S., Hong, Y. S., 1995 “The Control of Secondary Flow by Application of Splitter Vanes in the Turbine Stator Passages”, Yokohama International Gas Turbine Congress, Proceedings, Vol. 2, pp. II-81- II-84.

[24] Dénos, R., Paniagua, G., 2005, “Effect of Vane-Rotor interaction on the unsteady flow field downstream of a transonic HP turbine”, Journal of Power and Energy. Part A. Vol. 219, No 6, pp. 431-442.

[25] Fourmaux, A., 1994 “Assessment of a low storage technique for multi-stage turbomachinery Navier-Stokes computations” ASME winter annual meeting, Chicago, IL, (USA).

Doctoral Project Summary

On Steady and Unsteady Aerodynamic Performance of Two Very-High-Lift Low Pressure Turbine Blades

Michálek Jan*

Supervisor: Prof. Tony Arts†

von Karman Institute for Fluid Dynamics, Rhode-Saint-Genèse, 1640, Belgium

Promoter: Prof. Pavel Šafařík‡

Czech Technical University in Prague, Prague 6, 16607, Czech Republic

Abstract

The paper presents the experimental results regarding the aerodynamic performance of two low pressure (LP) airfoils with different geometries (T106C and T108) but comparable loading, with and without the presence of the incoming wakes. Some specific features of separated flow transition and wake induced transition are shown and discussed for the considered conditions. The experimental study was performed on two large scale linear cascades in the VKI high speed facility S-1/C, at high subsonic exit Mach numbers (0.65 and 0.6) and low Reynolds numbers (75,000-160,000). The overall aerodynamic performance of the airfoils was evaluated, based on mid-span measurements performed by means of static pressure taps, hot-film sensors and a 5-hole probe traversing downstream of the cascade.

1 Introduction

Gas turbine components have been undergoing considerable improvements through the last decades. This is particularly true in the case of low pressure (LP) turbines since the concept of high bypass ratios has been adopted in modern commercial jet engines. High power output requirements make LP turbines large and heavy, with a mass which may reach up to 30 % of the overall engine weight [1]. Since higher efficiency levels are increasingly harder to obtain, engine manufactures have focused mainly on the reduction of components weight in order to decrease operating and ownership costs. This results in LP turbines having a lower number of blades; however, the loading of each blade rises together with possibility of laminar separation at the low Re (about 5.10^4, Hodson and Howell [2]) of cruise flight, which leads to an increase of losses.

* michalek@vki.ac.be

† Professor, Head of Turbomachinery and Propulsion Department, tony.arts@vki.ac.be

‡ Professor, Department of Fluid Dynamics and Energetic, pavel.safarik@fsid.cvut.cz

Curtis et al. [3] showed that the suction side boundary layer is the primary source of losses in the LP turbine, with the eventual separation bubble having the main detrimental effect. Consequently, analyzing and predicting the evolution of the suction side boundary layer is of utmost importance to improve engine design.

Schulte and Hodson [4] reported the positive influence of the periodic passing wakes on profile loss for some flow conditions; they subsequently showed that turbulence spots induced by the wakes prevent the boundary layer from separating [5]. They identified the calmed regions following the turbulent spots as the agent responsible for suppressing separation, due to their full velocity profiles.

Each portion of the blade covered by distinct states of the flow – laminar, transitional, turbulent, calmed and separated flow – determines a certain amount of the overall profile loss. Decreasing Re at steady conditions, the extension of the separated flow increases, resulting in augmented losses. With unsteady inflow conditions, the separation is periodically suppressed by passing wakes, with lower losses produced by the calmed and turbulent regions respect to the separated flow.

The continuous deeper understanding of unsteady flows in turbomachines gave rise to the development of a generation of highly loaded blades based on the experimental work of Curtis et al. [3] and Howell et al. [6]. Cobley et al. [7] reported a 20% reduction of the blade count adopting these high-lift blades, while maintaining the efficiency level. Haselbach [1] then reported a further reduction of the blade counts by 11 % for the new generation of ultra-high-lift blades, with a loss penalty of only 0.5% respect to a datum blade. However, most of the experimental validations leading to the development of such highly loaded blades were performed at low speed (Brunner et al. [8], Howell et al. [6, 9]). Vera et al.[10] performed a high speed validation of low speed testing carried out by Zhang et al. [11] on an ultra high lift blade, showing that time mean quantities are comparable in both cases, with a similar development of the boundary layer.

Since more detailed measurements at high speed conditions are still needed, the objective of the present paper is to investigate two very high lift LP turbine blade geometries (T106C and T108) at realistic engine conditions (high Mach number and low Re number), in order to validate some general conclusions of low speed experiments. The study was performed at steady inflow conditions at first, then with periodically passing wakes in order to gain a better understanding of the separated flow and wake-induced transition.

2 Experimental Setup

The VKI S-1/C high speed facility (**Fig.1**) is a closed-loop wind tunnel operating with independently adjusted level of density (total pressure) and pressure ratio. Such arrangement thus allows to closely simulate the conditions found in real LP turbines (low Reynolds number and high exit Mach number). The level of total pressure is set up by means of a continuously running vacuum pump and a valve defining the sonic throat. The required cascade pressure ratio is imposed by a multiple-stages axial compressor, while the mass flow through the cascade is controlled with a by-pass circuit. The flow temperature is maintained close to the ambient one by a cooler located just downstream of the compressor. The flow passes through a set of screens and honeycombs embedded in a settling chamber before it enters the test section. The level of FSTI measured at the inlet of the cascade is of 0.9% (**Tab. 2**).

Two large-scale linear cascades were alternatively accommodated within the test section, depending on the blades under investigation (T106C or T108 airfoils). Both cascades consisted of six prismatic blades (7 blade passages) spanning the entire test

section with a width of 225 mm. Cascade characteristics are presented in **Tab. 1**. The T106C is classified as a very high lift LP turbine airfoil with peak suction at $s/s_0 = 0.5$ (mid-loaded) and strong diffusion rate at the rear suction part. Despite the similar diffusion factor and loading (see **Tab. 1**), the T108 airfoil presents the peak suction at $s/s_0 = 0.3$ (front-loaded), which leads to a fair lower diffusion rate respect to the T106C airfoil.

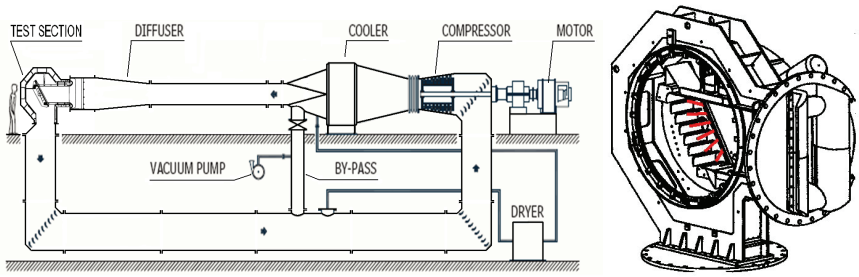

Figure 1: The S-1/C high speed, variable density wind tunnel (left), the test section with rotating bars (right)

The suction sides of the datum blades (the 3rd from the cascade top) were instrumented at mid-span with 31 and 40 static pressure taps, respectively for the T106C and T108. In a similar manner, hot-film sensors were deployed on the suction side of another set of blades, in the number of 16 and 15 for the T106C and the T108, respectively. Then the instrumented blades were placed in the cascade alternatively, depending on the measurement technique employed and the cascade under the study.

Table 1: Main cascade characteristics (T106C/ T108)

Chord	mm	93.01/ 98.42	Diffusion factor	0.39/ 33
Pitch to chord		0.95/ 0.90	Diffusion rate	0.5/ 0.28
Aspect ratio		2.4/ 2.3	Zweiffel coefficient	1.29
Blade stagger	deg	30.7/ 34.4	Reduced frequency	0.68
Inlet flow angle	deg	32.7	Flow coefficient	0.48
Peak suction		0.5/ 0.3 s/s_0	Cascade – bars gap	0.68 x/C_{ax}

A pneumatic 5-hole probe was also used for pitch-wise traversing downstream of the cascade, with the probe nose at the distance of $x/C_{ax} = 0.55$ from the trailing edge plane. A double sensor hot-wire probe (CTA) was employed upstream of the cascade, in order to characterize the inlet flow in presence of the rotating bars and also to evaluate the basic turbulence properties of the flow. The probe was traversed pitch-wised upstream of the cascade, at the distance of $x/C_{ax} = 0.32$. Some parameters [12, 13] computed for the inlet flow are given in **Tab. 2**.

Table 2: Flow characteristics at the inlet

FSTI (no bars)	%	0.9	Kolmogorov scale	m	$0.5 \cdot 10^{-3}$
FSTI (bars max)	%	15	Wake deficit (at probe location)	%	68
FSTI (bars min)	%	1.5	Max. relative incidence (bars)	deg	-18
Integral length scale	m	0.030	Mean relative incidence (bars)	deg	-4
Taylor microscale	m	$7.4 \cdot 10^{-3}$			

Rotating bars were optionally used within the test section (**Fig. 1**) in order to simulate the relative movement of the preceding turbine stage. The cylindrical bars (dia. 2 mm) were evenly mounted on the circumference of a rotating disc (dia. 0.9 m), entering the test section through a slot in the lateral wall. The distance between two neighboring bars at the blade mid-span was set to be equal to the cascade pitch ($g_b/g_c = 1$). The plane of rotation was aligned with the cascade leading edge plane, at a distance of $x/C_{ax} = 0.68$.

All pneumatic measurements were sampled at 200 Hz during 10 seconds. The hot-film and hot-wire signals were commonly sampled at 50 kHz and low-pass filtered at 12 kHz, considering the frequency response of both sensors.

The uncertainty was estimated for all the adopted measurement techniques within the full range of the flow conditions. In the following, the values are given for the maximum and minimum Reynolds numbers. Relative uncertainties on the kinetic energy losses were calculated ranging between 10 - 20%. The absolute flow angle uncertainty varied between 0.2 - 0.3 deg. Relative uncertainties on the isentropic Mach number and Reynolds number ranged between 0.4 - 1.2% and 0.5 - 1.3%, respectively. The uncertainty on turbulence intensity was estimated to be 12%. The relatively high values of uncertainty are due to the fact that the measurements were performed at very low pressure (~ 0.1 bar).

3 Results and discussion

The following paragraphs present the comparison of the performance of the two airfoils at high and low Reynolds numbers (high: $Re_{2,is}$ =160,000, for the both airfoils; low: $Re_{2,is}$= 80,000 for the T106C and $Re_{2,is}$= 75,000 for the T108). The steady inflow results are considered at first, followed by those obtained with incoming wakes.

3.1 Steady inflow results

The suction side Mach number distribution, normalized by the exit Mach number, measured for the T106C and the T108 airfoils at steady inflow conditions are plotted in **Fig. 2** and **Fig. 3**, respectively. The plots also present, for comparison, the results of steady numerical simulations performed by a RANS code – TRAF (fully turbulent boundary layer, Baldwin-Lomax turbulence model).

The Mach number distribution (**Fig. 2**) reveals a massive separation without reattachment at the lower Reynolds number, covering a substantial part of the suction side of the T106C. The flow blockage of the separated region profoundly alters the circulation around the blade (loading drop), thus causing severe losses (**Fig. 7**) and a reduction of blade turning (**Fig. 8**).

The high adverse pressure gradient, after the peak suction, forces the laminar boundary layer to separate just downstream of the maximum velocity. The data in **Fig. 2**, together with the signal from hot-film sensors in **Fig. 4**, suggest that the separation occurs around s/s_0=0.5. Despite a highly disturbed flow in the separated region (rms value in **Fig. 6**), the low Reynolds number prevents the detached laminar layer from undergoing transition until s/s0=0.75. This observation suggests that the laminar shear layer is not receptive to the length scales of the disturbances in the outer flow, resulting in a postponed onset of transition.

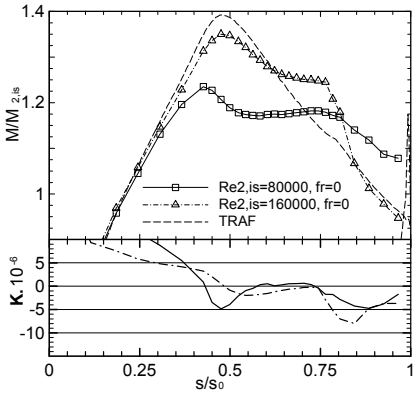

Figure 2: Composite picture of the isentropic Mach number (top) and acceleration parameter (bottom) distributions along the suction side of the T106C airfoil for selected $Re_{2,is}$, no wakes passing ($M_{2,is}$=0.65)

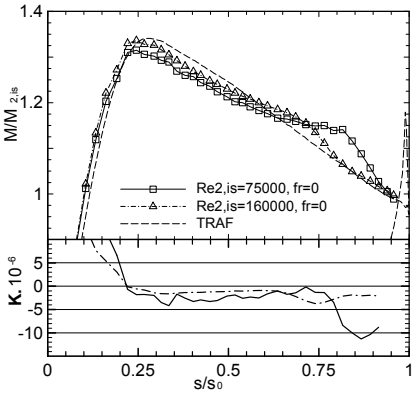

Figure 3: Composite picture of the isentropic Mach number (top) and acceleration parameter (bottom) distributions along the suction side of the T108 airfoil for selected $Re_{2,is}$, no wakes passing ($M_{2,is}$=0.6)

The positive acceleration parameter found in the rear part of the velocity plateau (**Fig.2**) probably contributes to reach a Re_{Ω} sufficiently high to promote the transition of the separated shear layer. The flow starts to diffuse again downstream of this point; however, the insufficiently energized shear layer fails to reattach before the trailing edge. The results illustrate that the Reynolds number is the driving parameter for flows with a separated shear layer and low FSTI. It is worth to mention that presence of an elevated FSTI considerably accelerates the transition process [14, 15, 16]. Michálek et al. [16] also showed that dissipation scales of the FSTI must be of the order of the thickness of the detached shear layer, or smaller, to be effective on the onset of transition.

In the case of the high Reynolds number, the Mach number distribution obtained for the T106C airfoil indicates a laminar separation bubble with a short velocity plateau and abrupt reattachment (**Fig. 2**). As such, according to the low speed measurements of Hatman and Wang [17] and the numerical simulations by Pauley et al.[18] and Alam and Sandham [19], it should be accompanied by a vortex shedding. This phenomenon could be indicated, in the present measurements, by the increased level of the energy content with a distinct frequency shown by hot film readings at s/s_0=0.684 and 0.724 (**Fig. 6**). However, the energy content increase at these locations is rather broad, suggesting a highly dissipative nature for such structure (if any); or it could be rather attributed directly to the transitional shear layer above the bubble. Further downstream, around the reattachment point, a turbulent boundary layer is indicated by the full spectra in **Fig. 6** (s/s_0=0.844).

The broad peak of the rms values (**Fig. 4**) in the separated region (s/s_0=0.603-0.844), with its peak at s/s_0=0.764, points out a relatively intensified transition process with a raised amplitude of disturbances just before the reattachment point. As mentioned above, the boundary layer was found turbulent downstream of the reattachment (**Fig. 4** and **Fig. 6**). The higher value of the Reynolds number enhances the propagation of disturbances within the detached shear layer, forcing the flow to undergo transition earlier. However, without a further insight in the separated shear layer it is difficult to draw any solid conclusions to which rate the inviscid transition mechanism (Kelvin-Helmholtz instability) plays a role in phenomenon under the

study. The frequency of the increased energy content in the separated region dimly suggest a link to the non-dimensional frequency $\omega^* = 1/4\delta_w(2\pi f)/\bar{u}$ measured or predicted for K-H instability by other authors (Pauley [18], 0.21; Lengani et al.[20], 0.215-0.22; Yang and Voke [21], 0.206-0.231).

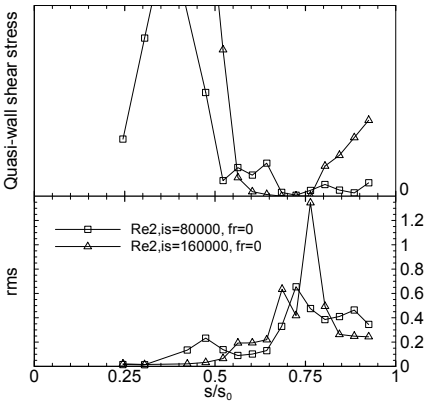

Figure 4: Quasi-wall shear stress (top) and its rms values (bottom) distributions along the suction side of the T106C blade, no passing wakes, ($M_{2,is}$=0.65)

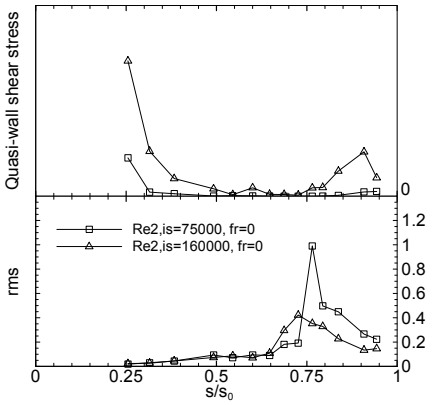

Figure 5: Quasi-wall shear stress (top) and its rms values (bottom) distributions along the suction side of the T108 blade, no passing wakes, ($M_{2,is}$=0.6)

The reattachment of the shear layer for the high Reynolds number case leads to a significant decrease of the losses (**Fig. 7**) and recovery of the blade turning (**Fig. 8**) respect to the low Reynolds number case.

The Mach number distribution (**Fig. 3**) of the T108 airfoil shows a reattached flow after the separation for both the high and the low Reynolds number test cases. However, the hot-film signal in **Fig. 5** suggests that the separated shear layer reattaches at the very end of the airfoil. The fact that separation bubbles appear to be somewhat smaller respect to the T106C (particularly for the higher Reynolds number) is a consequence of the lower diffusion rate of the T108 airfoil after the peak suction. This reduced bubble extension is then reflected in considerable lower losses of the T108 airfoil at the low Reynolds number (**Fig. 7**). Himmel [22] derived a correlation between bubble extension and loss generation in his experimental low-speed study on the same airfoils. Notably, the increase of the losses between the high and the low Reynolds numbers is relatively low in the present work (about 30%).

The quasi-wall shear stress in **Fig. 5** points at a very low skin friction just downstream of the peak suction, with unclear indication of the separation point. Indeed, the fluctuations of the acceleration parameter in **Fig. 3** reveal a separation-reattachment-like behavior for the shear layer in this region. Despite this fact, the rms values indicate relatively low disturbances level before s/s_0=0.54. Downstream of this point the rms values rise exponentially with the maximum at s/s_0=0.77, which is just upstream of the pressure recovery point (s/s_0=0.82), where the main flow restarts diffusion and the shear layer tends to reattach again. In their numerical simulation, Abdessemed et al. [23] related the exponential growth of disturbances to an amplification of the T-S waves in the region where the fluctuations in the shear layer are driven by the linear instability, before the pattern break-down to a non-linear nature. Despite the fact that a certain frequency peak in the energy spectra was detected (T108 at low Re, **Fig. 6**), another explanation of this event is given below.

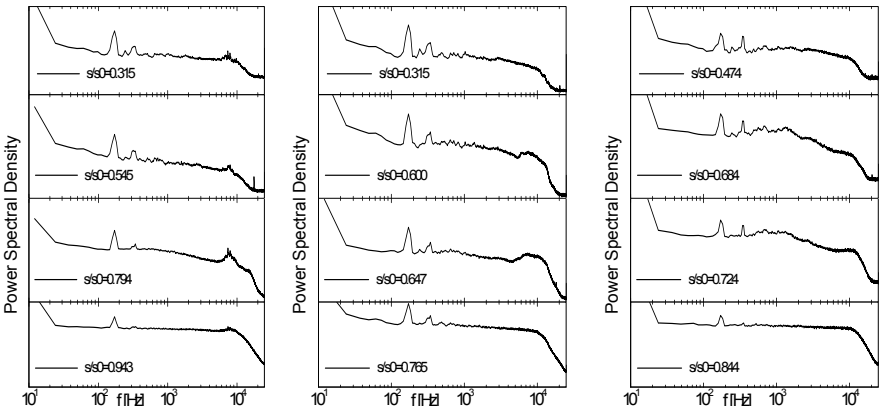

Figure 6: Power density spectra of quasi-wall shear stress for selected sensors along the suction side, $Re_{2,is}$=75,000, T108 (left), $Re_{2,is}$=160,000, T108 (middle), $Re_{2,is}$=160,000, T106C (right)

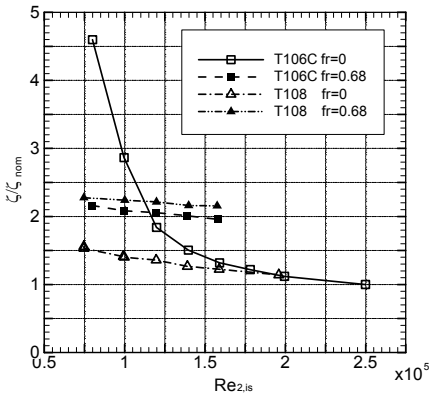

Figure 7: Non-dimensional mass-weighted kinetic energy losses for the T106C and the T108 airfoils at different Reynolds numbers, T106C- $M_{2,is}$=0.65, T108- $M_{2,is}$=0.6

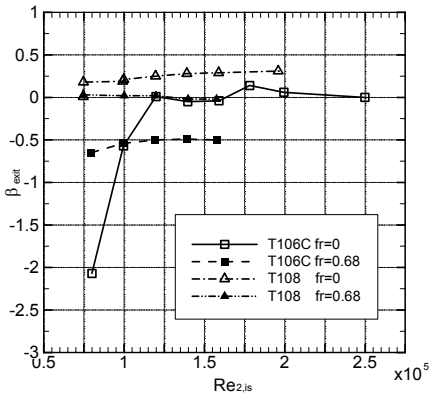

Figure 8: Mean exit flow reduction angles for the T106C and the T108 airfoils at different Reynolds numbers, T106C- $M_{2,is}$=0.65, T108- $M_{2,is}$=0.6

The presence of a peak in the energy spectra at around 8000 Hz (the 170 Hz peak is related to the environmental noise of the facility), for all the hot-films sensors (**Fig. 6**, left side), rises some questions about its origin. Such energy content upstream of the separation was not detected for any other test case. A similar spectral peak was found downstream of the separation point by Lengani et al. [20] in their low speed measurements inside a detached shear layer: they showed it to originate from the Kelvin-Helmholtz instability of inflexional velocity profiles. However, they probed the separated shear layer with a hot-wire sensor, which is not the case of the present work. Therefore, the frequency detected in the present study could be probably attributed to fluctuations of the bubble caused by very a late reattachment. This is also supported by a relatively high scatter in the loss and angle measurements obtained for this Reynolds number (not shown).

The plot of the Mach number distribution in **Fig.3** shows a relatively small separation bubble for the high Reynolds number case, with clear separation (s/s_0=0.55) and reattachment (s/s_0=0.84) points. The broad peak of the rms values in the separated region suggests a transitional process similar to that described for the T106C airfoil in the high Reynolds number case. Similarities can be also found in the energy spectra of both airfoils under investigation (**Fig. 6**, middle and right).

The losses in **Fig. 7** are shown to be comparable at this Reynolds number. The stronger separation bubble of the T106C is compensated by the longer diffusion length of the T108 blade; however, T106C measurements were performed at a slightly higher exit Mach number.

3.2 Unsteady inflow results

The plot in **Fig. 10** presents almost identical time-averaged isentropic Mach number distributions along the suction side of the T108 airfoil for both Reynolds numbers. Only a tiny separated region (time-averaged) is revealed at the region of s/s_0=0.49-0.68. The difference between two Mach number distributions in **Fig. 9** of the T106C airfoil is more distinct. Despite of the periodically passing wakes the time-averaged results indicate that the separation bubble is not completely suppressed (in time-averaged data) at the low Reynolds number. However, a clear benefit of the unsteady inflow conditions is put in evidence by a considerable loss reduction (**Fig. 7)** and a recovery of the blade turning (**Fig. 8)** at the low Reynolds number.

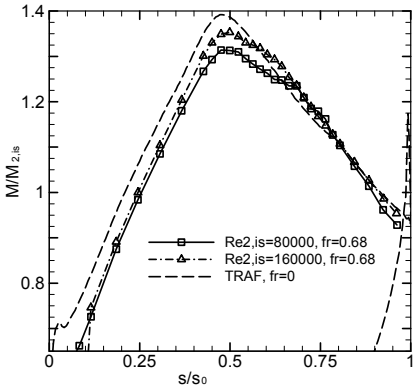

Figure 9: Time-averaged isentropic Mach number distributions along the suction side of the T106C airfoil for two $Re_{2,is}$, wakes passing ($M_{2,is}$=0.65)

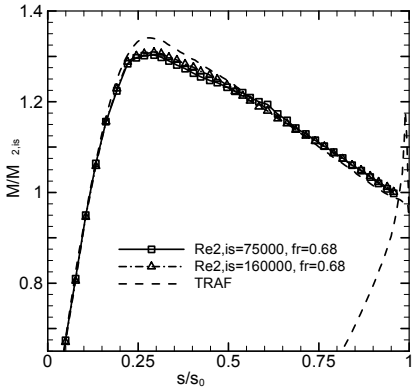

Figure 10: Time-averaged isentropic Mach number distributions along the suction side of the T108 airfoil for two $Re_{2,is}$, wakes passing ($M_{2,is}$=0.6)

It is worth to mention here, that the level of the losses for both blades under the influence of the periodically passing wakes is likely to be somewhat higher because of a separated flow region downstream of the leading edge at the pressure side of the airfoils (see elevated loss regions at the pressure side as indicated by the downstream wakes traversing in **Fig. 11** and **Fig. 12**). The separation is result of the altered velocity triangles (change of the incidence angle) by the incoming wakes. Similar results were observed within an off-design performance study by Brear et al. [24].

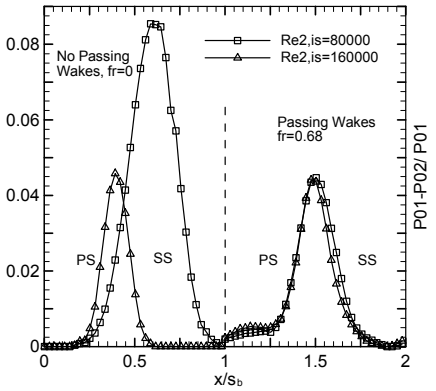

Figure 11: Downstream wake traversing of the T106C blade (time-averaged), no passing wakes (left), passing wakes (right), ($M_{2,is}$=0.65)

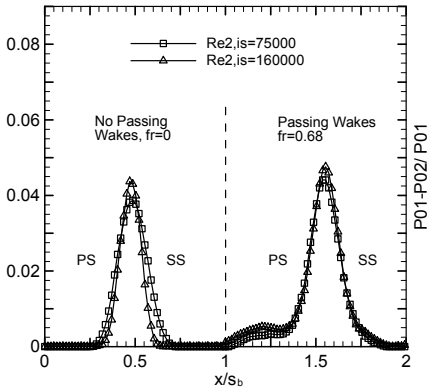

Figure 12: Downstream wake traversing of the T108 blade (time-averaged), no passing wakes (left), passing wakes (right), ($M_{2,is}$=0.6)

The interaction of the wake with the separated shear layer is presented for the T108 blade and the low Reynolds number in the form of space-time diagrams in **Fig. 13** (ensemble averaged rms) and **Fig. 14** (ensemble averaged shear stress). Further, time traces of the hot-film sensors are also presented in **Fig. 15**.

In the attached part of the boundary layer (upstream x/c_{ax}=0.6), the response of the hot-film sensors slightly lag behind indicated wake path in **Fig. 13** and **Fig. 14**, because of diffusion of the wake turbulence into the boundary layer. Halstead [25] described two generic transition paths which can be identified on the blade surface: the wake induced path and the transition path between the wakes. In the present measurements; however; all the details of the above mentioned transition paths can barely be recognized. The wake-induced transition path is highlighted in **Fig. 14** by the elevated region of the ensemble rms along the wake path, particularly downstream of x/c_{ax}=0.6. The wake is then followed by a transitional/turbulent boundary layer (downstream x/c_{ax}=0.6) caused by a diffusion of the wake turbulence to the attached boundary layer and/or eventually break-down of the roll-up vortices. The roll-up vortices, however, were not identified in the case of the T108. It is because of the lower diffusion of the T108 blade after the peak suction, which allows developed laminar boundary layer to start transition before the onset of the separation. Then this early transition prevents the formation of the roll-up vortices since the boundary layer remains reattached. Low speed measurements of Zhang and Hodson [11] reported similar results on the blade with a limited diffusion rate.

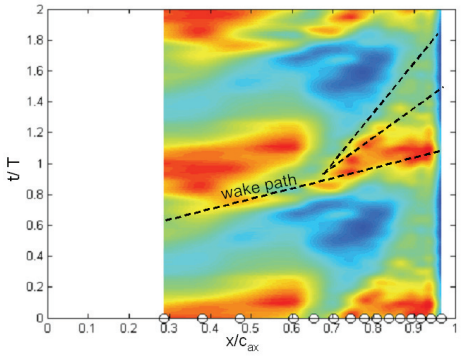

Figure 13: Space-time diagram of the ensemble-averaged rms of the T108 airfoil at $Re_{2,is}$=75,000 ($M_{2,is}$=0.6)

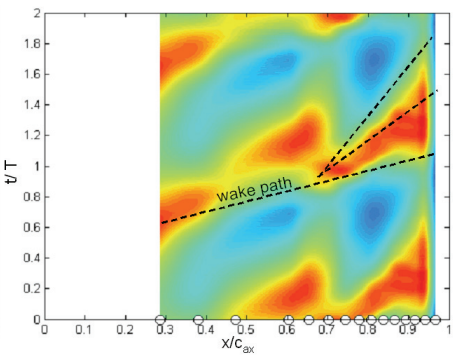

Figure 14: Space-time diagram of the ensemble-averaged rms of the T108 airfoil at $Re_{2,is}$=75,000 (M2,is=0.6)

The turbulent region, following the wake path, is indicated in **Fig. 14** by a wedge region of the increased ensemble averaged quasi-wall shear stress. Between the wakes, without the agent causing early transition, the boundary layer relaxes to a pre-transitional state, similar one of the steady inflow conditions. This results in the calmed region. Because of different velocities of the turbulent spots and the trailing edge of the calmed region, it is spreading as it propagates downstream (approximate end of the calmed region indicated in **Fig. 13** and **Fig. 14** with the line of the highest slope). The turbulent spot and calmed region are also indicated by label A and B, respectively, in the **Fig. 15**. The calmed region plays important role as a loss reduction mechanism in highly loaded LP turbines, because of their low dissipation and full velocity profiles (Schulte and Hodson [5]). After the calmed region the flow starts to separate again until arrival of the following wake. The transitional mechanism remains the same at the high Reynolds number and contrast only in extension of the wake and the separated region interaction.

In contrary, the difference in transitional mechanism was observed at the low Reynolds number of the T106C airfoil, where a structure suggesting roll-up vortices (inviscid K-H mechanism) was identified in the separated region. In fact, the roll-up vortices, indicated in **Fig. 16** by two parallel lines, propagate about a half speed respect to the local free-stream (indicated by the wake path) as also found by Stieger and Hodson [26]. Formation of this inviscid pattern is allowed by the strong diffusion, which prevents the laminar boundary layer from the transition onset before the separation. At the high Reynolds number, an early transition occurs most probably before the onset of the separation, again preventing of formation of the roll-up vortices as in the case of the T108 airfoil. Zhang et al. [11] also reported occurrence of the roll-up vortices in their measurements at low speed. Worth to mention, that formation of the roll-up vortices is an undesirable state in LP turbine design, because of their highly dissipative nature.

Despite a significantly lower kinetic energy loss of the T108 airfoil at the steady inflow conditions, losses in **Fig. 7** suggest a penalized performance with the periodically passing wakes (in spite of the formation of roll-up vortices of the T106C). It is mainly because of its extended length of the suction side diffusion causing premature transition in the attached suction side boundary layer of the T108 blade. However, it is difficult to conclude the exact level of the losses originating only from the suction side boundary layer since measured losses involve also the flow separation at the leading edge of the pressure side.

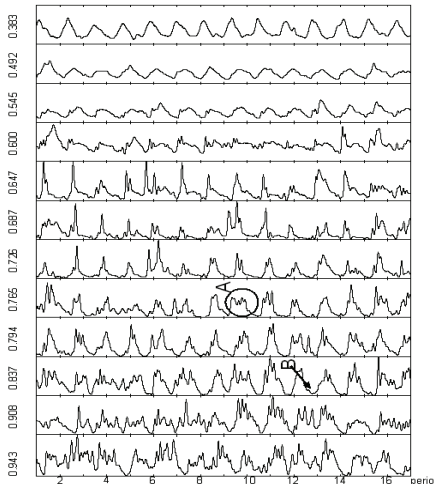

Figure 15: Instantaneous time traces of the hot-films sensors along the suction side of the T108 blade at $Re_{2,is}$=75,000, $M_{2,is}$=0.6, 17 wake passing periods

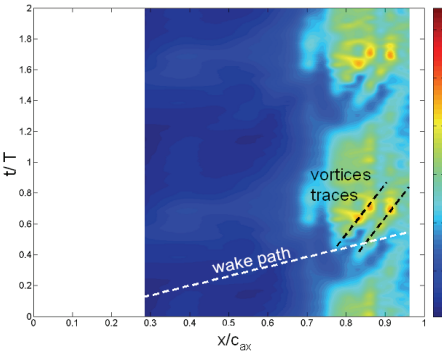

Figure 16: Space-time diagram of the ensemble-averaged rms of the T106C airfoil at the $Re_{2,is}$=80,000 with highlighted roll-up vortices paths

4 Conclusions

Two different blade geometries with comparable loadings were examined at the steady and unsteady inflow conditions. It was shown that the flow parameters of the suction side have the substantial influence on the performance of the blade thus should be carefully considered during a design phase.

The higher diffusion rate of the T106C airfoil leads to a massive laminar separation of the boundary layer without the reattachment before the trailing edge, which was not observed for the similar conditions of the blade with a controlled diffusion rate (T108) at steady inlet flow. The Reynolds number has, in both cases, the positive influence on the extension of the separated region and thus on the loss reduction.

Transition within the detached shear layer at a low FSTI seems to obey Reynolds number as a necessary precursor of the process. The receptivity of the separated shear layer respect to the length scales produced below the layer in the recirculation region was found to be rather low, with a limited impact on the transition process. The enhanced receptivity of disturbances at relatively higher Reynolds number seems to accelerate transition, which was documented by the increased level of disturbances just downstream of the separation point. The higher fluctuation amplitude could be possibly caused by inviscid K-H mechanism; however; any clear frequency was detected supporting its occurrence in the present study.

The T108 airfoil embodies a superior performance at the steady inflow conditions respect to the T106C profile, mainly at the relatively low Reynolds numbers, because of controlled diffusion resulting in the reattached shear layer after the separation.

Two mechanism of the transition process were described in the unsteady inflow conditions: 1) the early transition prior the steady state separation point, for the both investigated Reynolds numbers of the T108 airfoil and at the high Reynolds number of the T106C blade, and 2) the structure of roll-up vortices was identified at the low Reynolds number of the T106C airfoil.

Contrary to the flow without the periodically passing wakes, the results with the unsteady inflow conditions suggest the opposite trend in terms of the losses. Because of the extended diffusion length of the T108 suction side the performance of the airfoil suffers of an enhanced entropy production in the attached boundary layer related to premature transition onset. The measurements on the investigated airfoils suggest that the design of a highly loaded LP turbine blade with the peak suction moved towards the trailing edge is mostly preferred (aft loaded). Moreover, some authors [6, 11] suggests a gradual change of the blade diffusion in order to advance the early transition just before the separation onset and thus to avoid formation of highly dissipative roll-up vortices.

It was shown the positive influence of the turbulent and calmed regions on the loss production in the separated shear flows with the passing wakes. From a limited incidence of the calmed region in between two passing wakes, a suitable reduced frequency, respect to the desired operational condition of LP turbine, should be considered in order to maximally benefit of its influence.

Nomenclature

f	Frequency
g	Pitch
$K=\nu/U^2 \cdot dU/ds$	Acceleration parameter
Ma	Mach number
Re	Reynolds number
s	Curvilinear coordinate
FSTI	Free stream turbulence intensity
K-H	Kelvin-Helmholtz
T-S	Tollmien-Schlichting
u	Velocity
Greek symbols	
δ	Vorticity thickness
Ω	Momentum thickness
ω	Nondimensional frequency
Subscripts	
2	Downstream condition
ax	Axial
c	Cascade

b	Bars
o	Reference length

Acknowledgment

The reported work was performed within European research project “Turbulence and Transition Modeling for Special Turbomachinery Applications” (TATMo, 6FP, AST5-CT-2006-030939).

References

[1] Haselbach, F, Schiffer, H-P, Horsman, M, Dressen S, 2001, “The Application of Ultra High Lift Blading in the BR715 LP Turbine”, Proceedings of ASME Turbo Expo 2000, Power for Land, Sea and Air, New Orleans, Louisiana, USA.
[2] Hodson H. P., Howell R. J., 2005, “The role of transition in high-lift low-pressure turbines for aeroengines”, Progress in Aerospace Sciences 41 (2005), pp. 419-454.
[3] Curtis E. M., Hodson H. P., Banieghbal M. R., Denton J. D., Howell R. J., Harvey N. W., 1997, “Development of Blade Profiles for Low-Pressure Turbine Applications”, ASME J. of Turbomachinery., **119**, pp. 531-538.
[4] Schulte, V, Hodson, H P, 1994, “Wake-Separation Bubble Interaction in Low Pressure Turbines”, AIAA/SAE/ASME/ASEE 30th Joint Propulsion Conference and Exhibits, Indianapolis, IN.
[5] Schulte, V, Hodson, H P, 1998, “Unsteady Wake-Induced Transition in High Lift LP Turbines”, J. of Turbomachinery, **120,** p 28-35.
[6] Howell, R J, Ramesh, O N, Hodson, H P, Harvey, N W, 2000, “High Lift and Aft Loaded Profiles for Low Pressure Turbines”, ASME Paper 2000-GT-261
[7] Cobley, K, Coleman, N, Siden, G, Harvey, N W, and Arndt, N, 1997, “Design of New Three Stage Low Pressure Turbine for BMW Rolls-Royce BR715 Engine”, ASME Paper 97-GT-419.
[8] Brunner S, Fottner L, Schiffer H-P, 2000, “Comparison of Two Highly Loaded Low Pressure Turbine Cascades Under the Influence of Wake-Induced Transition”, Proceedings of ASME Turbo Expo 2000, Power for Land, Sea and Air, Munich, Germany.
[9] Howell, R J, Hodson, H P, Schulte, V., Schiffer, H-P Haselbach, F, 2001, “Boundary Layer Development on the BR710 and BR715 LP Turbines-The Implementation of High Lift and Ultra High Lift Concepts”, ASME Paper 2001-GT-0441
[10] Vera, M, Zhang, X, F, Hodson, H P, Harvey, N W, 2007, “Separation and Transition Control on an Aft-Loaded Ultra-high-lift LP Turbine Blade at Low Reynolds Numbers: High Speed Validation”, J. of Turbomachinery, **129**, pp 340-347.
[11] Zhang, X, F, Vera, M, Hodson, H P, Harvey, N W, 2006, “Separation and Transition Control on an Aft-Loaded Ultra-high-lift LP Turbine Blade at Low Reynolds Numbers: Low Speed investigation”, J. of Turbomachinery, **128**, pp 517-527.
[12] Hinze, J. O., 1959, “Turbulence”, McGraw-Hill, 1st edn.
[13] Brunn, H. H, 1995,. “Hot-Wire Anemometry, Principles and Signal Analysis”, Oxford University Press Inc, New York.

[14] Volino R. J., Hultgren L. S., 2001, “Measurements in Separated and Transitional Boundary Layers Under Low-Pressure Turbine Airfoil Conditions”, ASME J. of Turbomachinery., **123**, pp. 189-197.
[15] Volino R. J., 2002, “Separated Flow Transition Under Simulated Low-Pressure Turbine Airfoil Conditions: Part 1-Mean Flow and Turbulence Statistics”, ASME J. of Turbomachinery., **124**, pp. 645-655.
[16] Michálek, J, Monaldi, M, Arts, T, 2010, “Aerodynamic Performance of a Very High Lift Low Pressure Turbine Airfoil (T106C) at low Reynolds and High Mach Number With Effect of Free Stream Turbulence Intensity”, ASME Turbo Expo 2010, Power for Land, Sea and Air, Glasgow, UK.
[17] Hatman, A, Wang, T., 1998, “Separated Flow Transition. Part 3-Primary Modes and Vortex Dynamics”, ASME Paper 98-GT-463
[18] Pauley, L, Moin, P., Reynolds, W, 1990, “The Structure of Two-Dimensional Separation”, J. of Fluid Mechanics, **220**, pp. 397-411.
[19] Alam, M, Sandham, N D, 2000, “Direct Numerical Simulation of ‘Short’ Laminar Separation Bubbles With Turbulent Reattachment”, J. Fluid Mech., **400**, pp 1-28.
[20] Lengani, D, Simoni, D., Ubaldi, M., Zunino, P., Bertini, F., 2009, “An Experimental Study of the Reynolds Number Inlfuence on a Laminar Separation Bubble”, ERCOFTAC Bulletin 80, pp 24-28
[21] Yang, Z, Voke, P R, 2001, “Large Eddy Simulation of Boundary Layer Separation and Transition at a Change of Surface Curvature”, J. Fluid Mech., **439**, pp 305-333
[22] Himmel, C, Private communication, 2009
[23] Abdessemed, N, Sherwin, S J, Theofilis, V, 2009, “Linear Instability Analysis of Low-Pressure turbine flows”, J. Fluid Mech., **628**, pp 57-83.
[24] Brear, M J, Hodson H P, Harvey, N W, 2002, “Pressure Surface Separation in Low-Pressure Turbines-Part 1: Midspan Behavior”, J. of Turbomachinery, **124**, pp 393-401
[25] Halstead, D E, Wisler, D C, Okiishi, T H, Walker, G J, Hodson, H P, 1997, “Boundary layer Development in Axial Compressors and Turbines: Part 1-Composite Picture”, J. Fluid Mech., **119**, pp 114-127
[26] Stieger, R D, Hodson, H P, 2004, “The Transition Mechanism of Highly Loaded Low-Pressure Turbine Blades”, J. of Turbomachinery, **126**, pp 536-543

Doctoral Project Summary

Numerical investigation of squealer blade tip leakage flows in high pressure turbines

Peter Vass*

Supervisor: Prof. Tony Arts†

von Karman Institute for Fluid Dynamics, Rhode-Saint-Genèse, 1640, Belgium

Promoter: Prof. Tony Arts‡

Université Catholique de Louvain, Louvain-la-Neuve, Belgium

Abstract

The present contribution gives an overview of the numerical work which is being performed at the Von Kármán Institute in the framework of the European research program AITEB-2, concerning the numerical investigation of tip gap flows in linear turbomachinery cascades, representative of high pressure turbine rotor blade geometries. The primary goal of the project is the computation of four distinct blade tip geometries (TG1, 2, 3, and 4 hereinafter) in 3d, including the entire internal cooling setup inside the blade, and validation of the results versus the experimental campaign of Hofer et al. [2009]. The geometry and the numerical setup are described in detail, with emphasis on the grid generation and connection method between internal and external flow. Validation is performed on the most delicate, zero cooling flow case, in which internal flow in the cooling channels is driven exclusively by pressure difference between pressure side tip region and tip gap.

1 Introduction

In high pressure gas-turbine stages, a source of significant losses is the leakage flow in the gap between the tip of the unshrouded rotor and the casing, called tip clearance. In addition to that, the inlet temperature - which in modern high pressure turbines exceeds the melting point of the blade material - can cause serious damage, especially on the tip of the rotor blade, where cooling is rather difficult. The weak solution to this problem is to choose an infinitesimally small clearance, which would minimize the hot gas flow through the gap. This is unfeasible, since one has to take into account the deformation of the rotor, and avoid the rubbing of the blade into the end-wall. On the other hand an adequately designed tip geometry – including the use of squealer etc. – is supposed to lower the mass flow through the tip-gap and thus the losses and heat transfer in that region.

The current numerical campaign is a part of an ongoing project at the Von Kármán Institute (see Key and Arts [2004] and Arts et al. [2005]) concerning the thorough investigation of tip leakage flows. The present study focuses on the industrial

* PhD Candidate, Turbomachinery Department, Chaussée de Waterloo 72, vass@vki.ac.be

† Professor, Turbomachinery Department, Chaussée de Waterloo 72, arts@vki.ac.be

‡ Professor, Unité de Thermodynamique, Place du Levant, 2 à 1348 Louvain-la-Neuve, Tony.Arts@uclouvain.be

approach to the aero-thermal investigation of the tip-leakage flow phenomena. The project is conducted within the framework of AITEB2, which is a European consortium dedicated to the aero-thermal investigation of turbine endwalls and blades. The validation is supported by the experimental campaign by Hofer et al. [2009] and Hofer and Arts [2009].

2 Methodology

2.1 Geometry

High pressure turbine rotors are often modeled with a straight cascade, neglecting the effects of rotation and endwall movement. These simplifications are allowed after the studies of Mayle and Metzger [1982], Metzger et al. [1989] and Bunker [2004].
The test profile to be studied is derived from the TATEF HP rotor blade, and can be described with the following parameters: pitch to chord ratio g/C = 0.782, tip gap over channel height ratio t/H = 1.63%, squealer groove depth to chord length h_g/C = 3.44%, channel height to chord ratio H/C = 1.076, rim width to chord ratio w_g/C = 2.69%.
Cooling of the blade was modeled by sixteen cooling holes on the pressure side of the tip section and four dust holes exiting on the bottom of the squealer groove. These holes are supplied with coolant through a main cooling channel, which leads to a plenum, where the relatively cold air is distributed (see Figure 1d). Even though the majority of the results to be presented here belong to the non-cooled case, the abovementioned cooling setup plays an interesting role, due to the flow in the cooling channels, induced by the pressure difference between the pressure side and the tip gap.
There are four tip geometries to be studied: TG1 is the classic recessed tip geometry, where the clearance flow (and losses) is reduced by a rim around the blade tip (Fig 1a left). TG2 is also a frequently investigated type, where only the suction side of the blade tip is rimmed (Fig 1b). In the third case rims both on the suction and pressure side are present, but the leading and trailing edge of the blade are open (Fig 1c). This configuration is supposed to deliver better cooling performance around the trailing edge area, due to the convection of cooling flow - coming from the dust holes – toward the aft region. Finally TG4 is a representing TG1 in heavily worn condition (Fig 1a right), with shallower tip groove and an increasing tip clearance toward the trailing edge (rubbed trailing edge).

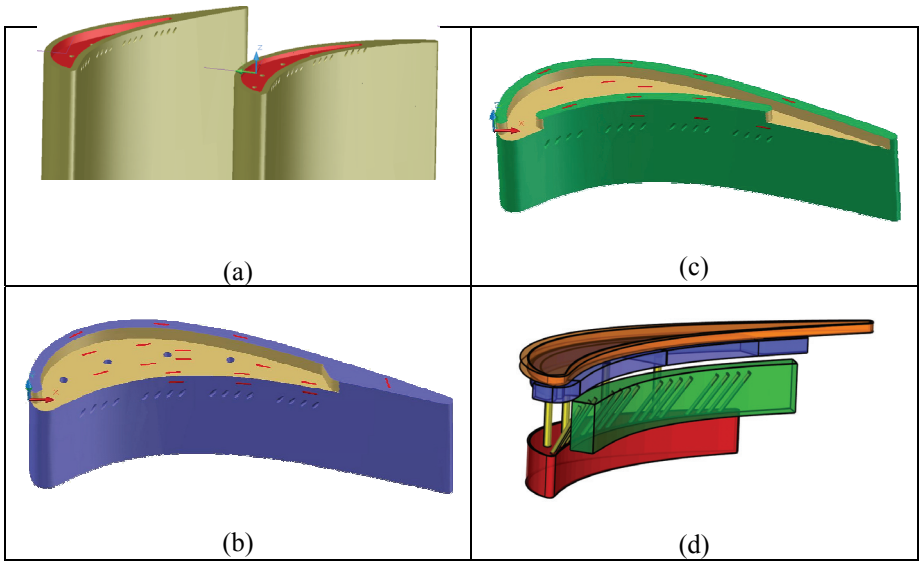

Figure 1 Geometries to be investigated: TG1 and 4 (a), TG2 (b), and TG3 (c), internal flow plenum and cooling holes with buffer block (d)

The test matrix includes two Reynolds (300 000, 900 000) and two Mach number cases (0.8, 1.1), with four distinct coolant mass flow cases (including zero cooling). The current tests are conducted with the two high Reynolds number cases with zero explicit coolant mass flow.

2.2 Numerical model

The results presented here were obtained from 3d Navier-Stokes computations using the parallel, compressible finite volume solver elsA (developed by ONERA, see Gazaix et al. [2002] for further details), on block-structured grids with overlapping boundaries and masking. The RANS equations were closed with the k-ω turbulence model of Wilcox with SST correction by Menter. For the spatial discretization of the convection fluxes the central scheme of Jameson was used, stabilized by scalar artificial viscosity. Time integration was solved with the backward Euler scheme. To decrease the difference between the propagation velocities of the acoustic and convective modes, and thus accelerate the convergence in low Mach number regions (i.e. internal flows), a low-speed preconditioning method was used.

The inlet boundary conditions (total pressure and temperature profiles) were obtained from former experimental investigations. Turbulence intensity was set to be 0.8% at the inlet, in the free stream for the aerodynamic simulations (measured values) and 3.7% for the simulations of heat transfer. The boundary layer was supposed to be fully turbulent, with a thickness of 16% of the channel height (H) at the inlet. The grid refinement in the boundary layer was chosen such that wall $y+ \sim 1$ values were realized in the entire domain, and the boundary layer was discretized with $15 \div 25$ cells. The flow was modeled as fully turbulent in the computational domain; no transition/relaminarization models were used whatsoever.

2.3 Grid

The external part of the flow domain is meshed with an HOH block-structured grid (see Figure 2a), with matching periodicity on the suction and pressure side of the O-mesh, non-matching elsewhere along the periodic boundary in case of TG1-3, and completely non-matching in case of TG4. The non-matching periodic structure is a tradeoff, sacrificing conservativity for the sake of highly regular cell shapes. Inlet-exit mass-flow divergence was hence monitored during the simulation, and a value in the order of 10^{-4} (normalized by the overall mass-flow) was reached. Grid refinement was applied at the trailing edge of the blade and in the wake. The entire grid is made up of ~6.5 (TG1)-9 (TG3) million cells. The tip clearance was discretized by 45 grid points in the quasi-radial direction, while the squealer groove contains 57 points.

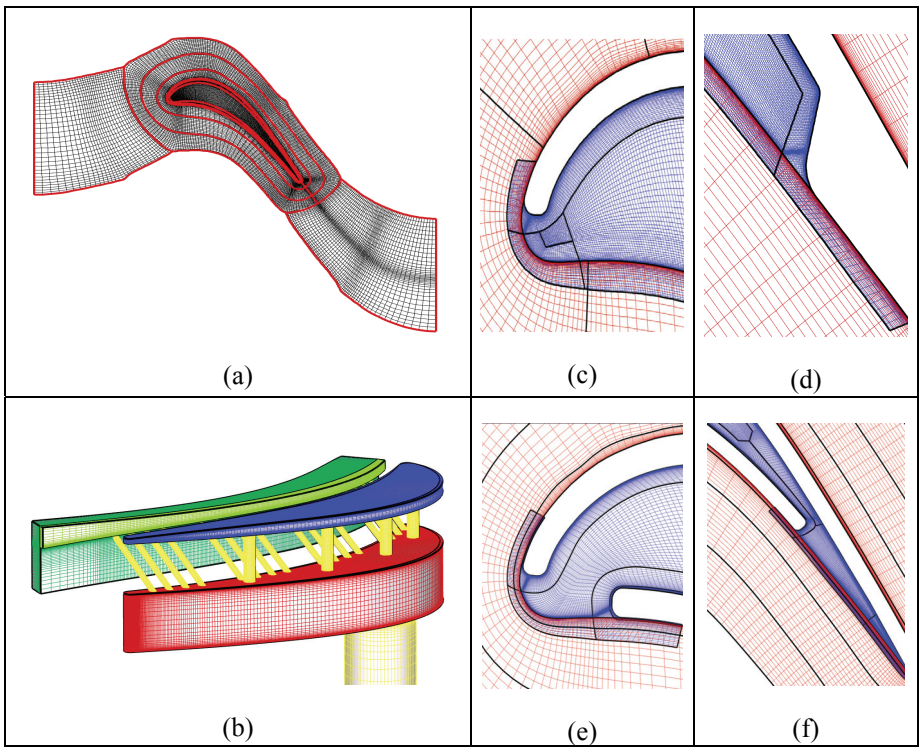

Figure 2 Multi-block structured grid in HOH configuration (a). Squealer groove grid at the leading, and trailing edge of TG2 (c and d), and TG3 (e and f). Internal grid, and buffer blocks between internal and external flow (green) in case of TG4 (b)

These two blocks were connected with overlapping grids, using the Chimera method. In case of TG2 (Fig. 2c and d) and 3 (Fig. 2e and f) the squealer groove blocks have connection with the external O-block as well. In the Chimera method information transfer between sub-domains is solved with interpolation, which is linear per tetrahedron (see Figure 2b for overlapping boundaries). These transfers are related to conservative variables, but are non-conservative (see Gillyboeuf et al. [1995] for details).
Multi-block overlapping is used in two distinct contexts within the current process: eased up meshing of sophisticated geometries by removing constraints of fully matching

connections, and enabled exclusion of certain sub domains from the computation (masking). On one hand, grid generation procedure could be scripted, semi-automated and speeded up, especially in the region of cooling hole-plenum and external-internal grid connections. With this method a large number of geometrical modifications (i.e.: tip clearance, groove depth, cooling- and dust-hole position, number and angle, etc.) could be solved changing only parameters of the grid generator script. On the other hand, the connection of internal and external flow domains poses a problem, which stems from the dissimilarity of the scales of the two flow regions. As a remedy, a buffer block is used at the cooling-hole outlets, with extreme refinement close to the exits, and growing cell size away from them, until the order of magnitude of external grid scale is reached. The external grid is masked in this wall region, where mixing between internal and external flow occurs. Chimera method is then used to connect the buffer block (green in Fig. 2b) and the external O-block. In case of TG4, the problem gets even more complicated, since the cooling holes partially exit on the top of the recessed rim close to the trailing edge. In this case a double refinement block was applied together with masking the pressure side of the O-block over the rim (light and dark green blocks in Fig. 2b).
Information transfers at the boundaries, based on interpolation pose the abovementioned problem of non-conservativity. In the current case the mass-flux difference between cooling- and dust-holes is in the order of 2 ÷ 4% of the internal mass-flow in the non-cooled (most delicate) case.

3 Results

3.1 Aerodynamics

The accuracy of the simulation from the aerodynamic point of view is controlled in the tip region around the blade, on the bottom of the tip groove, on the inner side of the rim and on the endwall. In the current summary we focus on the first area (see Fig. 3). In general, the low Mach number simulations yielded results, which are coherent with the measurements. There are some discrepancies on the suction side of TG2, which might be the consequence of the underprediction of the strength of the upper part of the tip leakage vortex. Although not shown here, similarly good matching was obtained at the rest of the control points also.
On the contrary, in case of high outlet Mach numbers (transonic condition), a regular mismatch was spotted on the aft of the suction side, not limited to the blade tip performance, but also present over the trailing edge area on the endwall. The only exception is TG1, where the outlet Mach number of the measurements was significantly lower than the nominal one (1.03 instead of 1.1).
To find out what is at the bottom of these problems, we studied the reaction of the system for changing geometrical and flow parameters. From the measurement point of view, there might be some uncertainty present in the tip gap height or the outlet Mach number. None of these parameters had an effect big enough to be responsible for the discrepancies alone. Their combined effect was already sufficiently huge, but only if they were departed from the nominal values in an unreasonable measure. On the other hand the midspan pressure measurements of Key and Arts [2004] agreed well with the current computation at nominal outlet Mach number.

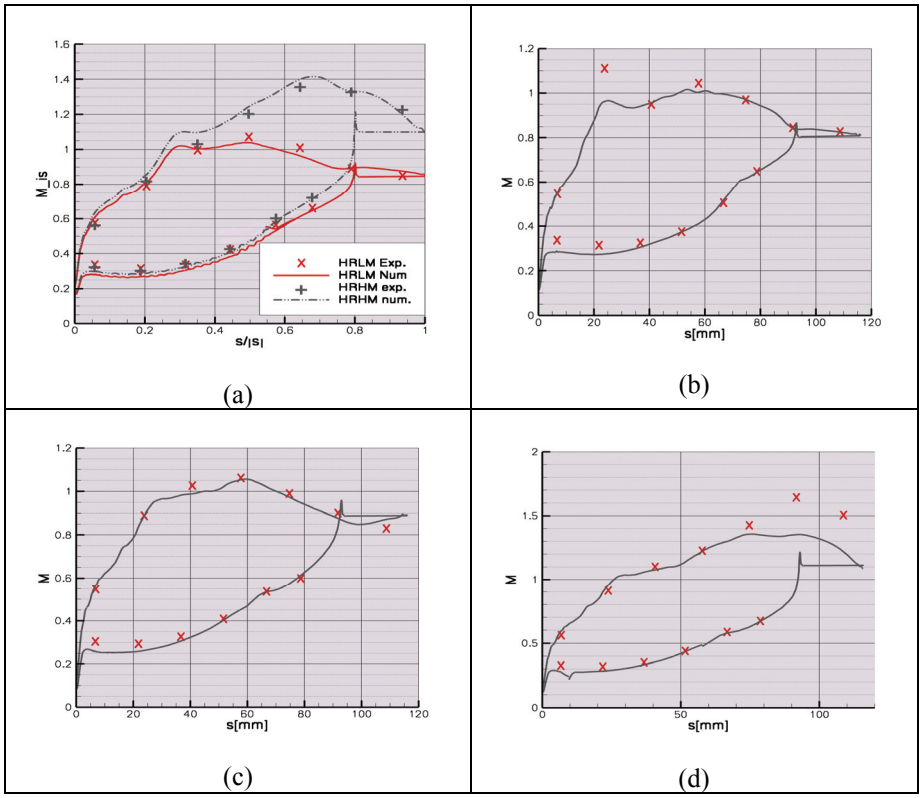

Figure 3 Blade performances in the tip region in case of TG1 low and high Mach numbers (a), TG2 (b) and 3 (c) low, and TG3 high outlet Mach numbers (d).

Considering the possible weaknesses of the simulation, one can mention the sensitivity of the k-omega turbulence model to the inlet boundary conditions. In our case the inlet turbulence level was measured, but the turbulence length scale was not known exactly, especially because there was no turbulence grid applied for the aerodynamic measurements. A wide range of inlet free stream turbulence viscosity ratios were investigated (1-50), but its effect was negligible on the tip leakage vortex, where the highest discrepancies were encountered.
As a next step, the Roe scheme will be tested in place of the stable and convenient, but dissipative Jameson scheme.

3.2 Heat transfer

The abovementioned question of inlet turbulent viscosity ratio returns in case of heat transfer, but this time it has much bigger impact, especially over the pressure side. Following the results of the investigations of Roach [1987], Hancock and Bradshaw [1983] and personal communication with Tony Arts, in the current study, values between 1 and 5 were chosen.

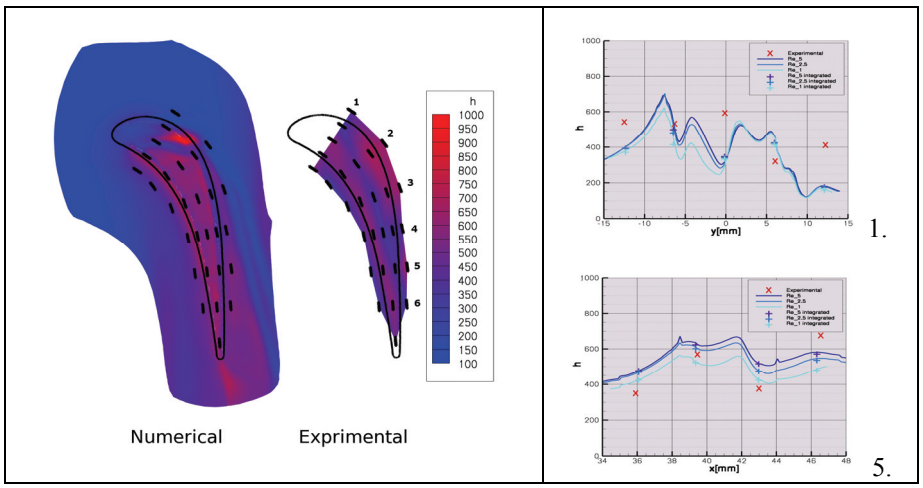

Figure 4 Heat transfer on the endwall

A comparison of heat transfer results are shown in Fig. 4. To enhance the quality of the validation, heat transfer coefficients were not only extracted along the lines of thin film gauges (perpendicular to the camberline), but were averaged over the area of the gauges, and indicated as discrete points. The numerical predictions are quite close to the measurements overall, but there are local discrepancies; the heat flux seems to be somewhat over predicted along the camberline in the middle, and underpredicted in the region of the tip leakage vortex.

4 Conclusion

During the last year, the model for TG3 and 4 were built and validated together with TG2. The numerical predictions for aerodynamics were sufficiently accurate – both qualitatively and quantitatively - in case of low Mach and high Reynolds number. However, comparisons showed discrepancies at the high Mach number simulations on the suction side, in the tip leakage vortex area. The remedy for this phenomenon has not been found yet, and needs further studies.

The boundary conditions for turbulence kinetic energy and dissipation were thoroughly tested on TG3 and 4, and the heat transfer simulations with the current setup yielded acceptable results, considering the model simplifications and assumptions.

Besides the amelioration of the accuracy of the high Mach number cases, simulations with maximum cooling are going to be performed, and validated. This case was already tested on the TG1 geometry with medium cooling mass flow. Finally the validation will be completed with an extensive flow visualization analysis.

References

[1] Arts, T.; Ginibre, P.; Oksuz, O.; Ililopoulou, V.; Key, N. [2005], Comparison of Turbine Tip Leakage Flows for Flat Tip and Squealer Tip Configurations –

Experimental and Numerical Investigation, *6th European Conference on Turbomachinery 2005, Lille, France, March 7-11, 2005.*

[2] Gazaix, M.; Jolles, A.; Lazareff, M. [2002], The elsA Object-Oriented Computational Tool for Industrial Applications, *23rd Congress of ICAS, Toronto, Canada, September 8-13, 2002.*

[3] Gillyboeuf, J.; Mansuy, P.; Pavsic, S. [1995], Two New Chimera Methods: Application to Missile Separation, *AIAA-1995-353, Aerospace Sciences Meeting and Exhibit, Reno, NV, Jan 9-12, 1995.*

[4] Hancock, P. E.; Bradshaw, P. [1983], The Effect of Free-Stream Turbulence on Turbulent Boundary Layers, *Journal of Fluids Engineering, September 1983, Vol. 105, pp 284-289.*

[5] Hofer, T.; Arts, T. [2009], Aerodynamic Investigation of the Tip Leakage Flow for Blades with Different Tip Squealer Geometries at Transonic Conditions, *Proceedings of ASME Turbo Expo 2009, Power for Land, Sea, and Air, Orlando, Florida, USA, June 8-12, 2009.*

[6] Hofer, T.; Legrand, M.; Pons, L.; Arts, T. [2009], Aerodynamic Investigation of the Leakage Flow for a Blade with a Squealer Tip at Transonic Conditions, *8th European Turbomachinery Conference 2009, , Graz, Austria, 23-27 March 2009.*

[7] Key, N. and Arts, T. [2004], Comparison of Turbine Tip Leakage Flow for Flat Tip and Squealer Tip Geometries at High-Speed Conditions, *Proceedings of ASME Turbo Expo 2004, Power for Land, Sea, and Air, Vienna, Austria, June 14-17, 2004.*

[8] Kwak, J. S.; Ahn, J.; Han J.-C.; Lee, C. P.; Bunker, R. S.; Boyle, R.; Gaugler, R. [2003], Heat Transfer on the Squealer Tip and Near-Tip Regions of a Gas Turbine Blade with Single or Double Squealer, *Journal of Turbomachinery, October 2003, Vol. 125, pp 778-787.*

[9] Papa, M.; Goldstein, R. J.; Gori F. [2003], Effects of Tip Geometry and Tip Clearance on the Mass/Heat Transfer From a Large-Scale Gas Turbine Blade, *Journal of Turbomachinery, January 2003, Vol. 125, pp 90-96.*

[10] Roach P. E. [1987], The Generation of Nearly Isotropic Turbulence by Means of Grids, *Journal of Heat and Fluid Flow, June 1987, Vol. 8, pp 82-92.*

[11] Vass, P.; Arts, T. [2009], Advanced Aero-Thermal Investigation of High Pressure Turbine Tip Flows, *ICHMT Heat Transfer in Gas-Turbine Systems – Turbine 2009, 9-14 August 2009, Antalya, Turkey.*

MULTIPHASE FLOWS

Doctoral Project Summary

Two-phase flow through singular geometries and safety valves

Vasilios Kourakos*

Supervisors: Prof. Jean-Marie Buchlin†, Prof. Patrick Rambaud‡, Dr. Saïd Chabane§

von Karman for Fluid Dynamics, Rhode-Saint-Genèse, 1640, Belgium,

Centre Technique des Industries Mécaniques

Promoter: Prof. Buchlin Jean-Marie

Université Libre de Bruxelles, Bruxelles, B-1050, Belgium

Abstract

Safety devices are of major importance in the nuclear and chemical industry. Examples of such systems are safety valves and rupture disks. A safety valve is used to discharge a certain amount of fluid in order to prevent excessive rising of pressure. The behaviour of this type of apparatus in single-phase flow (gas or liquid) has been described in detail in the literature, while for two-phase flow there is a lack of relative models. The proper design and sizing of this apparatus is an important issue which would prevent its wrong functionality that could cause a hazardous situation.

1 Introduction

The subject of modelling the discharge through a throttling device in two-phase flow has been recently studied; some models have been proposed from several authors, however until now no common practice has been widely adopted. The most important application of this problem is found in safety relief valves.

The model that has been established as the most appropriate for most conditions is the Homogeneous Equilibrium Model (HEM), the so called ω-method. It was developed by [11] and it is also the method for sizing of relief devices that is advised by the American Petroleum Institute (API) as referred in [1]. However, in Europe, although the standard concerning safety devices for protection against excessive pressure in incompressible and compressible fluid is described in ISO 4126 [8], for two-phase flow the latest standard ISO 4126-10 is to be updated and implemented.

* PhD Candidate, EA department, Chaussée de Waterloo 72, kourakos@vki.ac.be

† Professor, EA department, Chaussée de Waterloo 72, buchlin@vki.ac.be

‡ Assistant professor, EA department, Chaussée de Waterloo 72, rambaud@vki.ac.be

§ Engineer, TFE department, CETIM, Route de la Jonelière 72, 44326, Nantes, France, Said.Chabane@cetim.fr

The HEM assumes the same velocity for the two phases which appears to be an accurate hypothesis for a high level of mixing of gas and liquid. In this case, an expansion coefficient ω is determined and a theoretical critical mass flux is calculated for different operating conditions. This method can be applied both for nozzles, orifices and safety valves; hence the relief area is settled on. In Design Institute of Emergency Relief Systems, relevant studies have been carried out and in [5] and [6] the authors propose a boiling delay coefficient to account for this phenomenon. Thus, the parameter ω is corrected and a new Homogeneous Non-Equilibrium Diener-Schmidt model (HNE-DS) is proposed.
More studies in the same subject have been performed by [7] and [10]. Boccardi et al. [3] while giving an overview of the available models, they state that HEM does not predict correctly the maximum flow rate discharged from a safety valve and they propose a two-phase discharge coefficient correction.

In this project, two-phase air-water flow is studied initially in different singularities (sudden and progressive contraction and expansion) in order to build a database that would be used for the modelling of a more complex geometry such as a safety relief valve. As a next step, a transparent (made in PMMA) model of a safety valve is constructed and investigated (WEIR valve 1 in ½ G 3 in); this has allowed full optical access and therefore the identification of the structure of the flow and the observation of the different phenomena occurring. Instead of a spring, used to an actual safety valve, the disk is fixed and its position can vary from completely closed to fully opened position. Thus, the static flow behaviour of the valve is examined.

The valve is tested under different flow conditions (compressible-incompressible and two-phase) with varying parameters; the stagnation pressure, valve opening and void fraction. Depending on the flow conditions, flashing and non-flashing flow will occur and critical or subcritical flow regime is investigated. In most of the cases tested, local cavitation phenomena are observed. The discharge coefficient is determined as a function of the volumetric quality. The experimental findings are compared to the models found in literature such as the HEM. A reasonable agreement is noticed for the largest range of the measurement campaign.

2 Experimental facility and conditions

2.1 Experimental loop

An experimental closed loop is built and the flow rates of air and water and the static pressure at several locations are measured. In Fig. 1, a schematic of the facility with its different components is presented. In the first configuration simple geometrical singularities are tested (Fig. 2). In the second configuration, the test section is changed and it is replaced by the one shown in Fig. 3. The safety valve is placed on top of a small reservoir and the pressure is measured at different locations along the valve and the disk. The flow is discharged back to the big reservoir and the loop is closing. The force applied on the disk can be calculated through the pressure measured on three pressure taps along its radius. The variation of the force in function of the opening of the valve will be determined in single-phase flow and then compared to the one obtained for two-phase flow.

The valve used during the measurements is a model that was manufactured according to the plan of a 1 in ½ G 3 in valve of type WEIR. In Fig. 3 (right) the original metallic valve and the modified transparent one are compared. The main core and the inlet-outlet are of the same dimensions. However, the two disks are not exactly the same; in the transparent model it has the shape of a cylinder of the same diameter as the disk on the metallic valve. Therefore, in order to calculate the equivalent pressure this geometrical difference should be taken into account.

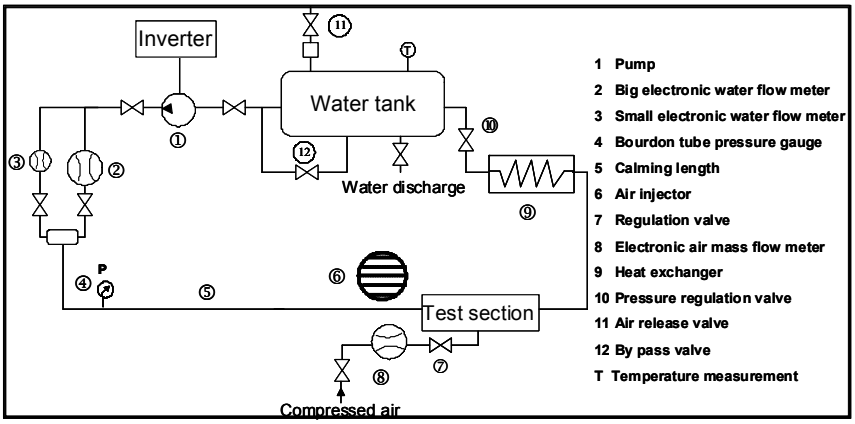

Figure 1: Experimental setup.

As it is depicted in Fig. 3, the spring of the valve is removed and it is replaced with a system that allows modifying and fixing the valve opening with an accuracy of 0.1 mm.

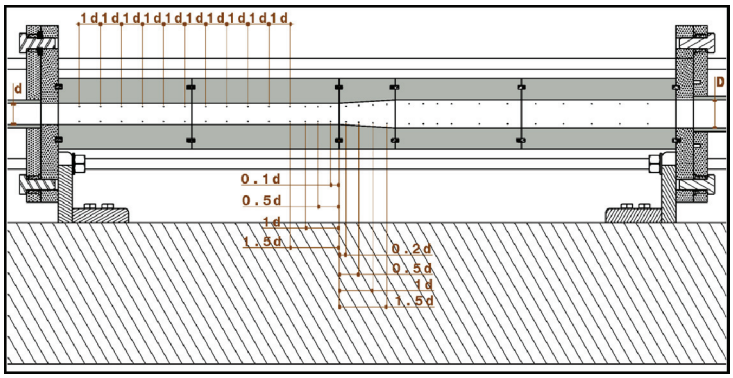

Figure 2: Test section for studying geometrical singularities (divergence).

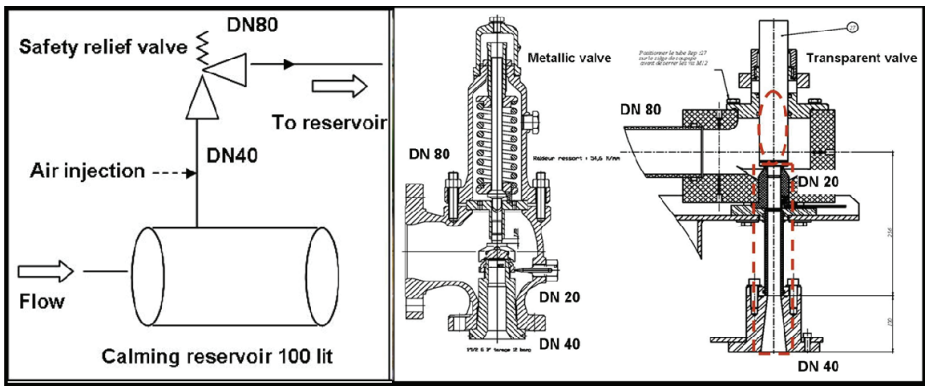

Figure 3: Detailed view of the test section for studying safety valve (left) and comparison of metallic safety valve with the transparent model (right).

2.2 Test conditions

In Table 1, the different conditions of the tests performed are given. During the measurements, the temperature is kept constant at around 20° C. The fluids used are air and water and a mixture of the two; different volumetric qualities β up to 50 % of air are examined. In each cell of the table, the extreme values are reported and in the brackets the exact number of points acquired is indicated. P_1 is the set pressure at the inlet and L the opening of the valve. The experimental campaign is carried out both in the metallic valve (only in single-phase flow) and in the transparent model (single and two-phase flow).

Additionally, the seat adjustment is another parameter under investigation for the metallic valve; for the transparent valve it is set at a fixed position (15 notches).

Finally, flashing and non-flashing and critical and subcritical regime are distinguished. In the transparent valve, due to the restrictions of the maximum pressure the critical regime could not be obtained.

Table 1: Test matrix

Conditions	*Transparent valve*		*Metallic valve*	
	Water	Two-phase	Water	Air
P_1 [bar]	1-3 (**5**)	1.5-3 (**2**)	0.5-11	0.5-11
L [mm]	0.3-7.3 (**15**)	1-7.3 (**11**)	0.5-7.5 (**12**)	0.5-7.5 (**12**)
β [%]	0	2-50 (**7**)	0	100
Seat adjustment [notches]	15 (**1**)	15 (**1**)	5-20 (**4**)	5-15 (**3**)
Flashing/non-flashing	Flashing & non flashing	Flashing	Flashing & non flashing	Flashing & non flashing
Critical/ subcritical	Subcritical	Subcritical	Critical & subcritical	Critical

3 Prediction models

3.1 Mass flux calculation

As already mentioned, the most common model to predict the mass flux through nozzles and safety valves is the Homogeneous Equilibrium Model (HEM). The so-called Omega method is based on theoretical calculations and the following assumptions:

-Both phases are at thermal and mechanical equilibrium
-Ideal gas behaviour
-Heat of vaporization and heat capacity of the fluid are constant throughout the nozzle
-Vapour pressure and temperature follow the Clapeyron equation
-The flow is isentropic (reversible adiabatic)

A coefficient ω that expresses the compressibility of the mixture is expressed for two cases; flashing and non-flashing conditions (Eq.1 and Eq. 2). The first term of ω in Eq. 1 denotes the compressibility due to the existing vapour and the second term the expansion due to phase change (depressurization).

- **Flashing**

$$\omega = \frac{x_1 v_{g1}}{v_1 k} + \frac{C_p T_1 P_1}{v_1}\left(\frac{v_{fg1}}{h_{fg1}}\right)^2 \tag{1}$$

- **Non-flashing**

$$\omega = \frac{x_1 v_{g1}}{v_1 k} \tag{2}$$

The next step of the method is to determine the critical flow conditions. The critical (or choked flow) is reached when the flow rate is maximum and a further decrease of the downstream pressure will not change the discharge rate.

- **Critical flow**

$$P_2 < \left(n_{crit} \cdot P_1\right) \quad , \qquad G = n_{crit}\sqrt{\frac{P_1}{v_1 \omega}} \tag{3}$$

- **Subcritical**

$$P_2 \geq \left(n_{crit} \cdot P_1\right) \quad , \qquad G = \frac{\sqrt{-2\left[\omega \ln\left(n_2\right) + \left(\omega - 1\right)\left(1 - n_2\right)\right]}}{\omega\left(\frac{1}{n_2} - 1\right) + 1}\sqrt{\frac{P_1}{v_1}} \tag{4}$$

For the determination of the critical pressure ratio n_{crit} two cases can be discriminated:

-If ω > 2

$$n_{crit} = 0.55 + 0.217\ln(\omega) - 0.046\left(\ln(\omega)\right)^2 + 0.004\left(\ln(\omega)\right)^3 \quad (5)$$

-If $\omega \leq 2$

$$n_{crit} + \left(\omega^2 - 2\omega\right)\left(1 - n_{crit}\right)^2 + 2\omega^2 \ln\left(n_{crit}\right) + 2\omega^2\left(1 - n_{crit}\right) = 0 \quad (6)$$

In the lateral case, the equation is solved iteratively for different values of ω.

3.2 Discharge coefficient

The discharge coefficient is defined as follows:

$$K_d = \frac{\dot{M}_{theor}}{\dot{M}_{\exp}} \quad (7)$$

which is the ratio of the ideal mass flow rate to the actual flow rate passing through the nozzle. This number indicates the difference of the nozzle from the ideal behaviour.
For two-phase flow, Darby [4] has proposed the correlation:

$$K_{dTP} = K_{dV}\beta + \left(1 - \beta\right)K_{dL} \quad (8)$$

4 Results and discussion

In this section the results obtained in the two configurations (singularities and safety valve) are briefly presented.

4.1 Singularities

4.1.1 Pressure measurements

The evolution of the static pressure is studied in several singularities. The pressure is measured along the pipe and inside the singularities. An example of such a measurement is shown in Fig. 4 for the case of divergence section and for different opening angles. It is found that the smallest is the enlargement angle, the largest the recovery pressure for the same flow conditions; the pressure drop caused by the singularity is higher in the case of a sharper enlargement.

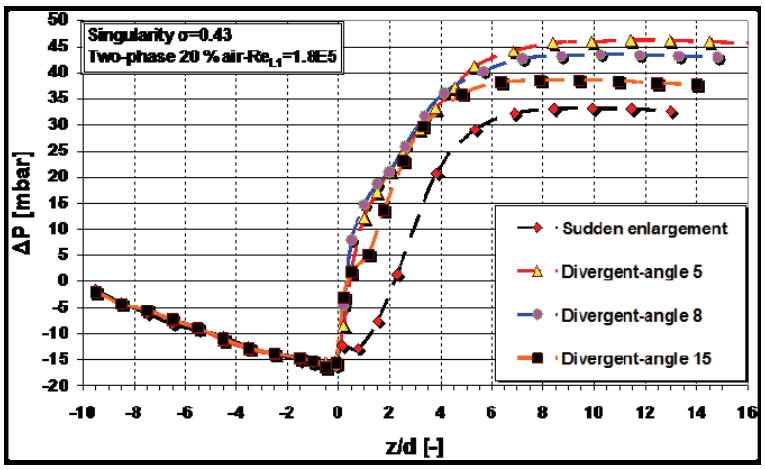

Figure 4: Static pressure evolution versus axial position for sudden and progressive enlargement of different opening angles for Re_{L1}=180000 and 20% of air.

The singular static pressure change is established through these plots for different volumetric qualities. A correlation for sudden enlargement proposed by Jannsen & Kervinen [9] is modified to take into account for the opening angle and the upstream liquid Re number:

$$\Delta P_{tot} = -\left[0.061\cdot\alpha^{0.8917} - 10717\cdot \mathrm{Re}_{L1}^{-0.8283} + 0.378\right]\cdot\frac{G_1^2}{2\rho_L}(1-\sigma)^2\left[1+x\left(\frac{\rho_L}{\rho_g}-1\right)\right] \qquad (9)$$

4.1.2 Flow visualization and flow regime maps

Flow visualization with high-speed camera is performed and four different flow patterns are identified downstream of the divergence section; Bubbly, Plug, Disperse and Annular flow. These are represented in the flow regime map of Baker [2] and a flow map is established. One should point out that this map is only valid for this configuration.

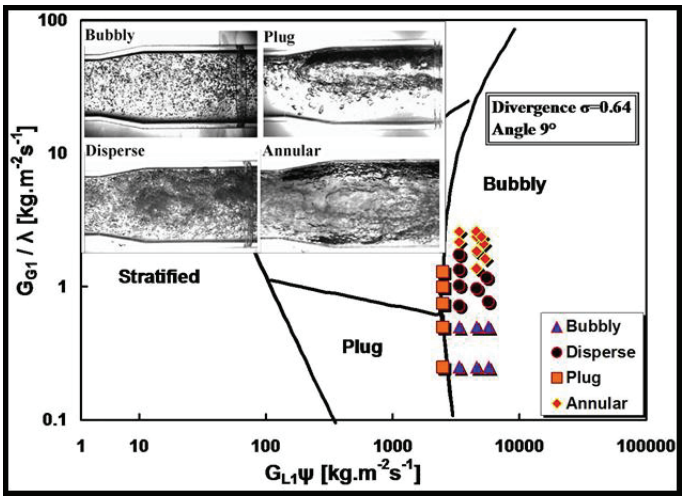

Figure 5: Baker flow regime map for two-phase horizontal flow (1954) with the different flow regimes determined by flow visualization.

4.2 Safety valve

The static pressure is measured at different locations of the valve. The dynamic pressure is computed at the different sections of the valve. Thus, the total pressure drop measured from a reference point far enough from the valve is calculated. An example of the pressure drop at the different locations for various set pressures and volumetric qualities is reported in Fig. 6.

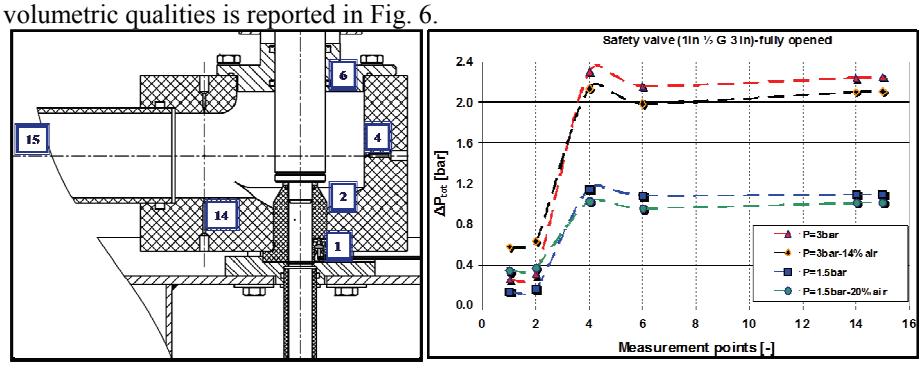

Figure 6: Total pressure drop at different measurement points for various set pressures and volumetric qualities.

The influence of the presence of air on the volume flow rate versus the valve opening can be deduced from Fig. 7. The set pressure P_1 is equal to 2.7 bar. We observe that the discrepancy of two-phase flow from single-phase flow is more important for intermediate valve openings (around 3-4 mm) and becomes less important for the biggest and smallest openings.

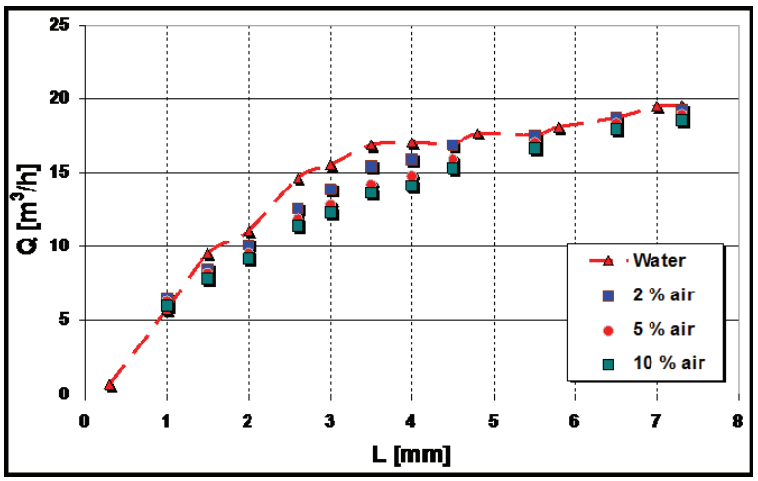

Figure 7: Volume flow rate versus valve opening for different volumetric qualities.

The force applied on the valve disk can be calculated by integrating the pressure measured at the three pressure taps located along the radius of the disk. For the same conditions (P_1=2.7 bar), the force is calculated and plotted against the opening of the valve for single (water) and two-phase flow of varying β. As a first remark, it can be concluded that the value of the force fluctuates more for the smallest openings and its behaviour seems more stable and linear for the highest ones.

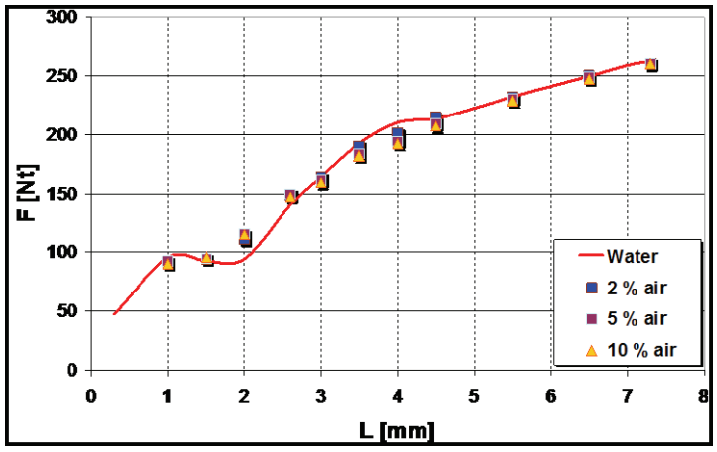

Figure 8: Force applied on the valve disk versus valve opening for water and air-water mixtures.

Figure 8 illustrates the influence of the gaseous phase on the force applied at the disk. Until up to 10 % of volumetric quality, no significant difference is remarked. Hence, in order to identify the small difference of the force in two-phase flow from single-phase, the ratio ΔF is defined:

$$\Delta F = \frac{F_{TP} - F_{SP}}{F_{SP}} \tag{10}$$

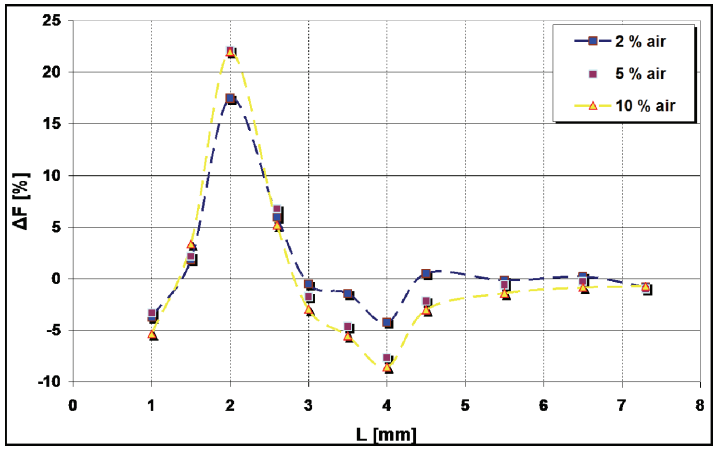

Figure 9: Discrepancy between the force in two-phase and the force in single-phase.

The mass flux through the valve for different mass qualities at maximum lift is measured experimentally and then calculated with the ω-method. In Fig. 10 the result is depicted for two set pressures; 1.5 and 3 bar. The agreement is satisfactory mainly for the lowest qualities and the highest pressures; this is also reported in [3], [5] and [11].

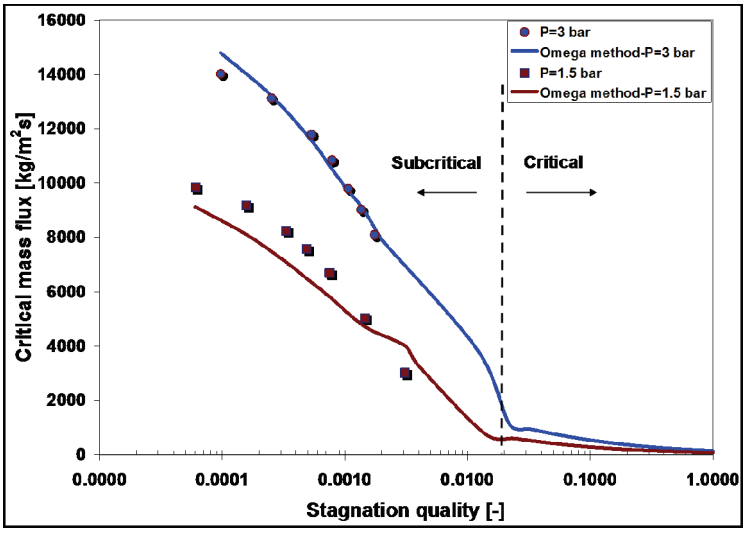

Figure 10: Critical mass flux measured and calculated with the Omega method.

The two-phase discharge coefficient K_{dTP} is calculated with the formula given in Eq. 8; the discharge coefficients for liquid and vapour are determined experimentally. The same parameter is estimated experimentally as the ratio of the theoretical mass flow

through the valve, calculated with the ω-method, and the measured mass flow rate. The results are plotted in Fig. 11. An important deviation is observed which shows the lack of accuracy of this formula for the present conditions.

Finally, flow visualization is carried out in the upstream part, downstream part and the core of the valve. In Fig. 12, an example is given for P_1=1.5 bar, L=2.6 mm and β=1.5 %. By means of image processing, a rough estimation of the bubble diameter upstream and downstream is obtained and no significant difference is observed with a mean value of D_{bubble}=1.55 mm.

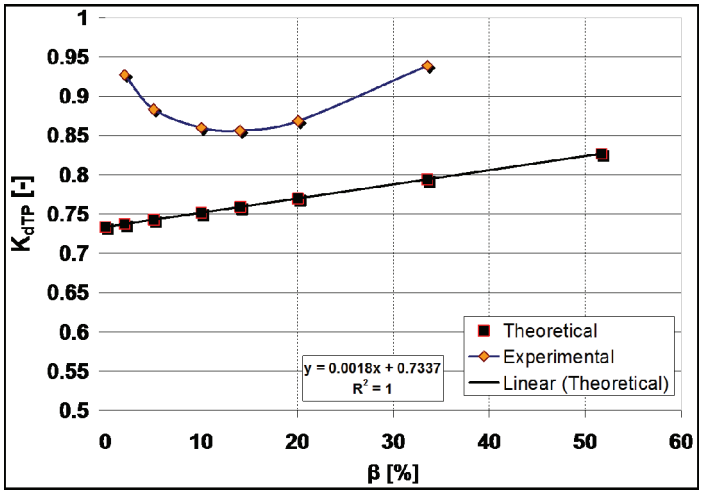

Figure 11: Experimental and theoretical two-phase discharge coefficient against the volumetric quality.

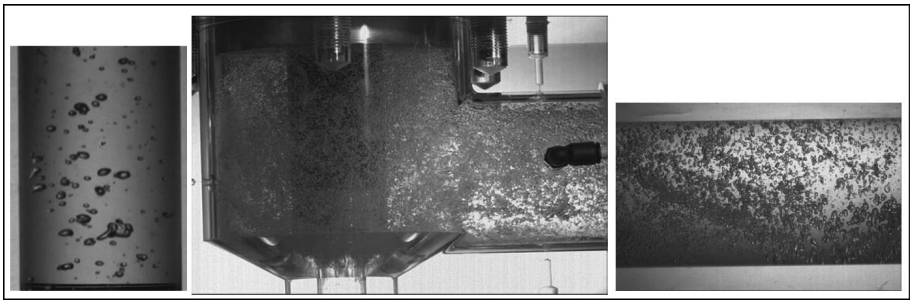

Figure 12: Flow visualization in the safety valve model-upstream (left), core of the valve (center) and downstream (right).

5 Conclusion

An important experimental database is built by testing several simple geometrical singularities, commercial metallic safety valve and transparent model of a safety

valve. The models existing in literature to predict the flow discharge through throttling devices are mainly based on the homogeneous flow assumption. However, it is found that the accuracy of these models is poor under certain conditions. Therefore, the importance of finding other models that will be able to handle with a larger range of applications should be stressed out. The determination of the slip ratio between the two phases will possibly lead to more realistic results. Finally, one should point out the significance of such an achievement for the correct design of safety relief valves.

Nomenclature

A	area (m^2)
C_p	specific heat at constant pressure
G	mass flux (kg/m^2s)
H	specific enthalpy (KJ/Kg)
K	ratio of specific heats of the vapour phase (-)
K	coefficient (-)
L	valve opening (mm)
□	mass flow rate (kg/s)
n_{crit}	P_{crit}/P_1
n_2	P_2/P_1
P	pressure (bar), 1bar=0.1 MPa
Q	volume flow rate (m^3/h)
Re	Reynolds number (-)
T	temperature (K)
v	specific volume (kg/m^3)
x	mass vapour quality (-)
Greek letters	
α	enlargement opening angle (°)
β	volumetric quality (-)
Δ	difference (-)
ρ	density (kg/m^3)
σ	surface area ratio (A_1/A_2)
ω	compressibility coefficient (-)
Subsripts	
crit	critical flow conditions
d	discharge
fg	difference between liquid and vapour phase
g	gas
L	liquid
m	mass
SP	single-phase
tot	total
TP	two-phase
V	vapour
1	upstream
2	downstream

Acknowledgments

The support of the French company CETIM (Centre Technique des Industries Mécaniques) situated in Nantes, France is gratefully acknowledged.

References

[1] API, American Petroleum Institute, Sizing, Selection and Installation of Pressure-Relieving Devices in Refineries, Part 1-Sizing and Selection. API Recommended Practice 520, seventh ed. (2000)

[2] Baker, O., Oil Gas J., Vol. 53, pp. 185 (1954)

[3] Boccardi, G., Bubbico, R., Celata G. P. & Mazzarotta B. Two-phase flow through pressure safety valves. Experimental investigation and model prediction, Chemical Engineering Science, Vol. 60, pp. 5284-5293 (2005)

[4] Darby, R., Evaluation of two-phase flow models for flashing flow in nozzles. Process Safety Progress, Vol. 19 No 1, pp. 32-39 (2000)

[5] Diener, R. & Schmidt, J. Sizing of throttling device for Gas/Liquid two-phase flow. Part 1: Safety valves, Process Safety Progress, Vol. 23 No.4, pp. 335-344 (2004)

[6] Diener, R. & Schmidt, J. Sizing of throttling device for Gas/Liquid two-phase flow. Part 2: Control valves, Orifices, and Nozzles, Process Safety Progress, Vol. 24 No.1, pp. 29-37 (2005)

[7] Henry, R. E., Fauske, H. K. The two-phase critical flow of one-component mixtures in nozzles, orifices, and short tubes, Journal of Heat Transfer, Vol. 93, pp. 179-187 (1971)

[8] ISO 4126-1, Safety devices for protection against excessive pressure

[9] Jannsen, E., Kervinen, J. A. Two-phase pressure drop across contractions and expansions of water-steam mixture at 600 to 1400 psia. In report Geap 4622-US (1966)

[10] Lenzing, T., Friedel, L., Cremers, J. & Alhusein, M. Prediction of the maximum full lift safety valve two-phase flow capacity, Journal of Loss Prevention in the Process Industries, Vol. 11, pp. 307-321 (1998)

[11] Leung, J. C. Easily size relief device and piping for two-phase flow, Chemical Engineering Progress, Vol. 92 No 12, pp. 28-50 (1996)

Doctoral Project Summary

Microscale Bubble Simulation in Electrochemical Processes

Pawel Skuza[1]

Supervisor: Prof. Herman Deconinck[2]

von Karman for Fluid Dynamics, Rhode-Saint-Genèse, 1640, Belgium

Promoter: Prof. Johan Deconinck[3]

Vrije Universiteit Brussel, Brussel, 1050, Belgium

Abstract

This paper is concerned with the microscale simulation of bubble formation and evolution in electrochemical processes. The flow simulation is achieved by using a single-phase stabilised Finite Elment solver (SUPG and PSPG) combined with a level set method to track the interface between bubble and liquid. So-called Mesh Alignment is proposed to increase the accuracy of the Level Set tracking and to allow application of surface tension in a sharp manner. The dissolved gas phase is electrochemically generated based on the Multi Ion Transport and Reaction Model (MITREM) which is coupled with the flow solver. Mass transfer through the bubble interface occurs when dissolved gas reaches saturation.

1 Introduction

The subject of this Ph.D. project is related with a multidisciplinary project MuTEch, which stands for: "Novel Multi-scale approach to **T**ransport phenomena in **E**lectro-chemical **P**rocesses". The project aims at providing new generic numerical and experimental tools to study heat and mass transfer, gas evolution and fluid turbulence in electrochemical systems of practical interest. One of the issues is the prediction of bubble formation and evolution close to an electrode during the electrochemical process, which is the subject of the presented research.

Bubly flow is a two-phase flow phenomenon, that can be described in several ways. One approach is a mathematical description of the physics for the whole computational field based on liquid and gas fractions, thereby eliminating the individual bubble behavior (Eulerian-Eulerian formulation). This allows a simulation at macro-scale. Another approach for two-phase computing is obtained by separating between a continuous carrier phase (which is the liquid) and a dispersed gas phase

[1] PhD Candidate, Aeronautics and Aerospace department, Chaussée de Waterloo 72, skuza@vki.ac.be

[2] Professor, Aeronautics and Aerospace department, Chaussée de Waterloo 72, deconinck@vki.ac.be

[3] Professor, Electr-mechanical Engineering, Pleinlaan 2, jdeconinck@vub.ac.be

which is modeled as a set of particles and individually tracked (Euler-Lagrange). This is a simulation at meso-scale. The last possibility is a simulation at micro-scale, where a bubble is relatively large in comparison to the size of the computational domain and much bigger than the element size of the mesh. The smaal scale resolution allows to observe bubble formation, growth and lift off from an electrode, as well as its influence (and dependence) on the electrochemical processes.
The study of the bubble behavior in electrochemical processes can be grouped into 3 topics:

- methods for tracking a bubble boundary,
- bubble mechanics (flow, surface tension),
- electro-chemical reaction kinetics and mass transfer.

The first topic describes the movement of a bubble boundary. Numerically this is achieved by a Level Set Method with additional techniques like reinitialization and extension velocities, and accurate computation of interface position, its normal and curvature.
Bubble mechanics is a driving force behind any bubble simulations. It consists of momentum and continuum equations, as well treatment of surface tension. Physical results with use of real parameters are shown.
Electro-chemistry is a huge subject of science, and for this reason an application to this field is done with an external library developed at Vrije Universiteit Brussel. A combination of bubble mechanics and a solver for multi-ion transport and reaction opens research of bubble manner in unique scope.

2 Level Set Method

Level Set Method is a set of methods initially developed by Osher and Sethian[1]. It is based on a definition of a scalar field valued by a function φ where an iso-contour of zero value has a special role as the boundary of an object. Negative values of the function determine a body (inner part) of the object, and positive values are the surroundings. In the present two-phase flow simulations the object is a bubble (dispersed gas phase) and the surroundings are the continuous liquid phase.

2.1 Features of the Level Set Method

A Level Set Method is chosen on purpose to describe an interface, because of following features:

- a definition of the object body,
- a straight forward calculation of interface normal and curvature as a normalized derivative of φ and divergence of the normal respectively. The normal and curvature are smooth, and they can be directly used to calculate of surface tension,
- an automatic coalescence and separation of an interface during body movement, even for very complex shapes.

Although very powerful, the Level Set Method has also disadvantages like:

- an explicit definition of an interface must be interpolated, which introduces an error in its position,

- normal and curvature of near interfaces are wrongly calculated due to differential equations, what require surrounding elements to calculation,
- a mass of the object is not preserved, because movement of the interface is done by an advection equation. The mass is slightly controlled with a medium by its continuous equation. Therefore any introduced error cannot be compensate,
- spontaneous interface connection is visible for a course mesh, where two near interfaces join due to lack of elements between them,
- a real case of a chaotic fluid field requires an extension velocities technique what preserve to change a Level Set function,
- the other technique, so-called reinitialization is used to preserve a Level Set function near a computational boundary. This technique is a main source of mass lack, because any interference to Level Set function causes an interface movement.

All the above mentioned disadvantages are improved all completely cured by the Mesh Alignment approach proposed in this work.

2.1.1 Mesh Alignment

The Level Set Method with some modifications can be successfully used in bubble simulations. The required changes use a mesh adaptation to the interface, where nodes are aligned to the object boundary, and an edge of an element belongs to the interface. Nodes are moved according to Level Set definition, therefore no interpolation error is introduced. Performance tests show an improvement of interface position up to 4th other. This technique also is very important in multi-physic simulations, because an interface divides a computational domain by a sharp edge. Therefore boundary conditions for a sub-domain can be applied directly. And also additional physic, like surface tension, can be applied directly to edge nodes. Another advantage of this method is treatment of a discontinuity of material properties, e.g. different medium can be used inside and outside of the object, and also discontinuity of physical variables can be treated accurately, e.g. a pressure jump due to surface tension.

3 Bubble mechanics

The physical behaviour of the bubble is determined by a two-phase solver[2]. This is an axisymmetric Finite Element solver with SUPG and PSPG stabilisation techniques[3] covering the complete domain (including bubbles). The bubble position and its body is described by the Level Set function. Therefore material properties, such as density and viscosity, are determined by a sign of Level Set function φ. Essential physics for bubble simulations is surface tension, because it shapes a bubble. Thus additional force proportional to interface curvature and normal is calculated and goes directly to momentum equations in an boundary integral form as a source term. That force is applied directly to interface nodes.

Surface tension creates a pressure jump on the bubble interface, and with huge density difference between phases, causes uniform pressure inside the bubble. This phenomenon is used during mass transfer, where a bubble extends or shrinks in all directions equally. Therefore any mass transfer is translated to an interface speed which acts in a normal direction to the boundary and has the same value on the whole interface. But yet surface tension has a side effect also. Pressure inside the bubble

should balance the surface tension effect. Nevertheless it causes a bubble shrinking together with surface tension growth. Therefore mass control described above is used.

Bubble simulations with a Mesh Alignment Method requires a special treatment of the computational domain. Three meshes are used to perform a simulation. One is used for a Level Set function and interface movement. This is a fixed mesh. The others are used for current and previous/next time step. Each time step has its own mesh, because of the alignment which follows the bubble movement. In that case, discontinuity in physical variables, like a pressure jump, cannot be interpolated from the whole sub-domain. Therefore a projection of data from one mesh to another (from one time step to another) must be done with extrapolation for these elements which are sticking out of given sub-domains in a new time step.

4 Electro-chemistry simulations

When bubble evolution, growth and lift up from the electrode has been achieved by the solver, the electro-chemistry can be applied and tested. The electrochemical solver has been developed at the Vrije Universiteit Brussel and a Mitrem (multi-ion transport and reaction [4]) library is used.
The computational domain is limited to the liquid phase, (therefore the interior domain of the bubble is not used in the electrochemical simulation). The Mesh Alignment method gives the boundary of the computational domain at the bubble interface, where a boundary conditions has to be applied. In the case of bubble simulations, three kind of boundaries are used. The first is a potential electrode – it is a place, on the wall not covered by the bubble. Another is a virtual electrode – it is a far-away place with zero potential. The last one is a gas-production source which is applied on the boundary given by the bubble interface. Position and size of these boundaries, as well as the computational domain are changing during the bubble simulations, it is a dynamic system determined by bubble mechanics and a gas production ratio which provides feedback to the electrochemical processes.

As a computational example, hydrogen evolution during bubble formation is shown in Fig. 1. A first picture (left) shows the hydrogen concentration, giving high concentrations because the large surface of the electrode, not shielded by the bubble. A potential electrode is at the bottom, partially covered by a bubble. A virtual electrode is at the top of computational domain. The bubble shape is covered by a gas-production source. The next frames show hydrogen consumption from dissolved phase in the liquid toward the gas phase in the bubble, thus inducing the growth of the bubble. The last frame shows a shielding effect, where a bigger detached bubble acts as a screen diminishing the influence of the upper electrode and therefore the gas production ratio is smaller even though electrode on the lower surface has again the initial size of the original surface.

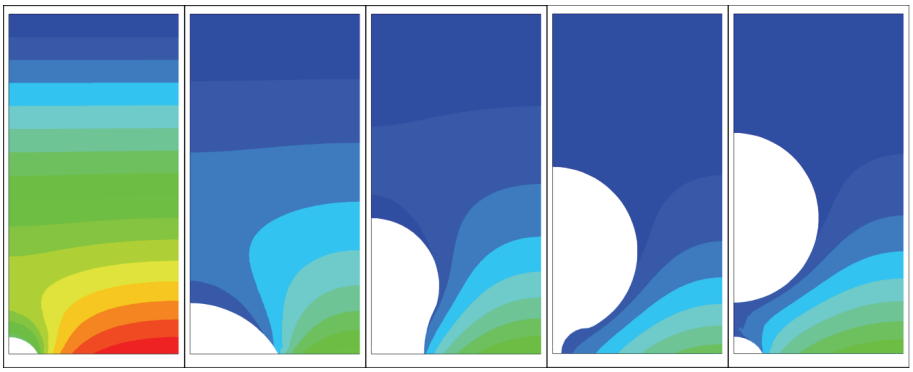

Figure 1: Hydrogen evolution during bubble formation.

5 Conclusion

Bubble simulation at micro-scale is a challenge. The computations are highly dominated by the surface tension effect, and very high density and viscosity ratios between the phases are present. These factors cause huge instabilities of velocity around the buble interface, so-called spurious currents, and also pressure oscillations in the whole computational domain. Higly accurate interface position and sharp treatment of the surface tension made it possible to minimize these destructive effects and to study the bubble physics.
The combination of bubble mechanics and a solver for multi-ion transport and reaction opens unique possibilities for the research of bubble behavior, which is the next phase of this PhD project.

Acknowledgments

The project was financed by Flemish government agency for Innovation by Science and Technology (IWT). A presented work was done in cooperation between the von Karman Institute and Vrije Universiteit Brussels under the supervision of Prof. Herman Deconinck (VKI) and Johan Deconinck (VUB-SURF).

References

[1] J. A. Sethian. Level Set Methods and Fast Marching Methods. Cambridge University Press, 1999.

[2] T. De Mulder, H. Deconinck, J-M. Buchlin, Technical note 184. von Karman Institute for Fluid Dynamics. 1994.

[3] M. Sussman, P. Smerka, S. Osher, Journal of Computational Physics, 114, 145-159, 1994

[4] G. Nelisen, A.V. Theemsche, C. Dan, B.V den Bossche, J. Deconinck. Journal of Elektroanalytical Chemistry. 563, 213-220, 2004.

ENGINE AND COMPRESSOR FLOWS

Doctoral Project Summary

Numerical investigation of the secondary flows in low pressure axial compressor stage for contra-rotating turbofan architectures

Balázs Farkas*

Supervisor: Jean-François Brouckaert†

von Karman Institute for Fluid Dynamics, Rhode-Saint-Genèse, 1640, Belgium

Promoter: Not deffined‡

Abstract

Secondary flows have major effects on turbomachinery performance. The following work presents an extended numerical study of a one and a half stage axial compressor designed to represent a possible architecture of the first stage of the booster for a contra rotating fan engine. The challenge of such an architecture is set by the fact that the rotor is mounted on the same shaft as the second stage of the fan which results in a low rotating speed and therefore needs much higher loading as usually seen in conventional high bypass-ratio aero-engines.

Particular interest is given in the study to the investigation of the effect of the tip leakage vortex and sealing leakage flow on performance and stability.

The computations are performed by using the Numeca developed Fine-Turbo code. The present calculations were performed with a steady-state RANS solver.

The compressor itself was also built and mounted in the VKI closed loop test facility (VKI-R4) The measurement results allow to perform validation of the computations. .

1 Introduction

The following work was done in the framework of Project Vital work package 3.2 Advanced aerodynamic technologies. The aim was to design, build and test a single stage axial compressor which represents the booster stage for a contra-rotating fan architecture aero-engine. In recent designs of such engines the booster stage rotors are mounted on the same shaft as the second stage of the fans. Due to this structure the rotational speed is lower and therefore the loading of the compressor is much higher than as it is in conventional high bypass-ratio aero-engines. Though its possible to decrease the loading with increasing the mean radius of the blade rows and by this

*PhD Candidate, Turbomachineryt, Chaussée de Waterloo 72, farkas@vki.ac.be.

†Assistant Professor, Turbomachinery Department, Chaussée de Waterloo 72, Brouckaert@vki.ac.be.

‡

increasing the circumferential speed of the rotor blades. This solution is limited since doing so the blade aspect ratio decreases proportionally as well which makes the stage more sensitive to secondary flows and increases the losses.

Recent study is focusing on investigation of the compressor behavior by determining the stability range and the evolution of secondary flows at different throttling conditions. Further investigations were performed to study the effect of passive stability control with using circumferential groove casing treatment (CT) and the effect of the seal-leakage flows on the global performance. The numerical predictions were compared with measurement data to estimate the capability of flow field analyzes.

2 Numerical setup

The simulations were done by using Fine Turbo software which was developed by Numeca. The computational domain can been seen on Fig. 1..The mesh have been generated with the AutoGrid5 software. In the passage, they are based on its general O4H default topology combined with a butterfly OH grid in the tip gap. The mesh counts 816465 grid points for the IGV, 1680131 for the rotor and 944097 for the stator. The global mesh holds 3506726 grid points.

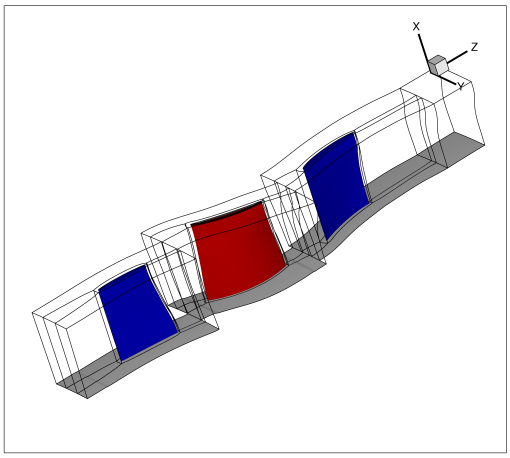

Figure 1: 3D view of the computational domain

After several turbulence-models had been investigated [1] Yang-Shih k-epsilon model was chosen for detailed investigation of the compressor. Regarding boundary conditions, the measured total pressure and total temperature profiles were imposed at the inlet combined with estimated turbulent quantities. As outlet boundary condition, radial equilibrium throttle condition was applied, fixing the static pressure at the shroud.

For modeling technical effects additional zones were attached to the base line mesh configuration as shown on Fig. 2.. The zone representing the circumferential casing treatment is connected to the main domain with using full non-matching connection meanwhile matching connection were applied between the the main domain and the leakage channel. The flat leakage channel between the outlet and the inlet of the stator stage is basically the most simplified representation of the leakage flow across the labyrinth sealing applied in the test rig. The predicted leakage mass-flow is expected

to be highly overestimated. In this case the aim was more to have an idea about the possible effects of leakage flow and saving computational time rather than having quantitative results.

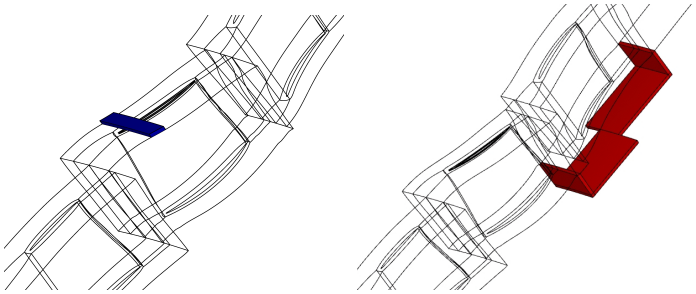

(a) (b)

Figure 2: 3D view of the added technical effects (Casing treatment (a), Sealing channel (b))

3 Results

3.1 Base line and CT simulations

Fig. 3. shows total pressure ratio,efficiency and static-to-total pressure ratio versus reduced mass flow. The experimental data were taken at 4 significant operation point from choke till the last stable operation point. In case of numerical simulations the stall limit is found by performing computations with a pressure ratio close to stall conditions. The static back-pressure is then increased step by step until the code does not converge anymore. Although steady computations cannot reproduce an unsteady phenomenon like stall, this approach can be quite well correlated with experiments [2]. The results shows fairly good agreement between experimental and numerical data but the there is considerable difference when predicting the effect of the CT. Meanwhile, computations with Fine Turbo show decrement in performance with circumferential groove CT, experimental results and computations made by Cenaero using elsA with k-epsilon, L-S turbulence model on the same geometry show slight improvement both on efficiency and pressure ratio. In former researches the effect of the circumferential grooves was mostly stated as slightly determinant as for example in [3]

Fig. 4. Shows the comparison of the pitch-vise averaged radial distributions of the Liblein Diffusion Factor between experimental and numerical results. Both data sets indicates slight changes in flow variables due to the applied CT and in both cases the differences have the same course. Rest of the extracted data shows similar tendencies. The results also showed that applying passive control at the tip area does not modify the stability limit.

3.2 Seal leakage flow simulations

Fig. 5. shows pitch vise averaged radial pressure ratio distribution of the stator stage. Here one can observe higher discrepancies at the hub area both in values and more significantly on the course of the curve. With modeling the effect of the seal leakage

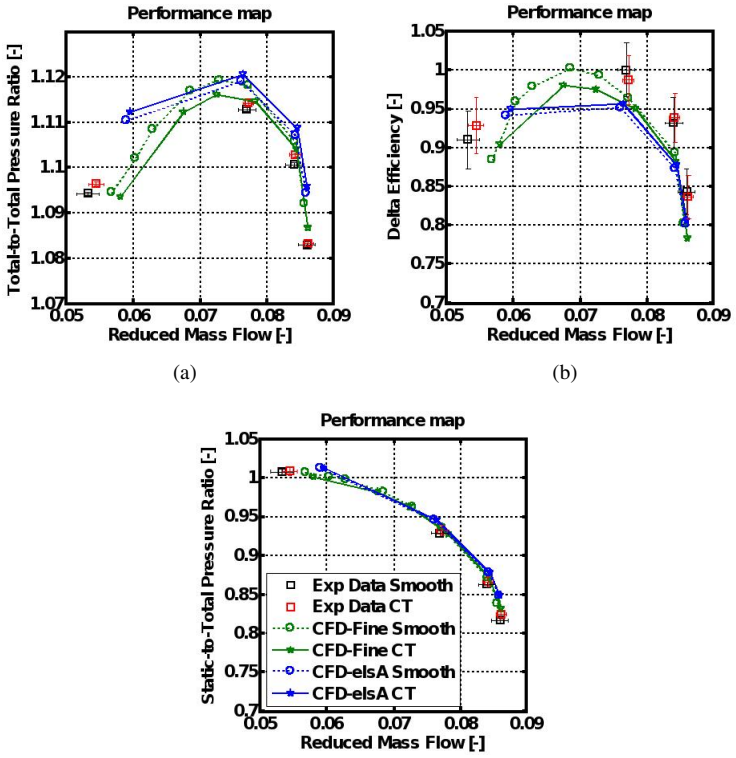

Figure 3: Total pressure ratio, relative efficiency and static-to-total pressure ratio versus reduced mass flow at nominal speed for smooth casing and casing treatment configurations.

flow the discrepancies tend to decrease. But even at mass-flow rates much higher than what could occur in the real machine across the labyrinth sealing, as it was mentioned in the numerical setup section, the pitch vise extent of the low pressure zone close to the hub is still predicted to be much smaller than as was experimentally observed(Fig. 6.). Another method was also applied to simulate the seal leakage flows where additional mass-flow was injected into the main flow at the position of the axial gap between the rotor and the stator. The change in performance at different injected mass-flow rates are presented on Fig.7. The degradation in total pressure and in efficiency is the result of the blockage which is generated by the radially injected mass flow.

Here is worth to mention that the experimentally defined output pressure distributions (Fig. 6.(a)) shows very similar tendencies to the contour plots which were extracted behind blade rows where hub-corner stall occurred as it can be seen in [4]. Meanwhile, simulations shows that even close to stall the reversed flow is confined to the suction surface of the stator blade.

3.3 Unsteady simulations with NLH method

Recently Numeca added the Nonlinear Harmonic Method to the Fine-Turbo software which allows investigating unsteady effects like rotor-stator interactions and by this it

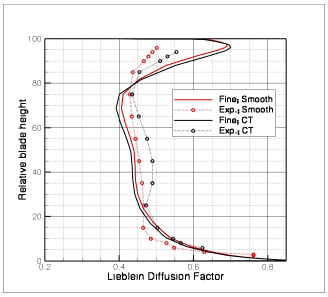

Figure 4: Lieblein Diffusion Factor of the rotor at maximum mid-span pressure ratio

also makes possible to study the effect of secondary flows on the whole stage since their trajectory does not brake down when they reach the mixing planes for lower cost than 'standard' unsteady models in turbomachinery [5]. Fig. 8 shows the result with using NLH method at three following time steps. The discrepancies in the pitch vise extension of the wake between the two sides of the mixing-plane is due to the coarse mesh which was applied for the first tests.

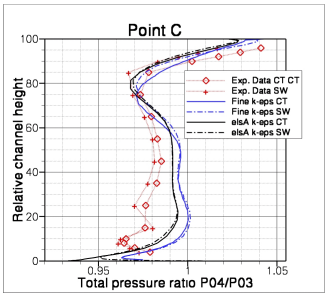

Figure 5: Pressure-ratio of the rotor at maximum mid-span pressure ratio

4 Conclusion

The importance of understanding the behavior of the secondary flows is unambiguous since they presence can not be fully eliminated from turbo machines.

First we can conclude that using casing treatment or any passive control on the tip leakage flow in booster stages has only slight effect on the performance. This is due to the fact that in high by-pass ratio aero-engines the booster stages are strongly hub loaded to redistribute the highly skewed flow, coming from the fan stage, before it enters to the high pressure compressor. Therefore the original aim to optimize the geometry of the casing treatment to achieve wider stability limits seems to be out of question

In the followings discrepancies between the numerical and experimental results needs further examinations in order to achieve better performance predictions in the future.

Further simulations with NLH method are also prepared to investigate the effect of the tip leakage vortex and the rotor wake on the performance of the stator row.

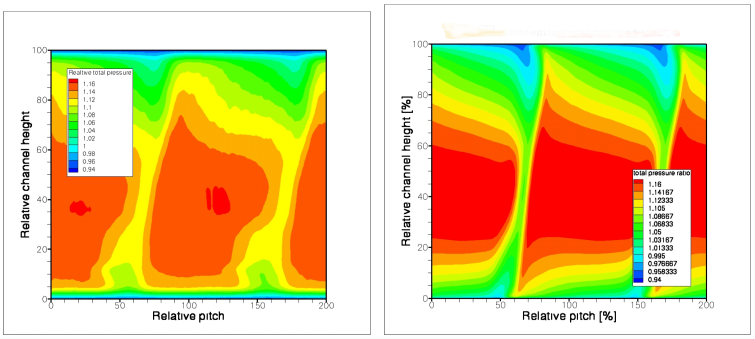

(a) (b)

Figure 6: Measured (a)and numerically predicted (b) total pressure distributions behind the stage,

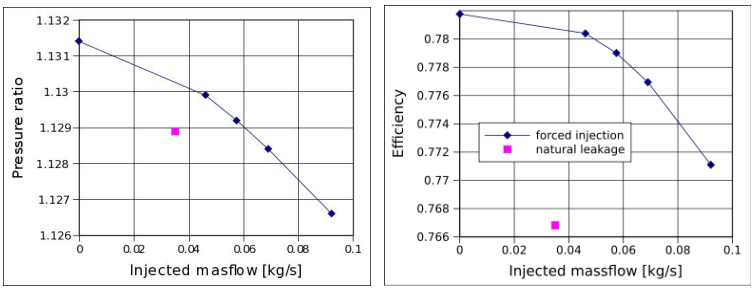

(a) (b)

Figure 7: Change in pressure ratio (a) and in efficiency (b) at different injected mass-flow rates at fixed throttling condition

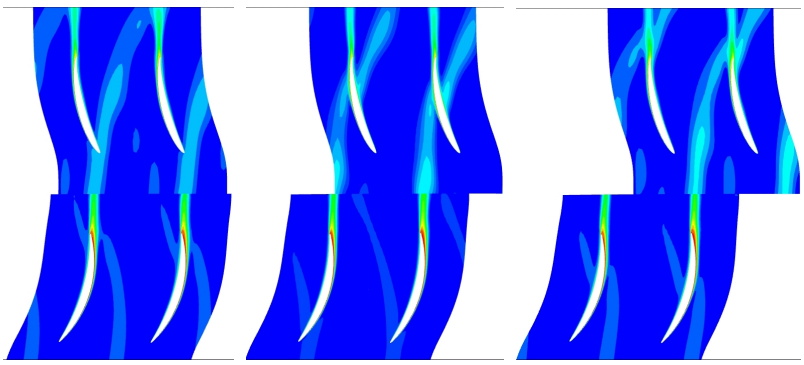

(a) (b) (c)

Figure 8: Entropy distributions at mid-span at different time steps Computed with NLH method

References

[1] J-F. Brouckaert, et al.,. Experimental and numerical investigation of a single stage low pressure compressor for counter-rotating turbofan engine architectures S . In *TURBO EXPO 2008*, Berlin, GERMANY, June 2008. ETC 2008.

[2] R. Denos. Literature Survay on the Effect of Flow injection and Removal and the Effectiveness of Casing Treatments to Enchance the Stability Margin of Axial Compressors. COntract Report Vital contract report VKI-1-ed1, von Karman Institute for Fluid Dynamics, 2005.

[3] A. Shabbir, and J.J. Adamczyk,. Flow Mechanism for Stall Margin Improovement due to Circumferential Casing Grooves on Axial Compressors. *Journal of Thermophysics and Heat Transfer*, GT-2004-53903, 2004.

[4] Z. S. Lei,, V.-M. Sparovszky, and E. M. Greitzer. A Criterion for Axial Compressor Hub- Corner Stall. *Journal of Turbomachinery*, 130:031006–1, 031006–10, July 2008.

[5] C. HIRSCH. Numerical methods in turbomachinery: fundamentals. *von Karman Institute for Fluid Dynamics Lecture Series*, VKI-LS 2009-08, September 2009.

Doctoral Project Summary

Numerical Simulation of the SABRE Rocket Based Combined Cycle Engine

Víctor Fernández Villacé*

Supervisors: Guillermo Paniagua† and Tom Verstraete‡

von Karman Institute for Fluid Dynamics, Rhode-Saint-Genèse, 1640, Belgium

Promoter: José L. Montañés§

Universidad Politécnica de Madrid, Madrid, 28040, España

Abstract

The programming environment EcosimPro and the European Space Propulsion Simulation System are used to model SABRE, a rocket based combined cycle for a single-stage-to-orbit launcher. SABRE operates initially as an air-breathing engine and then switches to rocket mode operation for the final ascent to orbit. New turbomachinery components have been developed, which allow off-design performance evaluations. A simulation of SABRE air-breathing mode from take-off to Mach 5 is presented.

1 Introduction

The space plane concept with air breathing engine benefits from an improvement of specific impulse that can lead, if properly applied, to an increase in available pay load. To this end, a single-stage-to-orbit space plane was proposed, Skylon [1] , which is powered by two SABRE engines that exploit the advantages of an initial air-breathing phase followed by a final rocket phase.

During the SABRE air-breathing ascent, the inlet air needs to be cooled prior to be compressed. This is due to the elevated recovery temperature at high speed (Mach 0 to 5), but also to facilitate the compression at the required pressure ratios needed for the injection in the rocket combustion chamber. With that aim, a pre-cooler HX1-HX2 is placed ahead of the compressor inlet, which delivers heat power to the helium loop that drives the helium turbine. Extra power si added in the loop by the pre-burner. Cryogenic hydrogen is the heat sink of the resulting helium absorption cycle, which

*PhD Candidate, Turbomachinery and Propulsion Department, Chaussée de Waterloo 72, villace@vki.ac.be.

†Associate Professor, Turbomachinery and Propulsion Department, Chaussée de Waterloo 72, paniagua@vki.ac.be.

‡Assistant Professor, Turbomachinery and Propulsion Department, Chaussée de Waterloo 72, verstraete@vki.ac.be@vki.ac.be.

§Head of Department, Aerothermodynamics and Propulsion Department, Escuela Técnica Superior de Ingenieros Aeronáuticos, Madrid, 28040, España, joseluis.montanes@upm.es.

additionally powers the liquid hydrogen pump and helium circulator by discharging through their corresponding driving turbines. Fig. 1 presents the layout of the SABRE engine cycle in air-breathing mode.

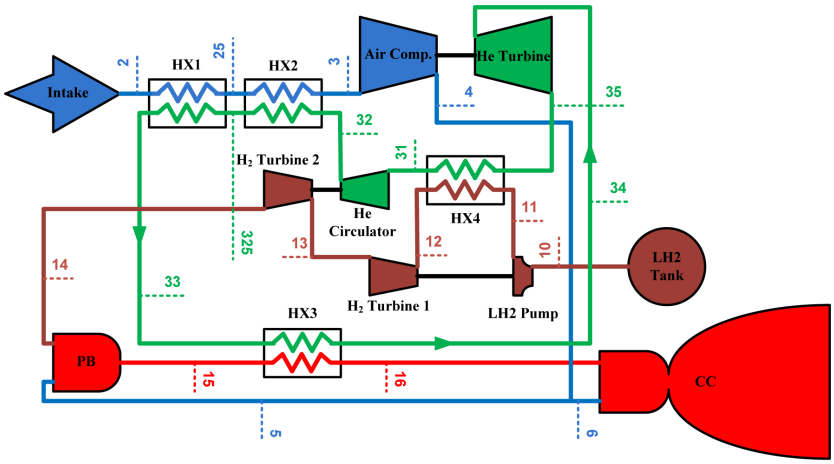

Figure 1: Scheme of SABRE air-breathing mode.

This paper presents a numerical model of SABRE engine which allows the evaluation of its performance during the air-breathing phase, from take-off to flight Mach 5. The programming environment EcosimPro together with the European Space Propulsion System Simulation (ESPSS) libraries are the numerical codes employed. In addition to ESPSS capabilities, new components compressor and turbine have been developed to allow SABRE performance evaluation under off-design conditions, provided the experimental characteristic maps of these turbomachinery components.

2 Computational Model

Ecosimpro is a code for the simulation of complex physical systems which can be made assembling its constituent components. Each component encapsulates the mathematical formulation as a set of algebraic and / or differential equations that represent its physical behavior. Different components are interlinked through their interface, which provides the rules for the interchange of information between them. The resulting system of algebraic / differential equations is solved during the simulation, provided that the boundaries and initial conditions are known. The numerical solver employed in present simulation is DASSL[2, 3] with special treatment for sparse Jacobian matrices.

The model components: preburner, combustion chamber, heat exchangers, LH_2 pump, valves and vessels belong to ESPSS[4], whereas the compressor and turbine have been formulated aside from ESPSS as explained in the following lines.

The performance of these tubomachinery components is specified by their characteristic maps, in which the pressure ratio, efficiency and corrected mass flow are given by:

$$\pi^*(\tilde{N},\beta), \eta^*(\tilde{N},\beta), \tilde{\dot{m}}^*(\tilde{N},\beta), \tag{1}$$

in function of the corrected shaft speed $\tilde{N}$ and β, which is an auxiliary variable that eases the numerical handling of the maps. Influence from the inlet conditions is re-

tained by the definition of the corrected variables. For the simulation of a compressor or turbine, the characteristic map is rescaled using constant coefficients to satisfy the requirements at design point. The rescaled map will be:

$$\pi = 1 + (\pi^*(\tilde{N}, \beta) - 1) \cdot C_\pi \tag{2}$$

$$\eta = \eta^*(\tilde{N}, \beta) \cdot C_\eta \tag{3}$$

$$\tilde{\dot{m}} = \tilde{\dot{m}}^*(\tilde{N}, \beta) \cdot C_{\dot{m}}, \tag{4}$$

where π, η and $\tilde{\dot{m}}$ are the performance of the rescaled machine and the rescaling coefficients are computed as:

$$C_\pi = (\pi_d - 1)/(\pi^*(\tilde{N}_d, \beta_d) - 1) \tag{5}$$

$$C_\eta = \eta_d/\eta^*(\tilde{N}_d, \beta_d) \tag{6}$$

$$C_{\dot{m}} = \tilde{\dot{m}}_d/\tilde{\dot{m}}^*(\tilde{N}_d, \beta_d), \tag{7}$$

being π_d, η_d and $\tilde{\dot{m}}_d$ the desired performance at design point and $\tilde{N}_d$, β_d the position of the design point in the non-scaled turbomachine map.

For the compressor only, the surge line is introduced as a limiting pressure ratio π_s in function of $\tilde{\dot{m}}$. The same scaling applies:

$$\pi_s = 1 + (\pi_s^*(\tilde{\dot{m}}) - 1) \cdot C_\pi \tag{8}$$

The total enthalpy flow that exits the machine is computed from the adiabatic efficiency $\eta(\tilde{N}, \beta)$ in (3) as:

$$\dot{H}_{t2} = \dot{H}_{t1} + (\dot{H}_{t2s} - \dot{H}_{t1}) \cdot \begin{cases} 1/\eta; & (if\ compressor) \\ \eta; & (if\ turbine), \end{cases} \tag{9}$$

where the subscript $_1$ / $_2$ stands for machine inlet / outlet and $\dot{H}_{t2s}$ would be the enthalpy flow rate that would exit an ideally isentropic machine.

It is known that using constant coefficients to rescale the operating map is only accurate in the vicinity of the design point because the map of machines with different nominal performances changes in shape[5]. Huge scaling factors are being used here to predict the off design performance (C_π=40 for the air compressor). Nevertheless this is a simple procedure to generate turbomachine characteristics in a per se quite complex model that integrates five different turbomachines. The aim of this work was to build a model of the engine without questioning the feasibility of its turbomachinery.

The maps used here come from machines working with air. For the hydrogen and helium turbines and the helium circulator no other correction for the working fluid than the change of the gas constant used in the definition of the corrected variables $\tilde{N}$ and $\tilde{\dot{m}}$ is done.

Reaction Engines Ltd. provided a description of SABRE configuration and design performance with quantitative data of each engine component[6]. Based on it, the model was built with the following assumptions:

- There are no redundant components, contrary to the real engine design, and mass flow rates have been diminished to achieve one fourth of the real engine thrust (which has four rocket nozzles).
- The intake is not considered, its recovery pressure and temperature are also provided.

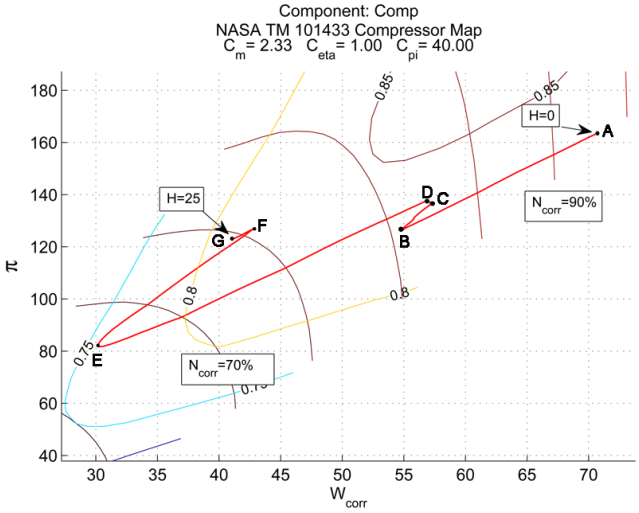

Figure 2: Air-Compressor operating line

- Helium and hydrogen state, thermal and transport properties are interpolated from tables, air state and thermal equations are those of a semi-perfect gas and combustion gases behave as a perfect gas.

3 Results

SABRE air-breathing operation along the trajectory of Skylon has been simulated. During the analysis the engine is controlled by imposing a fixed expansion ratio through the hydrogen turbine 1 and keeping constant the helium turbine inlet temperature.

Fig. 2 shows the operating line on the map of the air compressor. The compressor turns at a corrected speed $\tilde{N}$ between 65% and 95% and its efficiency varies only 5% because the operating line runs parallel to the iso-efficiency lines. Only in the last part of the trajectory the efficiency decays to $\eta = 75\%$, just at the point (E) where the turbine speed goes below $\tilde{N} = 60\%$ in Fig. 3. This low efficiency region corresponds exactly to the peak in recovery pressure seen at 25 km altitude due to the increase of flight speed. The same decay in efficiency is observed in Fig. 3, corresponding to the He-Turbine map.

There is a good agreement between the obtained trust and the prediction given by Reaction Engines, Fig. 4. The improvement of performance with altitude is due to the increase of flight speed during the ascent, which implies higher recovery temperature and more heat power transferred to the helium in the pre-cooler. The controller of the helium turbine inlet temperature reduces the air mass flow injected in the pre-burner to keep the temperature constant at $T_{34} = 1080K$. This increases the mass flow rate and pressure of the air diverted toward the combustion chamber, whose temperature and pressure increase and hence thrust as well.

In Fig. 5, A_t is the nozzle throat area, P_e is the nozzle pressure at the exit section and P_{amb} the ambient pressure at a given altitude. The nozzle has an exit area ratio of 100 and it runs full by the time that Skylon flies at an altitude of $16km$, but still over-expanded until $23km$, just before the end of the air-breathing mode.

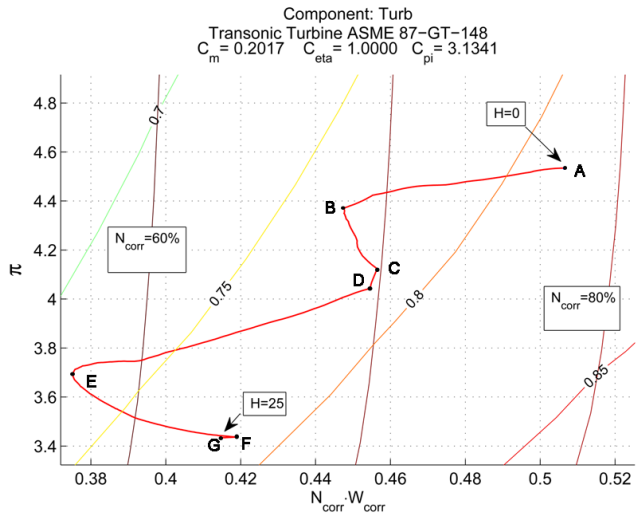

Figure 3: He-Turbine operating line

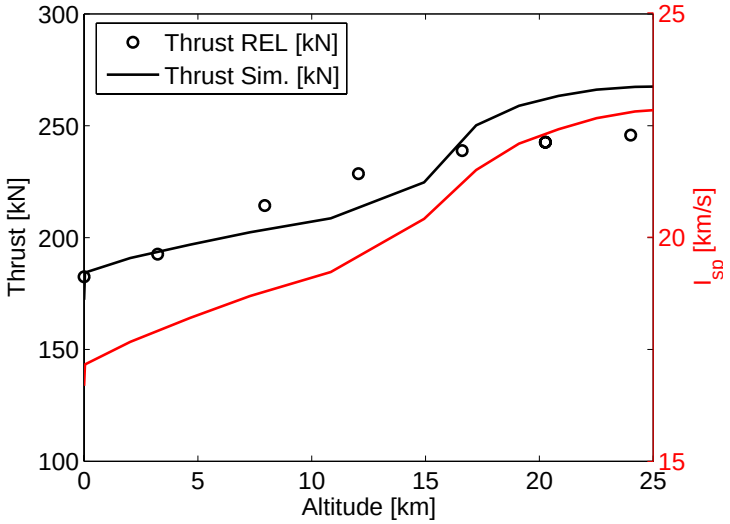

Figure 4: Evolution of uninstalled thrust and specific impulse along Skylon trajectory.

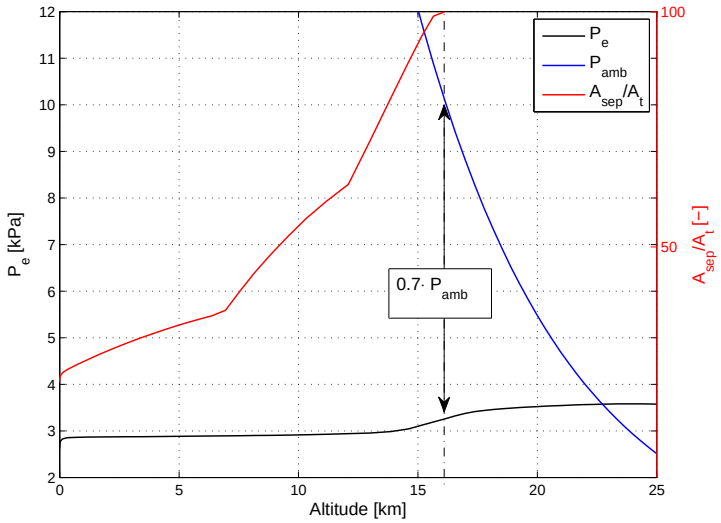

Figure 5: Area ratio A_{sep} at which separation occurs in the nozzle.

4 Conclusions

New components have been implemented to evaluate the performance of the turbomachinery, whose maps are input from rescaled tables with constant coefficients. Based on the results obtained, those components are appropriate for the off-design evaluation of SABRE performance during the air-breathing mode. Now a more realistic turbomachine behavior using other methods than map rescaling with constant coefficients can be easily implemented , like for instance the one proposed by Kurzke in [5].

The characteristic maps of compressors and turbines and their scaling is an important factor influencing the performance of the engine. An optimum design can be found by searching among a database with different turbomachines and its corresponding characteristic maps. Controlling the expansion ratio of the hydrogen turbines and the pre-burner outlet temperature, the engine performance along the trajectory can be varied. Therefore an optimal control law that would maximize the overall engine efficiency during flight could also be determined.

Next step is to optimize SABRE performance by coupling the engine model with an optimizer. But before doing so, a further understanding of engine control parameters needs to be achieved.

Acknowledgments

The author would like to thank A. Bond and R. Varvill from Reaction Engines Ltd. for making the SABRE design data available, which were essential to accomplish the model. Thanks also go to the technical support from the developers of ESPSS and EcosimPro for answering so quickly the inquiries of the author and to J. Kurzke for his explanations on the implementation of turbomachinery characteristics in GasTurb.

Finally, the author thank the European Space Research and Technology Center (ESTEC) for the founding of this doctoral research, and the contract 20366/07/NL/EM. In

particular, thanks to J. Steelant technical supervisor at ESTEC.

References

[1] Reaction Engines Limited, Culham Science Centre, United Kingdom. *Skylon Users' Manual*, September 2009. Revision 1.

[2] Empresarios Agrupados International. *EcosimPro: Mathematical Algorithms and Simulation Guide*. version 4.4.

[3] L. R. Petzold. Dassl: Differential algebraic system solver. Technical report, Sandia National Laboratories, Livermore, California, 1983.

[4] Astrium-Bremen, Cenaero, Empresarios Agrupados Int. and Kopoos. Espss ecosimpro libraries user manual. Technical Report TN-2240, European Space Agency, May 2009. version 1.4.1.

[5] J. Kurzke and C. Riegler. A New Compressor Map Scaling Procedure for Preliminary Conceptual Design of Gas Turbines. In *ASME IGTI Turbo Expo*, 2000-GT-0006, Munich, Germany, May 2000.

[6] Study on the aplications of the sabre engine for festip. Final report, Reaction Engines Limited, Culham Science Centre, United Kingdom, October 1997. Confidential.

Doctoral Project Summary

Boundary Layer Separation Control on a Compressor Blade

Fatma Ceyhun Şahin*

Supervisor: Dr. Jean-François Brouckaert,†

von Karman for Fluid Dynamics, Rhode-Saint-Genèse, 1640, Belgium

Promoter: Prof. Tony Arts‡

Université Catholique de Louvain, Louvain-la-Neuve, 1348,Belgium

Abstract

In a turbomachinery application, besides blade surfaces, unavoidable separation occurs on endwalls. Especially for low aspect ratio blades, secondary flow suppresses core region. Passive vortex generators(VGs) are to be designed for a compressor stage. Numerical simulations are conducted for the blade and VGs, separately. Those simulations provide a forecast for the scale of separation and vortices from different VGs.

1 Introduction

The current stage of that study is focused on reducing the losses in a compressor stage by controlling the secondary flow. Controlling the corner separation will enlarge the core of undisturbed flow. Cross flow from suction surface to the neighbouring pressure surface close to endwall and horseshoe vortices generated in the vicinity of leading edge stagnation point are also to be suppressed by various secondary flow control techniques in the literature.

Various flow control techniques like surface roughness, spanwise strips[4], inlet swirl or leading edge fillet[6] in the literature are observed to be insufficient in case of secondary flow.

Case treatment or endwall fences are recommended in control of secondary flows in turbomachinery[2,12]. Endwall fences are to be optimized according to parameters like the height, location or length of the fences. A fence height of 1/3 of boundary layer thickness located at midpitch[12] or closer to the blade pressure surface[2] is found out to be the best configuration for a single endwall fence focused on blocking the horseshoe vortices. Numerical studies on endwall fences also show that a fence length of 0.75 of camber line is enough to block horseshoe vortex without excessive additional drag loss[2].

* PhD Candidate, Tubomachinery Department, Chaussée de Waterloo 72, sahinc@vki.ac.be

† Assistant Professor, Turbomachinery Department at VKI, Chaussée de Waterloo 72, brouckaert@vki.ac.be

‡ Professor Tony Arts, Département de Mécanique. UCL, Louvain-la-Neuve, arts@vki.ac.be

A vortex generator (VG) is one step further in passive control, in terms of reducing drag penalty in unseparated flow while providing reattachment in separated flow. Low profile VGs which are submerged in the boundary layer are examined in the literature for different geometries, pitches and stagger angles, most of the time in 2-D boundary layers[7,8,11]. The point of submerging VGs in the boundary layer is avoiding to disturb the inviscid flow region.
Less size restrictions are expected for submerging VGs in corner separation. Considering secondary flow on a compressor blade, adverse pressure gradient effects should be taken into account as well as a new location parameter of blade surface or hub/shroud wall.

2 Background in Vortex Generators

Vortex generators usually have simple geometries like a rectangular or triangular. Most common types of VGs are illustrated in Figure 1.
Vanes of counter rotating VGs maybe joined or spaced. A parameter for optimizing the VGs is the merging of vortices. In boundary layer separation control, vortices should decay as soon as reattachment is obtained and a premature merging is to be avoided because decaying of vortices depends on the merging rate. Doublet VGs are applicable in cases of early decaying. They are mainly used in shock induced separation[7]. Wheeler type co-rotating VGs decrease the reattachment distance with minimum pressure penalty and reducing the height of those VGs results with weaker vortices which will decay earlier, however the effectiveness is as well as the large ones and the drag penalty is reduced more[11]. Vortices from a backwards wedge and co-rotating vortices are closer to wall and decay more quickly by more interaction with the wall shear[8]. Although vortices from joined vanes and wedge type VGs move apart from each other while the ones from spaced vanes move towards each other. Former rise rapidly and latter start to move apart from each other after a while. Thus, vortices from spaced vanes do not merge as quickly as the others, they remain longer[8].

In an adverse pressure gradient flow, which is the case in compressor flows, vortex strength just downstream of joined VGs is reduced more rapid than for the spaced or co-rotating VGs. Adverse pressure gradient also tends to promote interaction between the vortices of the spaced vanes but it has less effect on vortex decay for co-rotating vortices[8]. VGs are capable of reducing the shape factor and if the flow is zero pressure gradient, joined vanes decrease the shape factor most effectively. However, for adverse pressure gradient flows maximum decrease in shape factor is obtained by spaced vanes. It is also measured that increasing the space between vanes of a pair of counter rotating VG in an adverse pressure gradient flow reduces the drag from that VG type which gives high pressure recovery[8].
Optimizing the stagger angle of co-rotating VGs would give out a shape factor decrement with half of the wetted area of counter rotating VGs. According to that less drag loss, co-rotating VGs are suggested to be utilized on lifting aerofoils and flaps[8].

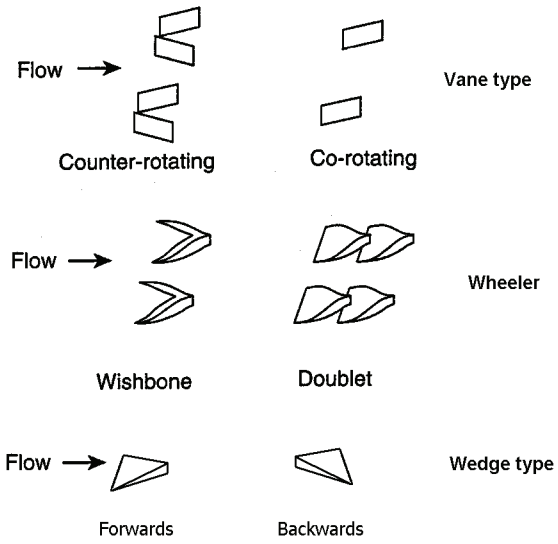

Figure 1 Common types of VGs in flow control.

3 Vortex Generators in Secondary Flow Control

Passive control of secondary flow in compressor stages include casing treatments as well as VGs on blades. Instead of endwall fences[1,2,12] or VGs which extend upto half chord[7,8], VGs as small as possible are to be investigated principally in the scope of this study.

In the literature, a single VG on the blade close to the endwall is not forced to be shorter than boundary layer thickness. Lean was introduced to push the flows towards the endwalls[5]. However avoiding corner separation did not mean decreasing global pressure loss, thus instead VGs on the endwalls are studied. Partial improvement of isentropic efficiency and total pressure ratio of the axial compressor, except choke and surge margins, are promising for the utilization of VGs in secondary flow control on the endwalls of a compressor stage[7].

Actually, in corner separation, it is easier to embed VGs in boundary layer since interaction of boundary layers results with larger separated region. If the VG is on the blade surface, leaning of the VG will also help to avoid disturbing the core flow. On the other hand, enhancing the momentum of flow on the endwalls will hinder a low momentum flow interfering the main flow through the stage.

4 Definition of the Problem

The main scope of this study will be controlling flow on a high pressure compressor stage. However, experimental approach will start with an incompressible case. Similarity analysis are conducted in order to increase the blade chord length according to the available experimental facilities. Full similarity is possible below atmospheric conditions. However keeping a Mach Number similarity does not allow to have an incompressible flow. Instead of exit and inlet Mach Numbers separately,

ratio between these two numbers or ratio between inlet and exit velocities are considered as similarity parameters.

4.1 Numerical Simulations

4.1.1 Numerical Simulations on Compressor Blade Cascades

Finally, blade geometry is scaled up to a span of 127 mm which is the distance between the endwalls of the facility C1. Numerical simulations using CFX software aid observing the results of scaling on pressure distribution. Developed boundary layer in C1 is already determined[10]. After introducing that ~20 mm thick of boundary layer profile at the inlet of cascade, pressure distribution decreased more. Nondimensional pressure distributions for four different cases, where $Cp = \frac{P_{01} - p}{P_{01} - p_1}$, is in Figure 2.

Separation regions resulted by the presence of endwalls are observed simply through surface streamlines on simulation outputs. In the present configuration, secondary flow suppress the compressor efficiency by blocking the undisturbed flow region aggressively as depicted in Figure 3. The blade was not able to give out sufficient velocity decrease without decreasing the flow incidence angle. According to that fact, VGs are to be designed on the endwalls of the stage. As an initial step in the scope of that study, VGs applicable on endwalls of C1 facility are to be designed. Because of the thick boundary layer in C1, separated zone covers the whole span as in Figure 4.

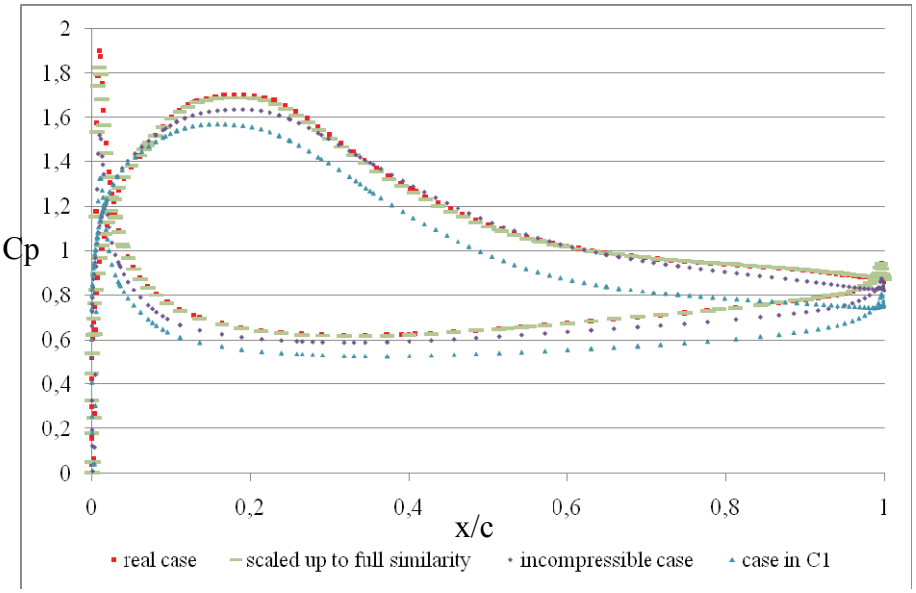

Figure 2 Pressure distributions at mid-chord.

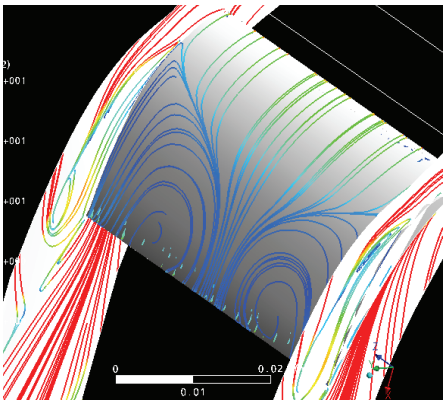

Figure 3 Surface streamlines on the balde and endwalls for the real case.

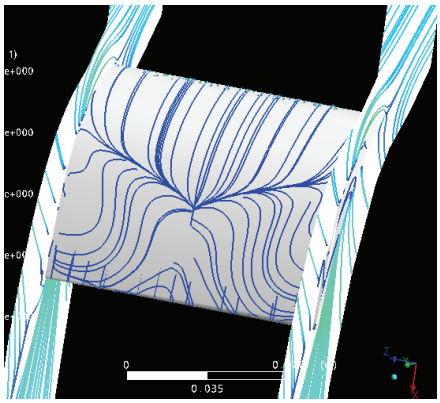

Figure 4 Surface streamlines on the balde and endwalls for a case in C1.

4.1.2 Numerical Simulations on VGs

In the literature, it is recommended to simulate VGs separate from the whole volume it will be used to control because of possible gridding problems[9].
Two triangular VGs are simply placed in a box which has half height of one chord length in C1, as depicted in Figure 5. Predefined boundary layer in C1 is the inlet boundary condition, compressor exit static pressure is the outlet boundary condition. Side walls have periodic boundary condition in order to provide a continuity in incoming flow which is not perpendicular to the inlet section and the top wall is symmetric.
Stagger angle of counter rotating VGs is 20° or 14° from the main flow direction. In case of co-rotating VGs, that angle is from the normal of flow direction. Initially, a couple of co-rotating VGs are simulated for different flow inlet angles like 20° and 70°.

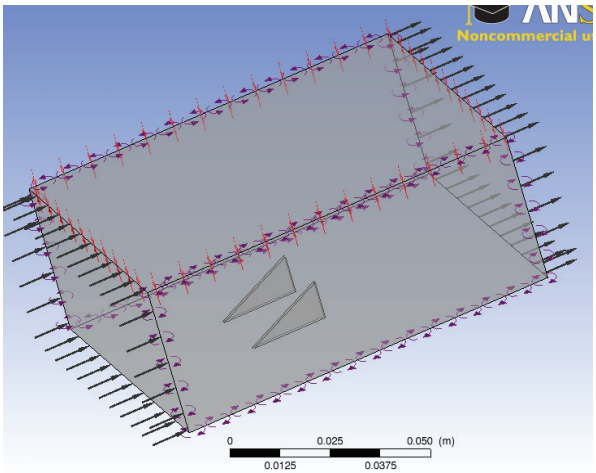

Figure 5 Numerical simulation domain for the flow around VGs.

5 Plans on Experimental Work

Experimental facility will be a compressor cascade in C1 which operates in atmospheric conditions, at incompressible velocities. Limits of C1 allows a free stream dynamic head upto 0.01 atm. Since the boundary layer thickness on the endwalls is predefined to be ~20mm[10], a VG height of 10 mm is appropriate.
After obtaining a foresight for the number of VGs, pitch, stagger angle from numerical simulations, experimental methodology will start with flow visualization utilizing oil on the surfaces in order to have a qualitative distinction between different VG configurations in the presence of compressor blades.
The baseline measurements on mid section of cascade will be to determine; inlet conditions in terms of velocity, flow angle; pressure distributions on endwall and blade surfaces; deviation angle at the trailing edge; vortices at the exit plane. Selected VG configurations from flow visualisations will be implemented on centre the blades of the cascade and flow behaviour behind the VGs will be measured in addition to the baseline measurements. Finally quantitative results for the selected VGs will be achieved.
Further steps will be repeating measurements at different Re, turbulence intensity or incidence angle in order to ensure feasibility of the selected VG design at different flow conditions.

6 Conclusion

Sets of numerical simulations for different configurations of VGs are in progress. After obtaining a comparison based knowledge on the behaviour of flow around VGs, a convenient construction to implement different VGs into cascade is to be designed.

References

1 D. Gregory-Smith; D. Bagshaw; G. Ingram; M. Stokes. Using Profiled Endwalls, Blade Leand and Leading Edge Extensions to Minimise Secondary Flow. ASME Turbo Expo 2008; June 9-13, 2008; Berlin.

2 J. Zhong; J. Han; Y. Liu; F. Tian. Numerical Simulation of Endwall Fence on the Secondary Flow in Compressor Cascade. ASME Turbo Expo 2008; June 9-13, 2008; Berlin.

3 A. Hergt; R. Meyer; M.W. Müller; K. Engel. Loss Reduction in Compressor Cascades by Means of Passive Flow Control. ASME Turbo Expo 2008; June 9-13, 2008; Berlin.

4 S.A. Gbadebo; T.P. Hynes; N.A. Cumpsty. Influence of Surface Roughness on Three-Dimensional Separation in Axial Compressors. Journal of Turbomachinery; Vol. 126, No. 4, p. 455-463; October 2004.

5 R. Meyer; D.W. Bechert; W. Hage. Secondary Flow Control on Compressor Blades to Improve the Performance of Axial Turbomachines. 5th European Conference on Turbomachinery-Fluid Dynamics and Thermodynamics; March 2003; Prague.

6 T.I.P. Shih; Y.L. Lin. Controlling Secondary Flow Structure by Leading Edge Airfoil Fillet and Inlet Swirl to Reduce Aerodynamic Loss and Surface Heat Transfer. Journal of Turbomachinery; Vol. 125, No. 1, p. 48-56; January 2003.

7 J.C. Lin. Review of Research on Low-Profile Vortex Generators to Control Boundary-Layer Separation. Progress in Aerospace Sciences; 38, p. 389-420; 2002.
8 P.R. Ashill; J.L. Fulker; Hackett, K.C.. Studies of flows induced by Sub Boundary layer Vortex Generators (SBVGs). AIAA 40th Aerospace Sciences Meeting and Exhibit; Reno, Nevada, 14-17 January 2002.
9 R.V. Chima. Computational Modeling of Vortex Generators for Turbomachinery. NASA/TM GT-2002-30677; April 2002.
10 T. Sasaki; F. Breugelmans. Comparison of Sweep and Dihedral Effects on Compressor Cascade Performance. Journal of Turbomachinery, Vol. 120, p. 454-464; July 1998.
11 J.C. Lin; F.G. Howard; G.V. Selby. Small Submerged Vortex Generators for Turbulent Flow Separation Control. Journal of Spacecraft; Vol. 27, No. 5, p. 503-507; October 1990
12 T. Kawai; S. Shinoki; T. Adachi. Secondary Flow Control and Loss Reduction in a Turbine Cascade Using Endwall Fences. JSME International Journal; Series 2, Vol. 32, No. 3, p. 375-387; 1989.

AERO-ACOUSTICAL FLOWS

Doctoral Project Summary

Numerical simulation of noise production and propagation

Lilla Koloszár*

Supervisor: Patrick Rambaud†
Jerome Anthoine‡
von Karman Institute for Fluid Dynamics, Rhode-Saint-Genèse, 1640, Belgium
Promoter: Herman Deconinck§
Université Libre De Bruxelles, Brussels, B-1050, Belgium

Abstract

The numerical prediction of aeronautical noise is still a challanging problem. The main reason that aerodynamically generated noise is usually broadband, contains huge spectrum of wavenumbers to resolve, moreover, acoustic waves of interest propagates over long distances. To cover these requirements a hybrid approach is considered, where noise production is resolved by compressible Large-Eddy simulation (LES), while the propagation region is simulated by Linearized Euler Equation (LEE). In this framework the compressible LES solver of the open source platform OpenFOAM is extended to be able to solve acoustic problems. The LEE and appropriate source terms are implemented in the COOLFluiD simulation environment which is a multiphysics code developed at the Von Karman Institute.

1 Introduction

Due to the complexity of the problem usually a whole spectrum of methodologies and approaches have to be included to be able to cover a given problem of interest (direct and Large-Eddy simulations with acoustic analogies, or other acoustic prediction models). Such a so-called hybrid method is employed here: in the sound production domain the compressible LES is employed and in the region where no sound production occurs, but where mean flow gradients can still be observed, the Linearized Euler Equations (LEE) describe completely the wave propagation including reflection, scattering and refraction effects.

*PhD Candidate, Environmental and Applied Fluid Dynamics Department, Chaussée de Waterloo 72, koloszar@vki.ac.be.

†Assistant Professor, Environmental and Applied Fluid Dynamics Department, Chaussée de Waterloo 72, rambaud@vki.ac.be.

‡Visiting Professor, Environmental and Applied Fluid Dynamics Department, Chaussée de Waterloo 72, anthine@vki.ac.be.

§Professor, Facult des sciences appliques, Avenue Franklin D. Roosevelt 50, Herman.Deconinck@ulb.ac.be

For the simulation of noise production the standard compressible LES solver is used with special boundary treatment. Than the resolved sources are reconstructed for propagation and finally the sound produced by these syntetic sources is propagated by the LEE solver. First the two solvers are tested with a generic acoustic testcase in Section 2. Than the new developements are described regarding the boundary treatments in Section 3, finally the two-step solution method is shown through an academic testcase in Section 4.

2 Acoustic pulse propagation

The implementation of the filtered Navier-Stokes equations is done in the open source computational fluid dynamics toolbox OpenFOAM. More details about the discretization can be found in the Ph.D thesis of Jasak [1]. By default the discretization is restricted to 3D, however with a degenerated mesh (just one cell in the third direction) it is possible to do quasi-2D simulations.

Acoustic wave production and propagation is included in the solution of the compressible simulations. As a test case, an initial value problem was solved in order to check the isotropy property of the computational algorithm. An acoustic pulse was placed in the middle of a two-dimensional square domain in quiscent flow. Wave propagation problem in general considered as non-viscous phenomenon. To fullfil this requirement, the Reynolds number was increased artificialy through the kinematic viscosity.

The acoustic wave propagate with the speed of sound in all directions uniformly, as expected. In the test 2nd order time integration combined with 2nd order central scheme was used. Figure 1 show the comparison with analytical solution. The discrepancy between the analytical results due to two kind of numerical error. First, the high dissipation of the low-order schemes is decrease the amplitude of the signal much stronger than the natural decay of the acoustic pulse would lead to. Moreover, at higher frequencies the phase velocity of the waves differ due to the dispersive nature of these schemes. The errors can be reduced with increasing the grid resolution, but cannot be cured. Changing the CFL number (Figure 2) did not change the accuracy of the solution, the small amplitude variation only due to the increasing number of time-steps executed for lower CFL numbers.

The LEE solver was already described in the last year presentation, so interested reader can find more details on it in [2] and [3]. Here, as a counterpart of the test of the LES solver, the same initial value problem was solved. The results of grid study can be seen in Figure 3. The results show very good agreement with the analytical solution even with much coarser grid.

3 Boundary conditions

In general, the waves that are leaving the computational domain should pass through the boundaries without reflecting back into the computational domain. Therefore, a major difficulty to resolve acoustic waves by compressible (and even incompressible) flow simulation is the application of the free space boundary condition. The applied condition has to be consistent with the acoustic far-field at an artificially truncated computational boundary which is finite distance away from the source region.

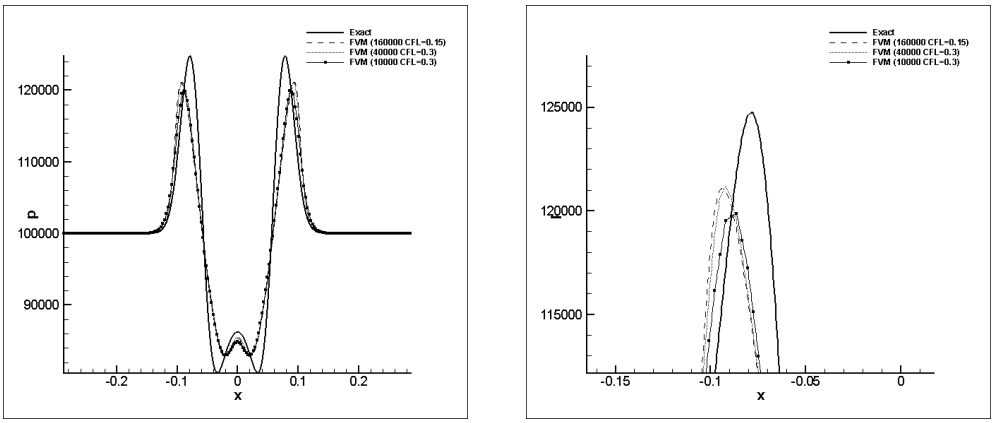

Figure 1: Comparison of results obtained by OpenFOAM with the analytical solution of an acoustic pulse placed in quiscent flow.

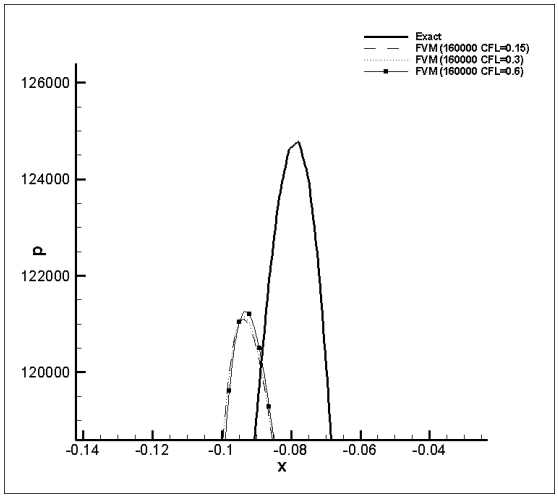

Figure 2: Solution of the pulse with differing the CFL number with LES.

In OpenFOAM there is a 1D characteristic based boundary condition implemented for unsteady computations following the work of Ref [4]. Figure 4/a shows the pressure field at $t = 0.001$, so when the pressure wave already should have left the domain for a while and the field should return to its steady state. Around the 46% of the outgoing wave reflected back by the boundary. In order to reduce the amplitude of these spurious reflections around the boundaries an artificial buffer zone [5] is defined where the numerical dissipation is increased gradually. The effect of this zone can be seen in Figure 4/b. In this way the perturbation is damped before it reaches the boundaries, and the reflection is reduces to around 12.5%. The damping zone had a with of $0.1m$.

The buffer zone approach was implemented to the LEE solver by E. Torres during his DC last year. Now the characteristic based boundary conditions are considered. The derivation of characteristic equations is based on the work of H. Deconinck et al. [6, 7, 8] . In 1D flow, the characteristic waves are decoupled in space and time so that

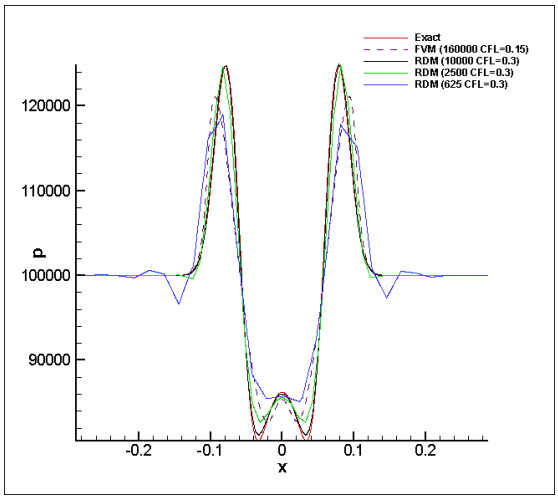

Figure 3: Solution of the pulse with differing grid resolution with LEE number.

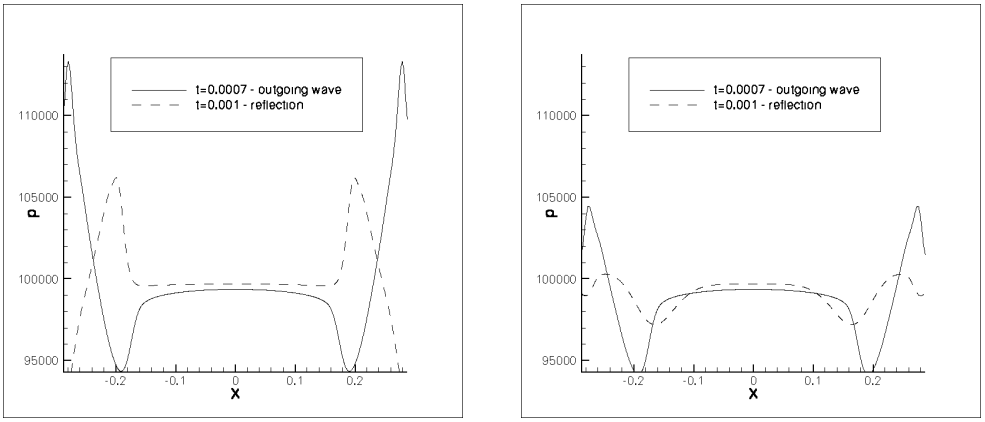

(a) Without damping

(b) With damping

Figure 4: Numerical reflection from the boundary.

the non-reflecting condition can be satisfied relatively easily. However in two or more dimensions the determination of these waves is not straightforward. The characteristic variables are defined as:

$$\overrightarrow{W_n} = \mathbf{L} \cdot \overrightarrow{U} = \begin{bmatrix} \rho' - \frac{p'}{c_0^2} \\ \rho_0 \cdot \overrightarrow{s}\,\overrightarrow{u}' \\ \rho_0 \cdot \overrightarrow{n}^{char}\overrightarrow{u}' + \frac{p'}{c_0} \\ -(\rho_0 \cdot \overrightarrow{n}^{char}\overrightarrow{u}') + \frac{p'}{c_0} \end{bmatrix} = \begin{bmatrix} S \\ \Omega \\ A^+ \\ A^- \end{bmatrix}$$

The characteristic variables represent in two spatial dimension the four information waves travelling through the domain: S represents the entropy wave, Ω the shear/vorticity wave, A^+ and A^- the positive and negative acoustic wave. At the outflow in case of a subsonic flowfield three eigenvalues are positive and therefore only one wave is entering back to the domain (A^-). Several different boundary conditions can be found in

the literature trying to eliminate A^- entering to the domain.

In the following, different boundary conditions applied to subsonic outflow are compared using a well-known benchmark problem[9] . This initial value problem consists of an acoustic pulse centred at the origin and a combined vortex/entropy pulse placed at $(x, y) = (67.0, 0.0)$. The mean flow is uniform with Mach number $M_x = 0.5, M_y = 0.0$. The time step related to $CFL = 1$ is $\Delta t = \frac{1}{1+M}$. The computational domain extends from $-100 \leq x, y \leq 100$, is embedded in free space and is discretized by 201X201 nodes. The perturbation velocities, density and pressure are normalized by c_0 (speed of sound), ρ_0 (ambient density) and, $\rho_0 c_0^2$ respectively. The evolution of the most used formulations are compared through this problem: the right boundary is set to different outflow formulations while the other three are handled as supersonic inflow setting all the perturbations to zero.

The most obvious choice is to set the income wave strength to zero at the outflow boundary,

$$A^- = 0 \tag{1}$$

The amplitude of the reflections measured with the previously described benchmark is 42% with respect to the outgoing wave amplitude.

The widely used characteristic outflow boundary condition was introduced by Thompson[10], who used Hedstrom's non-reflecting boundary condition in quasi-1D approximation. Hedstrom [11] suggested that the wave is defined as the change of amplitude of a variable in time. Therefore, not only the aplitude of A^- should be zero, but also its derivative with respect to time resulting in the condition:

$$\frac{\partial A^-}{\partial t} = 0 \tag{2}$$

In the present initial value benchmark problem the results computed with Hedstrom's boundary condition are identical to those obtained with the base formulation since $\frac{\partial A^-}{\partial t} = 0 \Rightarrow (A^-)^{n+1} = (A^-)^n = (A^-)^0 = 0$.

Colonius et al. [12] constructed boundary conditions for the Navier-Stokes Equations. At the boundaries they assume that the perturbations around the time-averaged flow are small, such that the viscous effects can be neglected. As a consequence, they solve the Linearized Euler Equations at the boundaries. Their boundary conditions attempt to take into account the coupling between the acoustic waves and the vorticity waves. Analysing the formulations they concluded that the results obtained are sufficient for hydrodynamic simulations, but not adequate for acoustic problems. Results obtained with these boundary formulations will be presented in the paper.

After the inadequate performance of the previous formulations it seems that the 1D characteristic formulation is not failing just because of the 1D assumption. Indeed, in the previous formulations no one-dimensionality was introduced. Then the question is rather what does it mean that there is no incoming wave? In the new treatment we assume a total absence of A^-.

If there are no perturbations due to the incoming wave A^- then A^- does not vary in time or space, leading to the conditions:

$$A^- = 0, \frac{\partial A^-}{\partial t} = 0, \nabla A^- = 0 \tag{3}$$

Taking into account these conditions, all the compatibility equations are changing except the entropy wave equation. The equation which belongs to A^- finally sets a

condition to the vorticity wave:

$$c_0 \cdot n_y^{char} \frac{\partial \Omega}{\partial x} - c_0 \cdot n_x^{char} \frac{\partial \Omega}{\partial y} = 0 \tag{4}$$

So, we find back that vorticity creates noise by exciting the domain, which is observed since long time in Large-Eddy Simulation. Inserting this condition in the equation belonging to the outgoing acoustic wave A^+, it is modified into a pure scalar advection:

$$\frac{\partial A^+}{\partial t} + (u_0 + c_0 \cdot n_x^{char}) \frac{\partial A^+}{\partial x} + (v_0 + c_0 \cdot n_y^{char}) \frac{\partial A^+}{\partial y} = 0 \tag{5}$$

Finally, the vorticity equation, modifies as following:

$$\frac{\partial \Omega}{\partial t} + u_0 \frac{\partial \Omega}{\partial x} + v_0 \frac{\partial \Omega}{\partial y} + \frac{c_0}{2} \cdot n_y^{char} \frac{\partial A^+}{\partial x} - \frac{c_0}{2} \cdot n_x^{char} \frac{\partial A^+}{\partial y} = 0 \tag{6}$$

From physical point of view this means that not only the incoming acoustic wave has to be killed, but the A^- created by vorticity shear has to be substracted, as well, in order to reduce the reflections from the boundaries. Applying this boundary condition we noticed that the reflection in this case reduces to 1% with respect to the outgoing wave amplitude (Figure 5).

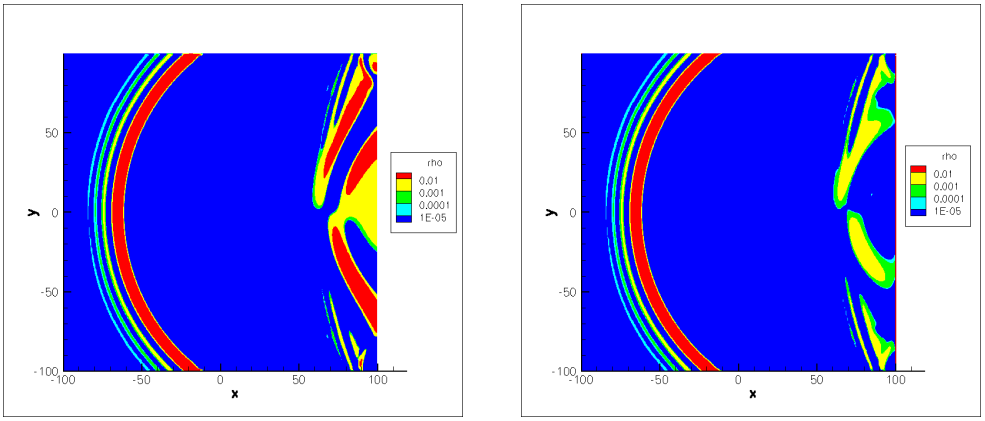

(a) Hedstrom's boundary condition

(b) Assumption that A^- does not exist

Figure 5: Comparison between Hedstrom's formulation (left) and the formulation based on the assumption that A^- does not exist (right) at t=250. Contours of density 10^{-5}, 10^{-4}, 10^{-3} and 10^{-2}.

4 Two co-rotative vortices

The information obtained by LES has to be provided for the LEE solver in order to propagate it. Different approaches exist to the modeling of physical sources in combination with the LEE. One approach follows the principle of insertion, meaning the instantaneous solution at a certain time and location is provided to the LEE by means of boundary conditions and transported through the acoustic domain. Usually, the location where this time-varying boundary condition is defined is exactly the boundary

between a defined source. Another approach is the reconstruction of the acoustic field by source terms on the right-hand side of the LEE [13, 14, 15, 16]. Using this approach with compressible or incompressible source simulation, the acoustic field can be reconstructed inside the source region where the source terms are active.

The formulation of the source terms obtained by Bailly et al. is particularly suitable for the implementation in the COOLFluiD LEE environment. COOLFluiD. The noise sources obtained by the LES simulation is then reconstructed by an acoustic analogy proposed and verified by Bailly et al.:

$$\vec{S} = \begin{bmatrix} 0 \\ S_1 - \bar{S_1} \\ S_2 - \bar{S_2} \\ 0 \end{bmatrix} \tag{7}$$

The reconstruction of the source terms is performed inside COOLFluiD. The preprocessing function first loads the source data and then averages it in order to compute the perturbations. Finally the source terms are computed at each time step and provided to the LEE module. The source terms obtained by COOLFluiD and the reference data can be seen in Figure 6.

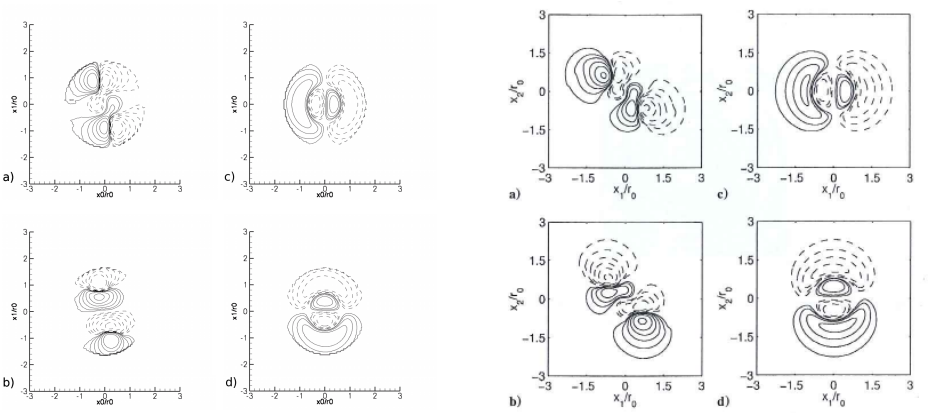

(a) OpenFOAM solution (b) Reference solution

Figure 6: Reconstructed sources. a) S_1 and b) S_2 with six contours from $6 \cdot 10^5$ to $1.1 \cdot 10^7 kgm^{-2}s^{-2}$ following a geometrical ratio of 1.8 and c) $\overline{S_1}$ and d) $\overline{S_2}$ with the first four contour defined earlier. Time step is $t = 2800\Delta t$. Dashed lines indicates positive values.

As can be seen qualitatively and quantitatively the results are very close to the reference one in case of the averaged source terms, however there is some deviation in the instantaneous source field. This is mainly due to the order of the discretization in our DNS simulation. Bailly et al. reported that the period of the rotation of the vortices are extremely sensitive to that parameter.

Comparing the dilatation field obtained by the LES simulation and the one from LEE shows overall acceptable agreement (Figure 7). The propagation pattern is captured, however the frequency of the propagated waves are closely the half of the one obtained by LES. In case of the Linearized Euler solver the high frequency oscillations have been removed by artificial numerical damping. The formulation is based on the

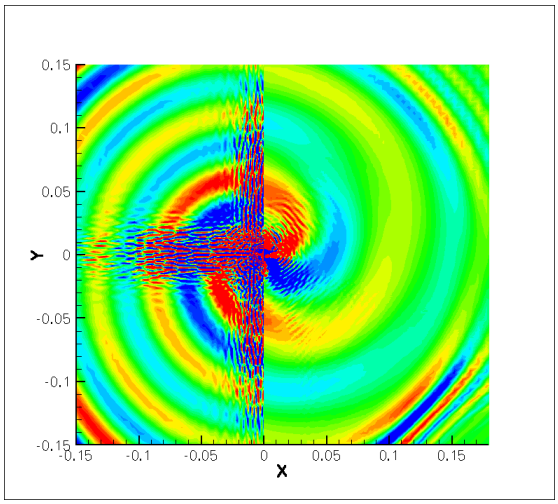

Figure 7: Comparison of DNS ($x < 0$) and LEE ($x > 0$) simulation for wave propagation. Contours of dilatation from $-15s^{-1}$ to $15s^{-1}$.

work of Tam and Shen [17] and extended for Residual Distribution Method. More information can be found about the filtering in [3].

5 Conclusion

A hybrid method for solvin aeroacoustic problems is under development. Both solver of the approach is tested through wave propagation problem. The results show that the numerical method has a great impact on the accuracy of the solution. New boundary formulations are implemented and tested in both cases to reduce reflections from the trunckation of the domain. Moreower, in this study it has been shown that the proposed LES by OpenFOAM and LEE by COOLFluiD system connected by source reconstruction is able to resolve acoustic wave generation and propagation.

Acknowledgments

This research is supported through the Marie Curie Research Training Network Project AETHER (contract no MRTN-CT-2006-035713).

References

[1] H. JASAK. *Error analysis and estimation for the Finite Volume Method with applications to fluid flows*. PhD thesis, University of London, June 1996.

[2] L. KOLOSZAR, N. VILLEDIEU, T. QUINTINO, J. ANTHOINE, and P. RAMBAUD. Application of residual distribution method for acoustic wave propagation. *AIAA 2009-3116*, 2009.

[3] L. KOLOSZAR, N. VILLEDIEU, T. QUINTINO, and J. ANTHOINE P. RAMBAUD. Artificial numerical damping for linearized euler equation implemented in residual distribution method. *EUCASS2009*, 2009.

[4] T. J. POINSOT and S. K. LELE. Boundary conditions for direct simulation of compressible viscous flows. *J. Of Comp. Physics*, 1992.

[5] J. B. FREUND. Proposed inflo/outflow boundary condition for direct computation of aerodynamic sound. *AIAA Journal*, 35:740–742, 1997.

[6] *Advances in Computational Fluid Dynamics*, chapter Upwind Methods and Multidimensional Splittings for the Euler Equations. Gordon and Breach Publishers, 1993.

[7] H. DECONINCK Ch. HIRSCH, C. LACOR. Convections algorithms based on a diagonalization procedure for the multidimensional euler equations. *AIAA Paper 87-1163-CP*, 1987.

[8] *Lecture Notes in Physics*, chapter Upwind Methods and Multidimensional Splittings for the Euler Equations. Springer-Verlag, 1986.

[9] Icase/larc workshop on benchmark problems in computational aeroacoustics (caa). *NASA CP 3300*, 1995.

[10] K. THOMPSON. Time dependent boundary conditions for hyperbolic systems. *J. of Computational Physics*, 68, 1987.

[11] G. W. HEDSTROM. Nonreflecting boundary conditions for nonlinear hyperbolic systems. *J. of Computational Physics*, 31, 1979.

[12] T. COLONIUS and S. K. LELE. Computational aeroacoustics: progress on nonlinear problems of sound generation. *Progress in Aerospace Science*, 40, 2004.

[13] C. BAILLY and D. JUVÉ. Numerical solution of acoustic propagation problems linearized euler's equations. *6th AIAA/CEAS Aeroacoustic Conference*, 2000.

[14] L. DAVIDSON, M. BILLSON, and L.-E. ERIKSSON. Acoustic source terms for the linearized euler equations in conservative form. *AIAA Journal*, 43, 2005.

[15] C. BOGEY. *Calcul direct du bruit aèrodynamic et validation de modèles acoustiques hybrides.* PhD thesis, Ecole Central de Lyon, 2000.

[16] M. E. GOLDSTEIN. A unified approach to some recent developements in jet noise theory. *Int. Journal of Aeroacoustics*, 1, 2002.

[17] C. K. W. TAM and H. SHEN. Direct computation of nonlinear acoustic pulses using high-order finite difference schemes. *AIAA 93-4325*, 1993.

Doctoral Project Summary

Numerical investigation of aerodynamic noise generation in confined flows

Anna Mueller*

Supervisor: Patric Rambaud†

von Karman Institute for Fluid Dynamics, Rhode-Saint-Genèse, 1640, Belgium

Promoter: Avraham Hirschberg‡

Universiteit Twente, CTW (Horstring), Postbus 217, 7500AE Enschede, Nedeland

Abstract

An academic case of a flow around a confined rod with square cross section is studied. The incompressible Large Eddy Simulation (LES) provides time history of pressure and velocity fields. The vortex shedding frequency, lift and drag coefficients and static pressure on the rod walls are monitored. The compact dipolar source of sound (fluctuating lift and drag forces) is used in a Curle's analogy[1] to propagate the sound in the duct. The average velocity field is compared with Particle Image Velocimetry (PIV) data from the literature[2].

1 Introduction

Prediction of aerodynamic sound by direct compressible numerical simulation is still prohibitive for industrial problems [3]. Flows with high Reynolds number require very small time steps and very large grid resolutions. Furthermore, at low Mach numbers the acoustic far-field begins at large distances from the source region and requires meshing a large domain. We consider therefore an alternative hybrid approach suited to low-Mach number applications, where the computation of the flow model is decoupled from the acoustic propagation problem. The time history of hydrodynamic forces is calculated by an incompressible Large Eddy Simulation (LES) and is used as an input to Curle's acoustic analogy.[1]

In order to validate our apporach and to select the acoustically 'interesting' configuration for future simulations we are preparing an experiment campaign. It will be the measurement of sound production by a rod of square cross section (dynamic and static pressure probes on the surface) placed in a flow of Mach 0.2 and Reynolds 144000.

*PhD Candidate, Environmental and Applied Fluid Dynamics Department, Chaussée de Waterloo 72, mueller@vki.ac.be.

†Assistant Professor, Environmental and Applied Fluid Dynamics Department, Chaussée de Waterloo 72, rambaud@vki.ac.be.

‡Prof. dr. ir., Mechanical Engineering, Universiteit Twente, CTW (Horstring), Postbus 217, 7500AE Enschede, Nedeland, A.Hirschberg@ctw.utwente.nl

The propagation of sound in the far field will be measured as well. The experiment will be performed by a master student in the low-noise wind tunnel of TU Twente in Enschede. The model of the square rod together with the supporting end-plates is prepared at the VKI. There will be also the timeresolved PIV (TU Delft) included in order to provide an insight into the flow field characteristics.

As a first step a relatively inexpensive preliminary LES calculation with moderately low Reynolds number 5000 (based on the uniform inlet velocity and the rod width) was done. The results of this prediction help to design an experimental setup and to gain experience. First simulations of high Reynolds = 144000 are available as well.

2 Aerodynamic calculation - LES

We assume that the aerodynamic characteristics of a sharp edged obstacle are not sensitive to Reynolds number [4]. Therefore we will use an LES calculation carried out at a lower velocity (and smaller mesh) to predict the sound field in experiment of much higher Reynolds number (hence much more expensive). We also possess the average aerodynamic field data obtained with PIV by Kurtulus et al.[2] for comparison.

2.1 Moderate Reynolds number

A rod with square cross section of width D and length $17D$ is positioned with a zero-degree angle of attack in the middle of the channel. The origin is located in the center of the rod. The corresponding PIV experiments carried out by Kurtulus et.al [2] were performed in a square test section wind tunnel (width $W = 17D$). In order to study the influence of spanwise dimension of the LES computational box, two models were solved: a quasi two-dimensional ($W = 1D$), and one with half of the experimental domain ($W = 8.5D$). The second configuration can be seen in Fig. 1 and has dimensions: $L = 65D$ ($14.5D$ upstream of the obstacle and $49.5D$ downstream), $H = 17D$, and $W = 8.5D$, in the longitudinal, transversal and spanwise direction respectively. The LES calculations were performed using Fluent version 6.3. The discretisation in space and time is of the second order.

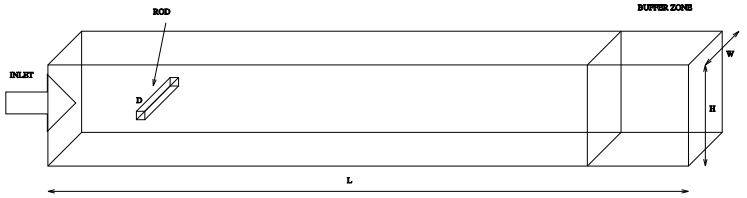

Figure 1: Geometry of the rod confined in a duct

Boundary conditions The preliminary study of CFD outlet conditions was carried out on a similar geometry with a laminar flow[5]. It showed that it is necessary to place a pressure reference cell in a region without fluctuations. A buffer zone was added to damp out spurious waves due to the crossing of vortical disturbances at the downstream boundary. It consists of a mesh stretched in the streamwise direction starting from $15D$

before the outlet face. It ensures that vortices are dissipated before reaching the downstream boundary of the computational box. The pressure reference cell is positioned at the downstream end of the buffer zone.

- Inlet - uniform profile with u = 2.37 m/s, $v = w = 0$. There is no turbulent disturbance.
- Outlet - buffer zone + zero gauge pressure boundary condition.
- Wall - upper, lower and cylinder walls - non-slip conditions
- Periodic - periodic boundary condition in spanwise direction (Z); no pressure drop in that direction.

Mesh In both cases ($W = 1D$ and $W = 8.5D$) cartesian hexahedral cells are used in most of the domain. The mesh is stretched in wall-normal directions in order to resolve the boundary layers on non-slip walls - varying stretch factor around cylinder from 1.2, to top and bottom walls at 1.005. The value of y^+ at the rod walls does not exceed 2, this resolution is sufficient for a wall resolved LES. On top and bottom walls of the duct it stays below 7, those walls are not properly resolved.

2.1.1 Comparison of LES with PIV

Averaged variables It was possible to compare the average velocity fields in the center plane of the model (Z = const).

In the detailed profiles of streamwise velocity (Figure 2) one can observe that $1D$-span model does not capture well the behaviour around the cylinder. A significant difference in RMS quantities is observed. In neither case the average field is symmetric. The LES results are averaged over 30 periods of vortex shedding ($\sim$ 6 flow-throughs).

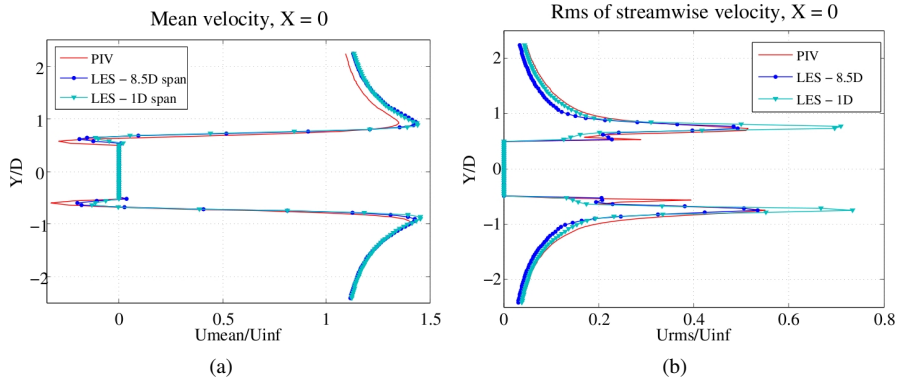

Figure 2: Streamwise velocity u (a) and u_{rms} (b), for X = 0 (center of the cylinder)

Lift and Drag In order to obtain the dipole source of sound from the flow around a body, one has to predict correctly the unsteady forces acting on a fluid. We monitored lift and drag coefficients on the cylinder (see Figure 3). In Table 1 we can see that the $1D$-span case gives acceptable values of mean lift and drag coefficients but fails to predict the rms and frequency correctly. Increasing the spanwise dimension to $8.5D$ gives already the results comparable with the ones available in the literature.

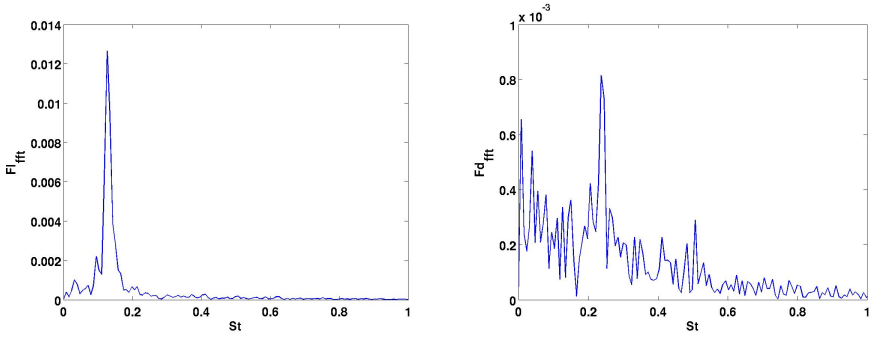

(a) Lift (b) Drag

Figure 3: Spectra of lift and drag forces obtained by LES Re 5000, case 8.5D

	Mean	RMS	Strouhal no.
Cl LES 1D	-0.02	1.4	0.07
Cl LES 8.5D	-0.02	1	0.127
Cl Literature	0-0.049	1	0.13 - 0.133
Cl LES Re 144000	0.01	0.8	0.128
Cd LES 1D	2.17	0.38	0.09
Cd LES 8.5D	2.29	0.1	0.24
Cd Literature	1.9-2.2	-	2 x 0.13
Cl LES Re 144000	2.2	0.13	0.26

Table 1: Lift and Drag coefficients, Re 5000, present study and literature[6, 7, 2]

2.2 High Reynolds number - preliminary result

We have performed a high Reynolds number calculation (Re = 144000) this time taking into account the side walls supporting the rod and the 'blockage' ratio of the experiment = 9.7. The rod will be placed in a semi-confined jet (see Fig. 4). This real configuration needs a more delicate treatment of the boundaries than a duct. However it is prohibitive to do a high Re number wall resolved LES of the domain taking into account the portion of the windtunnel outlet, resolving the endplates and posing correct boundary conditions on top and on bottom between the plates (including buffer zones in these directions). In the first approach we repeated a closed duct situation this time taking into account the side walls - which are more crucial for the experiment. the unresolved case with log law wall modelling is run. The target resolution at the rod walls is $y^+ = 100$.

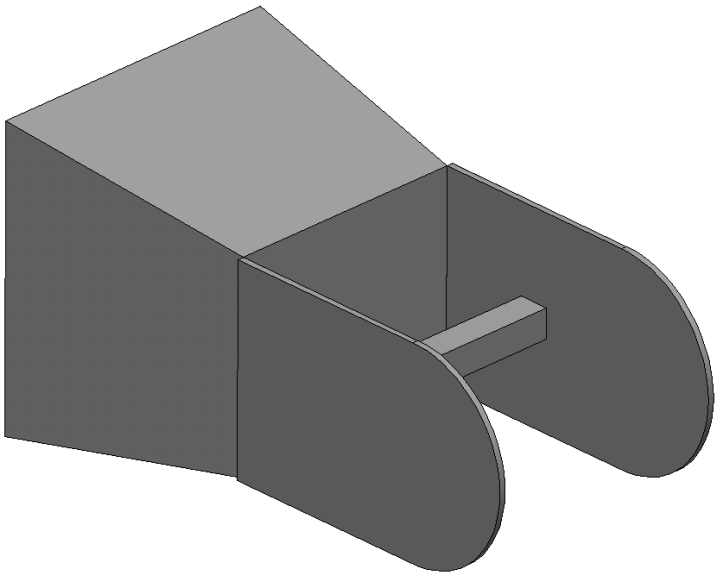

Figure 4: Layout of the experiment test section

The analysis of lift and drag coefficients shows that indeed one can see similar amplitudes and frequencies as in the lower Reynolds regime (see Table 1). Although drag coefficient spectrum reveals existence of very low frequency oscillation (St = 0.005, 0.025, 0.04 - in Fig. 5). The origin of this signal modulation will be investigated.

3 Acoustic simulation

As it was mentioned before, in the case of a sharp-edged body, where the separation points are fixed at the leading edges, the aerodynamic characteristics are relatively insensitive to Reynolds number[4]. This was documented[6, 7] for Reynolds numbers up to order 10^4. We assumed that the amplitude of lift and drag coefficients and their Strouhal numbers do not change at the Reynolds number of the order of 10^5 as well, and use the signal of the fluctuating forces obtained with a lower velocity calculation

(Figure 3). We scale its amplitude and frequency with:

$$F_l = \frac{1}{2} Cl \rho u^2 DW \quad (1)$$

$$F_d = \frac{1}{2} Cd \rho u^2 DW \quad (2)$$

and

$$f = \frac{uSt}{D} \quad (3)$$

This scaling procedue seems to be confirmed by the first results of the high Reynolds calculation (Figure 5).

Geometry The domain of LES is too short to cover the acoustic far-field. We created an acoustic mesh which is longer in order to cover this far-field. The requirements of Boundary Element Method (BEM) are much less stringent than the ones of LES in terms of the mesh size. As a rule of thumb, six elements per wavelength are enough to resolve a wave in the far-field[8]. The mesh is extended in both directions of the duct (along the X axis) between $-100D$ and $100D$. The other two dimensions correspond to the size of the wind tunnel section ($W = 9.7D$ and $L = 12.5D$). Three mesh resolutions were used. Very coarse one resolving well only waves up to lift frequency (200 Hz, 360 elements), a middle one up to drag frequency (400 Hz, 720 elements) and a fine one up to 1 kHz (4160 elements).

Source The width of the obstacle D is very small compared to the wavelength - $He < 0.25$ at the dominating frequencies of the phenomena. It means that it can be considered compact and replaced by an equivalent point dipole source. A superposition of lift and drag force is applied.

Boundary conditions and analysis settings A direct BEM solver is used.[9] The top, bottom and side surfaces are considered rigid, zero admittance walls. At the inlet and outlet of the duct the characteristic impedance of air $Z = \rho c$ is set. The Mach number of the calculation is of the order of 0.2.

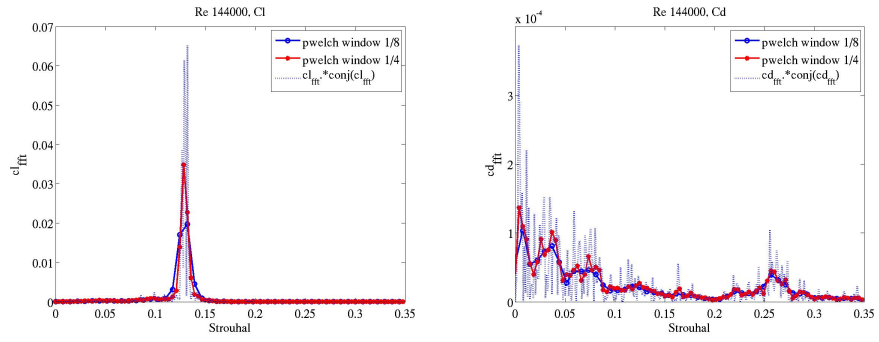

(a) Lift (b) Drag

Figure 5: Spectra of lift and drag coefficients obtained by LES Re 144000, duct case

Results The lift and drag forces are oscillating with the dominating frequency below the cutoff. Only the planar waves are propagating below that frequency. Since we applied a dipole source as a superposition of forces, drag is responsible for the planar wave propagation at the lift frequency as well. One can observe that in figure 6(a) representing the amplitude of acoustic pressure. Above the cutoff frequency (400 Hz) there are higher duct modes present (Figure 6(c)).

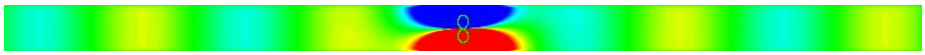

(a) Lift frequency

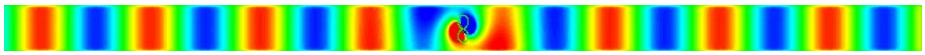

(b) Drag frequency

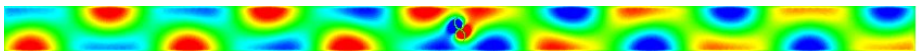

(c) Broadband frequency

Figure 6: Pressure amplitude (real part), the finest acoustic mesh resolution

4 Conclusion

In this paper we presented the hybrid approach to the solution of sound production and propagation in a duct. It has been accepted to an AIAA conference in Stockholm [10].

To resolve the unsteady forces acting on the fluid the wall normal resolution of the CFD calculation is important, but the spanwise dimension of the computational domain is crucial as well. One diameter thick domain gives a wrong prediction of the dominating frequency for periodic vortex shedding. In an incompressible LES a buffer zone is needed for a non-fluctuating reference pressure.

Assuming that in the presence of sharp-edged obstacle, the characteristics of the wake and vortex shedding are not sensitive to Reynolds number, we used a moderately inexpensive LES calculation to predict the sources and scaled them into the high Reynolds case.

This calculation was a first step to predict the diffraction effects of the experimental setup. In the future work we will perform the high Reynolds number LES simulation of a rod placed in a semi-confined jet. We will also investigate the quadrupolar source term and the effects of truncation errors. Together with the experiment results it will provide a verification of the approach proposed in this work.

Acknowledgments

The work is supported through the Marie Curie Research Training Network Project AETHER (contract no MRTN-CT-2006-035713).

References

[1] N. Curle. The influence of solid boundaries upon aerodynamic sound. *Proceeding of the Royal Society of London*, A231:505–514, 1955.

[2] D. F. Kurtulus, F. Scarano, and L. David. Unsteady aerodynamic forces estimation on a square cylinder by tr-piv. *Experiments in Fluids*, 42:185–196, 2007.

[3] Meng Wang, Jonathan B. Freund, and Sanjiva K. Lele. Computational prediction of flow-generated sound. *Annual Review of Fluid Mechanics*, 38:483–512, 2006.

[4] William K. Blake. *Mechanics of flow-induced sound and vibration*. Academic Press, London, 1986.

[5] A. Mueller, P. Martinez, P. Rambaud, C. Schram, and J. Anthoine. A prediction of low mach number sound production by a rod with square cross section in a duct. In *AIAA*, 2010.

[6] A. Okajima. Strouhal numbers of rectangular cylinders. *Journal of Fluids & Structures*, 123:379–398, 1982.

[7] C. Norberg. Flow around rectangular cylinders: Pressure forces and wake frequencies. *Journal of Wind Engineering and Industrial Aerodynamics*, 49:187–196, 1993.

[8] S. Moreau, C. Schram, and M. Roger. Diffraction effects on the trailing edge noise measured in an open-jet anechoic wind tunnel. *13th AIAA/CEAS Aeroacoustics Conference*, AIAA 2007-3706, 2007.

[9] LMS International. *Sysnoise 5.6 User's Manual*. 2008.

[10] Anna Mueller, Jerome Anthoine, and Patrick Rambaud. Vortex shedding in a confined laminar flow past a square cylinder. In *ECCOMAS*, 2008.

Doctoral Project Summary

Current status of propeller blade multidisciplinary optimization

Marinus Benoît G.*

Supervisor: Van den Braembussche René†
von Karman Institute for Fluid Dynamics, Rhode-Saint-Genèse, 1640, Belgium
Promoter: Bosschaerts Walter‡
Royal Military Academy, Brussels, 1000, Belgium

Abstract

Previous to performing aeroacoustic and aerodynamic optimization of propeller blades, the potential influence of different combinations of parameterization methods and optimization strategies on the attainable optimum and the optimization cost is evaluated by comparisons of optimized airfoils. The conclusions from these 2D optimizations are applied in the build-up of the 3D bidisciplinary optimization. Preliminary results concerning the database used to train a metamodel are presented.

1 Introduction

In the search for better performance of propellers, Evolutionary Algorithms (EA) offer the potential for improvement thanks to the large amount of design parameters that can be dealt with. To the authors knowledge, noise generation from propellers for high-speed transport aircraft has not been blended yet into multi-disciplinary design based on EAs because of the high computational cost of aerodynamic and aeroacoustic computations in the transonic domain.

2 2D airfoil optimization

When optimizing the performance of a propeller, the airfoils selected to shape the blades are of primary importance. Most recent works in airfoil optimization rely on spline or Bézier parameterization with typically 10 to 50 parameters. Unfortunately,

*PhD Candidate, Turbomachinery and propulsion Department, Chaussée de Waterloo 72, benoit.marinus@vki.ac.be.

†Honorary Professor, Turbomachinery and propulsion Department, Chaussée de Waterloo 72, vdb@vki.ac.be.

‡Professor, Dept. of Mechanical Engineering, avenue de la Renaissance 30, walter.bosschaerts@rma.ac.be.

few papers [1, 2] assess the influence of the combination of parameterization and optimization method, especially the particular case of b-spline versus Bézier parameterization. For this reason, the present effort investigates the effect of both blade parameterization and optimization technique on the attainable optimum and the numerical cost for reaching it. Comparisons are done in a realistic optimization environment where only a limited amount of parameters are dedicated to the airfoil shape.

2.1 Airfoil shape parameterizations

In total, four parameterization techniques have been investigated. The "*standard*" NACA-type parameterization uses 6 control points with 6 parameters to control the shape of the thickness distribution and 4 additional points with 2 parameters to control the shape of the camberline. The thickness distribution is then set upon the camberline in the way proposed by Abbott et al [3]. This parameterization is used in conjunction with both Bézier and b-spline interpolation of the curves. The "*direct*" parameterization uses 7 control points to control the shape of the suction side and 6 points for the pressure side with 9 parameters in total. For both parameterizations, the curves are again interpolated from the control points using either Bézier or b-spline interpolation. Although the direct parameterization has inherently more freedom to generate radical new shapes than the standard one, it is expected to be less suitable to produce efficient designs precisely because of the larger search space in terms of shape [4]. Indeed, for a comparable search space in terms of parameters, the *direct* parameterization delivers more non airfoil-like shapes even though the parameters are chosen such that a minimum thickness is guaranteed. Moreover, the standard description, on top of its intrinsic capability of delivering airfoil-like shapes, has demonstrated its efficiency [5, 6] thanks to a close relationship between the aerodynamic behavior and the thickness and camber distributions.

2.2 Optimization techniques and objectives

Two techniques have been investigated for multi-point optimization: a single-objective binary-coded Genetic Algorithm (GA) and Multi-Objective Differential Evolution (MODE). The airfoil obtained by each combination of the parameterization and optimization technique is used to define a propeller blade (figure 1(a)) with a prescribed radial distribution of chord, thickness and twist. Each radius defines a 2D high pitch cascade at fixed angle of attack as shown on figure 1(b). The objective of the optimization is to reduce C_d and $1/C_l$ concurrently for three cascades (50%, 75% and 97.5% radius). From blade element theory, it is easily shown that the efficiency of a blade element (see figure 1(b)) that produces the elemental lift $\overline{dL}$ and drag $\overline{dD}$ (resulting in the elemental thrust $\overline{dT}$ and the torque force $\overline{dU}$), is given by:

$$\eta_{el} = \frac{\tan\gamma}{\tan(\gamma+\varepsilon)} \tag{1}$$

where

$$\varepsilon = \arctan\frac{|\overline{dD}|}{|\overline{dL}|} \approx \arctan\frac{C_d}{C_l} \tag{2}$$

The binary-coded GA [7, 8] closely mimics natural evolution by coding the parameters in a binary string or genotype. Individuals of a generation proceed through

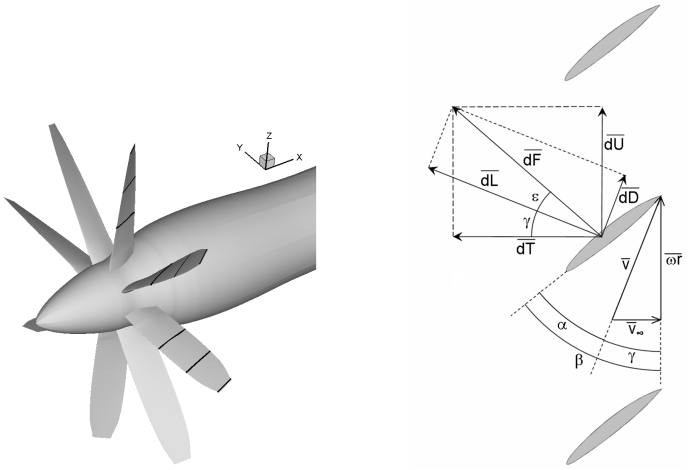

(a) View of the three radii (50%, 75% and 97.5%) chosen for the multi-point optimization of the airfoil in the corresponding blade passage.

(b) 2D geometry of a blade passage at given radius r.

Figure 1: Airfoil cascade geometry.

reproduction by pairs (they exchange parts of their genotype), mutation and ultimately selection based upon their phenotype to generate an hopefully better performing new generation. The selection procedure relies on performance estimates of an aggregated objective. These estimates are provided by an Artificial Neural Network (ANN). It is trained using a database of Navier-Stokes simulations. The accuracy of the surrogate model is safeguarded along the evolutionary process through recursive training each time the database is augmented with the most promising individual of every 1000 generations. On the other hand, Differential Evolution has recently been developed by Price and Storn [9] and does not require parameters to be coded in a binary string. New individuals consist in a random set of parameters originating from one parent combined with another set originating from a linear combination of parameters from individuals chosen randomly in the Pareto front. Selection is performed through Pareto ranking of both parent and child populations. Two cases have been considered: a two-level case in which the performance is assessed through an ANN-metamodel that is trained with RANS simulations every 1000 generations, and a single-level case for which only accurate RANS simulations are used.

2.3 Results

All accurate simulations rely on 2D RANS computations using the *TRAF 2D* solver for transonic flow [10]. It uses a a cell-centered finite volume scheme in conjunction with acceleration techniques on a H-type mesh. The effect of turbulence is accounted for by the Baldwin-Lomax two-layer mixing length model. For comparisons, a NACA 16-009 airfoil is used as benchmark because it is commonly used for propellers.

Table 1 gives an overview of the different cases together with the number of iterations necessary to reach the optimum. Despite converging early toward their respective

optimum, all optimizations were ran for 100 iterations (or generations in the MODE single level case) in order to ensure that absolute convergence is reached. For cases F, G and J, no solution better than the benchmark was found after 100 iterations in spite of modifications to the evolutionary and metamodel settings. For these cases, the optimization is considered as not having succeeded. Disregarding the parameterization type, all optimizations have an identical search domain. The overall performance of an airfoil is measured by its Σ-value (given in table 1) which is the mass-flow averaged area under the C_l/C_d curve normalized by the corresponding area for the benchmark:

$$\Sigma = \frac{\displaystyle\int_{R_{root}}^{R_{tip}} 2\pi\rho_\infty v(r) \frac{C_l(r)}{C_d(r)}\bigg|_{\text{airfoil}} rdr}{\displaystyle\int_{R_{root}}^{R_{tip}} 2\pi\rho_\infty v(r) \frac{C_l(r)}{C_d(r)}\bigg|_{\text{NACA 16-009}} rdr} \tag{3}$$

The Σ-values clearly show that significant overall gains can be achieved as all successful cases have gains ranging from 25% to 40%.

From table 1, the local modification property of the b-spline formulation appears to offer some advantage with a gain of over 15% with respect to the number of calls to the RANS solver before reaching the optimum. This is especially true when a surrogate model is used and a higher number of generations are assessed. Additionally, the b-spline formulation allows the metamodel to better represent the underlying input-output relationships as accuracy is significantly increased. Considering MODE, the results suggest also the effectiveness of using a metamodel as a gain of 23% is obtained globally in that configuration.

Case	Optimization method	Levels	Iterations	Calls to RANS solver	Σ-value
	Benchmark				1
A	GA - with ANN - standard b-spline	2	22	258	1.250
B	GA - with ANN - standard Bézier	2	60	372	1.246
C	GA - with ANN - direct b-spline	2	20	252	1.329
D	GA - with ANN - direct Bézier	2	34	294	1.303
E	MODE - with RANS - standard b-spline	1	49	3132	1.302
F	MODE - with RANS - standard Bézier	1	–	6192	0.950
G	MODE - with RANS - direct b-spline	1	–	6192	0.790
H	MODE - with RANS - direct Bézier	1	57	3612	1.408
I	MODE - with ANN - standard b-spline	2	37	2412	1.308
J	MODE - with ANN - standard Bézier	2	–	6192	0.801

Table 1: Cases and number of iterations to optimum solution. (Cases marked with '$-$' did not converge to an optimum better than the benchmark after 100 iterations.)

The off-design performance of the optimum airfoil is assessed by looking at the airfoil lift coefficient C_l and drag coefficient C_d in successive 2D cascades along the entire blade span. Lift-to-drag ratio for all radii are shown in figures 2(a) and 2(b) for the b-spline and Bézier parameterizations respectively. These figures reveal that most of the improvement is achieved at radii below 60% and above 80%. Around 75% radius, there is either a small improvement (cases E and I), no significant improvement (cases A, C, D and H) or even a local deterioration of the performance (case B). From these graphs, the unsatisfactory performance of cases F, G and J is also enlighted. These results are further investigated by looking at C_l and C_d distributions as well as C_p distributions and airfoil shapes.

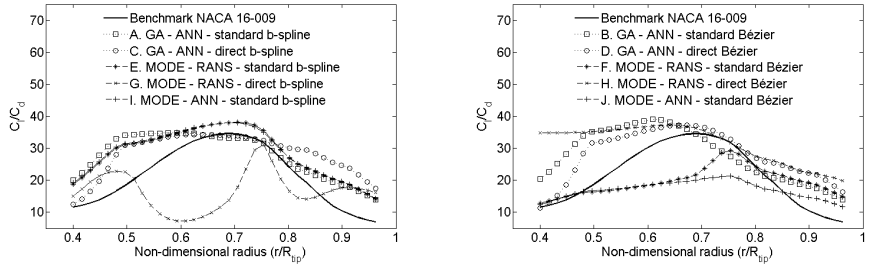

(a) B-spline parameterization.

(b) Bézier parameterization.

Figure 2: Off-design performance in terms of C_l/C_d.

2.4 Preliminary conclusions

Standard parameterization outperforms the direct one both in terms of aerodynamic performance at the optimum and convergence speed. B-spline parameterization essentially differs from Bézier parameterization in terms of convergence. Acceleration techniques based on surrogate models offer interesting advantages in terms of computational cost, without significantly affecting the attainable optimum because they allow the process to be spread over a large number of generations. Finally, the achievable gains are not influenced by the evolutionary process.

3 3D aeroacoustic and aerodynamic optimization

This work focuses on the integration of aeroacoustics and aerodynamics as parts of a multidisciplinary optimization algorithm. The simultaneous consideration of both disciplines in the framework of an EA offers the potential to achieve significant gains. Traditional variables affecting the blade shape over the entire blade span are considered as well as parameters related to the airfoil shape (see table 2), a feature that is seldom integrated in propeller blade optimization processes. MODE is used in conjunction with an ANN. In this way a large number of generations consisting of multiple individuals can be assessed while the proficiency of the metamodel is safeguarded through recursive training of the metamodel with accurate RANS simulations of selected individuals.

Variable		Number of Control Points	Number of parameters	
Chord length	$b(r)/D$	7	7	
Thickness ratio	$t(r)/b(r)$	4	3	
Sweep	$Sw(r)$	4	4	
Twist	$Tw(r)$	4	3	
Airfoil A thickness	t_A	6	5	from blade root to 35% radius
Airfoil A camberline	y_A	4	1	
Airfoil B thickness	t_B	6	5	from 45% radius to blade tip
Airfoil B camberline	y_B	4	2	
Total			30	

Table 2: Design parameters for 3D multidisciplinary optimization.

3.1 Optimizer architecture

The optimizer developed at the von Karman Institute is presented in figure 3. The process starts with a random population comprising N individuals. A new generation of N individuals is formed by mutation and recombination among the parent population. Multi-objective selection is performed in the way proposed by Madavan [11] through Pareto ranking of both parent and child population together with respect to the objective to be minimized. In this effort three concurrent objectives are considered together with seven constraints regarding minimum thrust (at take-off/landing and cruise) and cruise advance ratio $J_{CR,2}$. The aggregated objectives consist of:

1. an aggregate of the propeller power at three advance ratios both in the cruise and take-off/landing conditions (Ω_1),
2. an aggregate of the Sound Pressure Level (SPL) in the propeller plane both in the cruise and take-off/landing conditions (Ω_2),
3. and an aggregate of the SPL at three receiver locations both in the cruise and take-off/landing conditions (Ω_3).

The population size for the next evolutionary step is restored to its original size because only the N best ranked individuals are assessed while looking after the diversity of the population by rejecting individuals with a too high degree of similarity.

As shown on figure 3, a two-level approach is used where performance estimates in the generation loop are computed by a metamodel and performance values are obtained by RANS simulations in the iteration loop. The initial training is made with a database containing a set of RANS simulations of individuals obtained by a Design Of Experiments (DOE). The purpose of the DOE is to fill the search space with carefully selected sample points to provide maximum information about the underlying input-output relationships. This is achieved by assessing individuals obtained from a fractional factorial sampling of the search space.

3.2 DOE results

Aerodynamic computations rely on ANSYS Fluent® to perform steady RANS simulations of a single blade in free air under zero angle of attack. The full propeller is modeled using periodic boundary conditions. The $k-\epsilon$ turbulence model is used in combination with wall treatment. Adiabatic no-slip wall conditions are used for the spinner and blade surfaces and the test-section radial boundary is reproducing the effects of a free pressure far-field. This approach has proven its robustness and accuracy as satisfactory agreement with experimental results has been found for different operating conditions over a wide range of blade shapes [12]. To compute the SPL from the aerodynamic results, a retarded-time implementation of formulation 1A from Farassat [13] is used as long as the tip Mach number M_{tip} is below 0.95 or above 1.05. A truncated approach is used to circumvent the trouble related to the logarithmic singularity occurring when M_{tip} reaches unity. This approach has delivered accurate estimates at low computational cost [14]. In all cases, the SPL is computed in a medium-fixed reference frame and with the blade surface as integration surface.

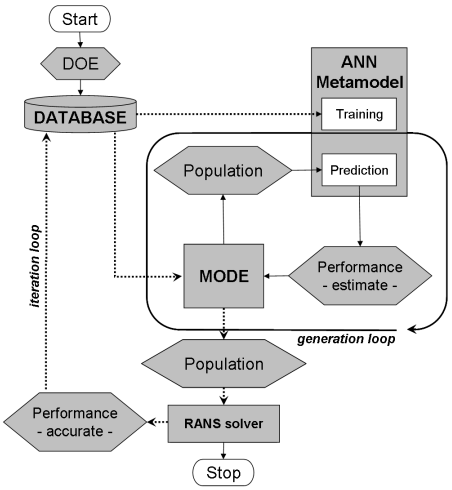

Figure 3: Layout of the two-level MODE-optimizers.

At present, 60 individuals (including the central individual) out of a total of 65 in the DOE-database, have been analyzed through RANS simulations. The central individual is characterized by all values of the design parameters equal to the center of their respective interval. Only 5 individuals could not be analyzed because of the impossibility to generate a correct mesh. An overview of their performance, in terms of objective value ($\Omega_{1,2,3}$), is shown in figure 4 where the diversity present in the database is visible. This diversity stems from the wide number of design variables as given in table 2. Previous to any kind of optimization, some individuals have already promising behaviors in terms of power (Ω_1-objective) and noise simultaneously (Ω_2- and Ω_3-objectives). Closer analysis of the central individual reveals that its poor performance is due to the non-optimal twist distribution although the built-in sweep and chord distributions were expected to deliver better performance than the benchmark. Interestingly, most individuals have better noise performance (both in terms of Ω_2 and Ω_3) than the benchmark. This behavior is at least partly explained by the fact that all those individuals have some sweep, in opposition to the sweepless benchmark. Satisfaction of the constraints of the individuals is represented in figure 5. In the present case, most individuals from the DOE-database satisfy the thrust at cruise constraints ($\Gamma_{CR,1}$ and $\Gamma_{CR,2}$). Concomitantly, some individuals have lower values for the constraint on the advance ratio $J_{CR,2}$. Considering the take-off/landing condition, most individuals do not satisfy the thrust constraints ($\Gamma_{CR,i}$). For the $\Gamma_{TO,2}$-constraint in particular, the difference between the required thrust ($35kN$) and the delivered one is of the order of $8kN$ for most individuals. Nevertheless, some individuals, including the central one, are within acceptable margins from the required value.

4 Conclusion

A multi-point and multidisciplinary optimization procedure based on MODE is being set-up and includes aerodynamics coupled with aeroacoustics. The procedure relies on

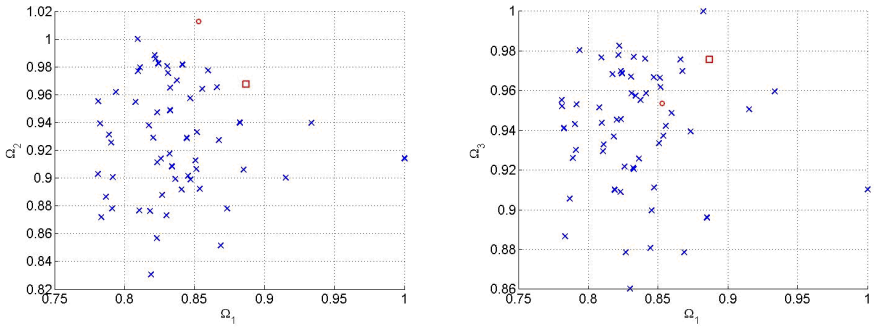

(a) (b)

Figure 4: Objective values for 60 individuals from the DOE-database. The Ω-value of individuals are marked with '$\times$', the central individual is marked with '$\square$' and the benchmark by '$\circ$'.

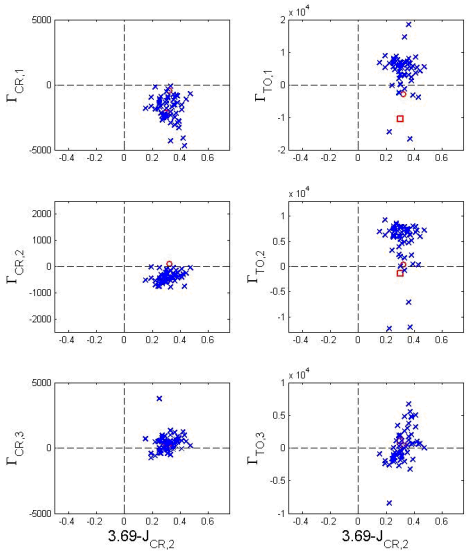

Figure 5: Constraints values for 60 individuals from the DOE-database. The Γ-value of individuals are marked with '$\times$', the central individual is marked with '$\square$' and the benchmark by '$\circ$'.

a scope of design variables that covers the radial distributions of standard blade-shape determining quantities (sweep, twist, chord and thickness) as well as the shape of the airfoils used to manufacture the blade. The parameters effectively used for the optimization are the coordinates of the control points that govern the shape of either the radial distributions or the airfoil, by b-spline interpolation combined with *standard* parameterization because the results from section 2 have indicated that significants gains could be achieved. The operating conditions used for this optimization correspond to the ones encountered by a high-speed transport aircraft. At present, the DOE-database used for metamodel training has been composed. The first results suggest that the diversity in the design search space is transferred into diversity in the objective space. These results reveal also that the DOE-database contains individuals with already promising features. Both the diversity and the presence of promising individuals are encouraging in the success of the overall optimization procedure.

Acknowledgments

References

[1] S. Obayashi and T. Tsukahara. Comparison of optimization algorithms for aerodynamic shape design. *AIAA Journal*, 35(8):1413–1415, August 1997.

[2] J. Hájek. Parameterization of airfoils and its application in aerodynamic optimization. In *Proceedings of the 16th Annual Conference of Doctoral Students - WDS 2007*, pages 233–240, Prague, June 5-8 2007.

[3] I.H. Abbott, A.E. von Doenhoff, and L.S. Stivers Jr. Summary of airfoil data. Report R-824, NACA, NACA-Langley aeronautical laboratory (USA), 1945.

[4] W. Song and A.J. Keane. A study of shape parameterisation methods for airfoils optimisation. In *10th AIAA/ISSMO Multidisciplinary Analysis and Optimization Conference*, number AIAA 2004-4482, Albany (USA), August 30 - September 1 2004. AIAA.

[5] S. Obayashi. Airfoil shape parameterization for evolutionary computation. In *Lecture Series on Genetic Algorithms for Optimisation in Aeronautics and Turbomachinery*, number LS 2000-07, Sint-Genesius-Rode (Belgium), 2000. von Karman Institute for Fluid Dynamics.

[6] A.J. Keane and P.B. Nair. *Computational approaches for aerospace design*. John Wiley & Sons, Chichester (United Kingdom), 2005.

[7] D. Goldberg. *Genetic algorithms in search, optimization and machine learning*. Addison-Wesley, Stuttgart (Germany), 1989.

[8] T. Verstraete. *Multidisciplinary turbomachinery component optimization considering performance, stress and internal heat transfer*. Phd thesis, von Karman Institute for Fluid Dynamics - Universiteit Gent, Rhode-Saint-Genèse - Gent (Belgium), June 2008.

[9] K. Price and R. Storn. Differential evolution, April 1 1997.

[10] A. Arnone and R.C. Swanson. A Navier-Stokes solver for turbomachinery applications. *ASME Journal of Turbomachinery*, 115(2):305–313, April 1993.

[11] N.K. Madavan. Multiobjective optimization using a Pareto Differential Evolution Approach. In *Proceedings of the Congress on Evolutionary Computation*, volume 2, pages 1145–1150, Honolulu (USA), 2002.

[12] B. Marinus. Multidisciplinary evaluation of known propeller configurations. Project Report 2007-15, von Karman Institute for Fluid Dynamics, Rhode-Saint-Genèse (Belgium), June 2007.

[13] F. Farassat and G.P. Succi. The prediction of helicopter rotor discrete frequency noise. *Vertica*, 7(4):309–320, 1983.

[14] B. Marinus, M. Roger, R. Van den Braembussche, and W. Bosschaerts. Truncated method for propeller noise prediction up to low supersonic helical tip mach numbers. In *15th AIAA/CEAS Aeroacoustics Conference*, number AIAA 2009-3330, Miami (USA), May 11-13 2009. AIAA.

Residual Distribution Scheme Development for Flows

Doctoral Project Summary

Development of H- and P- Solution-adaptive Techniques for Residual Distribution Schemes in Compressible Flow

S. D'Angelo*

Supervisor: Herman Deconinck†

Advisor: Tiago Quintino‡

von Karman Institute for Fluid Dynamics, Rhode-Saint-Genèse, 1640, Belgium

Abstract

The current PhD work concerns the study and the implementation of a new algorithm for error estimation in CFD computations. This estimate involves the dealing of the adjoint argument. By solving the adjoint problem, it is possible to obtain important information about the transport of the error towards the quantity of interest. The aim is to apply for the first time this procedure into the Residual Distribution (RD) method. In order to achieve this goal, firstly, properties of the discretization of the adjoint problem by RD have been studied.

Introduction

Over the last decade, much progress has been made in the area of Error Estimation. This theory provides a way to construct error indicators for CFD computations of PDE's. These error indicators can be used to drive automatic mesh adaptation algorithms. By adapting the mesh, we optimize the mesh spacings or reduce memory usage.

In this field, the *a posteriori* error analysis is one of the most used procedures to compute numerical error indicators. The relevance and generality of this estimation has been powerfully argued in the work of Johnson and his collaborators [1]. The *a posteriori* error bounds resulting from this analysis involve the numerical residual, obtained by inserting the computed solution into the current problem equations; this residual measures the extent to which the numerical approximation to the analytical solution

*PhD Candidate, Aeronautics and Aerospace Department, Chaussée de Waterloo 72, dangelo@vki.ac.be

†Professor, Aeronautics and Aerospace Department, Chaussée de Waterloo 72, deconinck@vki.ac.be.

‡Research Engineer, Aeronautics and Aerospace Department, Chaussée de Waterloo 72, quintino@vki.ac.be.

fails to satisfy the current problem. From this study, the *Type II a posteriori* error bounds have been defined. Becker and Rannacher worked also on this issue and they developed the so-called weighted-residual-based, or *Type I*, *a posteriori* error estimation ([2] and [3]). Here, the error representation formula defines the error in the target functional with the numerical residual, weighted by the solution of an adjoint problem. The key ingredient is this auxiliary problem, involving the formal adjoint of the current partial differential operator. For computing this product, also this adjoint problem will have to be implemented and solved numerically. The data for the adjoint problem is a quantity of interest depending on the application. In engineering applications, this is typically a functional of the analitical solution such as a mean, point value, boundary flux. In fluid dynamics, it may be the pression at the stagnation point, the pressure-drop between inflow and outflow or the drag or lift coefficients of a body immersed into the fluid.

For solving the adjoint problem, added cost rises. However, it is paid back by important information which helps us to identify where the real source of the error comes from. To understand the relevance and the adventages of *Type I* indicators over the *Type II*, we take a typical example of the adaptive mesh design for a supersonic flow past an airfoil. Computation results are taken from Hartmann's thesis ([4]). Figure 1a shows the mesh produced using an *ad hoc* indicator $\eta_\kappa^{\text{ad hoc}}$ that depends on the finite element residuals, only. This mesh is largely concentrated in the vicinity of both shocks of the flow. Let assume now that there is particular interest in the point value of the pressure at the leading edge of the airfoil. The mesh produced using the weighted indicator $|\eta_\kappa|$ (figure 1b) only refines the mesh in the vicinity of the point of evaluation and the part of the shock where the main part of the information crosses the shock. By considering the number of elements and the true error in the computed functional, we clearly observe the superiority of the *Type I* error estimation.

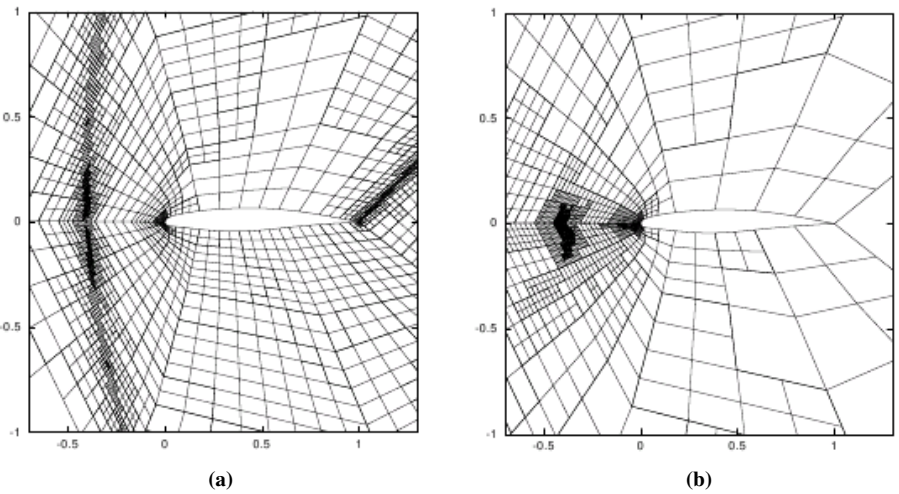

Figure 1: supersonic BAC3-11 flow. (a) Mesh constructed using *ad hoc* error indicator with 13719 elements ($||J(u) - J(u_h)| = 3.542 \times 10^{-2}$); (b) Mesh constructed using adjoint error indicator with 1803 elements ($|J(u) - J(u_h)| = 3.042 \times 10^{-3}$).

Objectives

In this work, we want to develop the *a posteriori* error analysis of the adaptive Residual Distribution method for compressible flows. This error estimation will be based on the adjoint argument in order to obtain the so-called Type I *a posteriori* error bounds. The error representation formula includes the element-residuals mutiplied by local weights involving the solution of the associated adjoint problem. Based on these weighted indicators, we disegn and implement an adaptive algorithm that produces meshes specifically tailored to the efficient computation of the quantity of interest.

Type II *a posteriori* error estimation

Primal problem model: Let's consider a linear problem

$$Lu = f \quad \text{in} \quad \Omega, \qquad\qquad Bu = g \quad \text{on} \quad \Gamma, \tag{1}$$

where $f \in L_2(\Omega)$ and $g \in L_2(\Gamma)$, L is a linear differential operators on the domain Ω and B denotes a linear boundary operator on Γ. To solve this problem a numerical discretization is given and an approximated solution, u_h, is sought in the place of u, by using a discrete numerical method. We consider the numerical solution as a linear combination of piecewise polynomial functions of degree p on a partition $\mathcal{T}_h$ of the domain Ω. For this reason we can write $u_h \in V_{h,p}$.

Error Estimation formula: In the field of *a posteriori* error bounds, the error estimation is computed once the numerical solution is given. By replacing u_h to the continuous problem we obtain the numerical residual, $R(u_h) = Lu_h - f$ and $r(u_h) = Bu_h - g$, inner and boundary residual, respectively. Since the exact solution u satisfies the current equation, by applying it into the residuals, these vanish $R(u) = 0$, $r(u) = 0$. The residual can be considered then as a sort of error indicator. It tells quickly how much the numerical solution fails to satisfy the current problem and therefore we have an idea of how far u_h is to the exact solution.
Some *a posteriori* error analysis base their bounds on a some function of the numerical residual. By using these error estimation, let's define a tolerance $\mathsf{TOL} > 0$, then the problem to solve will be, finding $u_h \in V_{h,p}$ such that

$$e = |u - u_h| = \mathsf{C}\big(R(u_h)\big) \leq \mathsf{TOL} \tag{2}$$

where $\mathsf{C}\big(R(u_h)\big)$ is a some function of the residual, depending on the current estimation. Type II error estimation is based on this assumption and defines the error representation by the norm L_2 of the local residual

$$||e||_{L_2(\Omega)} \approx \mathcal{E}_\Omega = \sum_\kappa \eta_\kappa = \sum_\kappa \left[h^s ||R(u_h)||_{L_2(\kappa)}\right] \tag{3}$$

with s an integer depending on the smoothness of the solution ([5]). Such an error estimation does not need any other information and once the numerical solution is computed, it gives directly the local error indicator over every element.

Transported and generated error in hyperbolic problems

The local residual is not always the most efficient choice as a kind of error indicator. This is true mostly when we deal with hyperbolic problems. A dimostrative example of this issue is given by Süli and Houston ([6]). A scalar first-order hyperbolic equation is taken into account for a function $u(x, y)$ on a unit square $\Omega = (0, 1)^2$

$$\boldsymbol{a} \cdot \nabla u = 0 \quad \text{in} \quad \Omega \qquad\qquad u = u_{\Gamma_-} \quad \text{on} \quad \Gamma_-$$

where $\boldsymbol{a} = (a_x, a_y) = (1/10 + \sin(\pi y), 2)$ and a particular inflow boundary condition, u_{Γ_-}, is given. We note that, letting $e = u - u_h$, the residual and the error are related via

$$\boldsymbol{a} \cdot \nabla e = R(u_h)$$

We decompose the global error and we define the element error e_κ as follows

$$e_\kappa = e_\kappa^{\text{cell}} + e_\kappa^{\text{trans}} \tag{4}$$

we shall refer to e_κ^{cell} as the *cell* error and e_κ^{trans} will be called the *transmitted* error.

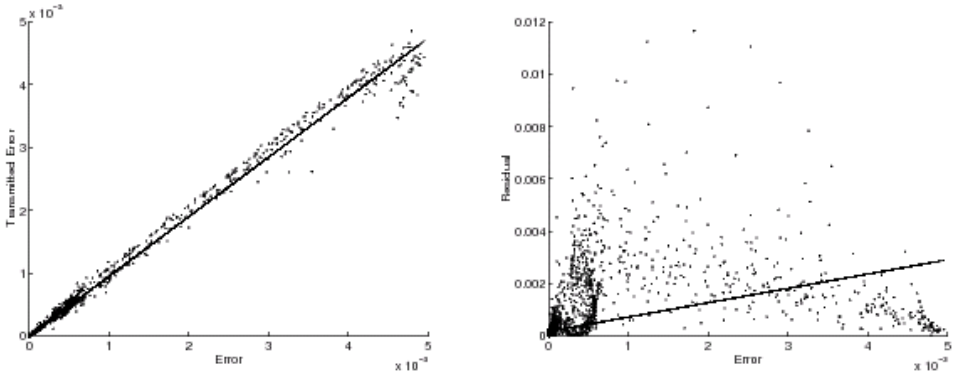

(a) transmitted error vs. error **(b)** residual vs. error

Figure 2: Scatter plots for the data-set-pairs $(||e_\kappa^{\text{trans}}||_{L_s(\kappa)}, ||e_\kappa||_{L_s(\kappa)})$ (a) and $(||R(u_h)|\kappa||_{L_2(\kappa)}, ||e_\kappa||_{L_s(\kappa)})$ (b)

The cell error e_κ^{cell} is the part of the error e_κ which is governed by the residual $R(u_h)|_k$ and is not influenced by the pollution effects from outside κ. On the other hand, the transmitted error e_κ^{trans} is indipendent of the residual on κ and is driven completely by the error that has been created outside κ and transmitted into κ through the inflow boundary of κ. They are defined as the respective solutions to the following problems

$$\begin{aligned} \boldsymbol{a} \cdot \nabla e_\kappa^{\text{cell}} &= R(u_h) \quad \text{in} \quad \kappa; \qquad e_\kappa^{\text{cell}} = 0 \quad \text{on} \quad \kappa_- \\ \boldsymbol{a} \cdot \nabla e_\kappa^{\text{trans}} &= 0 \quad \text{in} \quad \kappa; \qquad e_\kappa^{\text{trans}} = e_\kappa \quad \text{on} \quad \kappa_- \end{aligned}$$

The solution of this problem has been solved numerically and exactly by using the method of charateristics.
Figure 2a plots each $||e_\kappa^{\text{trans}}||_{L_2(\kappa)}$ against the error $||e_\kappa||_{L_2(\kappa)}$ while figure 2b shows $||R(u_h)|\kappa||_{L_2(\kappa)}$ vs. $||e_\kappa||_{L_2(\kappa)}$. In particular, we see from the right-hand figure that there is a cluster of points lying on the horizontal axis, i.e., as the error increases,

the residual remains small in magnitude. Clearly, this has serious implications in the context of mesh design; an adaptive algorithm based on refining elements κ, where the local residual is large may fail to refine all the elements where $||e_\kappa||_{L_2(\kappa)}$ is large.
From this example, we realize that it is not enough computed the magnitude of the local error. Mainly for hyperbolic problem, as in the current problem, we need also to know where the source of this error comes from. For this reason not only the local residual must be taken into account and another error estimation bound has to be developed.

Type I *a posteriori* error estimation

The functional $J(\cdot)$: In many problems of physical interest the quantity of interest for the current problem is an output or target functional of the solution rather the solution itself. This target functional is defined as $J(\cdot)$. Depending on the problem, it can be a different quantity, for example the drag or the lift coefficient

$$J_{\text{drag}}(u) = \frac{2}{\bar{l}\bar{\rho}|\bar{v}|^2}\int_S (\psi_d \cdot \boldsymbol{n})p(u)ds \quad \text{or} \quad J_{\text{lift}}(u) = \frac{2}{\bar{l}\bar{\rho}|\bar{v}|^2}\int_S (\psi_l \cdot \boldsymbol{n})p(u)ds$$

where in this case is $u = (\rho, \rho u, \rho v, \rho E)$ or a point value of the solution

$$J(u) = p(u)(0,0) \qquad \text{pressure at the stagnation point}$$

For the model problem, let's consider a linear target functional which can be written as

$$J(u) = \big(u, j_\Omega\big) + \big(u, j_\Gamma\big)_\Gamma \equiv \int_\Omega j_\Omega u d\boldsymbol{x} + \int_\Gamma j_\Gamma C u ds \tag{5}$$

where $j_\Omega \in L_2(\Omega)$, $j_\Gamma \in L_2(\Gamma)$, C is an operator on Γ which may be differential, and $(\cdot,\cdot)$ and $(\cdot,\cdot)_\Gamma$ are the $L_2(\Omega)$ and $L_2(\Gamma)$ inner products, respectively.
This functional will be computed numerically and evaluated by the numerical solution, $J_h(u_h)$. The final purpose is to compute as good as possible this quantity, trying to estimate the order of error that the numerical approximations generate. Given a tolerance $\mathsf{TOL} > 0$, then the problem might be defined as finding $u_h \in V_{h,p}$ such that

$$|J(u) - J_h(u_h)| \leq \mathsf{TOL} \tag{6}$$

Associated adjoint problem: Mathematical theory tells us that for each operator appearing in the primal problem, L, B and C, there exists a corresponding adjoint one, L^*, B^* and C^*. By these so-called *adjoint operators*, we build the adjoint problem associated to (1)

$$L^* z = j_\Omega \quad \text{in} \quad \Omega, \qquad\qquad B^* z = j_\Gamma \quad \text{on} \quad \Gamma. \tag{7}$$

Terms j_Ω and j_Γ on the right-hand side depend on the target quantity that we want to investigate and define the functional $J(\cdot)$, as we have seen.
The associated adjoint problem is hugely important. It provides how the information is transported towards the current quantity of interest. This property is extremely useful to derive where and how the source of the error of the target quantity is carried over the

domain. The error indicator derived by this further information will be able to refine only the terms that really affect the error of the quantity of interest.
Let's consider an example to better understand the last claim. We study the formation of an oblique shock when a supersonic flow is defected by a wedge, with an angle α. Under these conditions, a shock wave develops at an angle β, figure 3. The target functional is chosen to be the value of the density just in front of the shock, $J(u) = \rho(5, 2.05)$. In figure 4 we show the z_1 component of the adjoint solution computed on globally refined mesh ([4]). It consists of three 'spikes'. These spikes are

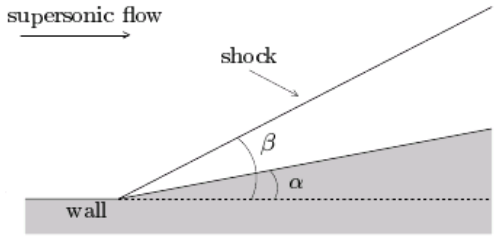

Figure 3: Geometry of the supersonic compression corner.

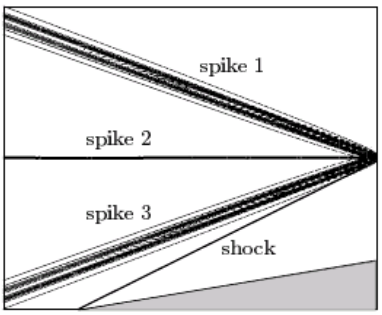

Figure 4: z_1 component of the adjoint solution for the supersonic compression corner for point evaluation of the density in front of shock.

transported upstream along the characteristics corresponding to the three eigenvalues $\bar{v}$ and $\bar{v} \pm c$, where v is the velocity of the gas and c is the speed of sound. In this case, the shock does not affect the value of the density at the point of evaluation and for this reason, it is not necessary to refine it.

We consider now the case where we are interested in the value of the density just behind the shock, for instance, $J(u) = \rho(5, 2.01)$. Figure 5a shows the z_1 component of the associated adjoint problem. In this case, the support of the solution intersects the region containing the shock and for this reason, z_1 has a rather complicated structure. The corresponding refined mesh is drawn in figure 5b. It has been refined only along the support of spikes 3 and 6 in the vicinity of the top part of the shock, and in the neighbourhood of the point where spike 3 crosses the bottom part of the shock. This

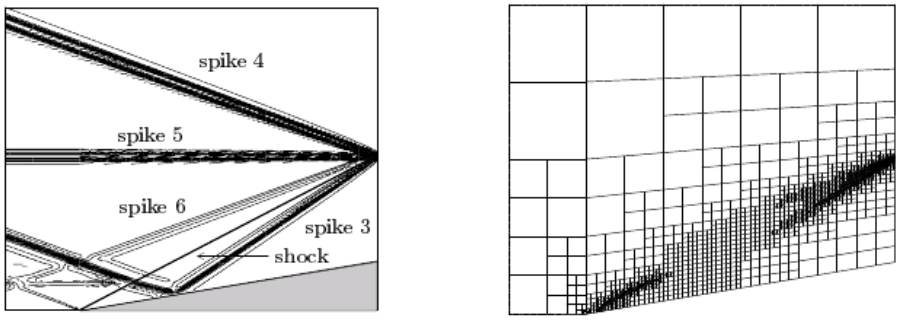

(a) **(b)**

Figure 5: (a) z_1 component of the adjoint solution for the supersonic compression corner for point evaluation of the density in behind of shock. (b) Mesh constructed using adjoint error indicator for point evaluation of the density behind the shock.

demostrates that it is not necessary to refine the entire shock to gain an accurate evaluation of the target functional under consideration.

Error Estimation formula According to the *compatibility condition*

$$\big(Lu, z\big) + \big(Bu, C^* z\big)_{\Gamma} = \big(u, L^* z\big) + \big(Cu, B^* z\big)_{\Gamma} \tag{8}$$

and by applying the *Galerkin orthogonality property*, we arrive to the following error representation formula

$$J(u) - J_h(u_h) = \big(R(u_h), z - z_h\big) + \big(r(u_h), C^*(z - z_h)\big)_{\Gamma} \tag{9}$$

where $R(u_h)$ and $r(u_h)$ are the inner and boundary residual, respectively, while z_h is the projection, interpolant or quasi-interpolant of z onto the subspace $V_{h,p}$. This error formulation to be completed needs to compute the adjoint solution z. Also the adjoint problem must be numerically approximated. The exact adjoint solution is replaced by the numerical solution $\tilde{z}_h$. From the (9), we remark that $\tilde{z}_h$ cannot be calculated by the same subspace $V_{h,p}$ used for the primal problem otherwise, the error representation formula will be identically zero, because of the difference $\tilde{z}_h - z_h$.
In practice, there are essentially three different approaches to computing a numerical approximation of z. The first one is to keep the degree p of the approximating polynomial used for u_h, but compute $\tilde{z}_h$ on another more accurated adjoint mesh T_{h_d} than the T_h; the second solution is to compute $\tilde{z}_h$ using an higer polynomial order $\tilde{p}$ than p and using the same mesh; and finally, it is also possible to compute the numerical solution $\tilde{z}_h$ by using the same mesh T_h and polynomial degree p than the primal problem and then taking a patchwise higher order recovery. Herebelow, the summary of the three approaches

- $\tilde{p} = p$ in $T_{h_d} \neq T_h$: $\tilde{z}_h \in V_{h_d,p}$
- $\tilde{p} > p$ in $T_{h_d} = T_h$: $\bar{z}_h \in V_{h,\tilde{p}}$
- $\tilde{p} > p$ in $T_{h_d} = T_{nh}$: $\tilde{z}_h \in V_{nh,\tilde{p}}$ from a temporary solution $\tilde{z}_h \in V_{h,p}$.

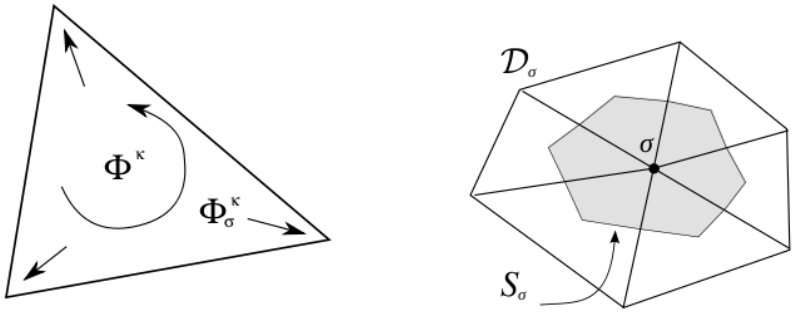

(a) **(b)**

Figure 6: (a) Distribution fractions of the integral residual to the surronding degrees of freedom. (b) Dual cell around the current degree of freedom.

This *a posteriori* error estimation is localized as

$$J(u) - J_h(u_h) \approx \tilde{\mathcal{E}}_\Omega = \sum_\kappa \tilde{\eta}_\kappa \tag{10}$$

with

$$\tilde{\eta}_\kappa = \big(R(u_h), \tilde{z}_h - z_h\big)_\kappa + \big(r(u_h), C^*(\tilde{z}_h - z_h)\big)_{\partial\Omega_\kappa}$$

According to their definition, these local error indicators, $\tilde{\eta}_\kappa$, are weighted by the adjoint solution. There let take care only of elements which actually affect the current quantity of interest. This means that even if the local residual error is high, if it does not influence the target quantity, the error indicator will be small.
Such an indicator becomes therefore a powerful and strong device for an accurate adaptive mesh design. By it, we are so able to refine the mesh or solve the solution more accurately only where we really need to.

Residual Distribution method

In a Residual Distribution (RD) method, the numerical solution is still defined as a linear combination of piecewise polynomial functions

$$u_h = \sum_\sigma u_h(x_\sigma)\varphi^p_\sigma \tag{11}$$

where x_σ is a general degree of freedom associated to the Lagrange interpolation φ_σ of order p on a partition $\mathcal{T}_h$ of the domain Ω, in element $\kappa \in \mathcal{T}_h$ of size h. Always considering the (1), let define the residual in the element κ as the integral value ([7])

$$\Phi^\kappa = \int_\kappa (Lu_h - f)d\boldsymbol{x} + \int_{\partial\kappa\cap\Gamma} (Bu_h - g)ds. \tag{12}$$

This numerical method consists of distributing fractions of the integral residual to the surronding degrees of freedom, with weights summing up to one for consistency (figure 6a). So introducing the distribution coefficient β^κ_σ, we require that

$$\Phi^\kappa_\sigma = \beta^\kappa_\sigma \Phi^\kappa, \qquad \text{and} \qquad \Phi^\kappa = \sum_{\sigma\in\kappa} \Phi^\kappa_\sigma$$

This leads to the following explicit update scheme

$$u_\sigma^{n+1} = u_\sigma^n - \omega_\sigma \sum_{\kappa,\sigma\in\kappa} \Phi_\sigma^\kappa \tag{13}$$

where $\omega_\sigma = \Delta t / S_\sigma$, with Δt the pseudo time-step of the explicit iterative solver and S_σ the area of the dual cell around x_σ (figure 6b). The coefficients β_σ^κ (or the functions Φ_σ^κ) can be specified so as to satisfy certain properties of monotonicity and accurancy in the solution, while maintaining the same compact stencil. This is one of the main advantage of the method compared to high-order finite volume schemes on unstructured meshes.

Consistency and adjoint consistency properties

The *consistency* property tells us if the numerical discretization used to get the numerical solution still holds when we replace u_h by the exact solution, u. In other words, if we are still solving the right equations after discretizing them. When also the adjoint problem is implemented, we need to verify the consistency of it, as well. This discretization is then *adjoint consistent* if the discrete adjoint problem is a consistent discretization of the continuous adjoint problem.

Galerkin method and peers According to Hartamann [8], Galerkin method and other methods deriving from it (for instance, Discountinuous Galerkin method), are mostly both consistent and adjoint consistent and then, the here-below diagram is followed

	primal problem		**adjoint problem**
continuous problem	$Lu = f$	$\longleftrightarrow$	$L^* z = j$
	$\downarrow$		$\downarrow$
discretized problem	$\mathcal{B}(u_h, v_h) = l(v_h)$	$\longrightarrow$	$\mathcal{B}(w_h, z_h) = J(w_h)$

According to this, it is possible to compute the numerical adjoint problem simply by switching the position of trial, v_h, and test, u_h, functions on the discretized operator of the primal problem. We do not care about the continuous adjoint problem. By the adjoint consistency property, the numerical adjoint discretization, so constructed, solves the continuous one.

Residual Distribution method The first step is to verify if this property is also available by using RD schemes.

	primal problem		**adjoint problem**
continuous problem	$Lu = f$	$\longleftrightarrow$	$L^* z = j$
	$\downarrow$		$\downarrow$
discretized problem	$u_\sigma^{n+1} = u_\sigma^n - \omega_\sigma \sum_{K,\sigma \in K} \Phi_\sigma^K$	$\overset{?}{\longrightarrow}$	$z_{\bar{\sigma}}^{n+1} = z_{\bar{\sigma}}^n - \omega_{\bar{\sigma}}^A \sum_{K,\bar{\sigma} \in K} \Phi_{\bar{\sigma}}^{K\,A}$

To do that, we need first of all to derive the variational formulation of the RD for a generic scheme and then apply it to both primal and adjoint problems.

primal problem		**adjoint problem**
$Lu = f$	$\longleftrightarrow$	$L^* z = j$
$\downarrow$		$\downarrow$
$\mathcal{B}(u_h, v_h) = l(v_h)$		$\mathcal{B}^A(w_h, z_h) = J^A(w_h)$

If the adjoint consistency is satisfied the two formulations are symmetrical, in other words

$$\mathcal{B}(w_h, z_h) \qquad \equiv \qquad \mathcal{B}^A(w_h, z_h) \tag{14}$$

Variational formulation for RD method

By following Abgrall's work ([9]), we are able to define the variational formulation for Residual Distribution method. The study has been developed for an hyperbolic scalar problem as a problem model. We adapted it to a Poisson scalar problem, as well. According to Abgrall, the variational operator $\mathcal{B}(\cdot, \cdot)$ consists of a symmetrical Galerkin term and a stabilizer term which depends on the current numerical scheme

$$\begin{aligned} \mathcal{B}(u_h, v_h) = \sum_\kappa \Bigg[& \int_\kappa v_h (L u_h) d\boldsymbol{x} \\ & + h \frac{h_\kappa / h}{(N_\kappa - 1)!} \sum_{\sigma, \sigma'} \vartheta_{\sigma,\sigma'} \frac{v_\sigma - v_{\sigma'}}{||x_\sigma x_{\sigma'}||} \int_\kappa (\gamma_{\sigma,\sigma'} - \psi_{\sigma,\sigma'})(L u_h) d\boldsymbol{x} \Bigg] \end{aligned} \tag{15}$$

with $\vartheta_{\sigma,\sigma'} = ||x_\sigma x_{\sigma'}||/h_\kappa$ which is bounded since the mesh is regular, $\gamma_{\sigma,\sigma'} = \beta_\sigma^\kappa - \beta_{\sigma'}^\kappa$ and $\psi_{\sigma,\sigma'} = \varphi_\sigma^q - \varphi_{\sigma'}^q$.
As far as the first studies, this added term does not seem to be symmetrical and hence, the adjoint consistency seems not to be applied for the Residual Distribution method. However, not final conclusion can be claimed now about it, since the analysis has not been completed yet. Further remarks will be defined for next months also by the collaboration with Abgrall himself.

Conclusions

We spent the first months of the project by studing and recovering the state of art about the error estimation theory. In particular we focused our attention on the *a posteriori* error bounds. Among different types of error representation formula, we interested in Type I error indicator. Unlike Type II error bounds where the only local residual is taken into account, Type I involves also the solution of the associated adjoint problem. By it, we are able to obtain further information concerning the trasport of the error of computing the quantity of interest.
For the first time, we want to apply this error analysis to the Residual Distribution method. Since the adjoint solution must be solved numerically, we started the study of the consistency and adjoint consistency property for the current method. Unfortunately, it seems that Residual Distribution is not symmetrical and the adjoint consistency is not satisfied. This means that the adjoint solution must be computed directly by the discretization of the continuous adjoint problem and not by using the discrete operator of the primal problem, like in a Galerkin method. However, the study is ongoing and by the collaboration with Professor Abgrall for next months, we will be able to confirm or not this issue.
Once properties of the numerical adjoint solution are known by applying Residual Distribution method, we implement this error estimation theory on a code. We start by simple scalar first-order hyperbolic problem to pass later to more complicated problems and by ending to a non-linear system of equations, like the 2D compressible Euler equations.

References

[1] P. Hansbo K. Eriksson, D. Estep and C. Johnson. Introduction to adaptive methods for different equations. *Acta Numerica*, pages 105–158, 1995.

[2] R. Becker and R. Rannacher. A feed-back approach to error control in finite element methods: basis analysis and examples. *Journal Numerical Mathematics*, 4:237–264, 1996.

[3] R. Becker and R. Rannacher. An optimal control approach to a-posteriori error estimation in finite element methods. *Acta Numerica*, 10:1–102, 2001.

[4] R. Hartmann. *Adaptive Finite Element Methods for the Compressible Euler Equations*. PhD thesis, Universität Heidelberg, 2002.

[5] P. Houston E. Süli. *hp*-adaptive discountinuous galerkin finite element methods for first-order hyperbolic problems. *SIAM Journal of Scientific computations*, 23:1225–1251, 2001.

[6] P. Houston E. Süli. *Adaptive Finite Element Approximation of Hyperbolic Problems*. Barth & Deconinck, 2002.

[7] M. Ricchiuto. *Construction and analysis of compact residual discretizations for conservation laws on unstructured meshes*. PhD thesis, Université Libre de Bruxelles, 2005.

[8] R. Hartmann. Numerical analysis of higher order discountinuos galerkin finite element methods. In *35th CFD VKI / ADIGMA*, 2008.

[9] M. Ricchiuto R. Abgrall, A. Larat and C. Tavé. A simple construction of very high order non oscillatory compact schemes on unstructured meshes. *Computers & Fluids*, 38:1314–1323, 2009.

Doctoral Project Summary

High–order $\mathcal{RDS}$ and p–multigrid Solution Algorithms for Compressible Flow

Martin Vymazal*

Supervisor: Herman Deconinck†
Advisor: Tiago Quintino‡
von Karman Institute for Fluid Dynamics, Rhode-Saint-Genèse, 1640, Belgium

Abstract

Residual distribution schemes are discussed in the context of higher order spatial discretization for hyperbolic conservation laws. The discrete solution is approximated by a finite element space based on triangular Lagrangian P_k elements. A natural subtriangulation of these elements allows the reuse of simple distribution formula previously developed for linear P_1 triangles. Curved elements with piecewise quadratic and cubic approximation of the boundaries of the domain are considered.

1 Introduction

The present work follows a Residual Distribution approach [1, 2, 3], which is close to continuous finite element methods, but allows the use of a maximum principle to construct nonlinear monotonicity preserving and truely multidimensional stabilizations. In previous papers [4] we have exploited the close relation with continuous finite element discretizations to present a class of higher order residual distribution methods defined on P_k Lagrangian triangular finite elements. Here we focus on the use of curved elements to allow for a higher order representation of the boundaries of the domain, using sub- or isoparametric transformation from physical space to a Cartesian parent element.

2 Notations

We consider the steady state solution of a conservation law on a two–dimensional spatial domain Ω:

$$\frac{\partial \boldsymbol{u}}{\partial t} + \nabla \cdot \boldsymbol{\mathcal{F}} = 0 \quad \forall (x, y) \in \Omega \subset \mathbb{R}^2, \quad \forall t \geq 0, \tag{1}$$

*PhD Candidate, Aeronautics and Aerospace Department, Chaussée de Waterloo 72, vymazal@vki.ac.be.
†Professor, Aeronautics and Aerospace Department, Chaussée de Waterloo 72, deconinck@vki.ac.be.
‡Research Engineer, Aeronautics and Aerospace Department, Chaussée de Waterloo 72, quintino@vki.ac.be.

where $\boldsymbol{u}$ is the vector of conserved variables and $\boldsymbol{\mathcal{F}}$ is the inviscid flux vector, $\boldsymbol{\mathcal{F}}(\boldsymbol{u}) = (\mathbf{f}(\boldsymbol{u}), \mathbf{g}(\boldsymbol{u}))$. We denote by $\mathcal{T}_{h,k}$ a triangulation of the domain Ω, whereby each triangular element T of the triangulation $\mathcal{T}_{h,k}$ is a Lagrangian P_k finite element equipped with $K = \frac{(k+1)(k+2)}{2}$ degrees of freedom.

In the simplest case the geometry of the P_k triangle is considered to be linear, defined by its three corner nodes. Hence, the intermediate nodes on the boundary of the element are all located on the straight edges and therefore the boundary of the domain Ω is approximated by a polygone. Such a discretization will be denoted as a P_1P_k discretization (P_1 for geometry and P_k for the solution). An example of a P_1P_2 element and its sub–triangulation is given in figure 1(a),1(b). We work with elements

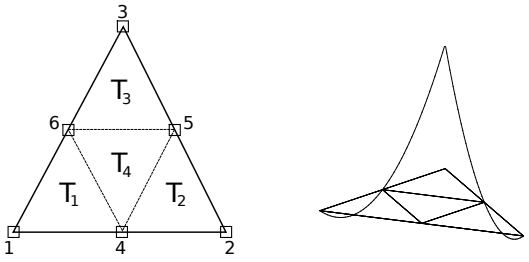

(a) P_2 element (b) Quadratic shape function

Figure 1: P_1P_2 triangle - first order in terms of geometry, second order in terms of solution

whose edges are described by second- and third- order polynomials. Elements with quadratic geometry will be denoted as P_2P_k elements (P_2 for geometry and P_k for the solution). P_2P_2 elements are called isoparametric, while P_2P_k with $k > 2$ are called subparametric elements. The notation for P_3 elements is analogous.

The geometry of the curvilinear $P_2\,(P_3)$ element is transformed to a parent element in ξ–η space. In our case, we define $\mathbf{F}(\xi, \eta)$ from figure (2) as isoparametric mapping

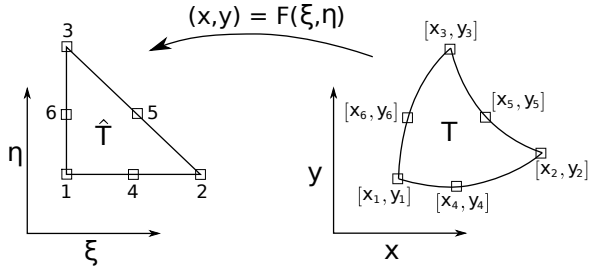

Figure 2: Transformation of triangle geometry from physical to reference space using Lagrange shape functions

$$\begin{bmatrix} x(\xi,\eta) \\ y(\xi,\eta) \end{bmatrix} = \sum_{i=1}^{N} \varphi_i^{h,k}(\xi,\eta) \cdot \begin{bmatrix} x_i \\ y_i \end{bmatrix} \tag{2}$$

where N is the number of degrees of freedom of P_2 or P_3 triangle, respectively. The number k refers to the order of shape functions φ_i and x_i, y_i denote the nodal coordinates of the triangle.

3 Residual Distribution method

For any triangulation $\mathcal{T}^{h.k}$ the cell residual for a given triangle is defined as the integral over the triangle of the spatial operator:

$$\begin{aligned} \boldsymbol{\phi}^T &= \oint_{\partial T} \boldsymbol{\mathcal{F}}(\boldsymbol{u}^{h,k}) \cdot \boldsymbol{n}\, dl = \int_T \nabla \boldsymbol{\mathcal{F}}(\boldsymbol{u}^{h,k})\, d\Omega \\ &= \int_{T_s} \boldsymbol{\lambda}(\boldsymbol{u}^{h,k}) \cdot \nabla \boldsymbol{u}^{h,k}\, dx\, dy \end{aligned} \tag{3}$$

where we have used the expression for the Jacobian of the flux $\boldsymbol{\mathcal{F}}(u)$ in (1),

$$\boldsymbol{\lambda}(\boldsymbol{u}) = \frac{\partial \boldsymbol{\mathcal{F}}(\boldsymbol{u})}{\partial \boldsymbol{u}} = \left(\frac{\partial \mathbf{f}(\boldsymbol{u})}{\partial \boldsymbol{u}}, \frac{\partial \mathbf{g}(\boldsymbol{u})}{\partial \boldsymbol{u}} \right) \tag{4}$$

We can also construct the residual over each P_1 subelement of $\mathcal{T}^{h,k}$

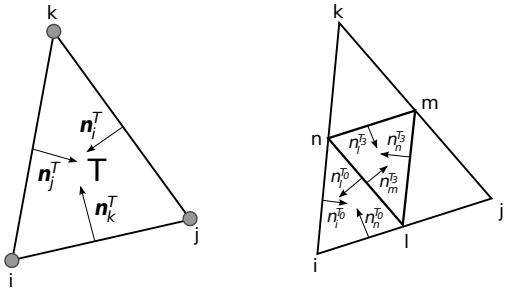

Figure 3: Definition of the normal vectors $\vec{n}_i$ in P_1 and P_2 elements

$$\begin{aligned} \boldsymbol{\phi}^{T_s} &= \oint_{\partial T_s} \boldsymbol{\mathcal{F}}(\boldsymbol{u}^{h,k}) \cdot \boldsymbol{n}\, dl = \int_{T_s} \boldsymbol{\lambda}(\boldsymbol{u}^{h,k}) \cdot \nabla \boldsymbol{u}^{h,k}\, dx\, dy \\ &= \boldsymbol{\lambda}^* \cdot \int_{T_s} \nabla \boldsymbol{u}^{h,k}\, dx\, dy \end{aligned} \tag{5}$$

with $\boldsymbol{\lambda}^*$ a properly defined local average of $\boldsymbol{\lambda}(\boldsymbol{u})$ over the sub–triangle such that conservation is preserved (so called Roe–average).

For a given P_1 triangle we consider the set of normal vectors $\{\boldsymbol{n}_j\}_{j \in T}$, defined by the inward normals to the edges of T facing each node $j \in T$ (see figure 3 left). The norm of $\boldsymbol{n}_i$ is equal to the length of the edge. In the general P_k case, with $k > 1$, we will assume that the $\boldsymbol{n}_j$'s are defined on the local P_1 sub-elements $T_s \in T$, as shown on figure 3 (right) for $k = 2$. For future use we define the upwind parameter

$$k_j = \frac{1}{2} \boldsymbol{\lambda}^* \cdot \boldsymbol{n}_j \quad \text{implying} \quad \sum_{i \in T_s} k_i = 0 \tag{6}$$

3.1 Residual distribution schemes on P_1 elements

In the case of P_1 elements it is easy to verify that the cell residual can be expressed using the upwind parameters k_i if a conservative linearization has been used:

$$\boldsymbol{\phi}^T = \oint_{\partial T} \boldsymbol{\mathcal{F}}(\boldsymbol{u}^{h,1}) \cdot \boldsymbol{n}\, dl = \int_T \nabla \boldsymbol{\mathcal{F}}(\boldsymbol{u}^{h,1})\, d\Omega = \sum_{i \in T} k_i u_i$$

The basic idea then consists of distributing fractions of this cell residual to the three nodes of the element T. The fraction sent to node $i \in T$ is denoted $\boldsymbol{\phi}_i$ and we require

$$\sum_{i \in T} \boldsymbol{\phi}_i = \boldsymbol{\phi}^T$$

This requirement can be written in terms of *distribution coefficients* β_i which for consistency sum to unity

$$\sum_{i \in T} \beta_i = 1, \qquad \beta_i = \frac{\boldsymbol{\phi}_i}{\boldsymbol{\phi}^T}$$

After assembling all contributions in the nodes, the nodal equation for node i reads, with $\mathcal{D}_i$ the set of all triangles that share node i.

$$\sum_{T \in \mathcal{D}_i} \boldsymbol{\phi}_i = 0$$

Since the distribution is restricted to the nodes of the triangle itself, the stencil of the scheme remains compact. This equation can be solved by embedding in a pseudo–time interation, i.e. by finding a steady state solution of

$$|S_i| \frac{d\boldsymbol{u}_i}{dt} + \sum_{T \in \mathcal{D}_i} \boldsymbol{\phi}_i^T = 0, \tag{7}$$

where $|S_i|$ is the area of median dual cell.

3.2 Residual distribution schemes on P_k elements

Consider now the extension of multidimensional upwind ($\mathcal{MU}$) schemes to high order P_k elements. First, we compute the residual on each sub-element :

$$\boldsymbol{\phi}^{T_s} = \int_{T_s} \nabla \boldsymbol{\mathcal{F}}(\boldsymbol{u}^{h,k})\, d\Omega = \oint_{\partial T_s} \boldsymbol{\mathcal{F}}(u^{h,k}) \cdot \hat{n}\, dl \tag{8}$$

Then, this residual is distributed to the 3 nodes of the sub-element, using any of the distribution schemes developed for P_1 triangles.

The linearization used to compute the parameters k_i can be based on any linearized state over the subtriangle, without affecting accuracy nor conservation. After assembling all contributions for a given node, we end up with the following system of nodal equations to solve:

$$\sum_{T_s,\, i \in T_s} \boldsymbol{\phi}_i^{T_s} = 0 \tag{9}$$

4 Conclusion

This work focused on curved boundary representation for high–order Residual Distribution schemes based on sub-parametric and isoparametric transformations of the curved element to a Cartesian parent element. Numerical experiments have shown that the curved boundary representation is needed to achieve high–order of accuracy for a P_2 and P_3 representation of the solution. This discretization yields a rate of convergence $\mathcal{O}(h^{k+1})$, where k is the order of the approximating polynomial. At the same time, element curvature is important to prevent unphysical behavior such as pressure oscillations or generation of spurious entropy.

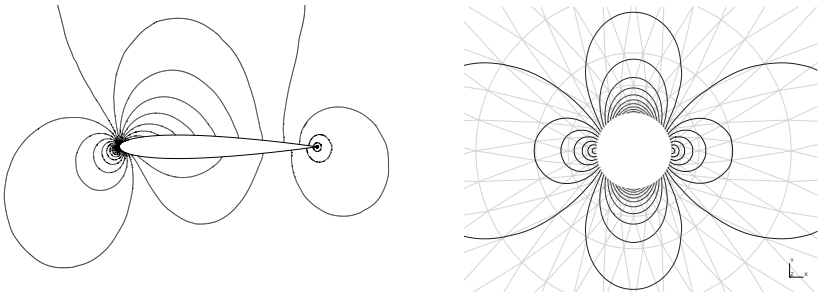

(a) Mach number isolines, P2 triangles, NACA0012, $M_\infty = 0.5$, $\alpha = 2^\circ$.

(b) Mach number isolines, P3 triangles, $M_\infty = 0.38$

Figure 4: Example simulations: subsonic flow around a NACA profile and a cylinder

References

[1] Deconinck H. and R. Abgrall. Introduction to residual distribution methods. *VKI Lecture Series 2006-01, Comput. Fluid Dynam.*, 2005.

[2] M. Ricchiuto. *Construction and analysis of compact residual discretizations for conservation laws on unstructured meshes*. PhD thesis, Von Karman Institute for Fluid Dynamics and Université Libre de Bruxelles, Faculté des Sciences Appliquées, 2005.

[3] E. van der Weide. *Compressible Flow Simulation on Unstructured Grids Using Multi–dimensional Upwind Schemes*. PhD thesis, Von Karman Institute for Fluid Dynamics and TU Delft, 1998.

[4] M. Ricchiuto, N. Villedieu, R. Abgrall, and Deconinck H. High–order residual distribution schemes: discontinuity capturing crosswind and extension to advection-diffusion. *VKI Lecture Series 2006-01, Comput. Fluid Dynam.*, 2005.

[5] L. Krivodonova and M. Berger. High–order accurate implementation of solid wall boundary conditions in curved geometries. *J. Comput. Phys.*, 221:492–512, 2006.

[6] M. Hubbard. Discontinuous fluctuation distribution. *J. Comp. Phys.*, 227(24):10125–10147, 2008.

TRANSITIONAL FLOWS

Doctoral Project Summary

Analysis of Transition to Turbulence of a Supersonic Flow over a Rigid Surface

Henny Bottini*

Supervisor: Prof. Guillermo Paniagua

von Karman Institute for Fluid Dynamics, Rhode-Saint-Genèse, 1640, Belgium

Promoter: Prof. Gerard Degrez

Université Libre de Bruxelles, Bruxelles, B 1050, Belgium

Abstract

Here are presented, first, test-article design and wind tunnel characterization for a test campaign aimed at detecting and tracking boundary–layer turbulence onset. Then a new approach, based on irreversible Thermodynamics, to investigate boundary–layer instability and turbulence onset. These experimental and theoretical researches are carried out in the frame of the LAPCAT2 project, related to the intake aerodynamics of a reusable hypersonic vehicle.

1 Introduction

The physics of turbulence onset within an initially laminar flow is not yet fully understood. The models so far proposed have often limits or heavy clouding assumptions. Furthermore, experimental evidences require often special facilities whose design and operation can be cumbersome. Direct Navier-Stokes simulations are still limited by huge computing requirements to the treatment of low-Re_∞ flows, and in some cases with restrictive assumptions.

An unprecedented approach has been developed based on the work of Glansdorff and Prigogine on irreversible Thermodynamics [1]. Section 3 of the present work explains the derivation from a more general theory of instability, which is also introduced in its essence.

The following Section 2 illustrates present author's contribution to the set up of some experimental tools to be used for experiments on transition detection. This comprises the design of the test article, the estimation of wind tunnel performance and the fitting of instrumentation in its test section.

2 Experimental Work

The experimental part of this PhD program comprises the setup and the post processing of experiments aimed at the visualization, tracking, and characterization

* PhD Candidate, Turbomachinery and Propulsion department, Chaussée de Waterloo 72, bottini@vki.ac.be

of turbulence onset over a flat plate in a freestream whose M_∞ will be in the range [1.1÷2.7].
These experiments will be carried on in the VKI CT2 facility equipped with a new nozzle/test-section designed specifically for transition experiments. This nozzle/test-section features a 2D geometry comprised of two lateral vertical fixed walls, and, perpendicular to them, two flat, movable walls (ramps) whose angle variation assures the selected M_∞ range. The facility will allow, along with thin-film measurements, Schlieren visualization, PSP and IR-camera measurements.

2.1.1 Facility Performance Estimation & Instrumentation

2.1.1.1 Estimation of the Re_∞ value in the Test Section

The CT2 facility allows different values of p_0 and different values of T_0, both determinant for the test Re_∞ and duration. Therefore, given a range of M_∞, it was in need to estimate those possible values of Re_∞ corresponding to test durations long enough to allow all the measurements to be completed. This estimation has required the calculation of the flow through the nozzle/test-section.
It turned out that the values of the possible pairs Re_∞/τ_{test} are practically the same throughout the M_∞ range to be considered and are illustrated by the following picture fro the M_∞-2 case:

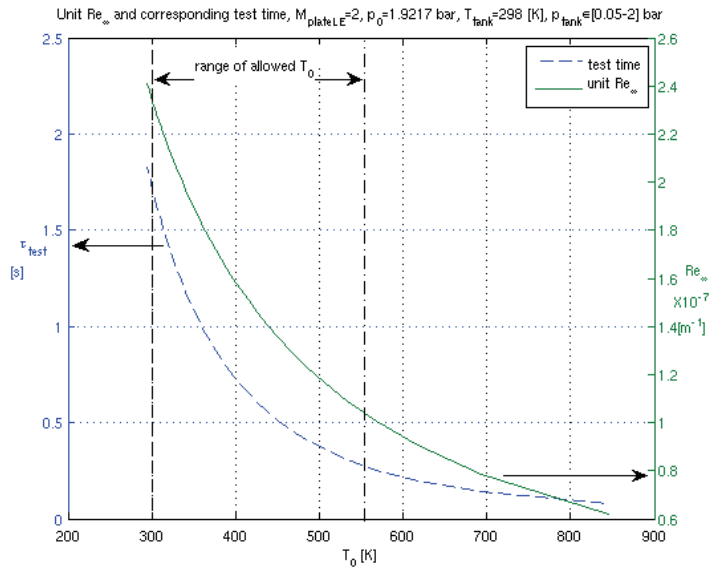

Fig. 1: Unit Re_∞ and relative test time vs. facility variable T_0 (M_∞=2 indicative for the entire M_∞ range of the experiments)

These values of unit Re_∞ will provide meaningful dynamic similarity between the wind tunnel flow and the real-flight flow along those parts of the LAPCAT2 M_∞-8 vehicle along which transition is expected. Finally, the corresponding test times do not pose any problem for measurements and data acquisition.

2.1.1.2 Test-Section Instrumentation Fitting

To fulfill the need of measuring the pressure evolution along the nozzle/test-section, arrays of pressure taps will be drilled on the movable nozzle ramps. However, these taps when flown above may cause acoustic tones that can seriously alter the natural transition process along the plate. This issue led to an estimation of a taps location from where they could not radiate noise directly onto the plate, whatever the walls angles—i.e. the M_∞ value. This estimation was made assuming at the tap location the M_∞ at the plate leading edge. This simplifies the mathematical treatment and should result in a conservative estimation. The result is in the plot below and shows that the constraint is set by the smallest nozzle-ramp angle (0°). This is expectable because, as this angle decreases, the ramp and the noise sources on it get more and more parallel to the plate on the nozzle centerline. As a result, and considering the Mach-angle values for each M_∞ of the range, the perturbation originated on the ramp would invest a larger and larger part of the plate.
In the end, the first tap in the row should have an axial position at least 27 centimeter behind the plate leading edge to avoid noise radiated directly from the ramp onto the plate.

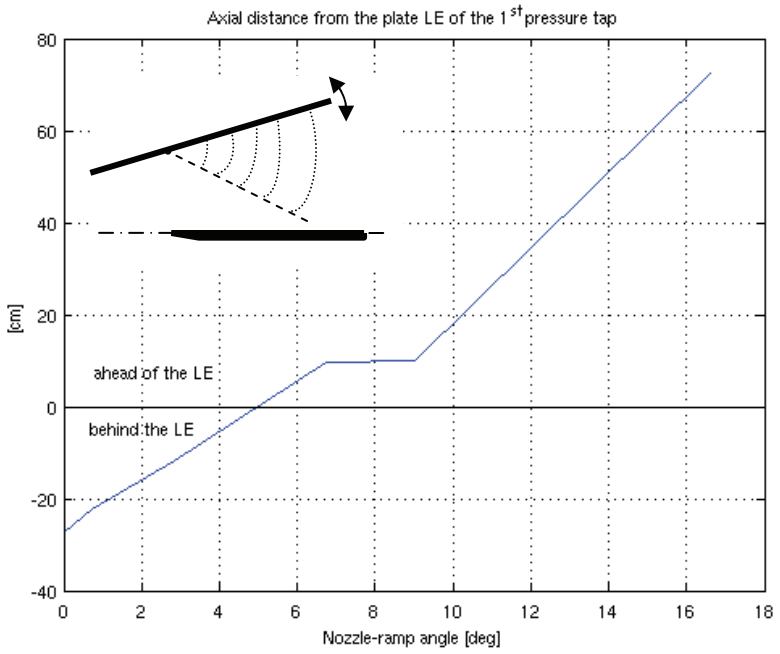

Fig. 2: First-tap axial distance from the plate LE versus the ramps divergence-angles

2.1.2 Design of the Test Article

The transition experiments will be specific for the last part of the transition process; after the growth of instabilities within the laminar boundary layer. These experiments will focus on the transonic/supersonic regime, for which more experimental data are still wanted.
To avoid un-wanted complicacies, and to withstand with the goal of basic-flow study, a simple flat plate has been chosen as surface flown. Measurements will be taken over

the plate in clean configuration, and downstream of a single roughness element placed on the plate centreline.
The sensor chosen to be on the test article surface is the thin-film (shortly TF), and thirty of them will be placed on the plate; this maximum is imposed by the limits of the selected DAS model.
The limit in the number of sensors implies an educated arrangement of them on the plate, because, evidently, they will not be enough to cover uniformly the entire plate surface (the ideal arrangement). This arrangement, then, shall fit both the clean and single-roughness configurations of the plate.
If TS-transition is assumed, instabilities develop and grow from the leading edge up to x_t , the distance flown to reach the transition Reynolds number, $Re_{tr}=u_\infty \cdot x_t / \nu$. within this zone turbulence does not yet appear. In case of non-TS (bypass) transition, instead, turbulence, in principle, may appear even at the leading edge. Clearly, then, in the TS-transition case the sensors should be located starting from the transition point, while, in the bypass-transition case, starting from the leading edge. However this latter case may not be covered in this test-campaign. In fact, as will be presented in the following, the TFs greatest part will have to be placed behind the roughness location, so rather downstream of the plate leading edge.
So in case of non-induced transition, the zone of interest starts at x_t and then ends at the spanwise line (strip) where the entire wall is covered by turbulent flow. So one may want the great part of TFs in this region, and there properly arranged to cover as much surface as possible.
If the single-roughness induces transition, instead, two possible situations arise.
In case of roughness maximum effectiveness, turbulence should spread downstream the roughness at the very roughness location, whilst, be the roughness not maximally effective, turbulence should spread somewhere more downstream. Turbulence onset widens the roughness wake in a characteristic shape called “turbulent wedge”. Thus, in both cases, one wants the great part of TFs on the surface downstream of and aligned to the roughness position and, again, properly arranged there as to cover the greatest area possible.
In conclusion, to locate the TFs one has to estimate x_t and the geometry and dimensions of the roughness wake. Both these estimations in the selected range of M_∞ have been done based on literature data [3, 4]. The resulting TFs arrangement is shown in
:

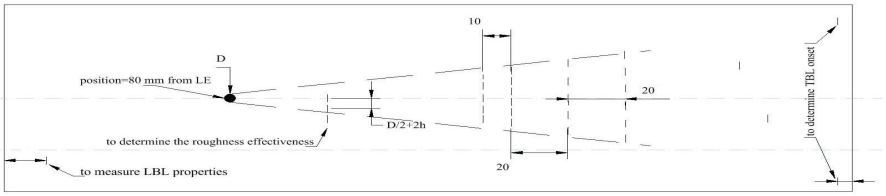

Fig. 3: Thin-films arrangements on the flat-plate to be used as test article

Here one sees that the final arrangement is heavily shaped by the need of covering the wake of the roughness, but, according to the estimations, the position of the four

larger rows of TFs should still be such to allow meaningful measurements in the clean-plate case.
Figure 3 also shows how some TFs are used for purposes other than transition detection and tracking. One TF is located just downstream of the leading edge to detect laminar-boundary-layer properties to be used as reference for turbulence detection. Three TFs, then, are located downstream and sideways from the centreline of the roughness to study its wake spread-angle. (This angle can be regarded as a measure of the roughness effectiveness in tripping turbulence, and roughness effectiveness is a property these experiments are requested to evaluate.) Then two TFs are located at the end of the plate, one close to each corner to measure the properties of the possibly fully-developed turbulent boundary layer there. The remaining two TFs have been located between the last row and the last pair as to give a minimal measurement capability also within that long part of the plate otherwise completely uncovered.

3 Analytical Work: the G-P Inequality

Following Glansdorff and Prigogine [1], thermodynamic systems close to the equilibrium state exhibit destruction of structures. Beyond the equilibrium and beyond the thermodynamic stability limit the creation of new structures is the main feature, accomplished by non-linear kinetic mechanisms. A new structure is seeded by a fluctuation amplified by the response of the thermodynamic system. A typical example of this situation is transition from laminar to turbulent state.
Classic Thermodynamics deals essentially with systems in equilibrium, thus it can be regarded only as a theory of structures 'destruction. Glansdorff and Prigogine developed a method based on a generalized Thermodynamics that includes a macroscopic theory of fluctuations. This method extends the range of irreversible Thermodynamics up to the inclusion of phenomena beyond the equilibrium and featuring fluctuations and non-linear interactions. It is based on the concept of "entropy-curvature" evolution, $\mathrm{d}(\delta^2 S)$, and is called *the general criterion of evolution of a fluid-thermodynamic system* (hereinafter referred to as the Glansdorff-Prigogine, i.e. G-P, inequality). It is mathematically expressed as*:*

$$\frac{\rho}{T}\sum_i v_i v_{i,i}\partial_t v_i - \underline{\nabla}\cdot(\rho e\underline{v})\partial_t\left(T^{-1}\right) - \frac{\rho}{T}F_i\partial_t v_i + \frac{P_{ij,j}}{T}\partial_t v_i - \underline{\nabla}\cdot\underline{\underline{W}}\partial_t\left(T^{-1}\right) - P_{ij}v_{i,j}\partial_t\left(T^{-1}\right) \le 0 \qquad (1)$$

The equality sign is satisfied when the system is in a stationary state of non-equilibrium (entropy production constant). The "lower than" sign is obeyed when the system state evolves in time, i.e. the non-equilibrium state is not anymore steady.
From the stability point of view, Eq.1 expresses that a perturbation satisfying the inequality will grow within the system to make it unstable. Conversely, if a perturbation does not satisfy the inequality, then its time evolution is not physically possible, therefore must be damped, and the system remains stable.
In the present work this general criterion has been specialized to the study of boundary-layer transition for the general case of a non-reactive, compressible flow.
The approach is based on the following assumptions:

- *The system is the boundary layer*. This reduction has been pursued because the sole boundary layer seemed to conform to the definition of system given by Glansdorff and Prigogine and not the entire flow field. In fact, the "new structures", i.e. the turbulent eddies, engendered by

fluctuations within the boundary layer, only appear and stay within the boundary layer and not in the entire flow field above the surface

- *The system stationary state of non-equilibrium is the stable laminar state*

- *The system unsteady state of non-equilibrium is the unstable laminar state*

The goal is to use the G-P inequality at first to study the stability of the laminar boundary layer and then, if it proves worthwhile, to try to extend its use for the ensuing, more-awkward part of the transition process.
The specialization of the G-P inequality to boundary layer studies has been accomplished including Eq.1 into the set of the Fluid Dynamics conservation equations and reducing it to its boundary-layer form by the customary Prandtl's treatment.
The first expression of the G-P inequality so obtained, and presented last year, has been found wanting modifications inspired by the derivation of other well-established instability-prediction methods. So it has been averaged over the boundary layer thickness with the aim to give a unique value for a given *x* location. Then this revised expression has been included in a code and run to predict stability behaviors for which experimental and theoretical results were available or producible. Its predictions always resulted erroneous.
This led to check anew the entire derivation process and its implementation, and a mistake (or a mistyping) in the original expression in [1] was found. Moreover, the present author found the need to include in the set of equations accounted for the derivation also the equations for the fluctuations, and not only those for the mean flow. In the end a new expression of the G-P inequality was obtained in what resulted once again a very short form:

$$-\left\{\frac{\partial}{\partial z}\left[k\frac{\partial\left(T+T'\right)}{\partial z}\right]\right\}\frac{\partial_t T'}{T_i}\le 0 \qquad (2)$$

with the index '*i*' meaning 'instantaneous', i.e. fluctuating quantity plus the mean quantity.
If one considers the energy equation for the instantaneous quantities, Eq. 2 can be put in these other terms:

$$-\left\{\rho_i u_i\frac{\partial e_i}{\partial x}+\rho_i w_i\frac{\partial e_i}{\partial z}+\rho_i\partial_t e'+p_i\frac{\partial w_i}{\partial z}-\mu\left(\frac{\partial u_i}{\partial z}\right)^2\right\}\frac{\partial_t T'}{T_i}\le 0 \qquad (3)$$

At this point, the G-P inequality needs a model for the fluctuations to be evaluated, but the customary complex notation for a sinusoidal wave may not be the right one. This is because complex numbers do not feature an order ($z_1>z_2$ cannot in principle be written), whilst, instead, Eq. 2 (or Eq. 3) is an inequality, so involving order between its terms. Thus an all-real version of the customary model of a space-evolving fluctuation has been derived from the complex one as:

$$q'(x,z,t)=\left|q(x,z)\right|\cos\left[\alpha_r x-\omega t+\phi(z)\right]$$

where $\phi(z)$ is the phase shift of the velocity fluctuations, which, in turn, according to experimental evidence [2], may be cast as a *Heaviside step function*:

$$\phi = \pi \cdot s(z - z^*) = \begin{Bmatrix} 0 \text{ if } z < z^* \\ \frac{\pi}{2} \text{ if } z = z^* \\ \pi \text{ if } z > z^* \end{Bmatrix}$$

with z^* the location where the amplitude of the velocity fluctuations is nil.
Eq. 2 is the version of the G-P inequality currently under test against linear stability results. For this purpose a linear stability code is used to calculate fluctuations trends corresponding to the stable, neutral, and unstable conditions of a low-speed boundary-layer flow. This flow is a test case whose stability has been experimentally studied and the resulting detailed stability curve is available in literature. The fluctuations trends will be input in the G-P inequality and the resulting prediction will be evaluated against the experimental results. (The correctness of the linear-stability code is also checked against these experimental results, complemented by calculations made by the experiments authors.)

4 Conclusions

The experimental campaign, which is part of the present PhD program, will exploit a "quiet", supersonic-flow-specific design for the wind tunnel nozzle/test-section. This should assure high-quality experimental results. Even not so, at least in the case of the roughness-induced transition, the "quietness" requirements are believed to be not as strict as for the natural-transition case, so the campaign results should still be valuable.
Results soundness shall also be assured by the proposed measurement techniques. Thin-films have been successfully used to track turbulent spots evolution, while IR-cameras have been used successfully to characterize and measure roughness-induced transition. The VKI has an established know-how in IR visualization and measurements applied to hypersonic transition and in TF measurements of turbomachinery flows.
The analytical part of this work, the derivation and utilization of the G-P inequality, may result in an entirely new approach to the problem of stability and transition to turbulence. The theory it is derived from can give hope of solid physical grounds, while the plain and customary way by which it is adapted to aerodynamic studies should guard from inconsistencies and mistakes in its final form. What is left then it is only the validation with proven, reliable results. This, however, may not be easy.
In fact, the dearth of detailed literature data or the incapability of producing needed theoretical results may be serious obstacles in the process of verifying and validate the G-P inequality. And this would be true especially for supersonic velocities, for which, in general, data scarcity is a well-known, old issue.

Acknowledgments

The authors want to thank the European Space Research and Technology Center (ESTEC) for the funding of this doctoral research in the frame of the LAPCAT2 EU/ESA Project, coordinated by Dr. J. Steelant from ESA\ESTEC.

References

[1] P. Glansdorff, I Prigogine . Structure Stabilité et Fluctuations. Masson et Cie Editeurs, Paris 1971 (in French)

[2] G. B. Schubauer, H. K Skramstad. Laminar-boundary-layer oscillations and transition on a flat plate. NACA Report No. 909, 1943

[3] K. F. Stetson. The second joint Europe/US short Course in Hypersonics. US Air Force Academy, Colorado Springs, USA 1989

[4] L. M. Mack. Linear Stability Theory and the Problem of Supersonic Boundary-Layer Transition. AIAA Journal, vol. 13, no.3 1975

[5] I. Wygnanski, M. Sokolov, D Friedman. On a turbulent 'spot' in a laminar boundary layer. J. Fluid Mech. vol. 78, pp.785-819, 1976

[6] G. B. Schubauer, P. F. Klebanoff. Contributions on the mechanism of boundary-layer transition. NACA TN-3489, 1955

[7] R. Narasimha, C. Subramanian, M. A. Badry Narayanan.. AIAA Journal vol 22, no 6, pp. 837-839, 1984

[8] J. W. Elder. An experimental investigation of turbulent spots and breakdown to turbulence. J. Fluid Mech. vol 9, pp.235-24, 1960

[9] L. Krishnan, N. D. Sandham. Effect of Mach number on the structure of turbulent spots. J. Fluid Mech. (2006), vol. 566, pp.225-234

Doctoral Project Summary

Characterization of Hypersonic Boundary Layer Transition Induced by Isolated Roughness

Davide Masutti*

Supervisor: Olivier Chazot†
von Karman Institute for Fluid Dynamics, Rhode-Saint-Genèse, 1640, Belgium
Promoter: Fulvio Scarano‡
Delft University of Technology, Delft, 2629, The Netherlands

September 1, 2010

Abstract

The research aims to define and understand the physics of the boundary layer transition mechanism, induced by an isolated roughness, in a hypersonic flow. Two of the many parameters that influence transition are surface roughness and freestream fluctuations. Experiments were performed in the VKI H3 Mach 6 Wind Tunnel and in the Boeing/AFOSR Mach 6 Quiet Tunnel with a flat plate model equipped with a 3D isolated roughness element. The quiet tunnel is unique in that, it can provide freestream fluctuations that are comparable to flight because its nozzle wall boundary layer remains laminar. Infrared thermography and temperature sensitive paint were used to observe the state of the boundary layer. Different solutions were used to infer the status of the boundary layer and the onset of transition between the two different facilities. A comparison between a ranging Reynolds number and quiet/noisy flow conditions have been performed.

1 Introduction

Laminar-turbulent transition in hypersonic regime is a critical design issue for re-entry vehicles because of its strong impact on heat flux distribution on the vehicle itself. The main reason that transition must be considered in defining both the vehicle and its trajectory is that transitional and turbulent heating can generate local heat flux levels that are significantly greater than the levels of typical laminar flow heating conditions. Boundary layer transition to turbulent flow along a re-entry trajectory is extremely difficult to predict and remains a major issue for the thermal protection system design.

*PhD Candidate, Aeronautics and Aerospace Department, Chaussée de Waterloo 72, masutti@vki.ac.be
†Associate Professor, Aeronautics and Aerospace Dep., Chaussée de Waterloo 72, chazot@vki.ac.be
‡Professor, Department of Aerospace Engineering, Kluyverweg 2, F.Scarano@TUDelft.nl

Databases, transition criteria and modeling have been developed in large number and the results obtained can help to address some cases of transition phenomena [1, 2].

However, when one considers roughness induced transition (RIT) by an isolated 3D element, in hypersonic flow the situation remain difficult to predict. Moreover 3D RIT can occur in a variety of occasions during a re-entry flight and dedicated studies on this topic appear fully relevant in the context of space exploration.

Yet the physics of the boundary layer receptivity and the process associated with the growth of the disturbances are still poorly understood. These factors highlight the need of experimental data to validate against with the results coming from the computational fluid dynamics (CFD). Unfortunately ground testing turns out to be not an easy task, especially when the wind tunnel characteristics have to match flight conditions. Several investigations have been carried out in quiet and noisy flows at various hypersonic freestream conditions and in different wind tunnels [3, 4, 5, 6]. All these experimental data point out the lack of theoretical or semi-empirical models that can perform extrapolation from ground to flight conditions.

In this frame, ESA started the EXPERT (European eXPErimental Reentry Testbed) program in 2000 [7]. The aim of the EXPERT program is to provide an opportunity to the European scientific community to propose and perform in-flight experiments in order to obtain aero-thermodynamic data for the validation of numerical models and of ground-to-flight extrapolation methodologies. For this purpose, a re-entry vehicle has been designed. The EXPERT vehicle is equipped with different instrumentations and flight experiments provided by several European research centers and universities. In particular for the boundary layer transition investigation, the EXPERT vehicle is equipped with two instrumentations, the payload 4 (PL4) and the payload 5 (PL5). The first one concerns the natural transition of the boundary layer, the latter aims to study the roughness induced transition and is provided by the von Karman Institute (VKI)[1].

The research topic aims to investigate the flow physics of a laminar to turbulent transition induced by a 3D roughness in hypersonic regime. This research activity meets different challenges that need to be address to be properly carried out.

2 Experimental Setup

2.1 Model and Roughness Configuration

A flat plate has bee used to perform the studies on the hypersonic induced boundary layer transition. The plate is 100 mm wide, 210 mm long, 16 mm thick and with a 0.5mm radius round leading edge. The flat plate model is made of steel with a Plexiglas insert as shown in figure 1(a). The Plexiglas insert was provided to make infrared thermography measurements in the VKI test facility. The flat plate is equipped with an isolated roughness element, ramp shape, with a height (h) of 2mm, pictured in figure 1(c). The roughness element was placed 60 mm from the leading edge of the flat plate (Fig. 1(b)).

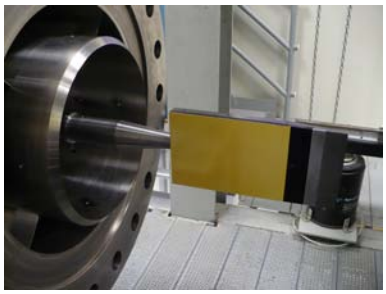

(a) The flat plate model



(b) Close-up of the flat plate with 3D isolated roughness element



(c) Isolated roughness element geometry

Figure 1: Model setup, prior to installation in the BAM6QT Wind Tunnel

2.2 Test Facilities

The VKI H3 test facility is a blow-down type wind tunnel figure 2. It can provide a uniform axisymmetric jet with a diameter of 12cm at a high speed at Mach 6. Dried air is supplied from a 40bar reservoir, which can provide stagnation pressures ranging from 7 to 35bar. Air is heated up to a total temperature of 500K to avoid condensation in the test section. The Reynolds number of the flow can be varied between $3 \cdot 10^6$ and $30 \cdot 10^6 m^{-1}$.

The wind tunnel model to be tested is kept retracted before the test to avoid blockage of the wind tunnel and also to avoid excessive heating of the model during start-up. The test chamber is vacuumed prior to the test using a supersonic ejector. The model is injected into the flow field with a model injection arm, once the Mach 6 flow is fully established in the test chamber. The pressure fluctuation in a conventional wind tunnel like the VKI H3 are on the order of 2-3%. The three standard VKI H3 conditions are summarized in table 1.

Table 1: VKI H3 wind tunnel conditions

	Mach	p_0, bar	T_0, K	Re, 1/m	Flow
Low Re	6	10	500	9.2×10^6	noisy
Med Re	6	20	500	18×10^6	noisy
High Re	6	30	500	26×10^6	noisy

The Purdue's Boeing/AFOSR Mach 6 Quiet Tunnel (BAM6QT) is a blowdown Ludweig tube capable of operating at stagnation pressures up to 20bar. It has a 38 m long, 450mm diameter driver tube with a 2m long nozzle section. The nozzle has a minimum diameter of 31mm at the throat and diverges to a final diameter of 242mm. The area expansion ratio sets the flow velocity to Mach 6 speed. A 305mm diameter

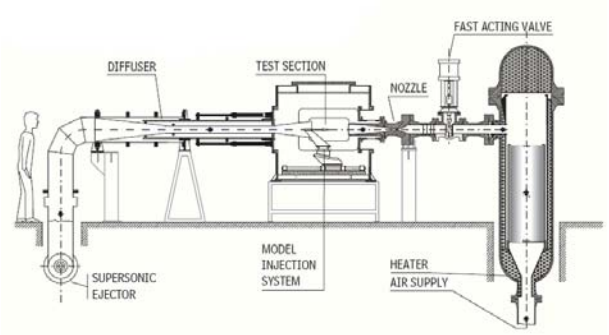

Figure 2: VKI H3 hypersonic wind tunnel schematics

diffuser section exists after the nozzle section. The facility also includes a 113m^3 vacuum tank. A section for the diaphragms, a large gate valve and 305mm piping further lead into the vacuum tank. The setup allows a runtime of up to 8 secs. The BAM6QT is currently the only wind tunnel in that can provide quiet flow at Mach 6 [8] with a pressure fluctuation around 0.07%, actually comparable to the in-flight turbulence level. The wind tunnel is capable also to change between quite flow conditions and noisy flow conditions for a restricted range of pressures (up to 11bar).

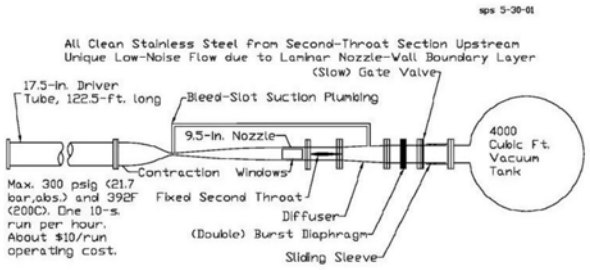

Figure 3: Boeing/AFOSR Mach 6 quite wind tunnel schematics

Table 2: Purdue BAM6QT conditions

	Mach	p_0, bar	T_0, K	Re, 1/m	Flow
Case 1	6	2.8	430	3.1×10^6	quiet/noisy
Case 2	6	5.5	430	6.1×10^6	quiet/noisy
Case 3	6	8.5	430	9.4×10^6	quiet/noisy
Case 4	6	10.5	430	12×10^6	quiet/noisy
Case 5	6	14.5	430	16×10^6	noisy
Case 6	6	17	430	19×10^6	noisy

2.3 Infrared Thermography Technique

Infrared Thermography is used to provide a quantitative measure of heat transfer and is useful for quantifying increased surface heating from laminar-to-turbulent transition. The Infrared Thermocamera measures and displays the emitted Infrared radiation from any object. Since the radiation is a function of the object surface temperature, this makes possible to compute accurately this temperature. However, the radiation measured by the camera is also a function of its emissivity. Moreover, radiation from the object and the reflected ambient radiation are influenced by the absorption in the atmosphere and in any external optics it passes through [9]. The Infrared Thermography is a very suitable technique to study high-speed aerothermodynamics and it is used very often on the study of atmospheric entry problems [10].



Figure 4: Infrared Camera and germanium window setup for VKI H3 Wind Tunnel

To capture the wall temperature evolution on the model, a FLIR ThermaCAM SC-3000 Infrared Camera has been used. The camera records a 320 x 240 pixels image at a max sampling frequency of 50Hz. The detector of the camera is cooled internally to 70K by a Stirling cycle. To assure a high IR transmissivity between the model surface and the IR camera, a germanium optical window is used. Despite this high transmissivity, some residual reflections are present on the germanium window. This effect is mitigated during the data reduction using a background subtraction procedure. Using the optical setup, a calibration was conducted on a black body to relate the measured IR intensity to the model surface temperature.

To investigate the laminar-to-turbulent boundary layer transition of the flow on the flat plate model by means of the Infrared Thermography, the non-dimensional Stanton number is introduced. This non-dimensional Stanton number is the ratio between the heat transferred to the wall over the heat that is convected through the boundary layer. In this study, a modified version of the Stanton number by Santarelli and Charbonnier [11] is used. In this new formulation (Eq. 1) the boundary layer edge quantities are substituted with the free stream quantities and the adiabatic wall temperature T_{aw} has been replaced with the stagnation temperature T_0.

$$St_M = \frac{\dot{q}_w}{\rho_\infty U_\infty c_P \left(T_W - T_0\right)} \tag{1}$$

2.4 Temperature Sensitive Paint

Temperature sensitive paint (TSP) can be sprayed or painted onto the test models to provide a temperature distribution or flow visualization on the surface of the object. As compared to the other methods of temperature measurement, this method is cheaper and easier to use and can be implemented to obtain a global temperature distribution as opposed to measurements at discrete points. The paint contains luminophore molecules that absorb and emit radiation depending on their temperature. An external light source is needed to provide the excitation energy to the luminophore molecules (figure 5). The intensity of the radiation emitted decreases with increase in the temperature of the paint layer [12]. Usually an insulating layer is added beneath the layers of TSP to thermally insulate the TSP from heat conduction into the model. This heat could be caused by phenomena such as vortices that can increase heat transfer to the model. The thickness of the insulation layer and its uniformity are critical in deciding the resolution obtained from the TSP. TSP can be used to study transition due to the effect of increased heat transfer in the transition and turbulent regions in the boundary layer.

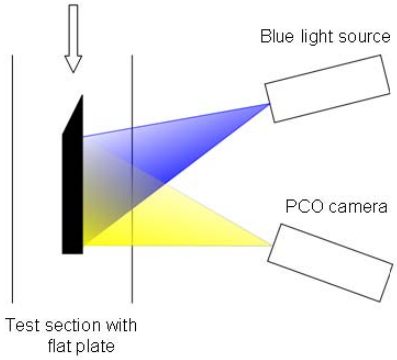

Figure 5: TSP setup schematic

To obtain the images for the TSP analysis a PCO 1600 camera was used, along with a light source. The camera was a 14bit CCD camera with a resolution of 1600 x 1200 pixels. The light source was a 100m diameter ISSI LM4 blue LED array and was used to excite the luminophore molecules, which emit a light in the orange region of the visible spectrum. In order to avoid picking up unnecessary light (such as reflected light from the window of the tunnel), the light was filtered through an orange filter. Theoretically none of the blue LED light is then picked up by the camera. The PCO camera was connected to a PC for storing and processing the images with the use of Camware software. The camera was capable of capturing images at a rate of 50 Hz.

3 Experimental Results

3.1 Effect of the Paint on Boundary Layer Transition

To determine the effect the step of paint on the flat plate model, several tests have been performed with no roughness elements. One concern with the use of the temperature sensitive paint is in fact the possible step created by the paint itself, that can affect the thin hypersonic boundary layer. In figure 1(b) it possible to observe the so called or-

ange peel finish on the flat plate. In figure 6 are now presented two images showing the temperature distribution on the flat plate for to different Reynolds numbers in the noisy flow of the BAM6QT. Figure 6(a) and figure 6(b) are referred to the lowest and the highest Reynolds numbers conditions available in the BAM6QT. To ensure the quality of the painted layer, both the test were done in noisy flow conditions. The resulted Stanton numbers computed streamwise on the flat plate are shown in figure 6(c) and 6(d). The results of these tests show no indications that the paint step is causing any strong disturbances in the boundary layer. The Stanton number distribution is decreasing in streamwise direction according with the thickening of the boundary layer and more over is following the theoretical Stanton number computed for a laminar boundary layer on a flat plate. The spanwise temperature profiles 6(e) and 6(f) show that the temperature is uniform across the span for different streamwise profiles, aside from the edge contamination. The edge contamination is caused by difference in pressure between the windward and the leeward side of the flat plate. This difference in pressure generates vortices (i.e. wing-tip vortices) that are affecting the temperature measurements on the edges of the flat plate. Higher the Reynolds number is (and the pressure), bigger is the energy of these vortices. The effect is clearly visible for the two Reynolds number 6(a) and 6(b).

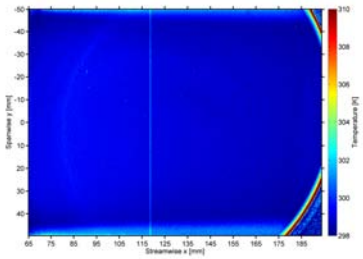

(a) Temperature distribution for BAM6QT, Re=3.1$\times$10^6/m, Noisy

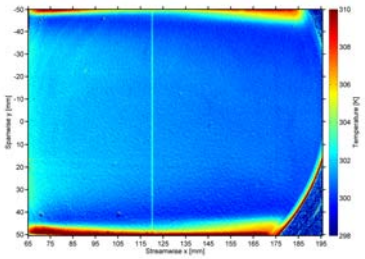

(b) Temperature distribution BAM6QT, Re=16$\times$10^6/m, Noisy

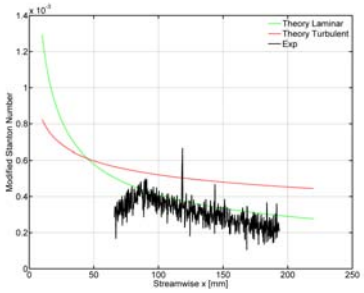

(c) Stanton number for BAM6QT Re=3.1$\times$10^6/m, Noisy

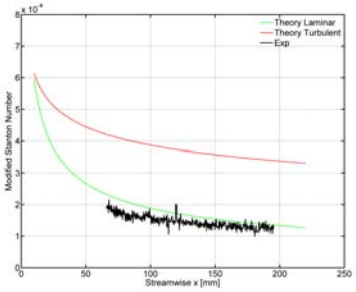

(d) Stanton number for BAM6QT Re=16$\times$10^6/m, Noisy

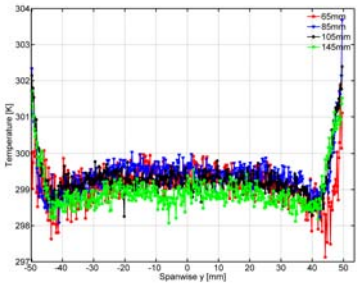

(e) Spanwise temperature distribution for BAM6QT Re=3.1$\times$10^6/m, Noisy

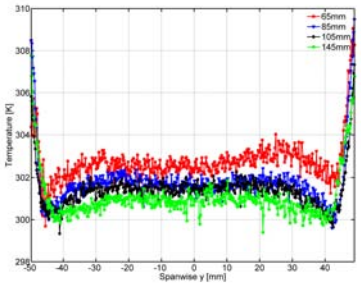

(f) Spanwise temperature distribution for BAM6QT Re=16$\times$10^6/m, Noisy

Figure 6: TSP on the smooth flat plate model at two different Reynolds numbers in the BAM6QT

3.2 Effect of Tunnel Noise at Re=9.4$\times$10^6/m

The results for a 2mm ramp with a Reynolds number of 9.4×10^6/m are shown in figure 7. In figure 7(a) we see the modified Stanton number distribution computed at the VKI with infrared thermography for a ramp of 0.8mm at a Reynolds number of 9.4×10^6/m. Figures 7(b) and 7(c) show the temperature distribution computed from the TSP on a flat plate with a 2mm ramp in the BAM6QT with quiet and noisy flow. Comparing figures 7(b) and 7(c) to the data gathered in the VKI H3 under the same Reynolds number (figure 7(a)), the Purdue BAM6QT noisy case shows a similar trend. Vortices generated on the flat plate by the isolated ramp are seen with the TSP and with the infrared thermography. Although it is not clear if there is a difference in the boundary layer state between noisy and quiet flow with the TSP, there is a clear effect of noise on the flow. In the quiet flow 7(b) the vortices produced by the ramp are less energetic and the trend suggest that they are damping down further downstream, on the contrary in noisy flow conditions 7(c) the vortices seem to interact with themselves to lead the boundary layer transition. Unfortunately the plate used in the BAM6QT was 210mm in length, opposed to the normal plate used in the VKI H3 of length 260mm. It could be argued that with a longer flat plate in the Purdue tunnel, a more pronounced spreading of the wake could be seen. Figure 7(d) shows the streamwise temperature profiles taken in the BAM6QT, both in the wake of the ramp and out of the wake where the boundary layer is supposed laminar. Comparing the out-of-wake temperature profiles between a quiet and a noisy run, the temperature, even if slightly different, tends to decrease along the flat plate, confirming the laminar status of the boundary layer. In the case of the in-wake profiles, the difference between the quiet and noisy flow is more appreciable. In the quiet flow the higher temperature, respect to the laminar flow, caused by the vortex heating tends to decrease, suggesting a damping of the vortices. On the contrary in noisy flow, the temperature of the wall behind the ramp is even higher and the bump in temperature is a clear sign of a strong interacting of the two contra-rotating vortices.

In an attempt to quantify the spreading of the wake, spanwise temperature profiles were taken. Figure 8 show the different profiles computed for quiet and noisy flow. The graphs show no significant spreading or contraction of the wake for both cases, although the difference in the temperatures between the quiet and noisy flow show the big influence of the noise of the facility.

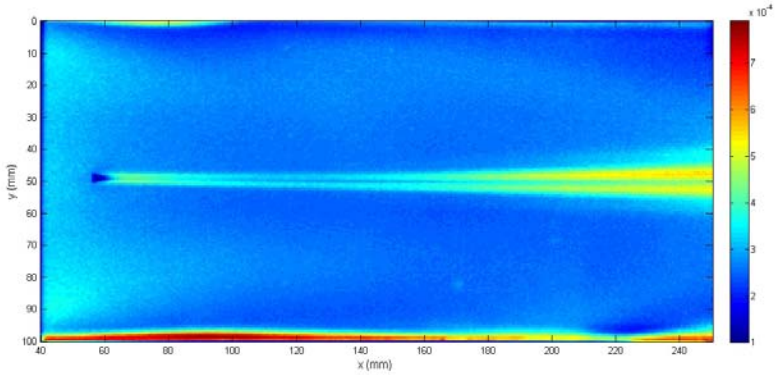

(a) Stanton number distribution for VKI, ramp h=0.8mm

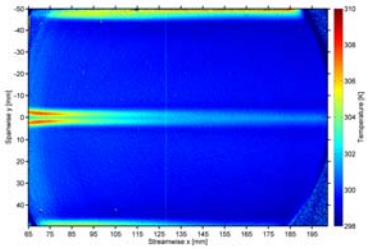

(b) Temperature distribution for BAM6QT, ramp h=2mm, quiet

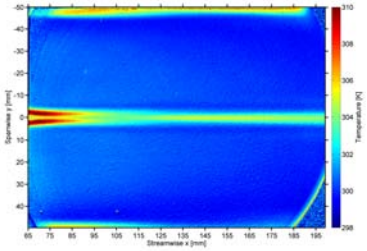

(c) Temperature distribution for BAM6QT, ramp h=2mm, noisy

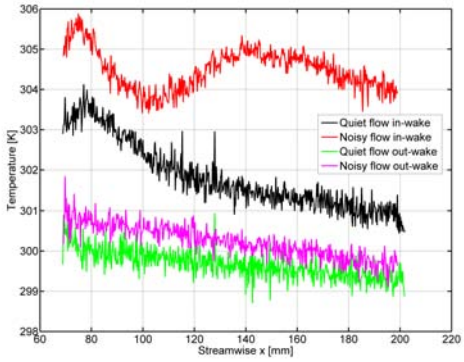

(d) Comparison streamwise temperature for BAM6QT

Figure 7: Comparison VKI-BAM6QT, Re=9.4$\times$10^6/m

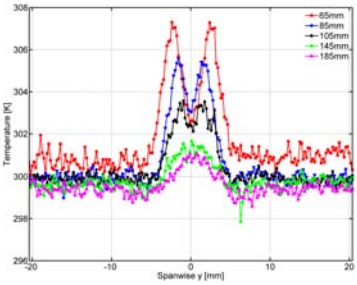

(a) Spanwise temperature profiles for BAM6QT, ramp h=2mm, quiet

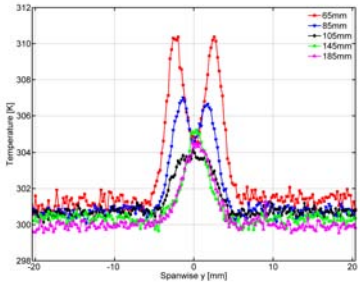

(b) Spanwise temperature profiles for BAM6QT, ramp h=2mm, noisy

Figure 8: Comparison of spanwise temperature profiles for BAM6QT, Re=9.4$\times 10^6$/m

3.3 Effect of Tunnel Noise at Re=12$\times$10^6/m

A similar conclusion can be made for the runs made at Reynolds number of 12×10^6/m. Figures 9(a) and 9(b) show respectively the test in quiet and noisy flow conditions. The TSP's results show a significant difference between quiet and noisy. In the noisy flow conditions the effect of the ramp as the effect of the sides are much evident. The comparison of the wakes suggest a surely transition flow behind the element for the noisy conditions. The streamwise temperature profiles are supporting the fact that the wake in noisy conditions is transition, while in quiet flow is difficult to discern. For both the out-of-the-wake profiles, there is a slightly difference in temperature, already observed for lower Reynolds number, the trend suggest that they are decreasing downstream typical of laminar boundary layers.

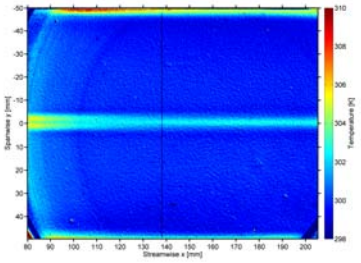

(a) Temperature distribution for BAM6QT, ramp h=2mm, quiet

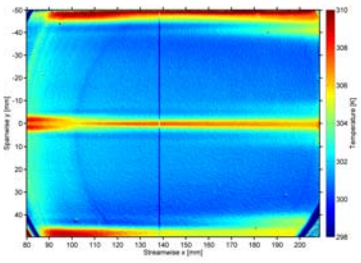

(b) Temperature distribution for BAM6QT, ramp h=2mm, noisy

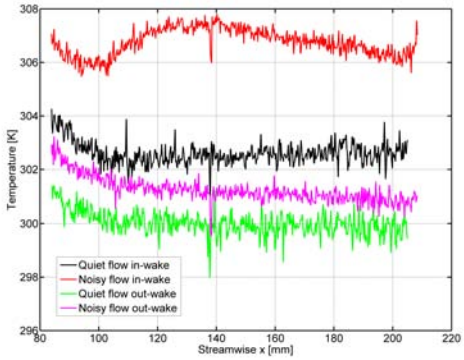

(c) Comparison streamwise temperature for BAM6QT

Figure 9: Comparison VKI-BAM6QT, Re=12$\times$10^6/m

Observing the spanwise profiles (figures 10(a) and 10(b)) it looks clear how the wake is stable in quiet flow and is slightly spreading for a noisy run at Re=12$\times$10^6/m.

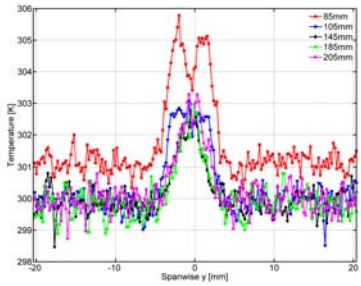

(a) Spanwise temperature profiles for BAM6QT, ramp h=2mm, quiet

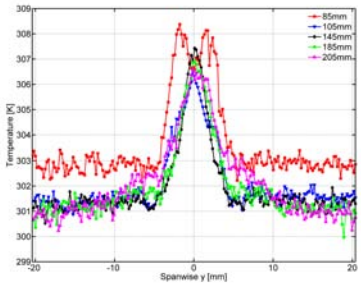

(b) Spanwise temperature profiles for BAM6QT, ramp h=2mm, noisy

Figure 10: Comparison of spanwise temperature profiles for BAM6QT, Re=12$\times$10^6/m

3.4 Effect of Tunnel Noise at Re=16 $\div$ 19$\times$10^6/m

Above a Reynolds number of 14$\times$10^6/m the BAM6QT is not more able to change between quiet and noisy flow conditions. From now on all the runs will be done and compared only in noisy flow conditions. Figure 11(a) shows the modified Stanton number distribution on a flat plate in VKI H3 Medium Reynolds conditions (Re=18$\times$10^6/m). The Stanton number has been computed using the infrared thermography technique. Figures 11(b) and 11(c) show the temperature on the flat plate, computed with the TSP technique in the BAM6QT at a Reynolds number ranging from 16$\times$10^6/m and 19$\times$10^6/m. In all the cases appear to be a pronounced spreading of the wake, which suggest that turbulence has been achieved. Inferring from the plots the location at which the wake begin to spread, we finds that in VKI conditions the onset of turbulence is between x=155mm and x=160mm, while in BAM6QT conditions transition occurs between x=170mm and x=180mm for Re=16$\times$10^6/m and between x=160mm and x=170mm for Re=19$\times$10^6/m. These locations on the onset of turbulence agree very well with each other. It is of particular interest observing how the onset of turbulence is moving upstream with the increasing Reynolds number in the BAM6QT. Over all the data prove that in noisy flow conditions the VKI H3 and the BAM6QT are very similar in terms of environmental noise.

The Stanton number distribution computed from the TSP is shown in figures 12(a) and 12(b). The in-wake and out-of-wake Stanton number profiles for both the cases in the BAM6QT agree very well with the theoretical computed ones. The out-of-wake is laminar and the in-wake of the ramp is fully turbulent. In figures 12(c) and 12(d) are plotted the spanwise temperature profiles for the BAM6QT at a Reynolds number of respectively 16$\times$10^6/m and 19$\times$10^6/m. From these figures it is possible to infer and confirm the location of the onset of turbulence looking at the spreading of the wake in the spanwise direction.

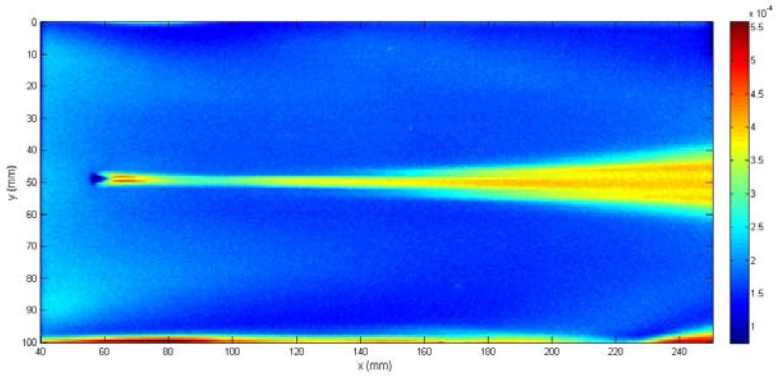

(a) Stanton number distribution for VKI, ramp h=0.8mm, Re=18$\times 10^6$/m

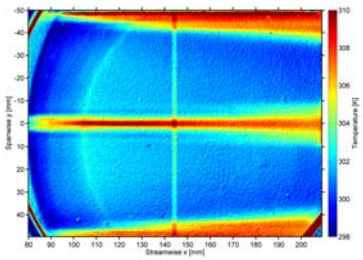

(b) Temperature distribution for BAM6QT, ramp h=2mm, noisy, Re=16$\times 10^6$/m

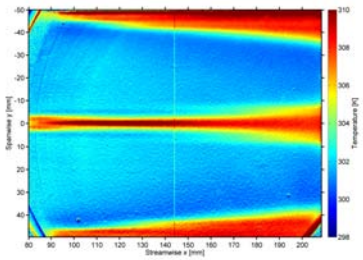

(c) Temperature distribution for BAM6QT, ramp h=2mm, noisy, Re=19$\times 10^6$/m

Figure 11: Comparison VKI-BAM6QT, Re=16$\div$19$\times 10^6$/m

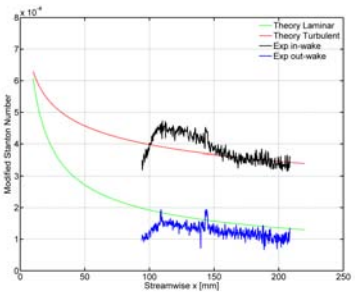

(a) Stanton number distribution for BAM6QT, ramp h=2mm, noisy, Re=16$\times$10^6/m

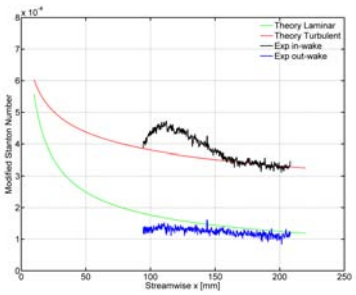

(b) Stanton number distribution for BAM6QT, ramp h=2mm, noisy, Re=19$\times$10^6/m

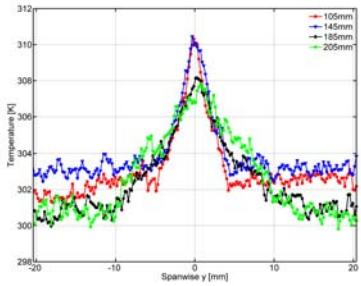

(c) Spanwise temperature profiles for BAM6QT, ramp h=2mm, noisy, Re=16$\times$10^6/m

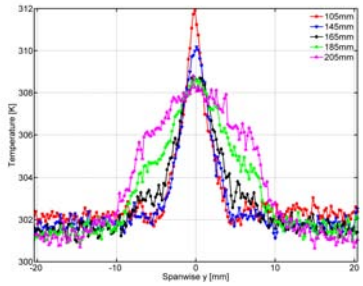

(d) Spanwise temperature profiles for BAM6QT, ramp h=2mm, noisy, Re=19$\times$10^6/m

Figure 12: Stanton number and spanwise temperature profiles for BAM6QT, Re=16$\div$19$\times$10^6/m

3.5 Effect of Reynolds Number on a 2mm Ramp

The temperature profiles for all the Reynolds number are plotted in figure 13 and show a clear effect of Reynolds number and environmental noise. For the two highest Reynolds number cases, which appear to be turbulent from the TSP images (figure 11(b) and 11(c)), the streamwise profiles show also a higher value of the temperature. In particular there is a sharp rise in the temperature at the onset of transition, then a steady decrease in temperature as the turbulent boundary layer thickened. The one curious thing is that the peaks in heating do not correspond to the spreading of the wake, which suggests that vortex heating from the vortices shedding off the roughness element may be obfuscating the peak due to the boundary layer state change. Generally from the profiles there is evidently a shift in the peak of the temperature profiles upstream towards the roughness element. Effect of unit increasing Reynolds number is shown to promote transition and move transition location forward. The shift of the peaks in the temperature profiles of the noisy flow data obtained from the Purdue BAM6QT possibly indicates a faster destabilization of the flow and a movement of the transition front upstream.

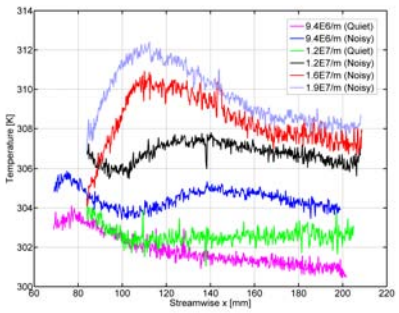

Figure 13: Streamwise temperature profiles (in-wake)

4 Conclusion

Infrared thermography and temperature sensitive paint were used to determine the state of the hypersonic boundary layer on a flat plate model with a 2mm isolated ramp. Experiments were run under noisy flow conditions in the VKI H3 wind tunnel as well as in noisy and quiet flow conditions in the Boeing/AFOSR Mach 6 Quiet Tunnel. Several different criteria were used to determine if the status of the boundary layer near the trailing edge of the plate. These included the computation of the modified Stanton number and the observation of the spreading of the wake in the TSP data. For a Reynolds number of 9.4×10^6/m in the VKI H3, the data for a 0.8mm ramp suggested that transition is occurring at x$\geq$180mm, while for a 2mm ramp in the quiet and noisy conditions of the BAM6QT, the data shows that it respectively fully laminar and transitional. The small length of the flat plate used in the BAM6QT make difficult to infer the possible location of the onset of transition. For a Reynolds number of 12×10^6/m the same conclusion for the lower Reynolds number can be drawn, except the fact that the onset of transition location is now visible around x=200mm in noisy conditions. For higher Reynolds number $16\div19\times10^6$/m, VKI data showed that the

flow transitions around x=160 mm, and the Purdue data suggests that transition occurs between x=160 mm and 180 mm. In general the stability of the boundary layer was influenced by Reynolds number. A general trend was that with an increase in Reynolds number, transition moved upstream. The results show that the VKI H3 Mach 6 tunnel noise has a great effect on transition location. The comparable results obtained in the VKI H3 and in the BAM6QT under noisy flow conditions, suggest to perform more experiments of induced boundary layer transition on different model's shapes.

Acknowledgments

A special thanks to prof. S.P Schneider (Purdue University) for transmitting me the energy to work on this fascinating topic. To my family, my friends and colleagues.

References

[1] S. Tirtey. *Characterization of a Transitional Hypersonic Boundary Layer in WindTunnel and Flight Conditions*. PhD thesis, ULB, 2009.

[2] *Advances in Laminar-Turbulent Transition Modeling, RTO-AVT / VKI Leture Series, W.S. Saric & M. Carbonaro directors*, 2008.

[3] Keisuke Fujii. Experiment of the two-dimensional roughness effect on hypersonic boundary-layer transition. *Journal of Spacecraft and Rockets*, 43(4):731–738, July-August 2006.

[4] Katya M. Casper, Brad M. Wheaton, Heath B. Johnson, and Steven P. Schneider. Effect of freestream noise on roughness-induced transition at mach 6. *38th Fluid Dynamics Conference and Exhibit*, 2008.

[5] Steven P. Schneider. Effects of roughness on hypersonic boundary-layer transition. *School of Aeronautics and Astronautics, Purdue University*, 2007.

[6] Andreas Strub. *Roughness induced transition in hypersonic boundary layer flows*. PhD thesis, Royal Institute of Technology, 2006.

[7] J.M. Muylaert, L. Walpot, and H. Ottens. European experimental reentry testbed (expert). Technical report, ESA/ESTEC, 2002.

[8] Steven P. Schneider. Development of hypersonic quiet tunnels. *Journal of Spacecraft and Rockets*, 45, August 2008.

[9] T. Arts, H.L. Boerrigter, J.M. Buchlin, M. Carbonaro, and G. Degrez. *Measurement Techniques in Fluid Dynamics*. von Karman Institute for Fluid Dynamics, 2001.

[10] C. O. Asma, J. Thoemel, S. Paris, and O. Chazot. Utilization of infrared thermography to investigate atmospheric entry aerothermodynamics of space vehicles at von karman institute. *QIRT 2008, 9th International Conference on Quantitative Infrared Thermography*, July 2008.

[11] P. Santarelli and J.M. Charbonnier. Heat transfer data reduction user guide for the vki-h3 wind tunnel. Technical report, von Karman Institute, February 1999.

[12] T. Liu and J.P. Sullivan. *Pressure and Temperature Sensitive Paints*.

Doctoral Project Summary

Numerical study of roughness induced transition from low to high Mach number

Fabio Pinna*

Supervisor: Prof. P. Rambaud†

von Karman Institute for Fluid Dynamics, Rhode-Saint-Genèse, 1640, Belgium

Promoter: P. Orlandi ‡- R. Paciorri §

Università degli Studi "La Sapienza", Roma, 00184, Italy

Abstract

Stability and transition are of wide interest in different areas of the fluid dynamic research. Despite the ease and simplicity of linear stability theory the extension to compressible flows introduce a more complex derivation and implementation of the stability code. This abstract will address these specific problems proposing solutions and methods to solve this difficulties. The solution of temporal problem is treated, retrieving the full eigenvalue spectrum for each case.

1 Introduction

Differently from the Orr-Sommerfeld (for more detail see [1], [2] [3]) equation compressible linear stability problem is completely described by a system of five ordinary differential equations. These include of course continuity, momentum and energy.
This summary proposes solutions to the eigenvalue problem associated with the linear stability of a compressible boundary layer under perfect gas assumption. Despite to the several techniques used to solve such a problem the author believe in the good performance of spectral methods, in the flavor of spectral Chebyshev collocation.

2 Governing Equations

The starting point remains the linearization of the Navier-Stokes equations though a new methodology has been adopted in this work. As the derivation of LST equations

*PhD Candidate, Aeronautics and Aerospace Department, Chaussée de Waterloo 72, fabio.pinna@vki.ac.be.

†Professor, Aeronautics and Aerospace Department, Chaussée de Waterloo 72, patrick.rambaud@vki.ac.be.

‡Professor Dipartimento Di Meccanica e Aeronautica, Via Eudossiana 18, 00184, Roma, Italy, paolo.orlandi@duniroma1.it.

§Professor Dipartimento Di Meccanica e Aeronautica, Via Eudossiana 18, 00184, Roma, Italy, renato.paciorri@uniroma1.it

is usually given by the superposition of a disturbance to a mean flow it seems obvious that this is causing a growth in the number of terms appearing in the equations. This is even more evident with the appearance of phenomena such as chemical reactions, bringing in more complex dependencies of the transport properties and therefore even more terms.
With the need of introducing more and more physics in stability calculations as well as different geometries, a completely automatic procedure has been coded to derive the Linearized Navier-Stokes equations. In this work we will refer only to the Cartesian coordinate system and therefore we will have the conventional set of governing equations (see [4])

$$\rho_t + (\rho q_i)_{,i} \tag{1}$$

$$\rho(q_{it} + q_j q_{i,j}) = -(p\delta_{ij})_{,j} + \tau_{ij\,,j} \tag{2}$$

$$\rho c_p(T_t + q_j T_{,j}) = (kT_{,j})_{,j} + p_t + q_j p_{,j} + \tau_{ij} q_{i\,,j} \tag{3}$$

.
As already said one superimposes a perturbation to the flow variables in the usual way

$$q = \overline{Q} + \hat{q} \tag{4}$$

Please note that this treatment needs to be applied also to the transport properties unless they are explicitly considered constant. In our computations only the specific heat at constant pressure c_p is considered as constant while viscosity is given by Sutherland's law and the thermal conductivity is retrieved by posing the Prandtl number and equal to 0.7. This assumption limits considerably the applicability of the equations but it is consistent with the fact the transport properties depend only on temperature.
Perturbations are considered very small with respect to the flow field thus their product is considered negligible. Anyway this fact should not confuse the reader with acoustic perturbations much weaker in amplitude. It has to be noted that what retrieved so far are the so called Linearized Navier-Stokes equations and could be used for other stability calculations. To derive the LST for a compressible boundary layer one still needs to assume the vertical velocity is zero and all the variable are dependent on y (the normal to the wall coordinate). Perturbations of the transport quantities could be written in the following form

$$\tilde{\mu} = \frac{d\mu}{dT}\tilde{T}, \quad \tilde{\lambda} = \frac{d\lambda}{dT}\tilde{T}, \quad \tilde{k} = \frac{dk}{dT}\tilde{T}. \tag{5}$$

It is worth to note the variable vector ϕ reads

$$\phi = \left[\tilde{u}, \tilde{v}, \tilde{p}, \tilde{T}, \tilde{w}\right] \tag{6}$$

and accordingly, terms involving ρ should be transformed using the state equation. Adimensional density, due to the boundary layer approximation is $\rho = 1/T$ while the perturbed value is

$$\tilde{\rho} = \gamma M^2 \frac{\tilde{p}}{T} - \frac{\tilde{T}}{T^2} \tag{7}$$

.
By representing our variables in wave form $\hat{\phi} = \tilde{\phi}(y)\,[u, v, p, T, w]\, e^{i\alpha x + \beta z - \omega t}$ we can retrieve the compressible linear stability equations. The parameters α and β are

the stream-wise and span-wise wavenumbers while ω is the frequency. The introduction of the already mentioned assumptions and hypothesis has been implemented in a computer algebra system in order to retrieve the compressible linear stability equations.

x-mom eq.

$$\begin{aligned}\frac{i\,\beta\,\tilde{u}\,\overline{W}}{\overline{T}}+\frac{\tilde{v}\,\overline{U}_y}{\overline{T}}+\frac{i\,\alpha\,\tilde{u}\,\overline{U}}{\overline{T}}+\frac{i\,\omega\,\tilde{u}}{\overline{T}}=\\ \frac{\tilde{T}\,\overline{\mu}_{\overline{T}}\,\overline{U}_{y\,y}+\tilde{T}\,\overline{\mu}_{\overline{T}\,\overline{T}}\,\overline{T}_y\,\overline{U}_y+\tilde{T}_y\,\overline{\mu}_{\overline{T}}\,\overline{U}_y+i\,\alpha\,\tilde{v}\,\overline{\mu}_{\overline{T}}\,\overline{T}_y+\tilde{u}_y\,\overline{\mu}_{\overline{T}}\,\overline{T}_y}{Re}\\ +\frac{-\alpha\,\beta\,\tilde{w}\,\overline{\mu}+i\,\alpha\,\tilde{v}_y\,\overline{\mu}+\tilde{u}_{y\,y}\,\overline{\mu}+\left(-\beta^2-2\,\alpha^2\right)\,\tilde{u}\,\overline{\mu}}{Re}\\ +\frac{-\alpha\,\beta\,\tilde{w}\,\lambda+i\,\alpha\,\tilde{v}_y\,\lambda-\alpha^2\,\tilde{u}\,\lambda}{Re}-i\,\alpha\,\tilde{p}\end{aligned}\tag{8}$$

y-mom eq.

$$\begin{aligned}\frac{i\,\beta\,\tilde{v}\,\overline{W}}{\overline{T}}+\frac{i\,\alpha\,\tilde{v}\,\overline{U}}{\overline{T}}+\frac{i\,\omega\,\tilde{v}}{\overline{T}}=\\ \frac{\tilde{T}\,\overline{\mu}_{\overline{T}}\,\left(i\,\beta\,\overline{W}_y+i\,\alpha\,\overline{U}_y\right)+2\,\tilde{v}_y\,\overline{\mu}_{\overline{T}}\,\overline{T}_y}{Re}+\\ +\frac{i\,\beta\,\tilde{w}\,\lambda_{\overline{T}}\,\overline{T}_y+\tilde{v}_y\,\lambda_{\overline{T}}\,\overline{T}_y+i\,\alpha\,\tilde{u}\,\lambda_{\overline{T}}\,\overline{T}_y+i\,\beta\,\tilde{w}_y\,\overline{\mu}+2\,\tilde{v}_{y\,y}\,\overline{\mu}}{Re}+\\ +\frac{\left(-\beta^2-\alpha^2\right)\,\tilde{v}\,\overline{\mu}+i\,\alpha\,\tilde{u}_y\,\overline{\mu}+i\,\beta\,\tilde{w}_y\,\lambda+\tilde{v}_{y\,y}\,\lambda+i\,\alpha\,\tilde{u}_y\,\lambda}{Re}-\tilde{p}_y\end{aligned}\tag{9}$$

z-mom eq.

$$\begin{aligned}\frac{\tilde{v}\,\overline{W}_y}{\overline{T}}+\frac{i\,\beta\,\tilde{w}\,\overline{W}}{\overline{T}}+\frac{i\,\alpha\,\tilde{w}\,\overline{U}}{\overline{T}}+\frac{i\,\omega\,\tilde{w}}{\overline{T}}=\\ \frac{\tilde{T}\,\overline{\mu}_{\overline{T}}\,\overline{W}_{y\,y}+\tilde{T}\,\overline{\mu}_{\overline{T}\,\overline{T}}\,\overline{T}_y\,\overline{W}_y+\tilde{T}_y\,\overline{\mu}_{\overline{T}}\,\overline{W}_y+\tilde{w}_y\,\overline{\mu}_{\overline{T}}\,\overline{T}_y+i\,\beta\,\tilde{v}\,\overline{\mu}_{\overline{T}}\,\overline{T}_y}{Re}+\\ +\frac{\tilde{w}_{y\,y}\,\overline{\mu}+\left(-2\,\beta^2-\alpha^2\right)\,\tilde{w}\,\overline{\mu}+i\,\beta\,\tilde{v}_y\,\overline{\mu}-\alpha\,\beta\,\tilde{u}\,\overline{\mu}}{Re}+\\ -\frac{\beta^2\,\tilde{w}\,\lambda+i\,\beta\,\tilde{v}_y\,\lambda-\alpha\,\beta\,\tilde{u}\,\lambda}{Re}-i\,\beta\,\tilde{p}\end{aligned}\tag{10}$$

mass equation

$$\begin{aligned}\frac{i\,\beta\,\gamma\,M^2\,\tilde{p}\,\overline{W}}{\overline{T}}-\frac{i\,\beta\,\tilde{T}\,\overline{W}}{\overline{T}^2}+\frac{i\,\alpha\,\gamma\,M^2\,\tilde{p}\,\overline{U}}{\overline{T}}-\frac{i\,\alpha\,\tilde{T}\,\overline{U}}{\overline{T}^2}-\frac{\tilde{v}\,\overline{T}_y}{\overline{T}^2}+\\ +\frac{i\,\gamma\,\omega\,M^2\,\tilde{p}}{\overline{T}}+\frac{i\,\beta\,\tilde{w}}{\overline{T}}+\frac{\tilde{v}_y}{\overline{T}}+\frac{i\,\alpha\,\tilde{u}}{\overline{T}}-\frac{i\,\omega\,\tilde{T}}{\overline{T}^2}=0\end{aligned}\tag{11}$$

energy eq.

$$\begin{aligned}
&\frac{i\,\beta\,\tilde{T}\,\overline{W}}{\overline{T}}+\frac{i\,\alpha\,\tilde{T}\,\overline{U}}{\overline{T}}+\frac{\tilde{v}\,\overline{T}_y}{\overline{T}}+\frac{i\,\omega\,\tilde{T}}{\overline{T}}= \\
&\tilde{T}\,M^2\,\overline{\mu}_{\overline{T}}\left(\frac{\gamma\,\left(\overline{W}_y\right)^2}{Re}-\frac{\left(\overline{W}_y\right)^2}{Re}+\frac{\gamma\,\left(\overline{U}_y\right)^2}{Re}-\frac{\left(\overline{U}_y\right)^2}{Re}\right)+ \\
&+\tilde{v}\,M^2\,\overline{\mu}\left(\frac{2\,i\,\beta\,\gamma\,\overline{W}_y}{Re}-\frac{2\,i\,\beta\,\overline{W}_y}{Re}+\frac{2\,i\,\alpha\,\gamma\,\overline{U}_y}{Re}-\frac{2\,i\,\alpha\,\overline{U}_y}{Re}\right)+ \\
&+\tilde{w}_y\,M^2\,\overline{\mu}\left(\frac{2\,\gamma\,\overline{W}_y}{Re}-\frac{2\,\overline{W}_y}{Re}\right)+Ec\,\left(\tilde{p}\,\left(i\,\beta\,\overline{W}+i\,\alpha\,\overline{U}+i\,\omega\right)\right)+ \\
&\tilde{u}_y\,M^2\,\overline{\mu}\left(\frac{2\,\gamma\,\overline{U}_y}{Re}-\frac{2\,\overline{U}_y}{Re}\right)+ \\
&+\tilde{T}\left(\frac{k_{\overline{T}}\,\overline{T}_{y\,y}}{Pr\,Re}+\frac{k_{\overline{T}\,\overline{T}}\,\left(\overline{T}_y\right)^2}{Pr\,Re}-\frac{\beta^2\,k}{Pr\,Re}-\frac{\alpha^2\,k}{Pr\,Re}\right)+ \\
&+\frac{2\,\tilde{T}_y\,k_{\overline{T}}\,\overline{T}_y}{Pr\,Re}+\frac{\tilde{T}_{y\,y}\,k}{Pr\,Re}
\end{aligned}\tag{12}$$

Our boundary conditions are $\left[\tilde{u},\tilde{v},\tilde{T},\tilde{w}\right]=0$ for $y=0$ and $y\to\infty$ and then our system is an eigenvalue problem. The final arrangement of the coefficients depends on the choice of performing a temporal or a spatial computation. Anyway in both cases it is possible to retrieve a general eigenvalue problem formulation

$$A\phi=\omega B\phi,\qquad \text{or,}\qquad A\phi=\alpha B\phi \tag{13}$$

.

It has to be noted that at this level properties coming from tables or special physical modelling codes such as MUTATION (see [5] [6]) could be used easily being these equations general. Nevertheless the extension to high temperature gas needs a brand new derivation of the whole set of equations.

2.1 Mean Flow

The mean flow used in these calculations comes by a compressible boundary layer solver inspired by [7]. The equations namely read

$$\left(cf''\right)'+ff''=0 \tag{14}$$

$$\left(a_1g'+a_2f'f''\right)'+fg'=0 \tag{15}$$

where

$$\begin{aligned}
f'=\frac{u}{u_e}\quad c=\frac{\rho\mu}{\rho_e\mu_e} \\
g=H/H_e\quad a_1=c/Pr \\
a_2=\frac{(\gamma-1)M^2}{1+\left(\frac{\gamma-1}{2}\right)M^2}\left(1-\frac{1}{Pr}\right)c
\end{aligned}$$

The first of 14 has the same boundary conditions of a Blasius flow

$$f'(0)=f(0)=0,\qquad \lim_{\eta\to\infty}f'(\eta)=1 \tag{16}$$

while the energy equation needs

$$g(0) = g_w, \qquad or, \qquad g'(0) = g'_w \tag{17}$$

$$\lim_{\eta \to \infty} g'(\eta) = 1 \tag{18}$$

We will not present the details of the numerical results, it suffices to know that two different methods have been set up; one is specifically conceived for the BVP (boundary value problem) while the other one combines a 4th order Runge-Kutta together with a shooting method. The two solutions coincide.

3 Numerical method

The equations presented before are very sensitive to perturbations and sources of error, and in order to achieve a good solution great care has to be take with respect of the discretization. The present approach utilizes a pseudo-spectral method based on Chebyshev polynomial in its collocation flavor. This technique has been selected after several tests on other similar methods and it has been chosen for its easy implementation and the straightforward manipulation of different boundary conditions. Detailed explanation about this and other spectral methods could be found in [8] or in [9]. Chebyshev polynomials are the heart of the method and they are defined as follows,

$$\begin{aligned} T_n(x) = cos(n \ \arccos(x)) \qquad & \forall \, n \in \mathbb{N}_0 \\ -1 \leq x \leq 1 & \\ x = cos(\theta) & \end{aligned} \tag{19}$$

It is possible to interpolate a function on a given set of polynomials and take its derivative. Being a linear operation this could be represented by a simple matrix multiplication $w = D_N \cdot v$ bringing in the concept of the *derivation matrix*. Obviously n-th power of D_N represent the n-th derivative.
Homogeneous Dirichlet boundary condition could be easily plugged into the collocation method as the first and last value in the approximated derivative have to be zero the differentiation matrix stays unvaried but computations could be carried out by skipping the first and the last rows and columns (D_N becomes a $(N-1) \times (N-1)$ matrix). Two zeros at the extremities of the resulting w should be appended so that the final vector has the correct dimension. In case of a Neumann boundary conditions the problem could be overcome by extracting the corresponding row from the matrix D_1. This row substitution technique can be generally applied to more complicated boundary conditions.
For instance condition on pressure could be imposed by means of Neumann boundary conditions

$$\left.\frac{\partial \tilde{p}}{\partial y}\right|_{y=0} = X_0 \tag{20}$$

$$\left.\frac{\partial \tilde{p}}{\partial y}\right|_{y=y_{max}} = X_m \tag{21}$$

These values could be easily found by manipulating the y-momentum equation already presented in the previous sections and it is not reported hereafter. What it is important to note is that the appearance of two discrete value $\tilde{p}_0$, $\tilde{p}_N$ modify the layout of the

matrices as two new columns and two rows should be added to take in account this two new terms.
The small definition interval of Chebyshev polynomials is one of the drawbacks of this method as it does not usually correspond to the physical space. One is forced to use for a boundary layer problem a mapping from the Chebyshev domain to the physical one. Supposing a function $y = g(x)$ where $a \leq y \leq b$ and $-1 \leq x \leq 1$ it is straightforward to find out that an equation $f'(y) = m$ correspond to

$$\frac{\partial f\left(g(x)\right)}{\partial x}\frac{\partial x}{\partial y} = m\left(x\right) \tag{22}$$

which means $f'(y) = f'(x) \cdot (1/g'(x))$. Moving back to the matrix collocation framework already presented eq. 22 becomes:

$$\overline{D_1} f = \mathsf{diag}\left(\frac{1}{g'}\right) \cdot D_1 f; \tag{23}$$

where $\overline{D_1}$ represents the "stretched" Chebyshev derivation matrix. Of course the complexity is growing with the derivative order but once the transformation is done no more mapping are required (see [10].). The transformation proposed in [11]

$$y = a\frac{1+x}{b-x} \tag{24}$$

is the one adopted in the present work as it gives enough freedom in the clustering of the points avoiding unnecessary complexities.

4 Results

Some tests have been performed for the temporal and the spatial version of the compressible LST after [11] and we will refer to it for the test case numbering. Only temporal calculations are shown here. Case 5 (see tab 1) is a Mach 10 flow at Re=1000 with adiabatic wall with a total temperature $T_0 = 2333.33K$. This is the hardest case to compute as it has been designed to generate a sharp peak in the temperature eigenvalue close to the boundary layer edge (pretty far from the wall in this case). The proposed converged value by [11] $\omega = 0,1158647 + i0.0001529$ is obtained by a fourth order compact finite difference scheme. In [11] single domain Chebyshev collocation does not converge at all while in our case converge with a high number of points to a slightly different result.
Case 3 (see tab 2) is a flow at Mach 2.5, Re=3000 , adiabatic wall and a total temperature $T_0 = 333,33K$. The solution in [11] for the single domain Chebyshev collocation method is $\omega = 0.0367339 + i0.0005840$ which is close to what we can see in tab. 2. At higher Mach we observe as the convergence is a bit slower than for other computations and that in any case the solution is largely comparable with [11] but not exactly the same.
Also Case 2 has been run, which is basically an incompressible flow at R=580 and temperature $T_0 = 277.78K$. In this case already with 40 point we retrieve $c = \omega/\alpha = 0,364123122364276 + i0,007959541607022$ for the first mode which is consistent with what reported in [11]. With our solver we are able to retrieve also the Orr-Sommerfeld case (as expected). Spatial calculation have been performed but are not reported here. Their behavior is consistent with the one already seen for the temporal case.

Table 1: Case 5 $\alpha = 0.12$ $\beta = 0$

N	ω	
80	0,115709047317130	- i 0,000073831933750
120	0,115492691606230	+ i 0,000035149671220
220	0,115514387430490	+ i 0,000059140123130
240	0,115514397746170	+ i 0,000059198903700
260	0,115514389779600	+ i 0,000059186629850

Table 2: Case 3 $\alpha = 0.06$ $\beta = 0.1$

N	ω	
40	0,036619773723988	+ i 0,000688436531086
60	0,036590025779941	+ i 0,000608466083413
80	0,036589418082481	+ i 0,000607374037741
100	0,036589422488298	+ i 0,000607384534109

5 Conclusion

A new automatic generator of linear stability equations has been introduced in this work and applied to compressible boundary layers. The equations presented [11] differ from the ones that have been shown here. Though the general good agreement our results suffer from small differences with respect to what has been investigated in [11]. This minor differences could be due to small implementation errors, as to the different boundary layer solvers, as well as minor bugs or rounding in the evaluation of the transport properties. Nevertheless the Orr-Sommerfeld behavior was retrieved once the input was set to "simulate" an incompressible flow. From this is possible to imagine the the methodology and the code presented are valid and working as well as the boundary layer solver.
One last remark is that some problems could be cured using a local refined search for the eigenvalue to be found, in fact in special cases our spectral solver can converge only with a "large" number of points. This is also due to the difficult tuning of the mapping from the physical to the computational domain not allowing to follow the outward movement of the critical layer at higher Mach

References

[1] H. Schlichting and K. Gersten. *Boundary Layer Theory*. Springler-Verlag, $8th$ edition, 2001.

[2] Leslie M. Mack. Transition and laminar instability. Technical Report JPL PUBLICATlON 77-1 5, Jet Propulsion LAboratory, California Institute of Technology Pasadena, California 9 1 103, 1977.

[3] Serkan Özgen. *Two layer flow stabiltiy in newtonian and non-newtonian fluids*. PhD thesis, VKI, May 1999.

[4] Rutherford Aris. *Vector, Tensors and the Basic Equations of Fluid Mechanics*. Dover - Prentice Hall, 1962.

[5] T. Magin. *A Model for Inductive Plasma Wind Tunnel*. PhD thesis, von Karman Institute for Fluid Dynamics, 2004.

[6] M. Panesi. *Physical Models for Nonequilibrium Plasma Flow Simulations at High Speed Re-entry Conditions*. PhD thesis, von Karman Institute for Fluid Dynamics, 2009.

[7] Tuncer Cebeci and A.M.O. Smith. *Analysis of turbulent boundary layers*. Applied mathematics and mechanics. Academic Press, 1974.

[8] C. Canuto, A. Quarteroni, M.Y. Hussaini, and T.A.Zang. *Spectral Methods in Fluid Dynamics*. Springler-Verlag, 1987.

[9] Lloyd Nicholas Trefethen. *Spectral Methods in MATLAB*. SIAM, 2000.

[10] John Philip Boyd. *Chebyshev and Fourier spectral methods*. Dover, 2001.

[11] M. R. Malik. Numerical methods for hypersonic boundary layer stability. *Journal of Computational Physics*, 86(2):376–413, 1990.

HEAT TRANSFER IN FLOWS

Doctoral Project Summary

Experimental Conjugate Heat Transfer Assessment in a Smooth Cooling Channel

Cukurel Beni*

Supervisor: Prof. Tony Arts†

von Karman for Fluid Dynamics, Rhode-Saint-Genèse, 1640, Belgium

Promoter: Prof. Anil Bajaj‡

Purdue University, West Lafayette, 47906, IN

Abstract

In order to characterize the conjugate heat transfer effects, the coupling between the conduction through the slab and the convection over the exposed surface, a series of Infrared Thermography experiments are conducted. The results showed highly non-1D conduction even for a flat smooth turbine internal cooling channel.

1 Introduction

The experimental study of turbulent flow and heat transfer in rib-roughened ducts is of high interest. From a fundamental point of view, these highly turbulent three-dimensional flows provide detailed test cases and information for the development and validation of advanced computational codes using techniques such as Large Eddy Simulation (LES) or Direct Numerical Simulation (DNS). From an applied point of view, this study supports the design and modeling strategy of critical gas turbine components such as the internal cooling channels of high pressure gas turbine blades. This approach has however been limited so far to a purely convective study [1, 2], mostly applying uniform heat flux thermal boundary conditions. The present research addresses the more advanced conjugate aspect of the problem. Most heat transfer data in the open literature do not consider the coupled aspect between convection and conduction, especially of importance where local heat pumping effects can be dominant.

A metallic slab of imposed thickness experimentally simulates one of the cooling channel walls. In the present set-up, on one side of the slab a uniform heat flux is applied and on the other side, the flow field imposes a heat transfer distribution, allowing the conduction pattern to develop across the slab thickness. This approach simulates the heat transfer occurring from the free-stream hot gas side, through the airfoil thickness, towards the internal cooling channels.

* PhD Candidate, Aeronautics and Aerospace department, Chaussée de Waterloo 72, cukurel@vki.ac.be

† Professor, Department at VKI, Chaussée de Waterloo 72, arts@vki.ac.be

‡ Professor, Mechanical Engineering, 401 S. Grant Street, bajaj@purdue.edu

2 Technical Approach

2.1 Experimental Facility

There are several test sections built to investigate the varying aspects of heat transfer, flat channel without ribs, ribbed channel and ribbed channel with cooling holes. The investigations reported here are conducted on the flat smooth channel without turbulators. The channel built is a simplified model of an internal cooling blade channel with geometric similarity scale of 15. It consists of three pieces such as the inlet, test (16 L/D_h) and exit sections. The inlet and exit sections are made of Plexiglas, and at the inlet, a honeycomb (3mm cells) with a NACA bellmouth provide flow conditioning. The inlet section is analogous to the colder base of the turbine blade where the flow starts to develop aerodynamically but not thermally.

The flow in the flat test section is shown to be in the turbulent regime, with an average turbulent intensity, integral length scale, ε dissipation rate and Kolmogorov length scales of 5.5%, 14mm, 8.5 Watts/kg and 0.15mm. For the test setup, at the inlet of the test section, the flow is found to be not fully developed, neither from a velocity profile nor from a turbulence intensity perspective, but neither is the flow at the actual serpentine passages. Thus, a greater similarity between the model and real turbine blade is established.

In the test section, the heating is supplied by means of a 25μm thick Inconel sheet, placed below the 25mm thick AISI 304 steel slab, powered by a 16V-150A DC power supply. The current is dissipated as thermal energy by the Joule effect and is conducted away towards the wetted surface.

Heat flux measurements on the Inconel have been conducted by applying energy balance over a control volume drawn over the entire heating element, $q''_{tot} = q/A = V_{INC} I_{INC}/A$. The voltage applied across the foil is measured at the two length-wise edges and the current is assessed by a shunt placed in series.

2.1.1 Channel Aero-thermal similarity considerations

The conjugate heat transfer is dominated by the Nusselts number which, by Buckingham Pi, is a function of $Nu = f(\mathrm{Re}, \mathrm{Pr}, T_b/\Delta T, Ec)$ [3], where $\mathrm{Re} = \rho V D_h/\mu$ (D_h being the hydraulic diameter), $\mathrm{Pr} = c_p \mu/k$, $T_b/\Delta T$ and $Ec = V^2/(C_p \Delta T)$ are Reynolds number, Prandtl number, scaled relative bulk flow temperature and Eckert number respectively. Influence of the relative bulk flow temperature is found experimentally to have a small influence on the Nusselts number. Especially for low speed applications, the relative importance of the kinetic energy with respect to the enthalpy is found to be very small, which largely reduces the influence of the Eckert number. Under the assumptions above, $Nu \approx f(\mathrm{Re}, \mathrm{Pr})$; the variation of Pr in the temperature range of the experiment is very small, thus in order to respect similarity, it suffices to maintain the same Reynolds number, in this case 40000±1%. Another consideration is the relative weight of forced convection with respect to natural convection: Gr/Re_L^2, where the Grashof number, $Gr = g\beta(T_w - T_b)/\mu^2$, $\beta \simeq -1/\rho \bullet (\rho - \rho_{film})/(T - T_{film})$ and $T_{film} = (\overline{T_w} + \overline{T_b})/2$. For this setup, $Gr/\mathrm{Re}_L^2 \approx o(10^{-3})$, clearly making the forced convection the dominant phenomena. Finally, for conjugate experiments, weight of conductive resistance with respect to the advective term is characterized by the Biot number,

$Bi = hL_c / k_s$. In serpentine channels of a turbine blade, Bi≈1, and this parameter is conserved through appropriate selection of the slab thickness.

2.2 Infrared Thermography

In this experimental campaign, a FLIR SC3000 infrared camera with long-wave Quantum Well Infrared Photo-detector has been used. The nominal response of the photo-detector peeks in the 8-9 micron wavelength range, and since each pixel relates to a single IR detector, the spatial image deformation due to the optical system aberration is negligible. The total resolution of the camera is 240x320 pixels, and thermal sensitivity of the camera is 0.02ºK. The camera is placed 30º from the perpendicular axis and the angle chosen is a compromise among the out of focus effect of the lens, the resolution and the area observed in the image. At each data point, 30 images are recorded and averaged temporally.

The infrared radiation, emitted by the model and its surroundings, is absorbed by the photon-detectors of the infrared camera and for which the intensity is a function of slab area and temperature, and relative orientation of the surfaces. The irradiation is then converted into electrical signals,"object signal", at each pixel. To get an accurate representation of temperature from the acquired object signal at each pixel, and avoid uncertainties that might arise from the camera out of focus effect, the existence of the polyethylene film (optical window), reflections, and influence of the surroundings, an experimental pixel-by-pixel calibration methodology is employed, where each pixel is calibrated with its own sensitivity to test section temperature. For this the surface is brought to uniform temperature and is gradually cooled down recording temperature and IR camera object signal images to accurately represent the thermal sensitivity of each pixel. Finally, the object signal data at each pixel is fitted with a second order polynomial with respect to the imposed temperatures. The average deviation for all temperature calibration points over the spatial mean is calculated to be 0.056K.

Due to the perspective image acquired by the camera, a projective image transformation procedure needed to be applied to the measured object signal through a bicubic interpolation scheme, and the resolution of the transformed image is superficially augmented in each dimension through sub-pixel interpolation. The mean scale factors corresponding to the original image acquired by the camera, and the transformed interpolated image are 2.64 pixels/mm, and 5.21 pixels/mm respectively. The images are then cropped to fit the width of the desired image.

2.3 COMSOL MODEL

The temperature measurements on the surface of the slab are applied to a COMSOL model to solve the energy equation with boundary conditions of uniform heat flux at the bottom, measured temperature distribution on the top, adiabatic condition on the sides and periodicity in the lengthwise direction. The output of this COMSOL model results in the surface heat flux distribution, which is then related to local heat transfer coefficient, $h(x,y) = q''_{top}(x,y) / \left(T(x,y) - T_\infty(x)\right)$, where $T_\infty(x)$ is estimated to be the air temperature calculated by the linear distribution of the mean test section inlet and exit temperatures, applied locally in the length-wise direction, and in tern can be related to Nusselt number, $Nu = h(x,y) \bullet D_h / k_f$.

The modeled portion of the slab is meshed with over 1.5million tetrahedral elements, which results in a maximum element size of 1.5mm and the edges are

further refined to consist of nodes max 0.1mm apart. The refinement of the edges is of special importance due to error propagation in the heat flux balance. The commercial code Comsol solves the 3-D Fourier equation through out the model to compute the temperature distribution at all directions, and for this case the convergence criteria is set to 10^{-10} for the relative pre-conditioned residuals. It has been shown that further grid refinement does not significantly affect the solution.

3 Results

While the blower supplies the experimental rig with ambient temperature air for convection over the slab at Reynolds number 40000±1%., the power supply connected to the Inconel foil is turned on, and the heat flux under the slab is gradually increased to 1167 W/m². Until steady-state conditions are reached, all temperatures along and under the slab, over the optical film (optical window) and in the test section are monitored periodically.

The acquired infrared images are averaged temporally, resulting in the mean object signal distribution over the slab, which is then transformed into the physical domain. The row temperature at each pixel is then calculated by applying the polynomial fits that vary pixel by pixel, and which are calculated by the calibration procedure. The directly measured temperature data seems to be fairly noisy and is further post-processed by a series of threshold and neighborhood validation filters. The applied filters still proved to be ineffective to reduce the noise in the temperature distribution, thus to be able to capture the global change in temperature across the entire interrogation region and impose it as a boundary condition while solving for the heat flux on the surface, a 10th order surface bipolynomial is fitted over the temperature distribution, the average error caused by this estimation is approximately 0.15K. These large peaks are clearly isolated regions which result in non-uniformities due to reasons like the surface finish of the slab as a consequence of the machining process and the quality of the applied paint.

3.1 Temperature Distribution

Examining the temperature distribution along the centerline length-wise direction, it can be observed that the temperature in this region increases almost linearly towards the exit within the uncertainty limits. When this distribution is compared with the thermocouple measurements made along the slab, upstream and downstream, along with a 4th order polynomial fit through the thermocouple data, the Infrared Thermography data show good consistency Fig. 1.

Investigating the temperature differences in the width wise direction across the slab center point, T(0,y), and comparing the experimental data with the thermocouples placed equidistantly upstream and downstream, temperatures measured by the infrared camera lie almost at the half way but closer to the downstream thermocouple measured temperatures, Fig. 2. This is rational since the cooling effectiveness decreases as the thermal boundary layer develops and the local freestream temperature rises, resulting in higher temperatures. While the maximum temperatures are observed for the test section centerline, followed by a gradual decrease towards the side-walls, there exists a sudden drop in temperature at each edge of the channel, in the order of 0.7K with respect to the local mean. This plunge in temperature is believed to be due to the corner vortices formed at the edges of the channel, locally enhancing heat transfer.

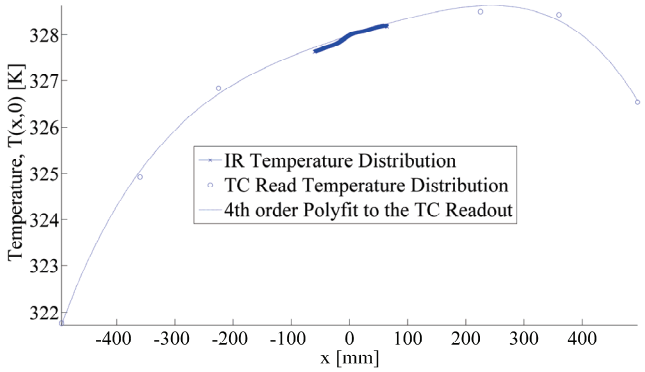

Figure 1: The Longitudinal Temperature Distribution along the Centerline.

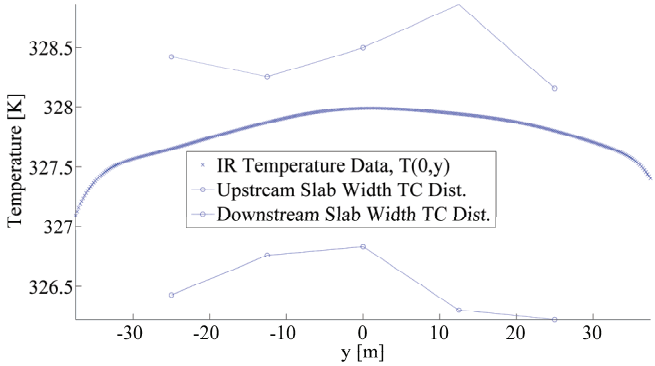

Figure 2: The Widthwise Temperature Distribution at the center, T(0,y).

The temperature profile in the width-wise direction is further investigated at 18 different length wise values, equidistant slices in the width-wise direction across the entire length observed by the camera, $T(x_i,y)$. When these temperatures are normalized by the local centerline temperature and multiplied by a global reference temperature, which in this case is the channel center point temperature, $T^*(x_i,y)=T(x_i,y)/T(x_i,0)\cdot T(0,0)$, it is observed that all the width-wise temperature profiles measured at different length-wise points collapse on one and another; and when fitted with a 4th order polynomial, the average maximum deviation is 0.078K.

3.2 COMSOL Results

From the results acquired from COMSOL, the mean heat transfer coefficient, h, is found to be 38.3±1.3 W/m^2-K. It is observed that the heat, through conduction in the slab, diffuses towards the edges and the error associated with assuming a 1-D conduction through the slab can be as high as 60% locally around the edges and in the order of 20% about the channel centerline.

By the known local heat transfer coefficient, h(x,y), Nusselt number distribution across the top surface can be computed, Fig. 3. It is of importance to compare the mean experimental Nusselt number with some preceding theoretical convective heat transfer correlations. From Dittus-Boelter Nusselt correlation, $Nu_D=0.0243\,\mathrm{Re}_D^{0.8}\,\mathrm{Pr}^{0.4}$ [4], confirmed for $0.7\le \mathrm{Pr}\le 160$, $\mathrm{Re}_D\ge 10000$, $L/D\ge 10$, the

resulting Nusselt number is Nu_{theo}=101.8 which is in good agreement with the measurements, Nu_{mean}=102.4±3.8, and well within the experimental uncertainty.

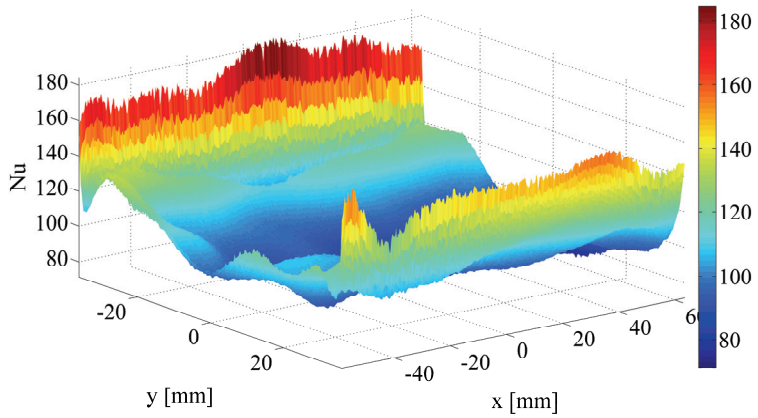

Figure 3: Distribution of Nusselt Number.

4 Conclusion

The temperature measurements on the top portion of the slab indicated that the width-wise temperature distribution can be normalized by the local centerline temperature, and all temperature profiles collapse into a single curve within the uncertainty of the measurements. In the length-wise direction, the temperature data appeared to be close to linear within the error bounds.

It is observed that the surface heat flux, through conduction in the slab, diffuses towards the edges and that the conduction from bottom to top of the slab is highly non 1-D. The experimental Nusselt number distribution is estimated within an uncertainty of 3.7% and the mean value is in good agreement correlations.

In the experiments conducted for the flat plate, the local heat transfer phenomena (the distribution of surface heatflux and Nusselt number) seems to be highly influenced by the existence of the slab and thus the effects of conduction, but the mean heat transfer does not seem to be as susceptible to the conjugate phenomena, indicated clearly by the close agreement with convective correlations. Similar Infrared Thermography experiments are to be conducted with the ribbed slab configuration where these results provide a baseline comparison.

Acknowledgments

I would like to thank my advisor and my promoter Prof. Tony Arts and Prof. Anil Bajaj for their support. This research was funded in part by the US Air force Office of Scientific Research. This support is most gratefully acknowledged. Finally, I would like to express my gratitude to Red Bull GmbH, and Sara Lee Coffee/Tea.

References

[1] M. Çakan. Aero-thermal investigation of rib-roughened internal cooling passages. VKI, Phd Thesis, July 2000.

[2] L. Casarsa. Aerodynamic performance investigation of a fixed rib-roughened internal cooling passage. VKI, Phd Thesis, July 2003.

[3] F .P. Incropera and D. P. DeWitt. Fundamentals of Heat and Mass Transfer, John Wiley & Sons, New Jersey, 2007.

[4] W. Kays, M. Crawford and B. Weigand. Convective Heat and Mass Transfer. McGraw-Hill, New York, 2005.

Doctoral Project Summary

Aerodynamic Research on Surface Heat Exchangers in the Engine Bypass Flow

Laura Villafañe*

Supervisors: Guillermo Paniagua† and Tony Arts‡

von Karman Institute for Fluid Dynamics, Rhode-Saint-Genèse, 1640, Belgium

Promoter: Francisco Payri§

Universidad Politécnica de Valencia, Valencia, 46022, Spain

Abstract

The design of a new blowdown wind tunnel to investigate an air/oil integrated surface heat exchanger placed in the secondary duct of a turbofan is described. The test section consists of a complex 3D geometry to reproduce the flow conditions encountered in a real engine during take off regime in the vicinity of the separator nose downstream of the inlet fan.

1 Introduction

High-bypass ratio engines are being developed with the objective to decrease specific fuel consumption and increase aircraft engines capabilities. The evolution towards increasing engine efficiency requires advanced cooling and lubricating systems.

The oil systems in their double function as lubricant and coolant fluid, require efficient coolers for continued successful operation of the aeroengines. Among others H. Streifinger [1] introduced fuel as the preferred oil heat sink for the lubricating oil systems. However its capacity is limited by several factors. Current limitations are fuel degradation, vapor locking that may occur at high temperatures within the fuel pump, and the creation of combustion instabilities in the engine burners. Additionally, the capacity of fuel as a heat sink tend to be also limited because of the limitation on the available fuel flow. It is a result of the lower consumption of future engines and the development of wings in composite material which will not stand hot fuel. On aeroengines, air as a cooling fluid is extensively used for airfoil cooling. Air is also used for the cooling of the lubrication oil generally to help the fuel cooled oil coolers with the

*PhD Candidate, Turbomachinery and Propulsion Department, Chaussée de Waterloo 72, laura.villafane@vki.ac.be.

†Associate Professor, Turbomachinery and Propulsion Department, Chaussée de Waterloo 72, paniagua@vki.ac.be.

‡Ordinary Professor, Turbomachinery and Propulsion Department, Chaussée de Waterloo 72, arts@vki.ac.be .

§Ordinary Professor, Máquinas y Motores Térmicos, Camino de Vera 14, fpayri@mot.upv.es.

thermal management in the different operational conditions [2]. The main limitation of air cooled heat exchangers is the drag penalty that they may cause when sited within the fan airstream, and the decrease of the main mass flow when the air is bleed from the compressor.

Research on an efficient Air Cooled Oil Cooler (ACOC) integrated surface heat exchanger located at the inner shroud of the secondary duct of a turbofan is currently performed at the von Karman Institute (Fig. 1). The global objective is the analysis of the flow structure resulting from the interaction between the secondary flow and the heat exchanger. This knowledge will lead to the design of an efficient surface heat exchanger placed within the bypass flow of a turbofan, in the vicinity of the air separator nose. The air-oil heat exchanger would satisfy needs for cooling the oil circuit without disturbing significantly the air stream or decreasing the overall efficiency of the engine.

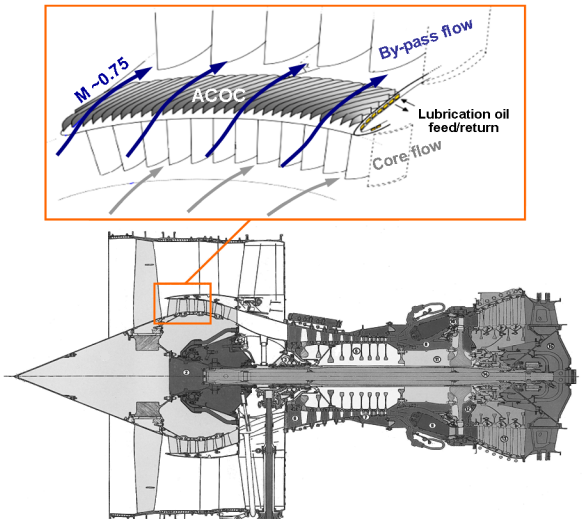

Figure 1: Location of the heat exchanger in the real engine

.

Multiple studies have been focused on air heat exchangers, and more specifically in the performance of heat sinks. This subject has been extensively treated experimentally, numerically and analytically. Most of the work deals with fully shrouded heat sinks, optimizing the geometry of the fins and the arrays [3, 4, 5, 6, 7, 8, 9, 10]. Heat sinks in ducted flow with tip and/or lateral clearance have been also addressed focused mainly in electronic applications [11, 12, 13, 14, 15, 16, 17]. Many authors have worked on the development of correlations [18, 19] and analytical models [20, 21, 22]. However, an analytical model is not still available for use in a optimization procedure for heat sink design, and each different situation requires experimental and numerical studies.

Nevertheless, low Reynolds numbers are considered in all the studies previously cited. Authors have focused on industrial, electronic or internal cooling applications. To the authors knowledge heat transfer and friction effects on finned arrays have not been addressed regarding high Reynolds number applications and high compressible flows. Although many patents propose the implementation of different heat transfer systems using the bypass flow coming from the fan. This unexplored field could lead

to improvements in the thermal managing of future turbofans.

A new wind tunnel test facility has been specifically designed for the reproduction of the real engine conditions during the take off regime in the bypass flow downstream of the inlet fan. The duplication of the flow structure in the area where the surface heat exchanger will be located imposes the necessity of simulating radial and azimuthal flow gradients. The resultant 3D test section geometry and its implications make this wind tunnel original and different from the usual facilities for turbomachinery testing. This paper is focused in the design of this innovative wind tunnel.

2 Design methodology

In this section the requirements from the engine conditions are outlined. The definition of the overall wind tunnel dimensions is obtained by simplified 1D model analysis. The different components and instrumentation are explained in the next section.

2.1 Wind Tunnel Requirements.

The main purpose of the wind tunnel design is to achieve the required flow conditions with a minimum power consumption and at the smallest possible cost. General design rules are given in fundamental books of experimental aerodynamics [23, 24, 25], and in works on existent wind tunnels [26, 27]

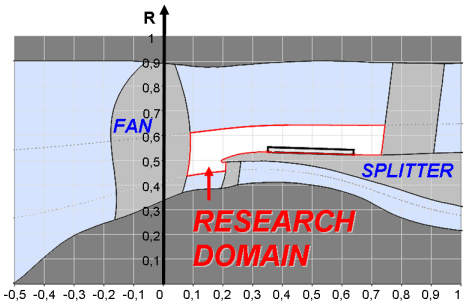

Figure 2: Research Domain

The model under investigation is the portion of the engine comprised between the fan trailing edge and the leading edge of the Outlet Guide Vanes (OGV) in the bypass flow. A sketch of the research domain is represented in Fig. 2. The aerodynamic conditions to be reproduced correspond to take off regime. The flow characteristics are known from non viscous computations on a model of the real engine in which the ACOC system is not incorporated. The Mach number in this configuration varies from 0.7 to 0.86, and the Reynolds based on a standard ACOC fin of 10 mm varies between $1.7 \cdot 10^5$ and $2 \cdot 10^5$. In this conditions both compressibility effects and Re effects play an important role.

2.2 Test Section Specifications

The objective of the wind tunnel is the reproduction of the significant flow parameters, with low turbulence level, long testing time, stable conditions and minimum wall effects. Data concerning flow characteristics in the real engine during take off regime are

known from non viscous Euler computations on the real engine geometry. The main design criteria is the reproduction of radial distributions of flow angle and Mach number by means of a specific 3D test section geometry and control of the upstream total pressure. It has been defined from the consideration of the next factors:

- Compressibility effects play an important role due to high subsonic mach numbers and the possible local supersonic conditions close to the ACOC fins.
- The azimuthal component of the flow velocity downstream of the fan is of the same order of magnitude as the axial component. In the region close to the separator nose the radial flow component can not be neglected. For a proper simulation of the problem three dimensional effects have to be considered and the radial gradients reproduced.
- Specified static pressure and temperature mean values are close to ambient conditions. Even if those quantities are not fully duplicated, resulting Reynolds numbers are of the same order of magnitude as those specified.
- Total pressure in the plenum chamber can be controlled by a regulating valve. Its ratio to the static pressure in the test chamber will define the operational Mach number. Control of the downstream pressure could allow the precise duplication of Mach and Reynolds number, but it would introduce significant pressure losses decreasing the testing time.

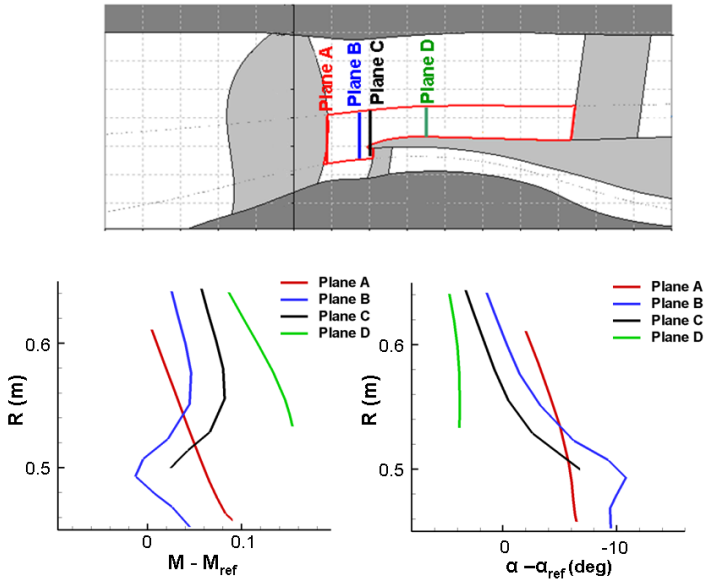

Figure 3: Radial Mach number and flow angle distributions in the real engine

Radial distributions of Mach number and flow angle along the research domain are shown in Fig. 3 with respect to reference values. They can be approached by a proper design of the Inlet Guide Vanes (IGVs) and the Test Section walls. In addition, the static pressure distribution over the separator nose is also known from the inviscid computations. Its reproduction depends on geometric duplication of the separator nose

as well as on the pressure losses in the diffuser, since the air is discharged to the atmosphere. The design of a efficient diffuser would allow the approximation to the real static pressure distribution and will increase the testing time.

2.3 One Dimensional Model

A symbolic sketch of the wind tunnel is shown in Fig. 4 for the enumeration of the main components: (1) pressurized air tank, (2) intake duct circuit, (3) regulation valve, (4) settling chamber, (5) contraction, (6) IGVs, (7) Test Section, (8) Diffuser and atmospheric discharge circuit.

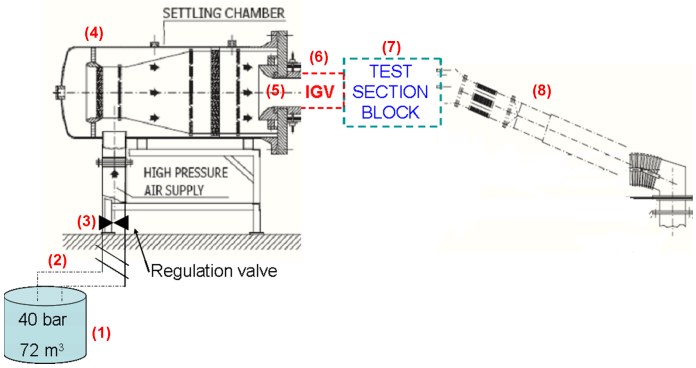

Figure 4: Wind Tunnel Sketch

The air been taken from the 40 bar deposit, will be discharged to the settling chamber through a regulation valve. From the settling chamber the air will be first accelerated in a contraction, and later turned and accelerated in the inlet guide vanes. Once in the test section the air passing under the separator nose will be evacuated. The so called bypass flow will be evacuated through a diffuser to the atmosphere, after impinging in the ACOC fins. Tests last until the pressure in the tank decreases to the value that gives the minimum operating pressure ratio.

One dimensional analysis have been done for the conceptual design assuming ideal perfect gas and isentropic processes. Safety coefficients are considered to account for pressure losses.

2.4 Dimensions of the Test Section

The test section includes the exact geometry of the splitter at real scale and reproduces the bypass flow and the core flow effects. The walls of the test section are designed to duplicate the radial gradients of Mach number and flow angle as is described in Section 3.3.

The high flow velocity implies high mass flow rate per unit of area. The selection of the test section area is limited mainly by two factors: the available air mass flow from the deposit, and the convenience of long testing time. Big area decreases the running time of the facility. Small area limits the duplication of the real phenomenon due to blockage effects and wall boundary layers.

In a one dimensional analysis the mass flow rate can be expressed as a function of flow parameters and the transversal area through the Eq. 1.

$$\dot{m} = C_D A \sqrt{\frac{\gamma}{R}} \frac{P_{01}}{\sqrt{T_{01}}} M (1 + \frac{\gamma - 1}{2} M^2)^{\frac{-(\gamma+1)}{2(\gamma-1)}} \quad (1)$$

where P_{01} and T_{01} are estimated values of stagnation pressure and temperature at the test section. A maximum mass flow rate of 6 Kg/s has been considered from previous experiences in the use of the 40 bar air tank at the VKI. It implies a maximum area about 0.021 m^2.

As first attempt the upper wall and the inner channel were chosen following streamlines considering the position of the splitter fixed by the real geometry. The shape of the upper and inner walls has been lately optimized iteratively using CFD results. The values of the radius at the test section inlet have been kept within the limits obtained from this 1D analysis. The cross section at the IGVs inlet finally adopted is an annular sector of 15°, the upper and inner radius been fixed to $R_{ext} = 0,60175m$, $R_{int} = 0,458m$.

3 Component Design

A review of the design of the two main wind tunnel components is presented. Numerical tools have been used to help the design.

3.1 Settling Chamber and Contraction

Compressed air from the storage tank is discharged to the settling chamber. The regulation valve is operated to establish a constant total pressure in the settling chamber as the deposit is discharged. The flow in the settling chamber nearly comes to rest, achieving total pressure recovery . It is therefore the place to install screens and honeycombs to provide flow homogenization and to reduce the both the lateral and the axial turbulence level, with the lowest pressure losses. Grid selection is treated in detail in Refs. [28, 29, 30].

The flow is re-accelerated in the contraction. The contraction also increases the uniformity of the flow and decreases the turbulence in the longitudinal direction.

3.2 Inlet Guide Vanes

The Mach number and flow angle radial distributions at the inlet of the research domain are duplicated downstream of the Inlet Guide Vanes block. The flow passing through this component is accelerated and turned. The specific design of the IGVs allows the reproduction of the radial distributions in the real engine. Its design[31] has been done in five main steps starting from 2D blade configurations and ending with an optimized 3D blade model. Different numerical tools as "Blades" and "TRAF" programs have been used.

The first step consists in the optimization of a 2D blade providing at its trailing edge the Mach number and flow angle correspondent to the values at middle height of the test section inlet plane. An optimized value of the pitch to cord ratio is also defined at this step. In the second phase three different blade sizes are considered leading to three different IGVs with different number of blades. They are used for wake homogenization analysis in the last step. Cylindrical three dimensional blades are generated from the different blade sizes considered and the flow field numerically computed. Radial distributions obtained from the numerical computations are used to iteratively modify the 3D blade models until the specified flow conditions at the test

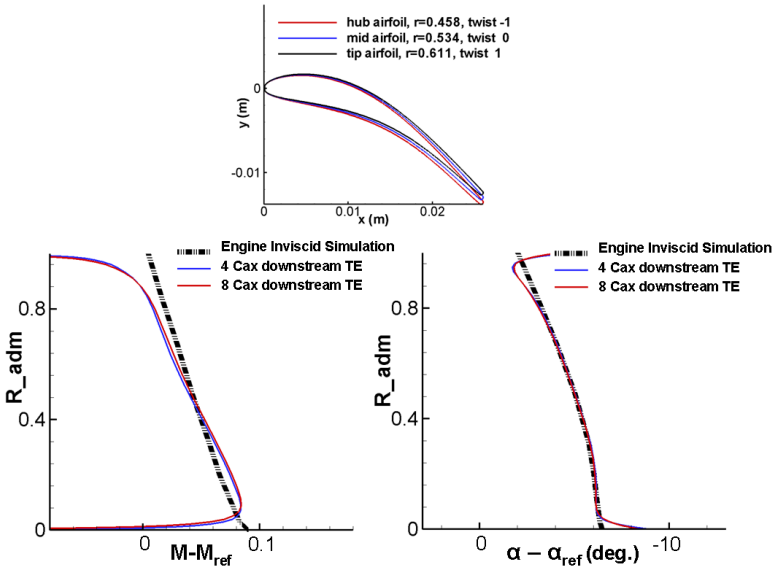

Figure 5: Isentropic Mach number and flow angle distributions downstream IGVs.

section inlet are duplicated. After analysis of wake homogenization at different axial positions downstream of the IGVs, the final configuration has been fixed. It is an array of 8 blades of 26mm axial cord in which the stagger angle of the blades varies linearly from hub to tip in 2 degrees. Radial distributions of Mach number and flow angle downstream of the IGVs are plotted in Fig. 5 with respect to reference values in non dimensional radial coordinates.

3.3 Test Section

The definition of the transversal area and the values of inner and upper radius at the inlet of the test section have been introduced in Section 2.4. The design of the upper and lateral walls is based on the duplication of the radial distributions of Mach number and flow angle from the inviscid computations on the real geometry at the four axial locations represented in Fig. 7. A sketch of the test section is shown in Fig. 6

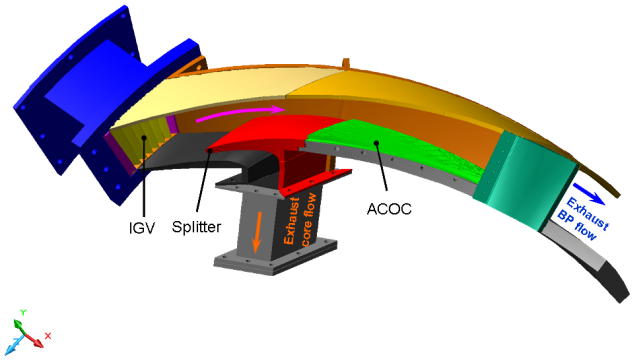

Figure 6: Test Section Sketch.

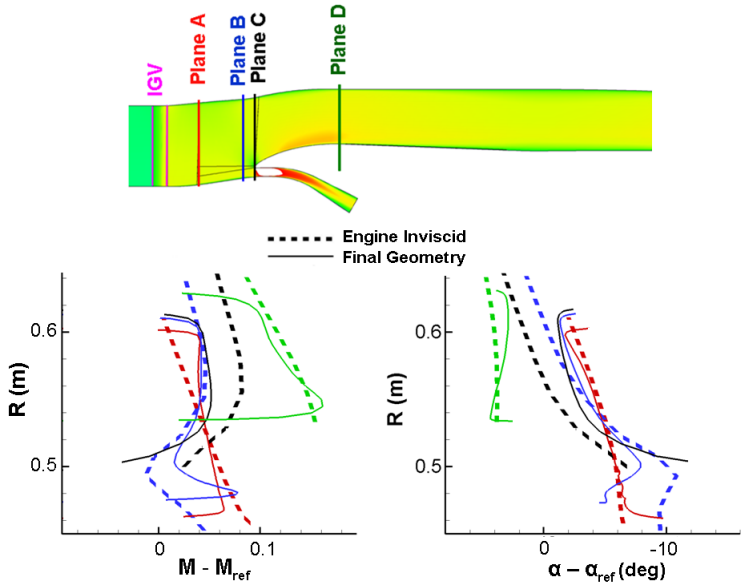

Figure 7: a)Meridional view of the final test section geometry. Absolute Mach number map. Comparison of radial distributions of b) flow angle, c) Mach number.

The design has been done in different steps based on numerical computations on the test section domain and the IGVs domain. The finned heat exchanger has not been included in the test section as it is not present in the inviscid simulations from the real engine. Attention was first focused on the upper and inner walls, considering a complete 360° axisymmetric domain. Next step was to link test section and IGVs domains. Iterative modifications of upper and inner walls, inner channel and boundary conditions have been performed in order to approach the radial distributions at the different axial locations to the specifications. A meridional view of the final geometry and the map of absolute Mach number is shown in Fig. 7. In the same figure radial variations of Mach number and flow angle are plotted together with the distributions from the engine inviscid computations. Attention has been mainly paid to the region where the heat exchanger will be installed (plane D). The static pressure distribution along the splitter from its nose to the location of the leading edge of the ACOC fins has been also compared to the specifications.

In the last phase the lateral walls of the test section have been defined as stream-surfaces obtained from the axisymmetric computation on the final geometry. In Fig. 8 the extraction of the streamsurfaces is shown as wells as the lateral walls and their intersection with the splitter.

3.4 Exhaust

Before been exhausted to the atmosphere, the air flow coming from the test section will expand in a diffuser. A good diffuser performance would enlarge the testing time since it would decrease the static pressure in the test section and consequently the necessary inlet total pressure to duplicate the Mach number. It would also approach the static pressure in the test section, and therefore the Reynolds number, to the specifications

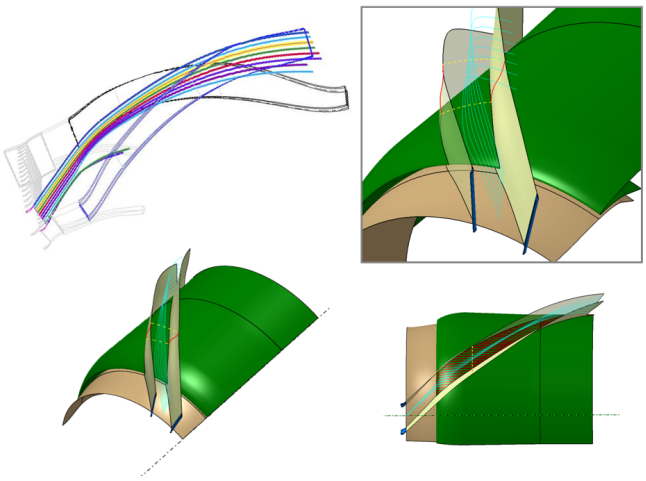

Figure 8: Lateral walls definition

from the inviscid simulations. Guidelines on diffuser design is addressed in [25, 32, 33].

4 Measurement techniques

Characterization of the flowfield will be performed using different measurement techniques. During the first experimental phase mappings of static and total pressure, total temperature, flow angle and turbulence intensity will be measured at five different planes upstream and downstream of the finned heat exchanger. Those measurements together with static pressure measurements along the test section centerline will allow a fully analysis of the flow behavior and the disturbances caused by the ACOC system. Different heat exchanger geometries will be tested.

For the first measurement phase pitot rake, five hole probe rake, shielded thermocouple rake, hot wire rake and combined temperature pressure probes have been specifically designed. Considerations regarding limited testing time, cross sectional dimensions and blockage effects, test section geometry and flow conditions to be measured, lead to the design of the different probes. Head probes dimensions have been reduced as much as possible to avoid blockage effects and allowing measurements close to the heat exchanger fins.

5 Conclusions

The design of an innovative high speed subsonic wind tunnel is presented in this paper. This new facility will help the aerodynamic research on an Air Cooled Oil Cooler integrated surface heat exchanger within the bypass flow of a turbofan. This new investigation is motivated by the increasing necessity of efficient refrigeration and lubrication systems on aeroengines, linked to the evolution of engine architectures and performances.

The heat exchanger will be located in the splitter surface close to the separator nose. The real flow will be reproduced in the test section of the new facility in terms of radial

distributions of Mach number and flow angle, the Reynolds number been of the same order of magnitude. A complex 3D test section has been designed to duplicate those conditions using numerical tools.

The new wind tunnel is an intermittent blowdown facility in which the air is taken from a pressurized deposit. The air is discharged to a settling chamber where the total pressure is kept constant by means of a regulation valve. The flow is accelerated and turned in a contraction and through Inlet Guide Vanes (IGVs). The IGVs have been specifically designed to reproduce at the inlet of the test section the radial flow distributions extracted from inviscid computations on the real model. The flow going out from the test section is discharged to the atmosphere through a diffuser.

Numerical computations not addressed in this abstract have been performed on the final test section geometry including the lateral walls. The objective of those computations is their comparison with the axisymmetric ones used for the test section design. Flow analysis regarding the effect of the lateral walls, the IGVs's wake mixing, the homogeneity of the flow and the 3D flow structure have been performed to predict the experimental flow behavior.

Heat transfer measurements will be performed in the following phases of the measurement campaigns. Also optical measurement techniques like PIV and PSP will be developed and implemented to characterize the flow around the final configuration of the heat exchanger.

Acknowledgments

Thanks to Claus Sieverding for the assistance in the IGVs design and many discussions on the tunnel conception. Likewise thanks to J. Desset for his contribution to the design process and to J. Prinsier for his valuable help on the CFD simulations.

This work is carried out in the frame of the INTELLIGENT COOLING SYSTEM project. The author would like to acknowledge the financial support of the Region Wallone, the pole of competitiveness Skywin, and the industrial support of TechSpace Aero.

References

[1] H. Streifinger. Fuel/Oil System Thermal Management in Aircraft Turbine Engines. In *RTO-Applied Vehicle Technology Panel, Symposium on Design Principles and Methods for Aircraft Gas Turbine Engines*, Toulouse, 1998.

[2] Andreas Linke-Diesinger. *Systems of Commercial Turbofan Engines: An Introduction to Systems Functions*. Springer, 2008.

[3] J. Armstrong and D. Winstanley. A Review of Staggered Array Pin Fin Heat Transfer for Turbine Cooling Applications. *Journal of Turbomachinery*, 110:94–103, 1988.

[4] R. F. Babus'Haq, K. Akintunde, and S. D. Probert. Thermal Performance of a Pin-Fin Assembly . *International Journal of Heat and Fluid Flow*, 16:50–55, 1995.

[5] E. M. Sparrow and V. B. Grannis. Pressure Drop Characteristics of Heat Exchangers consisting of Arrays of Diamond-Shaped Pin Fins. *International Journal of Heat and Mass Transfer*, 34:589–600, 1991.

[6] V. B. Grannis and E. M. Sparrow. Numerical Simulation of Fluid Flow Through an Array of Diamond-Shaped Pin Fins. *Numerical Heat Transfer, Part A: Applications*, 19:381–403, 1991.

[7] D. E. Metzger, C. S. Fan, and S. W. Haley. Effects of Pin Shape and Array Orientation on Heat Transfer and Pressure Loss in Pin Fin Arrays. *Journal of Engineering for Gas Turbinesand Power*, 106:252–257, 1984.

[8] T. Ota and H. Nishiyama . Heat Transfer and Flow Around an Elliptic Cylinder. *International Journal of Heat and Mass Transfer*, 27:1771–1779, 1984.

[9] Q. Li, Z. Chen, U. Flechtner, and H. J. Warnecke. Heat Transfer and Pressure Drop Characteristics in Rectangular Channels with Elliptic Pin Fins. *International Journal of Heat and Fluid Flow*, 19:245–250, 1998.

[10] Z. Chen, Q. Li, D. Meier, and H. J. Warnecke. Convective Heat Transfer and Pressure Loss in Rectangular Ducts with Drop-shaped Pin Fins. *Heat and Mass Transfer*, 33:219–224, 1997.

[11] E. M. Sparrow, B. R. Baliga, and S. V. Patankar. Forced Convection Heat Transfer from a Shrouded Fin Array with and without Tip Clearance. *ASME Journal of Heat Transfer*, 100:572–579, November 1978.

[12] E. M. Sparrow and T. J. Beckey. Pressure Drop Characteristics for a Shrouded Longitudinal-Fin Array with Tip Clearance. *ASME Journal of Heat Transfer*, 103:393–395, May 1981.

[13] E. M. Sparrow and D. S. Kadle. Effect of Tip-to-Shroud Clearance on Turbulent Heat Transfer from a Shrouded, Longitudinal Fin Array. *ASME Journal of Heat Transfer*, 108:519–524, August 1986.

[14] R. S. Lee, H. C. Huang, and W. Y. Chen. A Thermal Study of Extruded Type Heat Sinks in Considering Air Flow Bypass Phenomenon. In *Proc. Sixth IEEE Semi-Therm Symposium*, pages 95–102, 1990.

[15] K. Azar and C. D. Mandrone. Effect of Pin Fin Density of the Thermal Perfomance of Unshrouded Pin Fin Heat Sinks. *ASME Journal of Electronic Packaging*, 116:306–309, December 1994.

[16] H. Shaukatullah and M. A. Gaynes. Effect of Pin Fin Heat Sink Size on Thermal Performance of Surface Mount Plastic Quad Flat Packs. In *Proc. Int. Electronics Packaging Conference*, pages 232–241, Atlanta, September 1994.

[17] C. L. Champman, S. Lee, and B. L. Schmidt. Thermal Performance of an Elliptical Pin Fin Heat Sink. In *Proc. Tenth IEEE Semi-Therm Symposium*, pages 24–31, San Jose, February 1994.

[18] R. A. Wirtz, W. Chen, and R. Zhou. Effect of Flow Bypass on the Performance of Longitudinal Fin Heat Sinks. *ASME Journal of Electronic Packaging*, 116:206–211, 1994.

[19] H. Jonsson and B. Moshfegh. Modeling of the Thermal and Hydraulic Performance of Plate Fin, Strip Fin, and Pin Fin Heat Sinks - Influence of Flow Bypass. In *Proc. 2000 Intersociety Conf. on Thermal Phenomena (ITherm 2000)*, pages 185–192, Las Vegas, May 2000.

[20] S. Lee. Optimun Design and Selection of Heat Sinks. In *IEEE Transactions on Components, Packaging and Manufacturing Technologies*, volume 18, pages 812–817, December 1995.

[21] R. Simons and R. Schmidt. A simple Method to Estimate Heat Sink Air Flow Bypass. *Electronics Cooling*, 3(2):36–37, May 1997.

[22] M. A. Butterbaugh and S. S. Kang. Effect of Airflow Bypass on the Performance of Heat Sinks in Electronic Cooling. *Advances in Electronic Packaging*, 10:843–848, 19995.

[23] A. Pope and K. L. Goin. *High-Speed Wind Tunnel Testing*. John Wiley & Sons, Inc., 1965.

[24] Alan Pope and J. J. Harper. *Low Speed Wind Tunnel Testing*. John Wiley & Songs, 1966.

[25] R. C. Pankhurst and D. W. Holder. *Wind Tunnel Techniue*. Sir Isaac Pitman and Sons, 1952.

[26] *Aerodynamics of Wind Tunnel Circuits and their Components*, AGARD CP 585, 1997.

[27] W. T Eckert, K. W. Mort, and J. Jope. Aerodynamic Design Guidelines and Computer Program for Estimation of Subsonic Wind Tunnel Performance. Technical Report D-8243, NASA, 1976.

[28] G. B. Schubauer, W. G. Spangernberg, and P. S. Klebanoff. Aerodynamis Characteristics of Damping Screens. Technical report, NACA TN 2001, 1950.

[29] R. I. Loehrke and H. M. Nagib. Experiments on Management of Freestream Turbulence. Technical report, AGARD Report 598, September 1972.

[30] H. L. Dryden and I. H. Abbot. The Design of Low Turbulence Wind Tunnels. Technical report, NACA Report 940, 1949.

[31] C. H. Sieverding. Turbine Blade Design. Technical report, von Karman Institute for Fluid Dynamics, 2004.

[32] David Japikse. *Turbomachinery Diffuser Design Technology*. Concepts Eti; 2nd edition, 2000.

[33] B. Bottin. From Subsonic to Continuous Supersonic Wind Tunnels: Similarity laws, tunnel types and components, design consideration. CN 151, von Karman Institute for Fluid Dynamics, Rhode Saint Genese, Belgium, May 1998.

Doctoral Project Summary

Numerical Simulation of Hypersonic Flow in VKI-Longshot Contoured Nozzle.

Khalil Bensassi*
Supervisor: Patrick Rambaud †
von Karman Institute for Fluid Dynamics, Rhode-Saint-Genèse, 1640, Belgium
Promoter: Herman Deconinck ‡
von Karman Institute for Fluid Dynamics, Rhode-Saint-Genèse, 1640, Belgium
Universitè libre de Bruxelles, Belgium

Abstract

The accuracy of the rebuilded free stream conditions in the VKI-Longshot facility is investigated by means of numerical computations of axisymmetric hypersonic flow in a contoured nozzle. Both equilibrium and nonequilibrium cases are considered. The total conditions provided by experiments at test-time of zero and ten milliseconds were used for these simulations and the results is compared with measured and rebuilded data. Computational fluid dynamics simulations for the equilibrium case are generally in good agreement with experimental data, whereas thermal nonequilibrium simulations demonstrate that the vibrational temperature freezes near the throat at 65% of its initial value which affects the conditions downstream in the nozzle and leads to differences with the experimental rebuilded data. A new rebuilding procedure including thermal nonequilibrium is needed in order get accurate and reliable free stream conditions.

Nomenclature

e_v	=	Specific vibrational energy	n_i	=	Inward normal *s*
e_v^*	=	e_v at translational temperature	T	=	Translational temperature
H	=	Total enthalpy	T^v	=	Vibrational temperature
p	=	pressure	$\mathbf{u}$	=	velocity
ρ	=	density			

1 Introduction

The free stream conditions in most hypersonic wind tunnels are very difficult to assess and the uncertainties on their values could reach 20%. It's mostly due to the lack

*PhD Candidate, Aeronautics and Aerospace Department, Chaussée de Waterloo 72, bensassi@vki.ac.be.
†Assistant Professor, Aeronautics and Aerospace Department, Chaussée de Waterloo 72, rambaud@vki.ac.be.
‡Professor, Aeronautics and Aerospace Department, Chaussée de Waterloo 72, deconinck@vki.ac.be.

of experimental data on some part of the facility like inside the nozzle or the driven tube and the technical difficulties to measure some main flow parameters. The usual method is to rebuild these missing data using one dimensional solver based on shock relations and/or isentropic assumptions. In the VKI-Longshot wind tunnel as described in the next section, the measured data are the reservoir pressure, the stagnation pressure and heat flux in the chamber. The free stream conditions and the total temperature are computed assuming isentropic expansion in the nozzle and using Fay-Riddell[1] formula combined with shock relations. The full description of the VKI-Longshot rebuilding code could be found in Ref [2]. In order to investigate the accuracy of this rebuilding process, numerical investigations were previously done in Ref[3], however, high temperature effect ie. vibrational nonequilibrium was not taken into account. In this paper, numerical simulations of the flow field in the Longshot contoured nozzle are performed considering both equilibrium and thermal nonequilibrium. Real gas effect due to high pressure in the reservoir has been previously invetigated by Candler [4] for a hypersonic nozzle. It's has been shown that the free steram Mach number tends to increase due to real gas effects, however, in the present work, it will not be taken into account and we focus on thermal nonequilibrium effects.

2 Experimental Setup

The VKI-Longshot free piston tunnel is a short duration facility that can be operated with either nitrogen or carbon dioxide and it is designed to reach very high Reynolds number hypersonic flows. It is essentially based on two tubes (driver and driven tubes) and a nozzle which discharges into a test chamber. It has a Mach 14 contoured nozzle [5, 6] of 0.42 m exit diameter and a 6° conical nozzle of 0.60 m exit diameter which can be used throughout a Mach number range from 15 to 20. Figure 1 shows the VKI-Longshot contoured nozzle geometry and table 1 gives the general specifications.

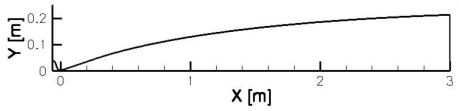

Figure 1: VKI-Longshot contoured nozzle Geometry.

Inlet radius [mm]	Throat radius [mm]	Exit radius [mm]	Length [mm]
38.1	3.225	213.34	3067

Table 1: VKI-Longshot Contoured nozzle dimensions.

Due to the very high pressure levels achieved into the reservoir, the Reynolds numbers simulated are very high (up to 14 millions per meter). Therefore, this facility is particularly well suited for the study of high Mach and Reynolds number flows and provides a good duplication of spacecraft re-entry trajectories with respect to these two non dimensional parameters.

The driver gas, usually nitrogen operates at a pressure between 300 and 1000 bars at room temperature, in a 12.5 cm diameter tube which is 6 m long. Before the shot, the driven tube is closed by the piston on the upstream side and on the downstream side

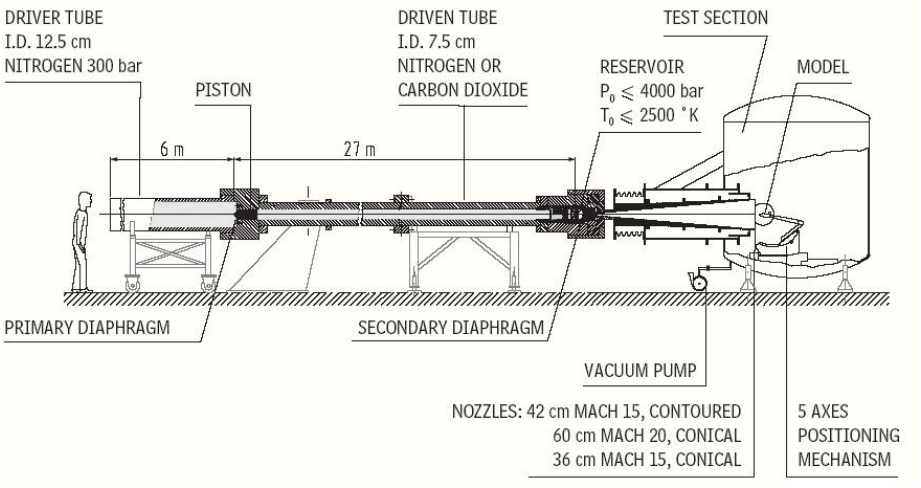

Figure 2: Schematic online of the Longshot tunnel

by a system of 48 valves followed by the reservoir and finally closed by a diaphragm. The initial pressure of the gas in the driven tube can vary from 1 to 15 bars and its temperature is the room temperature. The nozzle and chamber are evacuated down to about 1 Pa pressure.The piston, weighting is between 1.5 to 9 kg, it is maintained by a diaphragm made in aluminum at the end of the driver tube. In order to release the piston, a valve opens and applies the initial pressure on an extra surface of the piston front which is enough to break the diaphragm. The piston, then moves in the driven tube and it is accelerated at speeds of the order of 600 m/s, compressing the gas through a shock wave standing ahead. In front of the piston, the shock wave reflects when it hits the end of the driver tube leading to an increasing of reservoir pressure, then it strikes the piston and reflects again. A series of reflection occur between the piston head and the driver tube end which finally stops the piston. A decompression wave appears at the rear of the piston due to the rarefaction of the gas. It travels from the driver tube to eventually reach the rear part of the piston and causes the piston rebound. When the piston moves back in the driven tube, the pressure ahead of the piston decreases and finally becomes lower than in the reservoir. Therefore, in order to trap the gas in the $320cm^3$ reservoir, a plate check valves is installed at the end of the piston course which causes the closure of the 48 check valves. Once the gas is trapped, the second diaphragm breaks and this allows the gas to expand through the nozzle into a $16m^3$ vacuum vessel. In order to prevent the biggest particles caused by the rupture of the diaphragm from obstructing the nozzle or destroying the model, a particle shield has been placed just upstream the diaphragm.

The experimental data after each shot are the reservoir pressure, the stagnation pressure in the chamber and the stagnation heat flux obtained with a spherical heat probe of 12.7 [mm]. Detailed description of VKI-Longshot instrumentation could found in Ref [2]. The Total temperature and the free stream conditions are rebuilded using these mesured data. Figures 3(a) and 3(b) show respectively the measured total pressure in the reservoir and the measured stagnation heat flux in the chamber for two different shot with high and low Reynolds number. The test-time duration is about 20 ms and the reference free stream conditions are taken at a test-time of 10 ms. In This work, we

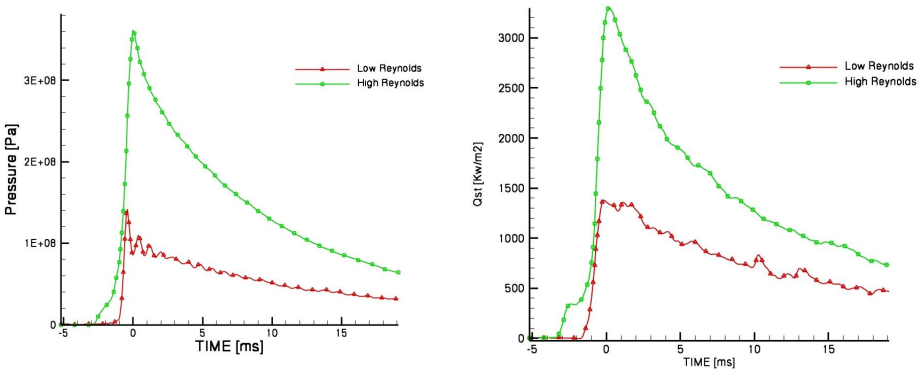

(a) **Measured pressure in the reservoir.** (b) **Measured stagnation heat flux in the chamber.**

Figure 3: VKI-Longshot experimental data

focus only on high Reynolds condition.

3 Governing Equations

The sets of governing PDE's (Navier-Stokes) describing a 2D axisymmetric flow in a continuum regime can be expressed in conservative and hyper-vectorial form as:

$$\frac{\partial \mathbf{U}}{\partial \mathbf{P}} \frac{\partial r\mathbf{P}}{\partial t} + \frac{\partial r\mathbf{F}_x^c}{\partial x} + \frac{\partial r\mathbf{F}_r^c}{\partial r} = \frac{\partial r\mathbf{F}_x^d}{\partial x} + \frac{\partial r\mathbf{F}_r^d}{\partial r} + \mathbf{S} \tag{1}$$

where x and r are the axial and radial directions. Herein, $\mathbf{U}$ are the conservative variables, $\mathbf{P}$ the variables used for the solution update, $\mathbf{F}^c$ and $\mathbf{F}^d$ respectively the convective and diffusive fluxes, $\mathbf{S}$ the source term.
In the most comprehensive case here considered, namely that of a gas mixture in thermal and chemical non-equilibrium, the conservative and natural variables corresponding to a 2-temperature model for neutral mixtures [7, 8] can be expressed as follows:

$$\mathbf{U} = (\rho_s, \rho\mathbf{u}, \rho E, \rho e_v)^T, \quad \mathbf{P} = (\rho_s, \mathbf{u}, T, T_v)^T \tag{2}$$

where, in particular, ρ_s represents the partial densities, e_v is the vibrational energy per unit mass and T_v stands for the vibrational temperature.

3.1 Convective and diffusive fluxes

In this case, the convective and diffusive fluxes are defined by:

$$\mathbf{F}^c = \begin{pmatrix} \rho_s\mathbf{u} \\ \rho\mathbf{u}\mathbf{u} + p\hat{I} \\ \rho\mathbf{u}H \\ \rho\mathbf{u}e^v \end{pmatrix}, \quad \mathbf{F}^d = \begin{pmatrix} -\rho_s\mathbf{u}_s^d \\ \bar{\bar{\tau}} \\ (\bar{\bar{\tau}}\cdot\mathbf{u})^T - \mathbf{q} \\ -\mathbf{q}_v \end{pmatrix}. \tag{3}$$

The tensor of viscous stresses $\bar{\bar{\tau}}$ appearing in Eq. 3 is defined as

$$\tau_{ij} = \mu \left[\left(\frac{\partial u_j}{\partial x_i} + \frac{\partial u_i}{\partial x_j} \right) - \frac{2}{3} \nabla \cdot \mathbf{u} \, \delta_{ij} \right] - \delta_{ij} \frac{2}{3} \mu \frac{v}{r} \tag{4}$$

and it is computed using Stokes' hypothesis of negligible bulk viscosity effects. Herein, the dynamic viscosity μ is computed rigorously from kinetic theory by using the transport algorithms described in [9].
The mass diffusion fluxes $\rho_s \mathbf{u}_s^d$ are computed by solving the Stefan-Maxwell system [10, 11] of equations which consist of a linear system (in the diffusion fluxes) of as many equations as the chemical species are present in the mixture. The roto-translational and vibrational heat fluxes $\mathbf{q}$ and $\mathbf{q}_v$ are defined as

$$\mathbf{q} = -\lambda \nabla T - \lambda_v \nabla T_v - \sum_s \rho_s \mathbf{u_s} h_s, \quad \mathbf{q}_V = -\lambda_v \nabla T_v - \sum_s \rho_s \mathbf{u_s} h_s^v \tag{5}$$

where the λ is the roto-translational thermal conductivity, λ_v is the vibrational thermal conductivity and the species enthalpies h_s include translational, rotational, vibrational and formation contributions.

3.2 Source terms

The source terms in Eq. 2 can be expressed as

$$\mathbf{S} = \begin{pmatrix} \mathbf{0} \\ 0 \\ p - \tau_{\theta\theta} \\ 0 \\ 0 \end{pmatrix} + \frac{1}{r} \begin{pmatrix} \dot{\omega}_s \\ 0 \\ 0 \\ 0 \\ \dot{\omega}^v \end{pmatrix} \tag{6}$$

where, in particular, $\tau_{\theta\theta}$ represents the following additional viscous stress component in the circumferential direction θ, due the axisymmetric formulation:

$$\tau_{\theta\theta} = -\frac{2}{3} \mu \left(\frac{\partial u}{\partial x} + \frac{\partial v}{\partial r} - 2 \frac{v}{r} \right) \tag{7}$$

The mass production/destruction term $\dot{\omega}_s$ for chemical species with partial densities ρ_s which appears in Eq. 6 is formulated as follows:

$$\frac{\dot{\omega}_s}{M_s} = \sum_{r=1}^{Nr} \left(\nu_{sr}^{''} - \nu_{sr}^{'} \right) \left\{ k_{fr} \prod_{j=1}^{Ns} \left(\frac{\rho_j}{M_j} \right)^{\nu_{jr}^{'}} - k_{br} \prod_{j=1}^{Ns} \left(\frac{\rho_j}{M_j} \right)^{\nu_{jr}^{''}} \right\} \tag{8}$$

where the forward reaction rates k_{fr} corresponding to a 2-species nitrogen mixture used in this work are taken from [12].
The term $\dot{\omega}^v$ expresses the energy exchange (relaxation) between vibrational and translational modes and the vibrational energy lost or gained due to molecular depletion (dissociation) or production (recombination):

$$\dot{\omega}^v = \sum_s \rho_s \frac{(e_{v,s}^* - e_{v,s})}{\tau_s} + \sum_s \tilde{D}_s \dot{\omega}_s \tag{9}$$

where the relaxation time τ_s is given by Millikan and White [13] with Park's correction for high temperatures [14]. More details about the thermo-chemical model can be found in [15].

4 Numerical Technique

4.1 Finite Volume method

All the results to be presented have been obtained by means of the parallel FV solver for unstructured grids [16] provided by the COOLFluiD framework [17, 18]. The FV discretization is applied to the system of governing equations written in integral conservation form:

$$\frac{\partial}{\partial t}\int_{\Omega}\mathbf{U}\,d\Omega+\oint_{d\partial\Omega}\mathbf{F}^{c}\cdot\mathbf{n}\,d\partial\Omega=\oint_{d\partial\Omega}\mathbf{F}^{d}\cdot\mathbf{n}\,d\partial\Omega+\int_{\Omega}\mathbf{S}\,d\Omega \tag{10}$$

We apply a conventional cell centered approximation, which assumes solution vectors located at the centroid of each computational cell. Inverse-distance weighted least square reconstruction [19] is utilized to yield second order accuracy. Oscillation free solutions are obtained with the multidimensional limiter of Venkatakhrisnan [20]. In particular, a version of the Roe scheme [21] which combines the consistent linearization described in [8] and an entropy fix from [22] has been utilized for discretizing the convective fluxes in all our computations, as described hereafter [16].

4.1.1 Convective Flux discretization

In its general formulation [21] Roe's scheme reads:

$$\mathbf{F}^{Roe}=\frac{1}{2}\left[\mathbf{F}_{n}(\mathbf{P}^{L})+\mathbf{F}_{n}(\mathbf{P}^{R})\right]-\frac{1}{2}\mid\mathbf{A}(\bar{\mathbf{Z}})\mid\left[\mathbf{U}(\mathbf{P}^{R})-\mathbf{U}(\mathbf{P}^{L})\right] \tag{11}$$

with

$$\mathbf{A}=\frac{\partial\mathbf{F}_{n}}{\partial\mathbf{U}},\quad\mid\mathbf{A}\mid=\mathbf{R}\mid\mathbf{\Lambda}\mid\mathbf{R^{-1}},\quad\mid\mathbf{\Lambda}\mid_{ij}=\mid\lambda\mid_{i}\delta_{ij} \tag{12}$$

where $\mathbf{R}$ is the matrix of right eigenvectors, $\mathbf{\Lambda}$ the diagonal matrix of eigenvalues,$\mathbf{U}$ are the conservative variables and $\mathbf{P}$ are the natural variables in our case. A key ingredient of the method is the linearization of the flux jacobian matrix $\mid\mathbf{A}\mid$, projected onto the direction of the face normal $\mathbf{n}$. However, for the system of equations describing a mixture of perfect gases in thermo-chemical non equilibrium such a linearization is not readily available. As recalled in [8], one of the properties that the matrix $\bar{\mathbf{A}}$ has to satisfy is:

$$\Delta(\mathbf{F}_{n})=\bar{\mathbf{A}}\Delta(\mathbf{U}) \tag{13}$$

where $\Delta(.)=(.)_{R}-(.)_{L}$. Eq.13 is rigorously valid for all the flux components which are homogeneous quadratic functions in the components of Z, except for the pressure flux. In the case of a neutral gas mixture with N_s chemical species, the momentum components of Eq. 13 are satisfied if the following condition holds:

$$\Delta(p)=\sum_{s=1}^{N_{s}}\bar{\alpha_{s}}\Delta(\rho_{s})+\bar{\beta}\Delta\rho(e_{tr}) \tag{14}$$

where

$$\beta=\frac{\partial p}{\partial\rho E},\quad\alpha_{s}=RT/M_{s}-\beta e_{tr,s},\quad e_{tr,s}=(f_{s}RT+\Delta h_{f,s})/M_{s} \tag{15}$$

with $f_s = 2.5$ for molecules and $f_s = 1.5$ for atoms. Different methods have been proposed in order to satisfy Eq.14, like the approximate and relatively complex solution in [23], the recipe based on computational experience in [24], the choice of a simple average of left and right states in conservative variables as in [22]. In our case, following the simple and yet accurate approach presented in [8], requiring that $\bar{\alpha_s}$ and $\bar{\beta}$ form a consistent set of thermodynamic variables together with the other Roe-average variables, we define $a = \sqrt{\rho_L}/(\sqrt{\rho_L} + \sqrt{\rho_R})$ and $b = (1 - a)$. Consequently, the following relations hold:

$$\bar{y_s} = a(y_s)_L + b(y_R)_R, \qquad s = 1, ..., N_s \tag{16}$$

$$\bar{\mathbf{u}} = a\mathbf{u}_L + b\mathbf{u}_R, \quad \bar{H} = aH_L + bH_R, \quad \bar{e_V} = a(e_V)_L + b(e_V)_R \tag{17}$$

Moreover, if we choose the following definitions for $\bar{\beta}$, $\bar{\alpha_s}$,$\bar{e}_{tr,s}$ and $\bar{a}^2$:

$$\bar{\beta} = \left[\sum_{s=1}^{N_s} \bar{y_s}/M_s\right] / \left[\sum_{s=1}^{N_s} f_s\bar{y_s}/M_s\right] \tag{18}$$

$$\bar{\alpha_s} = R\bar{T}/M_s - \beta\bar{e_{tr,s}} \tag{19}$$

$$\bar{e}_{tr,s} = (f_s R\bar{T} + \Delta h_{f,s})/M_s \tag{20}$$

$$\bar{a}^2 = \sum_{s=1}^{N_s} \bar{\alpha_s}\bar{y_s} + \bar{\beta}(\bar{H} - \bar{q} - \bar{e_V}) \tag{21}$$

As shown in [8], those relations lead to some remarkably simple results like

$$\bar{T} = aT_L + bT_R, \quad \bar{e}_{tr} = a(e_{tr})_L + b(e_{tr})_R, \quad \overline{p/\rho} = a(p/\rho)_L + b(p/\rho)_R \tag{22}$$

which allow us to perform a consistent linearization $|\ \mathbf{A}\ |$.
In order to prevent the appearance of unphysical expansion shocks in the rapidly accelerating flow, we apply one of the entropy fixes proposed in [22] to correct the linearized eigenvalues:

$$|\ \tilde{\lambda_l}\ | = max(|\ \lambda_l(\bar{\mathbf{Z}})\ |, \eta). \tag{23}$$

4.2 Implicit Time integration

The choice of a linear Backward Euler for driving the solution to steady state leads to rewrite the system Eqs. (10) as follows:

$$\frac{\mathbf{U}(\mathbf{P}) - \mathbf{U}(\mathbf{P}^n)}{\Delta t} + \mathbf{R}^{FV}(\mathbf{P}) = 0 = \tilde{\mathbf{R}}(\mathbf{P}) \tag{24}$$

where $\tilde{\mathbf{R}}(\mathbf{P})$ is a *pseudo-steady* residual, $\mathbf{U} = \mathbf{U}(\mathbf{P})$ an explicit analytical relation and $\mathbf{P}$ the vector of natural variables (defined in Eq. 2) in which the governing equations are explicitly closed and in which it is therefore convenient to store the solution vector. The application of a one step Newton method yields the following linear system:

$$\left[\frac{\partial\tilde{\mathbf{R}}}{\partial P}(\mathbf{P}^n)\right]\Delta\mathbf{P}^n = -\tilde{\mathbf{R}}(\mathbf{P}^n), \tag{25}$$

where the jacobian matrix $\frac{\partial \tilde{\mathbf{R}}}{\partial \mathbf{P}}$ is computed numerically with respect to the natural variables and assuming a first order stencil. The GMRES algorithm with an Additive Schwartz preconditioner provided by the PETSC library [25] serves to solve in parallel the corresponding linear systems arising from Newton linearizations. The solution update is also performed in natural variables.

5 Grid Convergence study

Computational fluid dynamics simulations are performed using different meshes. The stagnation conditions used for this gird study are P_t = 3168 [bar] and T_t = 2481.8 [K]. The test gas, nitrogen is assumed to behave as a perfect and in equilibrium state and the flow is laminar. The Mach number profile along the symmetry axis is taken as a criteria for the grid convergence. The design of the grid for the contoured hypersonic nozzle was done using two strategies for the mesh refinement. The first method is a global mesh refinement, the grid is refined in both axial and radial directions. Six different grids were generated and numerical computations were performed. Figure 4(b) shows the Mach number profile along the symmetry axis for different meshes. In the second method the grid was refined only in the supersonic region close to the throat. In this region the flow is expanding rapidly which affects the Mach number at the exit of the Nozzle as shown in Figure 4(b).

.

Figure 4(a) shows that a grid with a 300000 nodes is needed in order to achieve the grid convergence. However, one could reduce the number of node combining general mesh refinement and local mesh refinement. Figure 4(c) shows that the same Mach number profile could be achieved using only 150000 nodes. This mesh is the reference mesh used for all the computations presented in this paper.

6 Results

A series of numerical steady state computations simulating the flow in the contoured hypersonic nozzle are performed. Nitrogen is considered as a perfect gas for both equilibrium and thermal-nonequilibrium cases. The flow is assumed to be laminar. The Inlet conditions for the computations were obtained from shot1427 [26] which corresponds to high Reynolds number. The experimental data were given in time as shown in figures 3(a) and 3(b). The data at t= 0 [ms] and = 10 [ms] are extracted for our simulations. These conditions correspond respectively to the pic and the mid-test values. Table 2 gives the total conditions needed for the nozzle computations and Table 3 the corresponding rebuilded free stream conditions.

	$P_t[Pa]$	$T_t[K]$	$Qst[Mw/m^2]$
$t = 0ms$	316886848	2481.82	3180
$t = 10ms$	121932304	1699.49	1360

Table 2: Total conditions and Stagnation Heat flux: Shot1427.

Figures 5 shows that the Mach number profile along the symmetry axis is almost constant between the beginning of the test and the mid-time-test at 10 [ms].

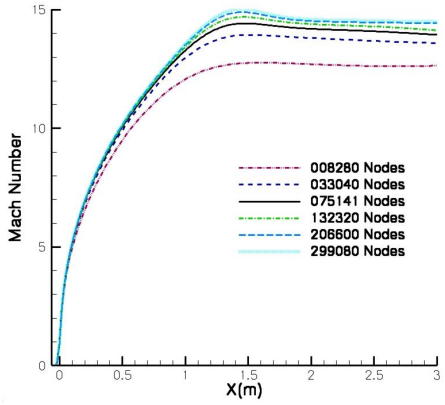

(a) **Global mesh refinement.**

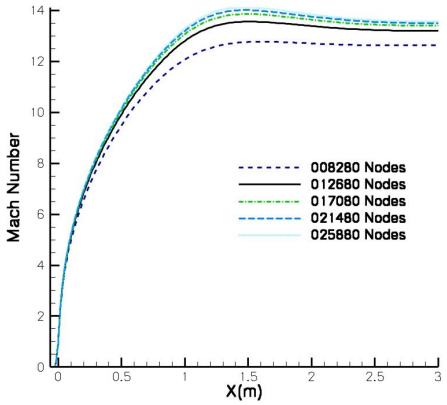

(b) **Local mesh refinement.**

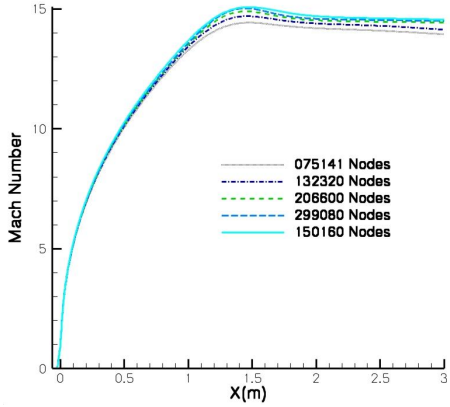

(c) **Local and global mesh refinement combined.**

Figure 4: Mach number profile along the symmetry axis for different meshes.

	$p_\infty[Pa]$	$T_\infty[K]$	$U_\infty[m/s]$
$t = 0ms$	490.61	2242.65	50.26
$t = 10ms$	230.02	1857.97	37.81

Table 3: Rebuilded free stream conditions: Shot1427.

However, The conditions in the nozzle are not completely steady, as shown in Figures 6 and 7. The static pressure and the static temperature are decreasing during the first 10 ms because of the decrease of the total conditions in the reservoir.

It can be seen from figure 5 that the maximum Mach number is reached in the middle of the nozzle at about 1.3 m from the throat and there is a slight decrease of the Mach number until it reaches its exit value, This unexpected behavior could be due to a compression wave traveling from the wall and propagating to the symmetry axis. Figures 6, 7 show that the pressure and the temperature increase in that region which confirm the compression of the flow.

Table 4 shows that agreement between the rebuilded exit conditions and the simulations at test time of 0 ms is good for the static pressure and slightly difference for

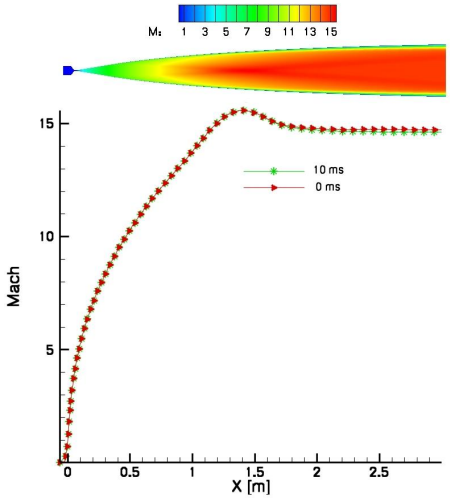

Figure 5: Mach number distribution along the symmetry axis.

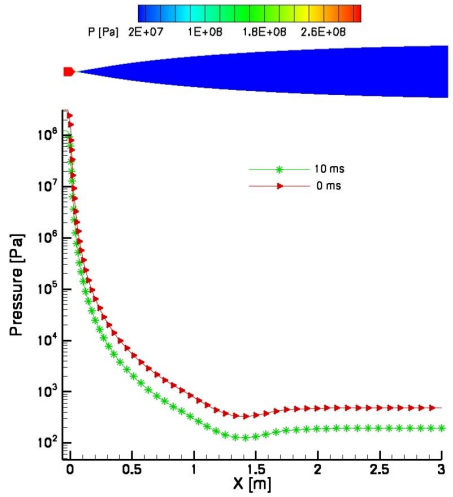

Figure 6: Pressure distribution along the symmetry axis.

the velocity and the static temperature. This is due the fact that a thick boundary layer is present in the nozzle which modify the effective exit section leading to a lower exit velocity value and higher temperature. This boundary layer effect is not taken into account in the rebuilded process which leads to these differences. Therefore, the expansion is overestimated by the rebuilding code. Table 5 shows the results at 10 ms. The agreement is good for the temperature and the velocity but the pressure is 15 % lower than the rebuilded data. The reason of this difference is still unknown at this time and it is under investigation.

In the following results, we consider vibrational nonequilibrium. Figure 8 shows the effect of thermal nonequilibrium on Mach number profile at test-time 0ms and 10ms. The Mach number at the exit is slightly higher in both cases compared to equilibrium simulations. It's due to the fact that the speed of sound used for nonequilibrium

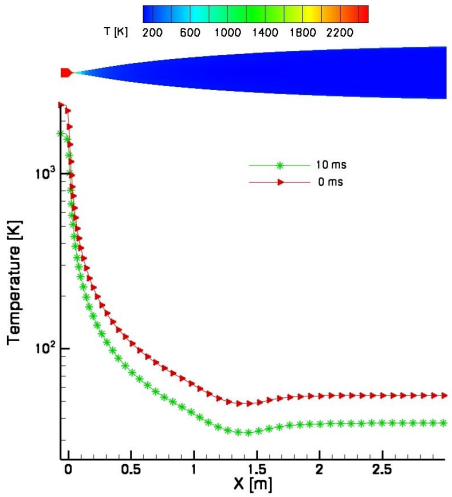

Figure 7: Temperature distribution along the symmetry axis.

0 [ms]	P_∞ (Pa)	U_∞ (K))	T_∞ (K)
Equilibrium	486.4	2208.61	54.1805
Rebuilded data	490.6	2242.7	50.3

Table 4: Nozzle exit conditions at 0ms: CFD vs Experimental Rebuilded data.

10 [ms]	P_∞ (Pa)	U_∞ (K))	T_∞ (K)
Equilibrium	196.43	1827.38	37.6
Rebuilded data	230.0	1858	37.8

Table 5: Nozzle exit conditions at 10ms: CFD vs Experimental Rebuilded data.

computations is the frozen speed of sound. Thus, the nonequilibrium effect tends to increase the Mach number in the nozzle.

In figure 10, it can be seen that the vibrational temperature is frozen at 65% of it's initial value for the testcase corresponding to test-time of 0 ms and 85% at test-time of 10 ms, which affect the conditions downstream the nozzle. Figure 9 shows that the over expansion inside the nozzle is dumped by the thermal nonequilibrium effects. Tables 6 and 7 summarize the exit conditions given by CFD and the rebuilding process.

Run	P_∞ (Pa)	U_∞ (K))	T_∞ (K)	$T_v(K)$
Equilibrium	486.4	2208.61	54.1805	-
Thermal nonequilibrium	438.819	2309.77	58.44	1672.71
Rebuilded data	490.6	2242.7	50.3	-

Table 6: Nozzle exit conditions at 0 ms: CFD vs Experimental Rebuilded data.

It should be noted that thermal nonequilibrium effect is not taken into account in the rebuilding process ,therefore, it was expected that the result of equilibrium computation

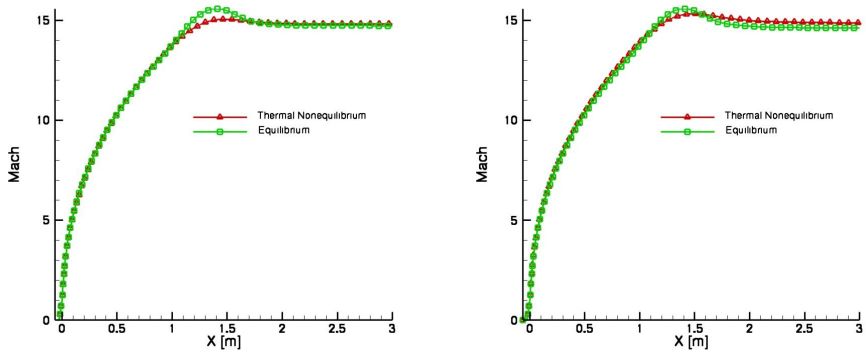

(a) **Mach number distribution at t = 0ms.** (b) **Mach number distribution at t = 10ms.**

Figure 8: Mach number distribution along the symmetry axis

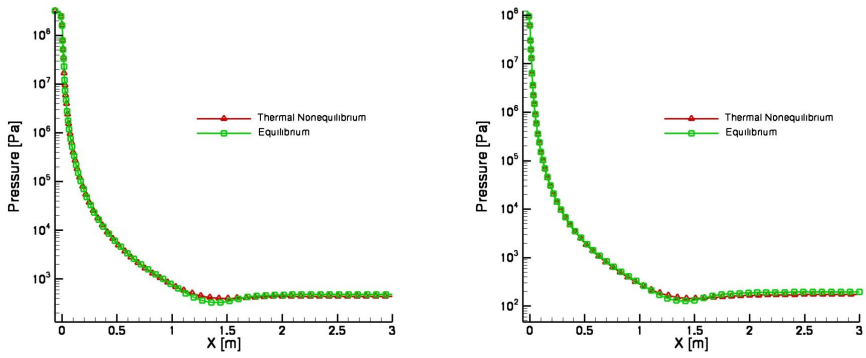

(a) **Pressure distribution at t = 0ms.** (b) **Pressure distribution at t = 10ms.**

Figure 9: Pressure distribution along the symmetry axis

is closer to the rebuilded data than the nonequilibrium computation, specially in case of strong vibrational nonequilibrium.

Run	P_∞ (Pa)	U_∞ (K))	T_∞ (K)	$T_v(K)$
Equilibrium	196.43	1827.38	37.6	-
Thermal nonequilibrium	174.58	1871.74	38.11	1445.18
Rebuilded data	230.0	1858	37.8	-

Table 7: Nozzle exit conditions at 10 ms: CFD vs Experimental Rebuilded data.

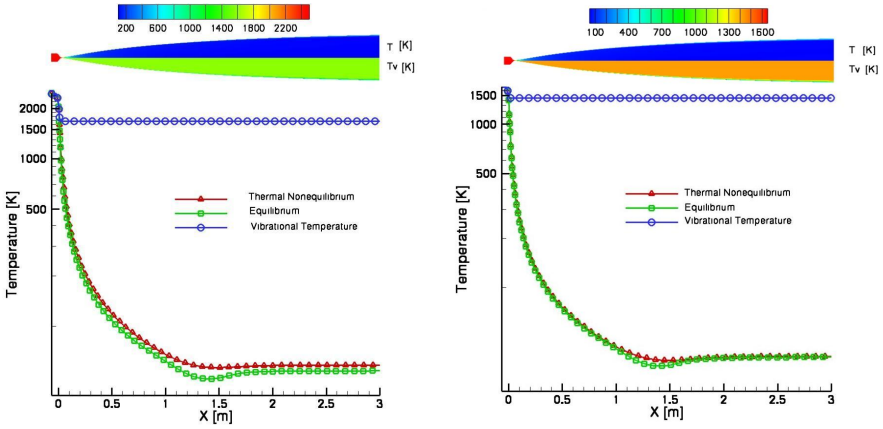

(a) **Temperature distribution at t = 0ms.** (b) **Temperature distribution at t = 10 ms.**

Figure 10: Temperature distribution along the symmetry axis.

7 Conclusion

Numerical simulations of hypersonic flow in the VKI-Longshot hypersonic contoured nozzle have been performed for two different test-time conditions of a high Reynolds number experimental shot. Grid convergence study has been done considering general and local refinement. It has been shown that the mesh in the supersonic region just after the throat has a strong effects on the exit Mach number and local refinement in that region allowed a global reduction of the number of grid points by 50%. Equilibrium computations showed that the Mach number remains constant during the 10 first milliseconds of the test and good agreement was obtained between the computed and the rebuilded exit conditions. Thermal nonequilibrium simulations demonstrate that energy is frozen in the vibrational mode which affect the conditions downstream the nozzle. This strong nonequilibrium effect is not taken into account in the VKI-Longshot rebuilding process, which leads to differences between the computed and rebuilded free stream conditions. A new procedure of rebuilding the total temperature and the free stream conditions is needed in order to include thermal nonequilibrium. To account real gas effects due to high pressure in the reservoir, other equations of state specific for nitrogen should be considered and the effects of intermolecular force on the free stream conditions and the total enthalpy have to be investigated.

Acknowledgments

The author would like to thank Dr. A. Lani for his close collaboration during this work and Mr. S. Paris for the experimental data.

References

[1] Fay, J. and Riddell, F. R., "Theory of Stagnation Point Hheat Transfert in Dissociated Air," *Journal of the Aeronautical Sciences*, Vol. 121, 1958, pp. 73–85.

[2] Simeonides, G., "The VKI hypersonic wind tunnels and associated measurement techniques," VKI TM 46, von Karman Institute for Fluid Dynamics, St. Genesius-Rode, Belgium, 1990.

[3] Bensassi, K., "Numerical investigations of hypersonic flow in the Longshot facility," VKI PR 2007-05, von Karman Institute, St. Genesius-Rode, Belgium, 2007.

[4] Canupp, P. W., Candler, G. V., Perkins, J. N., and Eickson, W. D., "Analysis of Hypersonic Nozzles Icluding Vibrational Nonequilibrium and Intermolecular Force Effects," *AIAA Journal*, Vol. 31(7), 1993, pp. 1243–1249.

[5] Simeonides, G., "The VKI Contoured Mach 15 Longshot nozzle: final design parameters and construction." VKI IN 87/AR, von Karman Institute for Fluid Dynamics, St. Genesius-Rode, Belgium, 1989.

[6] Simeonides, G., "The aerodynamic design of hypersonic countoured axisymmetric nozzles including real gas effets." VKI TM 43, von Karman Institute for Fluid Dynamics, St. Genesius-Rode, Belgium, 1987.

[7] Gnoffo, P. A., Gupta, R. N., and Shinn, J. L., "Conservation equations and physical models for hypersonic air flows in thermal and chemical non-equilibrium." Technical Paper 2867, NASA, 1989.

[8] Prabhu, R. K., "An implementation of a chemical and thermal nonequilibrium flow solver on unstructured meshes and application to blunt bodies," Tech. Rep. NASA-CR-194967, NASA Langley Center, Aug 1994.

[9] Magin, T. and Degrez, G., "Transport Algorithms for Partially Ionized and Unmagnetized Plasmas," *Journal of Computational Physics*, Vol. 198, 2004, pp. 424.

[10] Abeele, D. V., Barbante, P., Degrez, G., and González, J.-P. M., "Numerical Simulation of Multi-Component Inductive Plasma Flows under Chemical Non-Equilibrium," *Heat and Mass Transfer under Plasma Conditions (Ed. P. Fauchais, J. van der Mullen, J. Heberlein)*, Vol. 891, Annals of the New York Academy of Sciences, New York, 1999, pp. 340–347.

[11] Barbante, P. F., Degrez, G., and Sarma, G. S. R., "Computation of Nonequilibrium High-Temperature Axisymmetric Boundary-Layer Flows," *Journal of Thermophysics and Heat Transfer*, Vol. 16, No. 4, 2002, pp. 490–497.

[12] Nompelis, I., *Computational Study of Hypersonic Double-Cone Experiments for Code Validation*, Ph.D. thesis, University of Minnesota, May 2004.

[13] Millikan, R. C. and White, D. R., "Systematics of vibrational relaxation." *Journal of Chemical Physics*, Vol. 39, No. 12, 1963, pp. 3209–3213.

[14] Park, C., "Review of Chemical-Kinetic Problems of Future NASA Mission, I: Earth Entries," *Journal of Thermophysics an Transfer*, Vol. 7, July-Sept 1993, pp. 385–398.

[15] Panesi, M., Lani, A., Magin, T., Pinna, F., Chazot, O., and Deconinck, H., "Numerical investigation of the non equilibrium shock-layer around the EXPERT vehicle," *AIAA Paper 2007-4317*, 38th AIAA Plasmadynamics and Lasers Conference, Miami (Florida), Jun 2007.

[16] Lani, A., *An Object Oriented and High Performance Platform for Aerothermodynamics Simulation*, Ph.D. thesis, Von Karman Institute for Fluid Dynamics, 2009.

[17] Lani, A., Quintino, T., Kimpe, D., Deconinck, H., Vandewalle, S., and Poedts, S., "The COOLFluiD Framework: Design Solutions for High-Performance Object Oriented Scientific Computing Software," *Computational Science ICCS 2005*, edited by P. M. A. S. V. S. Sunderan, G. D. van Albada and J. J. Dongarra, Vol. 1 of *LNCS 3514*, Emory University, Springer, Atlanta, GA, USA, May 2005, pp. 281–286.

[18] Quintino, T., *A Component Environment for High-Performance Scientific Computing. Design and Implementation*, Ph.D. thesis, Katholieke Universiteit Leuven, 2008.

[19] Barth, T., "Aspects of unstructured grids and finite volume solvers for the Euler and Navier-Stokes equations," 25th Computational Fluid Dynamics Lecture Series, Von Karman Institute, March 1994.

[20] Venkatakrishnan, V., "Convergence to steady state solutions of the Euler equations on unstructured grids with limiters," *Journal of Computational Physics*, Vol. 118, 1995, pp. 120–130.

[21] Roe, P., "Approximate riemann solvers, parameters vectors and difference schemes," *Journal of Computational Physics*, Vol. 43, 1981, pp. 357–372.

[22] Sanders, R., Morano, E., and Druguet, M.-C., "Multidimensional dissipation for upwind schemes: stability and applications to gas dynamics," *Journal of Computational Physics*, Vol. 145, No. CP986047, 1998, pp. 511–537.

[23] Liu, Y. and Vinokur, M., "Upwind algorithms for general thermo-chemical nonequilibrium flows," *27th AIAA Aerospace Sciences Meeting*, Reno, Nevada (US), Jan 1989, AIAA 89-0201.

[24] Gnoffo, P. A., "Upwind-biased, point-implicit relaxation strategies for viscous hypersonic flows," *AIAA Paper*, , No. 89-1972-CP, 1989.

[25] Laboratory, A. N., "PETSc: Portable, Extensible Toolkit for Scientific Computation," 2007.

[26] Paris, S., "VKI-Longshot Experimental Data," Vki data file, von Karman Institute, St. Genesius-Rode, Belgium.

HAZARDS IN FLOWS

Doctoral Project Summary

Determination of Concentration and Velocity Fields by Means of MIE Scattering and Digital Image Post-processing

István Horváth*

Supervisor: Prof. Jeroen van Beeck†

von Karman Institute for Fluid Dynamics, Rhode-Saint-Genèse, 1640, Belgium

Promoter: Prof. Jean-Marie Buchlin‡

Université Libre de Bruxelles, Brussels, 1000, Brabant

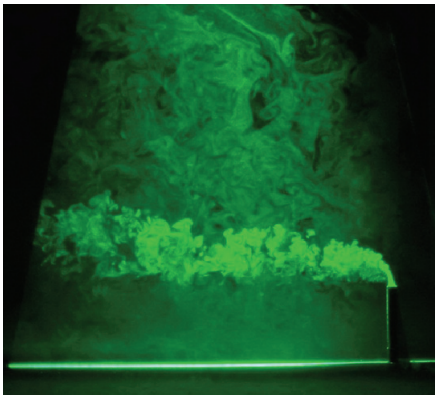

Abstract

The main purpose of this research is to extend the capability of Particle Image Velocimetry (PIV) systems in order to obtain simultaneous information of concentration and velocity in large field of view from the same set of particle images. As this method evolves, it can be a powerful tool for full-scale measurements as well.

* PhD Candidate, Environmental and Applied Fluid Dynamics department at VKI, Chaussée de Waterloo 72 Rhode-Saint-Genèse, 1640, Belgium, horvath@vki.ac.be

† Associate Professor, Environmental and Applied Fluid Dynamics department at VKI, Chaussée de Waterloo 72 Rhode-Saint-Genèse, 1640, Belgium, vanbeeck@vki.ac.be

‡ Professor, Head of Environmental and Applied Fluid Dynamics department at VKI, Chaussée de Waterloo 72 Rhode-Saint-Genèse, 1640, Belgium, buchlin@vki.ac.be

1 Introduction

Research on air pollution has reached major interest in the last few decades, resulting in a growing demand for precise modelling of pollutant concentrations, both experimentally and numerically. Although studying the dispersion of gasses in complex urban environments is essential and directly related to the life quality and safety of people living and working in such areas, it is more convenient to study simplified geometries for validation purposes of CFD simulations. In the present research project, gas dispersion from a single stack in an atmospheric boundary layer is studied, which is a well understood common test case.

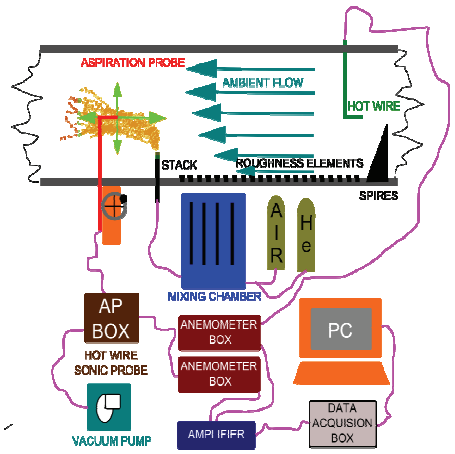

Figure 1. Aspiration Probe Setup

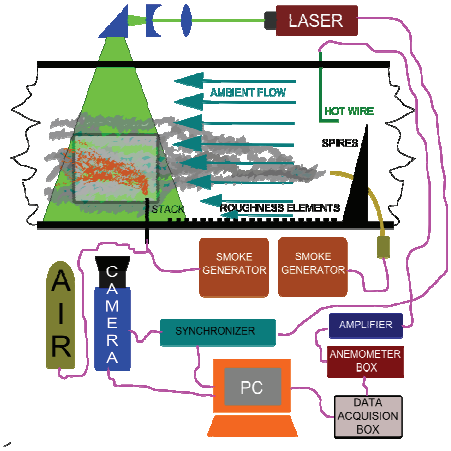

Figure 2. LS-PIV / Mie Scattering Setup

The measurements were performed in the VKI Wind Gallery, which is an atmospheric boundary layer wind tunnel at the von Karman Institute. This facility, equipped with roughness elements and spires upstream of the stack, was able to provide the appropriate boundary layer in which the investigated stack with the plume was immerged. In the field of interest the velocity was acquired by means of Large Scale Particle Image Velocimetry (LS-PIV), while the concentration was obtained by means of both hot-wire Aspiration Probe and Mie Scattering q.v.: Figure 1-2.

2 Large Scale Particle Image Velocimetry

Contrary to standard PIV (**Error! Reference source not found.**) LS-PIV (**Error! Reference source not found.**) treats cloud structures instead of individual particles [1,2]. Capturing and post-processing these distinct structures it is capable to provide both the instantaneous and average velocity fields (**Error! Reference source not found.**-6) and so all the properties which can be deduced from these parameters. The most favourable feature of this new measurement technique is the fact that it uses the armature of standard PIV. In the present study the WIndow-Displacement-Iterative-Multigrid (WIDIM) PIV software was used which was developed in the Von Karman Institute [3].

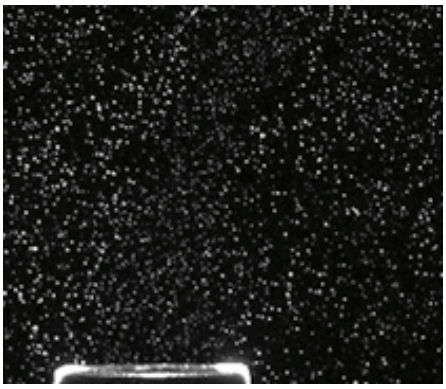

Figure 3. PIV

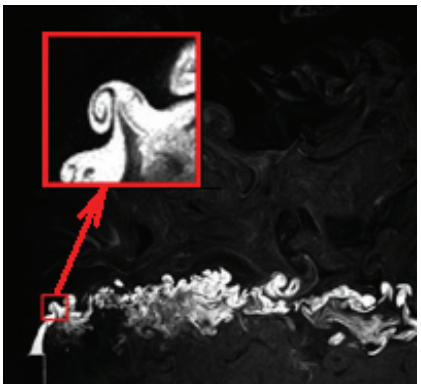

Figure 4. LS-PIV

A signal-to-noise ratio filtering was used to process interrogation windows. If the ratio is below the threshold, the window is not considered as a sample in the accuracy estimation, leading to a low accuracy in regions with a lower number of samples, as for instance, near the stack exit, where turbulent structures where not yet developed.

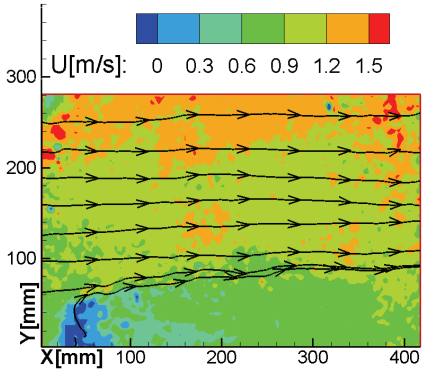

Figure 5. Instantaneous Velocity

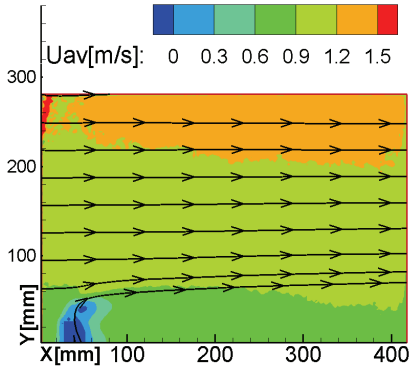

Figure 6. Average Velocity

3 Mie Scattering and Aspiration Probe Concentration measurements

Mie Scattering was employed to determine the concentration of the pollutant. In addition, Aspiration Probe concentration measurements [4] were performed for calibration and comparison purposes. **Error! Reference source not found.** has to be applied on the light intensity values, where C, Cref and I, Iref are the concentration and light intensity at any point and at the reference point respectively. '0' and 'bg' indices correspond to calibration images taken without any smoke and with only upstream smoke. The computations were carried out in MATLAB computing environment. Subsequently, the obtained relative concentration values for the Mie Scattering technique were compared to those measured by an AP in **Error! Reference source not found.**.

$$\frac{C}{C_{ref}} = \frac{I - I_0}{I_{ref} - (I_0)_{ref}} \frac{I_{bg\max}}{I_{bg}} \tag{1}$$

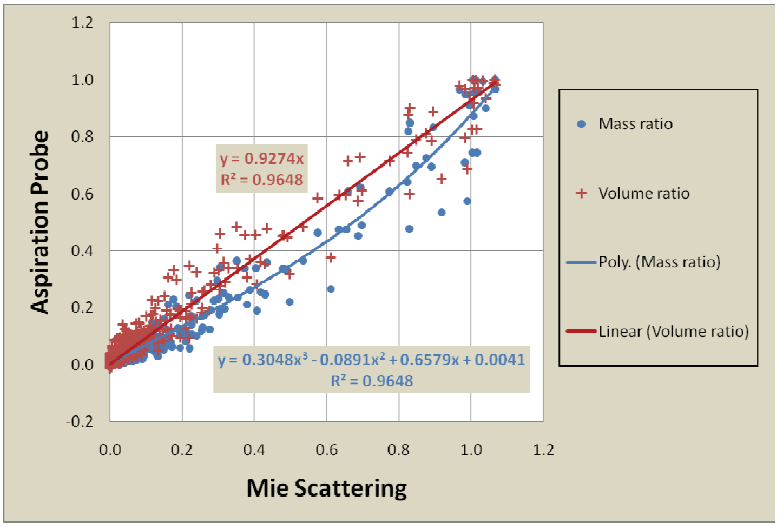

Figure 7. Aspiration Probe vs. Mie Scattering results

The relative light intensity values show a polynomial relationship with mass ratio and a more interesting linear connection to volume ratio for the same least-squares fitting value. The linear fit is very favourable. It provides as such a simple tool for the simultaneous and instantaneous velocity and concentration measurements from the same set of PIV-type images.

4 Conclusion

LS-PIV was employed successfully to determine the average and fluctuating component of the velocity field. It was shown that the same set of images used in LS-PIV can also be used for concentration measurements through LST. Although the accuracy of LST measurements is not as high as aspiration probe measurements, the estimations are reasonable and after applying equation 1, no further correction is needed in order to obtain the relative volumetric ratio of the pollutant.

Up to this point the described measurement technique was only applicable to couple the average fields of concentration and velocity. The reason is the different demands of the velocity and concentration measurements. For the former one the upstream flow is seeded in order to have particles everywhere in the field of interest, while in the latter case it has to be only the source of the pollutant (stack) which introduces scattering particles into the flow. At the present time promising attempts are being carried out in order to overcome this conflict and acquire the corresponding instantaneous values of velocity and concentration as well. In case of a successful output this method can be a break-through of studying the turbulent diffusion. The

turbulent mass flux vector up to now was barely measured and if so, in combination with intrusive techniques, or Laser Induced Fluorescence (LIF) [5, 6].

Acknowledgments

I am heartily thankful to my supervisor Prof. Jeroen van Beeck, whose never ending encouragement, guidance and support gave me momentum in the downs and enabled me to develop an understanding of the subject.
It is a pleasure to thank Prof. Jean-Marie Buchlin. The sensation that I can always turn to him gives me an important assurance.
Thank You…

References

[1] RIETHMULLER, M.; PLANQUART,P. ; *.A New PIV Technique For Very Large Heat-Induced Flow-Fields*; 13th International Heat Transfer Conference IHTC-13 , Sydney, Australia, August 13-18, 2006

[2] I.HORVATH; P.AUDIER; J.P.A.J. VAN BEECK: *Determination of Concentration and Velocity Field by Means of Light Scattering and Digital Image Processing*, "PHYSMOD 2009", An International Workshop on Physical Modelling of Flow and Dispersion Phenomena, August 24-26, 2009, von Karman Institute for Fluid Dynamics, Rhode-Saint-Genèse, Belgium, In Proc.

[3] F.SCARANO; M.L.RIETHMULLER: *Advances in Iterative Multigrid PIV Image Processing,Experiments in Fluids* 29, 1999, S51-S60b

[4] D. MAROTEAUX ;F.MAROTEAUX; M.MURAT: *Experimental Study of a Hot Wire, Sonic Nozzle Probe For Concentration Measurements*, Review of Scientific Instruments, 62(4), April 1991, p1057-1062

[5] G.D-WEIDINGER ; A.STITOU ; J.P.A.J. VAN BEECK; M.L.RIETHMULLER: *Measurement of the Turbulent Mass Flux with PTV in a Street Canyon*, Journal of Wind Engineering and Industrial Aerodynamics 91, 2003, p1117-1131

[6] M.KOOCHESFAHANI; R.COHN; C.MACKINNON: *Simultaneous Whole-Field Measurements of Velocity and Concentration Fields Using a Combination of MTV and LIF*, Measurements Science and Technology. 11, 2000 p1289-1300

Doctoral Project Summary

Experimental characterization and modeling of hazards: BLEVE and Boilover

Delphine Laboureur*

Supervisor and Promoter: Jean-Marie Buchlin †
von Karman Institute for Fluid Dynamics, Rhode-Saint-Genèse, 1640, Belgium
Co-Supervisor: Patrick Rambaud ‡
von Karman Institute for Fluid Dynamics, Rhode-Saint-Genèse, 1640, Belgium

Abstract

BLEVE and Boilover are two types of devastating accidents, involving pressure liquefied reservoir and atmospheric vessels respectively. This extended abstract provides a synthetic review of the work done so far in the two topics; an extensive literature survey and preliminary medium scale experiments. They allowed a better definition of the area of investigation, that will be performed in future laboratory experiments thanks to a new VKI setup.

1 Introduction

Nowadays, more and more chemical process plant sites include storage sites based on pressure liquefied reservoir and/or atmospheric vessels, depending on the industrial activity. These sites can suffer from two types of devastating accidents: BLEVE and Boilover. The BLEVE is defined by Walls [1] as an explosion resulting from the catastrophic failure of a vessel containing a liquid at a temperature significantly above its boiling point at normal atmospheric pressure (i.e. superheated liquid). The Boilover is a violent ejection of fuel due to the vaporization of a water sub-layer, resulting in an enormous fire enlargement and formation of fireball and ground fire.
The objective of the thesis is twofold: to understand the occurrence factors and consequences of these two phenomena, and to model them. The methodology involves extensive literature survey, laboratory and medium field tests experiments as well as CFD simulations. The final outcome is a robust engineering tool able to describe both BLEVE and Boilover phenomena. This short communication provides a synthetic review of the work done so far in the two topics.

*PhD Candidate, Environmental and Applied Fluid Dynamics Department, Chaussée de Waterloo 72, laboureu@vki.ac.be.

†Head of Department, Environmental and Applied Fluid Dynamics Department, Chaussée de Waterloo 72, buchlin@vki.ac.be.

‡Assistant Professor, Environmental and Applied Fluid Dynamics Department, Chaussée de Waterloo 72, rambaud@vki.ac.be

2 BLEVE research

BLEVE is an acronym for Boiling Liquid Expanding Vapor Explosion. It is a complicated phenomenon; it starts from the rupture of reservoir, which is followed by liquid vaporization aspects, which leads generally to gas explosions and fire ball formation. The BLEVE scenario is illustrated in figure 1.



Figure 1: BLEVE principle

From literature survey, the main BLEVE theory was first proposed by Reid [2] and completed by Birk [3]. These authors relate the severity of BLEVE with the superheat limit temperature; it is the border between heterogeneous and homogeneous nucleation. The literature about explosive vaporization is rather vast for bubble and liquid front evaporation but has never been surprisingly studied from a small scale pressurized vessel due to the complexity both of the phenomenon and the instrumentation to be involved.
The occurrence of a BLEVE can lead to 3 major consequences: blast wave generation and fireball and fragments formation. This PhD work aims to obtain sets of relevant experimental data to compare them to predictions of different existing models. Fluid temperature, type of rupture, vessel design, presence of a fire prior to rupture, etc... can influence the apparition of a BLEVE.
To try to establish more clearly the BLEVE event factors, two preliminary experimental campaigns have been conducted in CEG (Centre d'Études de Gramat, France) by using Campingaz bottles of 0.5 and 1.8kg. It is observed that as the reservoir is attacked by a projectile impacting in the liquid zone, a jet release is formed without fragment generation (as shown in 2).



Figure 2: Visualization of BLEVE experiments: (left) impact test at t=0,0.043,0.21s, (rigt) fire and impact test at t=0,0.015,0.068s

A catastrophic rupture of the vessel was obtained with the reservoir placed in reverse position (if normal position, the rupture appears at the shutting valve, leading to a jet release) and subjected to a fire source. Further campaigns will be performed in 2010 with internally instrumented reservoirs to get systematic and mastered BLEVE formation to acquire more insight of the phenomenon.

The configuration of the experimental campaigns performed inside a $3.6m$ diameter tunnel did not allow relevant development and measurements of fireballs and fragment trajectories. However the blast wave following the vessel rupture has been tracked and compared to literature models. Figure 3 (left) shows the results. The pressure signal was recorded by transducers placed at 0.62m, 1.79m and 2.68m from the bottle, respectively. Two overpressure peaks are systematically detected. They represent the vapor expansion and the fluid vaporization, respectively. The models used for comparison in figure 3 (right) are based on correlations of overpressure and explosion energy, on graphs elaborated by Baker & Al. [4]. Good prediction of the second peak is obtained with modeling of irreversible expansion of liquid and vapor following rupture as proposed by Planas-Cluchi [5] and Casals [6]. Genova model [7] using energy released due to excess of heat stored in the liquid fits also rather well the experimental findings. In general the models overestimate the first peak although the Van den Berg model [8] based on a released time can be tuned to match the experiments as depicted in figure 3,right. Of course, further measurements are needed to confirm the more relevant overpressure model.

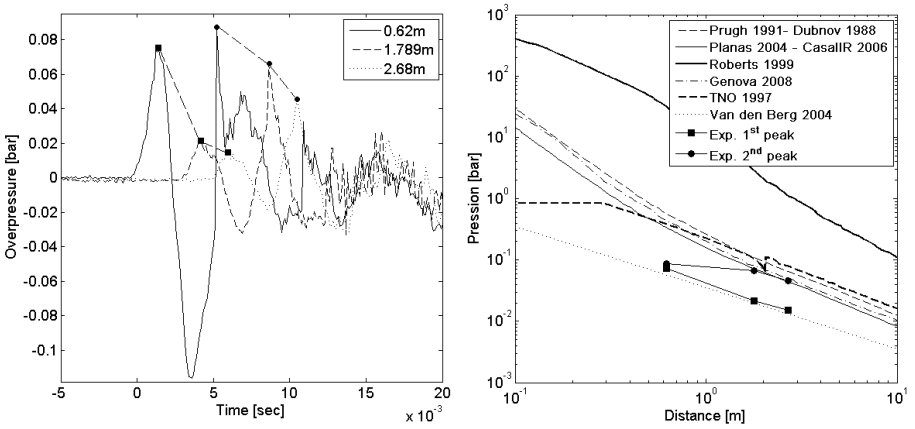

Figure 3: Overpressure in function of distance following the rupture at 17bar of a vessel containing 0.5kg of LPG: (left) Measured signals (right) Model (using propane) & Experiment comparison

3 Boilover research

The principal theory of Boilover, first proposed by Hall [9], links the phenomenon with the apparition of a zone of more or less constant temperature inside the fuel, called "hot-zone" , which is developed at rate higher that the burning rate of the hydrocarbon free surface. Figure 4 sketches the situation.

This hot zone will enhance the heat propagation towards the water layer, decrease time of Boilover occurrence and augments the intensity of consequences. If the fuel nature or the geometry of the reservoir or other parameter does not allow the formation of a hot-zone, the temperature gradient at the fuel-water interface will be smaller and a bigger part of the fuel will burn before water vaporization; consequently much lower intensity of consequences will be observed.

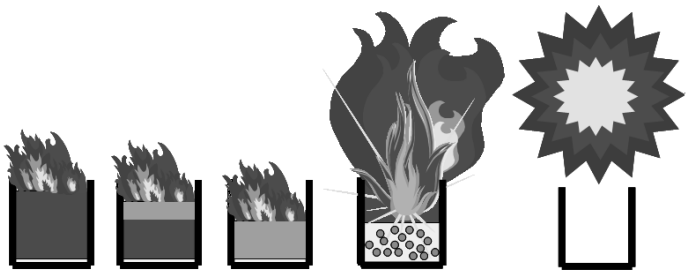

Figure 4: Boilover principle

This hot-zone has been clearly identified in literature, however, no theory is universally yet accepted concerning the heat transfer mechanisms that lead to its creation and development as well as Boilover apparition. Moreover, the modeling of the flame shape and thermal radiation during the Boilover is also poorly reported in literature. The objective of the present work is to make small and medium scale experiments to understand and model the phenomenon.

Two experimental campaigns have already been performed at the von Karman Institute. Reservoirs of 0.15 and 0.3m in diameter and 0.09m high have been tested. They were filled with 0.06m of a mixture of diesel and Valvata oil to obtain a higher viscosity, needed for the fuel to form a piston effect, and a 0.02-0.025m water sub-layer. Every test allowed measuring the temperature at center of the reservoir at different heights, with a spatial resolution of 5 to 15mm. The mass loss due to fuel combustion is monitored and thermal radiation is measured at distance of 6D to 7.25D. Visualization is recorded with color camera.

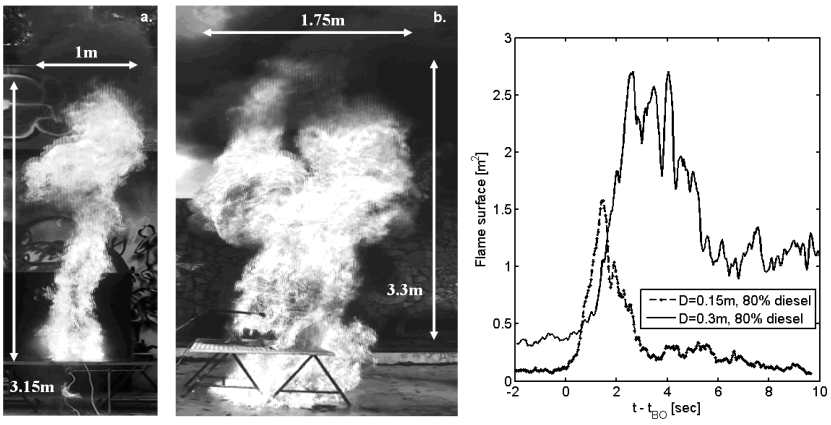

Figure 5: Flame shape (left) Visualization of maximum flame shape during Boilover for a reservoir of a. 0.15m diameter and b. 0.3m (right) Temporal evolution of flame surface for 2 different pool size.

Figure 5 (left) shows how the Boilover event looks. The fuel ejection by water vaporization is increasing the flame shape by 7 to 12 times (for reservoir of 0.3m and 0.15m in diameter, respectively). The flame grows first as column, ending in a mush-

room fireball resulting from turbulence vortices on the edges.
The measured temperature agrees with the data found in literature, dividing the Boilover phenomenon in two periods. At first, the fuel combustion heats gradually the fuel-water interface. This period is called *stationary* because the fuel burning rate and the radiation produced by the flames are constant. The fuel temperature distribution exhibits the presence of a hot-zone of approximately constant temperature that grows in height and in temperature level as shown in Figure 6, left. This zone is clearly identified for reservoirs with low shape factor $H_f/D = 0.2$, but does not appear or is less pronounced from temperature measurements for higher shape factor reservoirs $H_f/D = 0.4$. The most common theory [10] explains the hot-zone formation by distillation process as the light element of the fluid vaporize in small bubbles first, and when rising to the fuel free surface, induce liquid motion, leading to uniform temperature zone. To demonstrate such a mechanism, further experiments on transparent reservoirs and application of visualization techniques are in preparation. The second period starts when the water

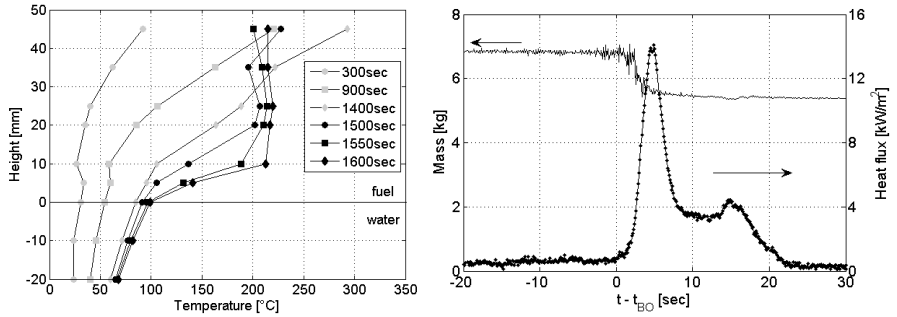

Figure 6: Boilover development and onset for 0.3m pan diameter and 80% diesel fuel (left) : Vertical temperature profiles (right) : Evolution of heat flux at 6D and mass loss

sub-layer is heated enough to violently vaporize and eject the fuel above. It is observed that the water is superheated by $6 - 7°C$ before Boilover occurs. This finding is much smaller than data obtained in previous experiments reported in literature [11] that identify a water sub-layer temperature of $120°C$ at Boilover onset; that discrepancy may be explained by the different fuel composition. From the measurements, this period is clearly identified by a peak of thermal radiation and a significant drop of fuel mass as plotted in Figure 6, right.
The time at which Boilover arises can be determined by analyzing the behavior of the

	$D = 0.15m$, 70% diesel	$D = 0.15m$, 80% diesel	$D = 0.3m$, 70% diesel	$D = 0.3m$, 80% diesel
Mass Loss	3956.7	4083.2	1640.5	1725.6
Radiation	3957.8	4083.2	1640.7	1725.1
$T_{int} = 110°C$	3953.1	4083	1639.7	1723.6
Visualization	3957.3	4083.1	1639.56	1727.4
Average	**3956.2**	**4083.1**	**1640.1**	**1725.4**
	(0.12%)	*(0.005%)*	*(0.07%)*	*(0.22%)*

Table 1: Boilover time determination [sec]

physical quantities as mass loss, thermal radiation and temperature. Table 1 lists the results. Very good agreement is obtained between the different experimental techniques since the maximum deviation is 0.22%. From these results, it can be concluded that the Boilover time is decreasing by a factor of about 2.4 when doubling the reservoir diameter.

This observation can be explained by the increase of the burning rate with the pan diameter (from $0.59mm/min$ to $1.15mm/min$ for experiments with 70% diesel and 0.62 to $1.05mm/min$ for 80% diesel). This is consistent with the Hottel's data [12] that showed already in 1959 that for a pool fire of diameter between 0.1 and 1m, the burning rate is directly proportional to the pool diameter. The measured burning rates have also been compared to published models as depicted in Figure 7, left. The correlations of Rew [13] and Babrauskas [14] fit well with the present data. The experiments with 0.3m pan are characterized by lower Boilover time due to the presence of a hot-zone that increases the fuel heating rate.

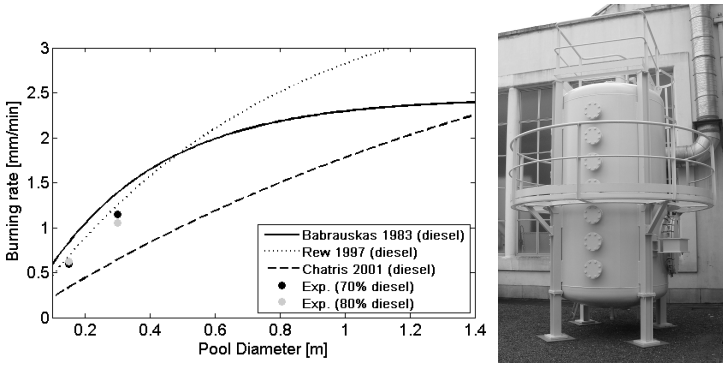

Figure 7: (left): Burning rate modeling and experiments (right) New VKI setup

Boilover intensity is generally defined as the value of a physical quantity at Boilover occurrence compared to the value before. Table 2 summarizes the data. The intensity based on mass loss agrees with the results of Koseki and Garo [15] [16], i.e. decreasing when the pan diameter increases. Two new definitions of Boilover intensity are elaborated here. They rely on the flame height, either normalized by the value before Boilover or normalized by the reservoir diameter; both follow the same trend. However, the intensity based on radiation ratios shows an opposite trend, probably because the sensors are not at same distance in both configurations.

	$D = 0.15m$, 70% diesel	$D = 0.15m$, 80% diesel	$D = 0.3m$, 70% diesel	$D = 0.3m$, 80% diesel
$\dot{m}_{BO}/\dot{m}_S$	769.28	697.42	215.62	286.66
q_{BO}/q_S	5.56	4.17	16.58	29.48
H_{fl-BO}/H_{fl-S}	12.13	12.61	4.78	7.61
H_{fl-BO}/D	25.14	22.7	7.23	10.9

Table 2: Boilover Intensity

4 Conclusion

The bibliographic research about BLEVE and Boilover shows that these multi-phase and multi-physic phenomena are very complex. The important bibliographic study and the first experimental campaigns helped to point the future areas of study. The first experimental BLEVE campaigns showed the difficulty of BLEVE generation, and allowed to decrease the list of occurence factors. The pressure signals recorder allowed also a first comparison with literature models. The first experimental Boilover campaigns ended in two new conclusions: a Boilover of strong intensity can happen without a hot-zone, and the hot-zone formation seems to be dependent on the H_f/D ratio of the reservoir. They also allowed a first Boilover flame characterization.
Future small scale experiments will be conducted in a new setup, developed and now available at the von Karman Institute. A general view of this facility is provided in figure 7, right. It consists of a cylinder of 2m diameter, and 3m high, with round shape extremities, made in steel and that can stand up to a 0.5 MPa pressure. It has 3 series of 7 optical access of 0.1m diameter, separated by $90°$, and a door of $0.57 \times 0.77m^2$. The setup allows air venting thanks to openings in the bottom and upper part of the chamber. It also contains a ladder and a circumferential walking area at mid-height for better accessibility of the upper optical access. This setup has been design to allow secure BLEVE and Boilover experiments in a calm and uniform environment.

Nomenclature

$\dot{m}$	= Burning rate $[mm/min]$	**subscripts**	
q	= Heat flux $[kW/m^2]$	BO	= Boilover onset
H	= Height $[m]$	S	= Stationary period
D	= Pool diameter $[m]$	f	= Fuel
t	= time $[s]$	fl	= Flame

Acknowledgments

The author wishes to thank the CEA Gramat (France) for supporting this study. The von Karman Institute and the Ecole des Mines d'Alès are working in this joint research projet about source term characterization in major hazards.

References

[1] Walls W.L. The BLEVE - part 1. *Fire Command*, pages 22–24, 1979.

[2] Reid R.C. Possible mechanism for pressurized liquid tank explosion or BLEVEs. *Science*, 203:1263–1265, 1979.

[3] Maillette J. Birk A.M. Z.Ye and Cunningham M. Hot and Cold BLEVEs: Observation and discussion of two different kinds of BLEVEs. *AIChE Symp. Series*, pages 119–130, 1993.

[4] Kulesz J.J. & Al. Baker W.E. Workbook for predicting pressure wae and fragment effects of exploding propellant tanks and gas storage vessels. Technical

Report NASA CR-134906, NASA Scientific and Technical Information Office, Washington D.C., 1977.

[5] Salla J.M. Planas-Cuchi E. and Casal J. Calculating overpressure from BLEVE explosions. *J. of Loss Prev. in Process Ind*, 17:431–436, 2004.

[6] Casal J. and Salla J.M. Using liquid superheating energy for a quick estimation of overpressure in BLEVE and similar explosions. *J. Hazardous Materials*, 137:1321–1327, 2006.

[7] Silvestrini M .& Al. Genova B. Evaluation of the blast wave overpressure and fragment initial velocity for a BLEVE event via empirical correlations derived by a simplified model of released energy. *J. of Loss Prev. in the Process Ind.*, 21:110–117, 2008.

[8] Van der Voort M.M. & Al. Van den Berg A.C. Expansion-controlled evaporation: a safe approach to BLEVE blast. *J. of Loss Prev. in the Process Ind*, 17:397–405, 2004.

[9] Hall H.H. Oil tank Boilovers. *Mechanical Engineering*, 47(7):540–544, 1925.

[10] Hasegawa K. Experimental study on the mechanism of hot-zone formation in open tank fires. In *Proc. Fire Safety Science, 2nd Int. Symp*, pages 221–230, 1987.

[11] Garo J.P. and Vantelon J.P. Effect of the fuel boiling point on the boilover burning of liquid fuels spilled on water. In *26th Int. Symp. on Combustion*, 1996.

[12] Hottel H.C. Review: "Certain laws governing the diffusive burning of liquids ", by Blinov and Khudiakov. *Fire Research Abstracts and Reviews*, pages 1–41, 1959.

[13] Hulbert W.G. Rew P.J. and Deaves D.M. Modelling of thermal radiation from external hydrocarbon pool fires. *Trans. IChemE*, 75:81–89, 1997.

[14] Babrauskas V. Estimating large pool fire burning rate. *Fire technology*, 19:251–261, 1983.

[15] Koseki H. Boilover and crude oil fire. *J. Applied Fire Science*, 3(3):243–272, 1993.

[16] Koseki H. & Al. Garo J.P. Combustion of liquid fuels floating on water. *Thermal Science*, 11(2):119–140, 2007.

FIRST YEAR DOCTORAL SUMMARIES

Doctoral Project Summary

Modeling and Analysis of the Laminar to Turbulent Transition in a Low-Pressure Turbine

Jayson BABAJEE *

Supervisor: Prof. Tony ARTS †

von Karman Institute for Fluid Dynamics, Rhode-Saint-Genèse, 1640, Belgium

Promoter: Prof. Francis LEBOEUF ‡

Ecole Centrale de Lyon, Lyon, France

The aerodynamics of a commercial jet aircraft engine is still a tricky topic for the aerodynamicists and the designers because of the complexity of the flow field due to the numerous stator/rotor interactions. The current and future main stakes are to get more efficient engines while being more environmentally friendly in terms of fuel consumption.

To fulfill those constraints, the trend is to design higher by-pass-ratio engines and to reduce the weight of the LP turbine. This component represents about 30% of the overall weight of the engine.

The LP turbine blade flow might be prone to separation and in some worst cases to open-separation due to the combination of the low Reynolds number working conditions seen during cruise and the large aft diffusion that the LP blades experience. This results in high losses and performance deterioration.

The purpose of this thesis is to analyse the laminar to turbulent transition mechanisms occurring in new LP turbine designs. To meet these goals, the study and modeling of the effects of the roughness coupled with the unsteady wake induced transition phenomenon will be highlighted in order to control the boundary layer behaviour and particularly to promote transition before separation. However, the aim is to find a good trade-off between those effects. This issue will be mainly addressed numerically (by using the ONERA code elsA) in addition to a correlation of several test cases and might be subjected to an experimental approach as well.

* PhD Candidate, Turbomachinery and Propulsion department, Chaussée de Waterloo 72, jayson.babajee@vki.ac.be

† Professor, Head, Turbomachinery and Propulsion department, Chaussée de Waterloo 72, arts@vki.ac.be

‡ Professor, LMFA (Laboratoire de Mécanique des Fluides et d'Acoustique), 36 avenue Guy de Collongue - 69134 Ecully Cedex - France, Francis.Leboeuf@ec-lyon.fr

Doctoral Project Summary

Micro-scale Assessment and Prediction of Wind Resources for Wind Farms Based on Numerical Modeling and Simulation

Antonino Bonanni

Supervisor: Prof. Deconinck Hermann

von Karman for Fluid Dynamics, Rhode-Saint-Genèse, 1640, Belgium

Promoter: Prof. Lacor Chris

VUB University, Bruxelles, 1050, Belgium

Wind Energy is one of the fastest growing industry worldwide. An increase of more than 700% of the currently installed capacity is expected in the next twenty years. Despite this fact, the prediction of the wind conditions inside the wind farm has still to be drastically improved. The European Wind Energy Technology Platform, in fact, identifies Wind Conditions assessment as one of the key areas for research activities of this sector, aiming to reach a prediction accuracy better than 3% by the year 2030, regardless of the terrain and atmospheric conditions. To reach such ambitious objective, a paradigm shift is needed for the prediction tools at the industry disposal.

At present, state-of-the-art tools used by industry are still dominated by solvers based on linear models of the wind flow, which are not appropriate for flows over complex topographic features. Turbulence RANS models are also used but the uncertainties related to the modelling of the physics are still dominant. More advanced and expensive methods like hybrid RANS-LES still need to be improved and validated before they can be successfully used by industry.

The aim of this project is to develop a new, innovative tool for Computational Fluid Dynamics (CFD) tools in order to achieve accurate simulations of wind farms located on complex terrains. This mainly includes the effect of the terrain (e.g. causing flow separation), the energy extraction by the wind turbines and the wakes influencing the neighbouring turbines. In particular, both Large Eddy Simulation (LES) model and hybrid RANS-LES model will be investigated. The LES method is recognized to be the most accurate but it can be extremely expensive in terms of computational time and therefore RANS-LES hybrid methods represent the optimal compromise between accuracy and computational efficiency.

Doctoral Project Summary

Distorsion and temperature measurement on high-temperature object by near infrared camera

Delmas Anthony*

Supervisor: Prof. Jean-Marie Buchlin†

von Karman for Fluid Dynamics, Rhode-Saint-Genèse, 1640, Belgium

Promoter: Dr. Yannick Le Maoult‡

Ecole des Mines d'Albi-Carmaux, Albi, 81000, France

The ICA-Albi and VKI conduct since numerous years works about IR radiometry with the aim to do quantitative thermography (true temperature measurement without contact). Studies done in this specific domain have pointed out the presence of optical perturbations at high-temperature. These perturbations come from convective effect present around high-temperature object. This phenomena brings inevitably distorsion of spatial informations received by the camera. The work starts with the computation of the temperature field around specific object (starting with simple geometry). Then, thanks to the Gladstone-Dale relation, we will deduce the refractive field causing object distorsion. After that, an experimental part includes observations of the deformed object with different near infrared camera and optical system such as PIV or Schlieren methods to accurate data on the hot air around the object. Finally, the infrared picture stored will have to be treated in order to obtain informations, corrected of any distorsions coming from refracive index variations.

* PhD Candidate, Environmental and Applied Fluid Dynamics Department, Chaussée de Waterloo 72, anthony.delmas@vki.ac.be

† Head of Department Environmental and Applied Fluid Dynamics, Chaussée de Waterloo 72, buchlin@vki.ac.be

‡ Enseignant-chercheur, ICA-Albi, Campus Jarlard, Route de Teillet, 81013 Albi, Cedex 09, yannick.lemaoult@mines-albi.fr

Doctoral Project Summary
Multi-Disciplinary Optimization For Concurrent Design of Turbomachinery Blades

Michael Joly*

Supervisors:

Prof. Tom Verstraete†, Prof. Guillermo Paniagua‡

von Karman Institute for Fluid Dynamics, Rhode-Saint-Genèse, 1640, Belgium

The design of gas-turbine or wind-turbine blades is a sophisticated process, requiring demanding trade-offs between aerodynamic performances, structural integrity and cost efficiency. In the industry, traditional design procedures require several iterations and validation loops involving different departments. With the recent progress in numerical methods and computational power, the development of optimization techniques could lead to an integrated design strategy to solve multi-disciplinary challenges.

Part of Research activities at the von Karman Institute for Fluid Dynamics focuses on Evolutionary Algorithms to address Multi-Disciplinary Optimization problems. The present project aims at extending developments of the self-made optimization code and would demonstrate its capacity to perform efficiently on various applications.

Multi-Disciplinary Optimization enables to find compromises in blade design between the conflicting requirements on efficiency, structural integrity and noise emission. Continuous improvements of the method will be implemented in terms of geometry parametrization, mesh generation, multi-physics performances evaluation and metamodel assistance.

The parametrization defines the way to represent a geometry from a set of parameters. By fixing parameter ranges, the design space and corresponding shape variety is determined. It is critical for the optimization process to ensure an unique and as direct as possible impact of each individual parameter on performances. Each application will require a case-specific parametrization.

The mesh generation should be an automatic and robust process applicable to several different airfoil geometries. A self-made algorithm will be developed and should also be adaptable to allow different optimization applications.

Multi-physics performances evaluation enables the multi-disciplinary capacities of optimization techniques. Part of the present project could be dedicated to solver

* PhD Candidate, Turbomachinery and Propulsion department, Chaussée de Waterloo 72, joly@vki.ac.be

† Assistant Professor, Turbomachinery and Propulsion department, Chaussée de Waterloo 72, verstraete@vki.ac.be

‡ Associate Professor, Turbomachinery and Propulsion department, Chaussée de Waterloo 72, paniagua@vki.ac.be

development, including fluid dynamics, aero-acoustics and structural analysis. Adaptation of the CoolFluid multi-physics solver to turbomachinery application could be an option.

Metamodel assistance enables a fast prediction of performances and reduces consequently the computational cost of the whole process. An artificial Neural Network is trained from a database of shape samples and provides an approximation of the relation between parameters and shape performances. Developments will enable to improve metamodel accuracy and robustness.

Different applications will be conducted to assess the effectiveness of the optimization code, including high-pressure turbines, contra-rotating fans and wind turbine winglets.

High-pressure turbines often operate in the transonic regime, resulting in strong shock interactions between the vane and the rotor blades. It is proposed in the present project to redesign the stator blade of a transonic stage tested at the VKI. The objective of the 3D steady-flow optimization is to attenuate the propagation of shock waves downstream of the vane. Computation of the resulting unsteady forcing on the rotor will be performed to validate the reduction in risk of high-cycle fatigue.

The design of a contra-rotating two-stages fan for hypersonic flight vehicle application will be performed. It is proposed to investigate an innovative and robust design method incorporating preliminary, 2D section and 3D design in a single optimization procedure. In order to consider as well mechanical integrity and noise emissions, structural and aero-acoustic evaluations could be integrated into the optimization.

Wind turbine performances could be improved in terms of aerodynamics, structural integrity and possibly noise reduction. Adaptation of the optimization code to wind turbine blades will be performed with particular focus on mesh generation and performance evaluation. Also, enhanced geometry parametrization would enable the design of 3D wind turbine blades including winglets, with the perspective to reduce the vortical flow intensity at the blade tip.

In summary the present project aims at extending developments of the VKI Optimization code. Application on high-pressure turbines, contra-rotating fans and wind turbine winglets would allow to assess the effectiveness of the proposed enhancements and to demonstrate the promising capacity of optimization strategies to address multi-disciplinary design challenges.

Doctoral Project Summary
High enthalpy CO_2 plasma jet characterization by means of Optical Emission Spectroscopy diagnostics

Damien Le Quang*

Advisor:Yacine Babou†
von Karman Institute for Fluid Dynamics, Rhode-Saint-Genèse, 1640, Belgium
Supervisor: Olivier Chazot‡
von Karman Institute for Fluid Dynamics, Rhode-Saint-Genèse, 1640, Belgium

High enthalpy VKI-Plasmatron wind tunnel produces radiative flows at elevated temperature in order to replicate incident convective heat fluxes on a vehicle during atmospheric entries. The achievement of Local Thermodynamic Equilibrium (LTE) is investigated using Optical Emission Spectroscopy (OES) diagnostics applied to CO_2 plasma jet produced by VKI-Plasmatron operating at constant mass flow rate and maintainig the static pressure in the chamber at 15 mbar.

Emission spectra of the plasma are spatially resolved in the radial direction of the jet and translational motion of the optical bench allows axial measurements. C and O atomic lines are recorded in the visible spectral range fig.1. Absolute calibration is performed and local emission is rebuilt applying Abel transform.

Relative population probing is performed for the upper energy levels involved in the observed atomic transitions. Boltzmann population distribution of electronic energy levels is evidenced, therefore excitation temperature T_{exc} is defined. From spatial profiles of the excitation temperature, mappings of the jet thermodynamic and transport properties are deduced at LTE fig.2. Taking into account chemical composition of the plasma at equilibrium, absolute population probing gives rise to a slightly higher temperature T_{LTE} compare to previously obtained T_{exc} . This discrepancy is due to chemical non equilibrium and it decreases along the axis of the jet to reach quasi thermal and chemical equilibrium ($T_{LTE} \approx T_{exc}$) beyond 46 cm from the exit of the jet.

It is relevant to investigate kinetic phenomena in such plasmas. Examination of thermodynamic state of a low pressure CO_2 plasma jet evidences rapid thermalization and slower chemical relaxation processes along the jet.

*PhD Candidate, Aeronautics and Aerospace Department, Chaussée de Waterloo 72, lequang@vki.ac.be.
†Research engineer, Aeronautics and Aerospace Department, Chaussée de Waterloo 72, babou@vki.ac.be.
‡Associate Professor, Aeronautics and Aerospace Department, Chaussée de Waterloo 72, chazot@vki.ac.be.

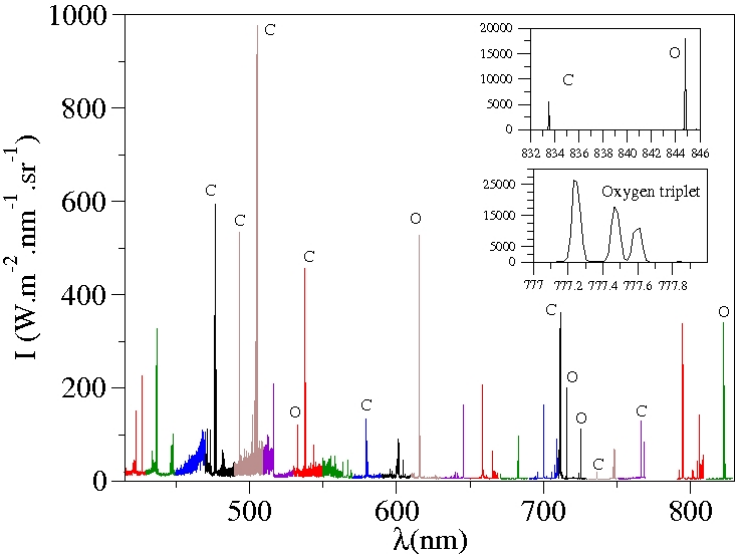

Figure 1: Low pressure $C0_2$ plasma radiative signature in the visible spectral range

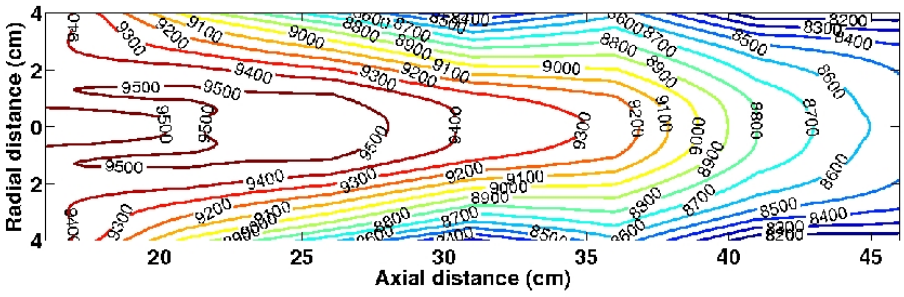

Figure 2: Excitation temperature isocontours for low pressure CO_2 plasma jet

Doctoral Project Summary

Multiscale Models and Computational Methods for Aerothermodynamics

Alessandro Munafó[1]

Supervisor: Prof. Thierry Magin[2]

von Karman Institute for Fluid Dynamics, Rhode-Saint-Genèse, 1640, Belgium

Promotor: Ch.mo Prof., Enrico Primo Tomasini[3]

Università Politecnica delle Marche, Ancona, 60131, Italy

The accurate modeling of physico-chemical phenomena in hypersonic regime is essential to the fundamental understanding and development of many different applications of interest for space agencies. These go from the accurate design of space vehicle heat shields to a correct interpretation of experimental measurements in high enthalpy facilities such as shock/expansion tubes. Also the success of future manned space missions will strongly depend on the reliability of available physico-chemical models. The reason underlying the need for accurate modeling can be inferred from an application, such as the flow over a capsule entering a planetary atmosphere. The most important quantity for its design is the convective and radiative heating on the vehicle surface. In such a situation, an intense bow shock is formed in front of the spacecraft and the flow passing through that experiences a steep increase of density, pressure and temperature leading to excitation of internal energy modes of atoms and molecules, dissociation, and, if the velocity is high enough, ionization as well. The flowfield is extremely complex because of *nonequilibrium* of kinetic processes characteristic time becoming of the same order of magnitude of flow macroscopic time scales. Moreover since each process has its own characteristic time one ends up with a large spectrum of scales, at both temporal and spatial level. An example of distinct temporal scales is found in the dissociation process of molecular nitrogen. This occurs in two steps: first, a rapid excitation of the internal energy levels of nitrogen, then dissociation of the molecules at the flow time scale. The above situation is even more complicated at high speeds (more than 11 km/s for earth re-entry) where radiative processes become extremely important in determining the state of the gas and energy transfer by radiation becomes the dominant mechanism for heating. Unfortunately current physical models plugged in CFD codes are not able to resolve the whole scale spectrum of before, and this leads, despite the availability of increasing computational resources and power, to unsatisfactory results in terms of heat flux predictions.

[1] PhD Candidate, Aeronautics and Aerospace department, Chaussée de Waterloo 72, munafo@vki.ac.be

[2] Assistant Professor, Aeronautics and Aerospace department, Chaussée de Waterloo 72, magin@vki.ac.be

[3] Full Professor, dipartimento di Meccanica, Universita' Politenica delle Marche, Ancona 60131, Italy, e.p.tomasini@uivpm.t

This problem can be explained in view of physical models and assumptions adopted for the numerical simulations of high-enthalpy *nonequilibrium* flows. Excitation and relaxation of internal energy modes, together with dissociation and ionization reactions, are generally described by means of *multi-temperature* models where the population of internal states is supposed to be given by *Boltzmann distributions* at temperatures to obtained as part of the solution. This approach is extremely simplified and doesn't work for strong *nonequilibrium* conditions (i.e. high re-entry speed and low pressure). Despite that, its use is often stretched out of the condition for which it has been conceived (i.e low departure from equilibrium). Moreover *multi-temperature* models are based on highly averaged experimental data (i.e. stagnation point heat flux measurements) and as consequence cannot provide detailed information about the specific state of the gas (a crucial aspect as said before). This lack of physical meaning also shows itself through the presence of tunable numerical parameters (with a limited range of validity) used in model formulation to be determined by trial and error procedures in numerical or experimental work. In order to overcome this difficulty, *Collisional-Radiative* models have been recently formulated as possible tools to be used for a both a better resolution of kinetic time and space scales and a better quantitative description of internal state dynamic behavior. This can be achieved by rejecting the assumption of *pseudo-Boltzmann distribution* and treating each internal state as a *separated pseudo-species*.
The further step is to study the dynamics of each kinetic process in great detail by means of classical and quantum mechanical calculations to be repeated for a wide range of initial conditions. Once this done, *rate coefficients* for elementary processes can be obtained by means of suitable averaging procedures. An excellent example of that is the work recently performed by the NASA Ames quantum chemistry concerning the collisional excitation and dissociation of ro-vibrational levels of the ground state of molecular nitrogen. The method applied there consisted in a two step process. First, first principle quantum chemistry computations where carried out in order to obtain realistic interaction potentials (see fig. a). After that the quasi-classical trajectory method (QCT) was applied in order to study collision dynamics and obtain *rate coefficients* at different temperatures. It is sure that this kind of approach, when applied to a blunt body flow, will give on one hand to a physical description much closer to reality than that provided by *multi-temperature* models, but on the other it will lead to a series of problems making its application currently unfeasible for 2D and 3D CFD applications. The former are due to huge stiffness (a feature common to all problems involving kinetics) and number of differential equations to be solved. The last is due to the fact that a species continuity equation must be written for all internal energy levels. As an example, for the NASA Ames nitrogen database of before, the number of ro-vibrational levels is equal to 9390. Therefore 9390 species equations should be coupled with global momentum and energy conservations equations.

Actually, the lack of accuracy characterizing the computation of *nonequilibrium* flows, is not just due to inadequate models, but also to lack of robustness and physical insight of numerical schemes used to obtain a discrete solution of the set of equations. Most of CFD codes always make use of Finite Volume Method (applied to Navier-

Stokes equations) because of its robustness and simplicity of implementation. There, numerical flux functions are obtained by using a *straightforward extension* of original formulations of Flux Difference Splitting (FDS) and Flux Vector Splitting (FVS) techniques (valid for a calorically perfect gas), leading thus to a loss of physical representation of the problem. A typical example of that is the absence of an entropy jump for free electrons through a shock when using current approximate Riemann solvers. Moreover, even in this area, tunable parameters are always found in order to overcome well known scheme drawbacks (such as the carbuncle phenomenon for approximate Riemann Solvers or FDS schemes). And last, but not least, the aforementioned method cannot be employed in regimes where the flow can still be treated as a continuum medium but the *Navier-Stokes* equations no longer apply because of extreme gradients (such as those within bow shocks at high altitudes). In this conditions shock thickness assume non negligible values and therefore the main hypothesis at the basis of shock capturing methods (where shock waves are treated as discontinuities and kinetics is assumed to be frozen) breaks down. An attractive alternative in this field is provided by *moment methods* based on the *Boltzmann equation* of kinetic theory of gases.

In the framework of the present thesis what is proposed is to work in parallel both on physical modeling and numerical methods. Since, as said before, the application of *Collisional-Radiative* models is unfeasible for 2D or 3D computations, simple flows (such as normal/oblique shocks and quasi 1D nozzle flows) will be considered as starting point. There, use will be done of detailed kinetic models (such as the NASA Ames Database for molecular nitrogen) coupled in a first stage with *Euler/Navier-Stokes* equations, in order to investigate the differences with the results given by *multi-temperature* approach. The comparison will then be employed for the formulation of *new reduced and physics based* macroscopic models feasible for 2D and 3D blunt body flows (see fig. b) in order to have more reliable predictions of surface heat flux. At the same time, efforts will be devoted to solve some deficiencies of typical flux functions currently used in Finite Volume Method (such as the problem of free electron entropy of above). After that, *Navier-Stokes* equations will no longer be adopted. In place of that a new set of conservation equations will be used. This will be obtained by taking suitable moments of the *Boltzmann* equation where the influence of internal energy states will be taken into account. There, the detailed modeling of kinetics will enter in the formulation of the *collisional operator*. Once the equations obtained, suitable discretization techniques will be seek and the resulting set of discrete equations will be employed for studying flow features not correctly modeled by *Navier-Stokes* equations and related numerical methods (such as shock structure, influence of internal mode excitation processes on shock structure, etc., etc.).

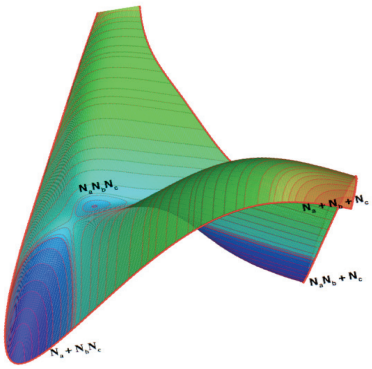

Fig a: Potential energy surface (PES) for the computation of molecular nitrogen collisional excitation and dissociation. (Courtesy NASA Ames Research Center).

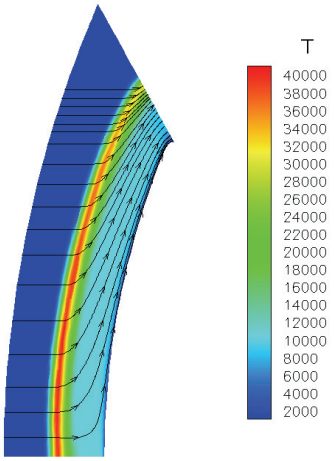

Fig b: FIRE II t = 1634s case afterbody temperature distribution for a 2 temperature model (COOLFluiD and Mutation).

Doctoral Project Summary
Assessment of Wind Resource in Complex Terrain by Physical Modeling

Boris Conan*

Supervisor: Prof. van Beeck Jeroen†
von Karman for Fluid Dynamics, Rhode-Saint-Genèse, 1640, Belgium
Promoter: Prof. Devinant Philippe‡
Université d'Orléans, Orléans, 45072, France

Europe, by means of long term projects, is definitely making an important impulse for the development of wind energy; however, giving the large number of field already occupied, its expansion goes through a development of standard and reliable tools for forecasting wind in complex terrains: hills, mountains, forest, ridge, cliffs or cities. This is challenging giving EU targets of, regardless the complexity of the terrain, 3% uncertainty on both wind power production and local wind conditions in 2030.
In this context, the WAUDIT project (Wind resource assessment Audit and Standardization) scope is to go over differences of approach and to give, to some extent, a validated standardized methodology to assess wind resource. The project (30 European partners) is covering all aspects of wind forecasting: field measurements, meso-scale forecasting model, CFD and wind tunnel simulation.
PhD project aims are to demonstrate wind tunnel suitability for wind expertise and to improve wind tunnel assessment of wind in complex terrain by defining key parameters and validating methodologies. Main issues are the model definition (scaling factor, roughness) and the modeling of the oncoming atmospheric boundary layer.
As a first action, a "state-of-art" blind test comparison is being setting-up together with partners to exchange experience, methodology and result on a common complex test case. In a second time, deep parametric study will be conduct and shared with partners to have a better knowledge of relevant modeling parameters. In parallel, new techniques should be implemented to increase the number of possibilities in measuring and visualizing the flow (ie PIV). The final goal is to define a common and, to some extent, a standard methodology for wind assessment in complex terrain by wind tunnel modeling and to validate it with existing field tests, meso-scale forecasting and CFD models. Several complex terrains are considered for the project,

* PhD Candidate, Environment and Applied fluid dynamics department, Chaussée de Waterloo 72, boris.conan@vki.ac.be
† Associate Professor, Environment and Applied fluid dynamics department, Chaussée de Waterloo 72, jeroen.vanbeeck@vki.ac.be
‡ Professor, Institut PRISME-Polytech'Orléans, 8 rue Léonard de Vinci, philippe.devinant@univ-orleans.fr

mainly isolated mountains: Alaiz (Pamplona, Sp), Bolund (Risoe, Dk) and Askervin (Scotland, UK).

Doctoral Project Summary
Residual Distribution methods for atmospheric entry aerothermodynamics

Jesús Garicano Mena[1]

Supervisor: Prof. Herman Deconinck[2]

von Karman for Fluid Dynamics, Rhode-Saint-Genèse, 1640, Belgium

Any space vehicle intended to survive an atmospheric entry process must be protected by a thermal protection system (TPS). Optimized design of these TPS requires an accurate prediction of the flowfield around the vehicle, since this one defines the aerothermal loads to be endured. Given the high velocities involved, aerodynamics have to be coupled with additional physical phenomena, such as chemistry and high temperature effects. Prediction of these aerothermal loads by means of CFD techniques has proven to be a demanding problem, since one has to deal with larger system of equations and extended modeling.

Finite volume (FV) methods are the standard numerical technique for these problems. Well established in the field as they are, some issues remain open, as the heat flux sensitivity to the grid employed and its alignment with the bow shock. FV methods typically rely on hybrid meshes (made up of tetrahedra everywhere but close to the bow shock region, where prisms/hexaedra adapted to the shock surface are used) to circumvent the problem.

However, alternative numerical techniques able to avoid use of such complex meshes exist. This work focuses on the so called residual distribution (RD) schemes, offering enough advantageous characteristics (true multidimensional upwinding on unstructured tetrahedral meshes, 2nd order accuracy on compact stencils and minimum cross-diffusion) to justify its application to the aerothermodynamics field.

Since RD schemes work with local but relatively expensive dense matrix operations within mesh elements, a reformulation of the equations in terms of entropic variables that reduces the cost of the advective residual distribution has (already) been derived. Current work studies the effect of the distribution technique for the source term on the stability of the method. Next issues to cover include, on the numerical side, shocks over blunted geometries and associated carbuncle problems and comparisons of efficiency-accuracy with FV methods; while on the modeling side, an extension of the aforementioned reformulation to include electrons is planned.
Finally, extension of the previously stated goals for higher order schemes -i.e., use of P2/P3 elements- arises as a natural closure for this doctoral work.

[1] PhD Candidate, Aeronautics and Aerospace department, Chaussée de Waterloo 72, jesus.garicano.mena@vki.ac.be

[2] Professor, Aeronautics and Aerospace Department, Chaussée de Waterloo 72, deconincl@vki.ac.be

Doctoral Project Summary

Multiphase Fluid Hammer: Modeling, Experiments and Simulations

Marcos Lema*

Supervisor: Prof. Rambaud, Patrick†

von Karman Institute for Fluid Dynamics, Rhode-Saint-Genèse, 1640, Belgium

Promoter: Prof. Buchlin, Jean-Marie‡ and

Université Libre de Bruxelles Brussels, 1050, Belgium

Prof. López Peña, Fernando§

Universidade da Coruña, A Coruña, 15071, Spain

The operation of spacecraft propulsion systems is regularly faced with adverse fluid hammering effects during the priming operation. This maneuver is done by fast opening of an isolation valve, which results in the filling and pressurization of the propellant lines of the spacecraft. The classical water hammer taking place also involves multi-phase phenomena such as cavitation, boiling front and absorption-desorption of a non-condensable gas. Due to the complexity of the phenomena involved and the lack of experimental studies modeling the spacecraft's hardware, the physical models implemented in the numerical codes cannot be validated properly and they fail when computing the over-pressures during priming

This study proposes an experimental and numerical investigation of the fluid hammer phenomenon in a confined environment. The experimental approach uses an experimental setup which reproduces all the physical phenomena taking place in the propellant lines during the priming process, where two interchangeable measurement modules are attached to the impact location. The first module allows the instantaneous fast response measurements of pressure and temperature when the fluid impacts at the forward end. The second module is transparent to allow flow visualization of the pressure front through high speed imaging, in order to characterize the multiphase phenomena, i.e. cavitation and/or column separation occurrence, and boiling front manifestation. The influence of absorption-desorption rates of the driving pressure gas on the fluid hammer is estimated by measuring the speed of sound in the pressurized liquid with an ultrasonic transducer. The numerical study is performed with two numerical tools used by the European Space Agency to simulate this phenomenon in satellites: EcosimPro and CFD-ACE, and which do not yield reliable results yet when applied to the present flow configuration. The creation of an extensive experimental database, together with numerical simulations of the experimental configuration, will allow the validation and improvement of the physical models implemented in these numerical codes.

* PhD Candidate, Environmental and Applied Fluid Dynamics Department, Chaussée de Waterloo 72, lema@vki.ac.be

† Assistantte Professor, Environmental and Applied Fluid Dynamics Department at VKI, Chaussée de Waterloo 72, rambaud@vki.ac.be

‡ Professor, Applied Mechanics Department, F.D. Roosevelt avenue, 50, B-1050 Brussels (Belgium), buchlin@vki.ac.be

§ Professor, Naval and Oceanic Engineecing Department, Campus de Esteiro. 15403 Ferrol (Spain), flop@udc.es

Doctoral Project Summary

High-resolution mesoscale and microscale numerical modeling of wind over complex terrains

Domingo Muñoz Esparza*

Supervisor: J.P.A.J. van Beeck†

von Karman Institute for Fluid Dynamics, Rhode-Saint-Genèse, 1640, Belgium

Promoter: J.-M. Buchlin‡

Université Libre de Bruxelles, Belgium

The present thesis is framed within the WAUDIT European Project, coordinated by CENER (Spanish National Center for Renewable Energies), where 30 research institutions and companies from 8 different countries are involved.

The goal of this research project is to obtain accurate predictions of the wind potential over complex terrains using numerical tools, in order to optimize the location of wind farms. The main test case which is going to be analysed is a complex terrain located in Alaiz, close to Pamplona in the north of Spain. Alaiz hill is 4 km long, 1.300 m high a.s.l. and is surrounded by a complex terrain associated to a ruggedness index (RIX) of 16%.

Two different and complementary numerical approaches will be used. In one hand, mesoscale simulations will be performed using the Weather Research and Forecasting (WRF) model. WRF is a finite differences non-hydrostatic fully compressible Euler solver which allows to resolve global phenomena. Typically, the spatial resolution of this kind of mesoscale codes is about 1km at maximum, covering domains of the order of 1000 km. Effort will be made in readapt WRF for higher resolutions around 10-50 m, suitable for accurate predictions inside the Atmospheric Boundary Layer (ABL).

On the other hand, microscale modeling will be assessed by means of OpenFOAM code. OpenFOAM is a finite volume Navier-Stokes solver which allows to resolve small scales reaching grid resolutions of less than 1 meter. Information from WRF dynamic downscaling will be employed to improve the boundary and initial conditions. In addition, wind tunnel experiments (performed at VKI) will be reproduced numerically, to compare and validate them.

Finally, field measurements from six masts located in Alaiz hill will be used in order to highlight the strength and suitability of each technique.

*PhD Candidate, Environmental and Applied Fluid Dynamics Department, Chaussée de Waterloo 72, domingo.munoz.esparza@vki.ac.be

†Associate Professor, Environmental and Applied Fluid Dynamics Department, Chaussée de Waterloo 72, vanbeeck@vki.ac.be

‡Professor, Faculté des sciences appliquées, buchlin@vki.ac.be

Doctoral Project Summary
Numerical Algorithms For Multiphysics Coupling Applications

Alessandro Sanna[1]

Supervisor: Prof. Herman Deconinck[2]

von Karman Institute for Fluid Dynamics, Rhode-Saint-Genèse, 1640, Belgium

Since some years the field of Computational Fluid Dynamics (CFD) is playing an ever increasing role in many industrial applications ranging from aeronautics and aerospace to industrial production processes. As part of an integrated design tool, CFD can indeed lead to huge saving both financially and in development times.
In the last years however, the request of design complex and complex objects has pushed the research to develop simulation tools integrating CFD along with Computational Structure Mechanics (CSM), Conjugate Heat Transfer, Radiation Transfer, Gas-Surface Interaction (such as Ablation), Two Phase Flow and many others, has increased. These multi-physical tools have to combine the complex physical modeling of each of the domains involved with the complexity of re-conciliating the various physical models.
For instance, the design of the heat shield for atmospheric entries is a complex multiphysics problem: the pyrolysis gas and the surface roughness of an ablative material can trigger transition of the flow from laminar to turbulent, leading to a strong increase of the convective heat-flux, whereas the boundary layer can absorb radiation coming from the atoms and molecules excited in the post-shock plasma, decreasing substantially the radiative heat-flux to the wall.

The purpose of these doctoral project is to develop and implement strategies, methods and algorithms to deal with multi-physics applications; especially in the field of radiation transfer, fluid-structure interaction, aerothermoelasticity.
This study is integrated in the COOLFluiD (Computational Object-Oriented Library for Fluid Dynamics) framework. The developments take into account different methods for solving the fluid domain, like Finite Volume, Finite Element and Residual Distribution Scheme.
These tools are being developed with the goal of obtaining an efficient, robust and versatile parallel multi-physics coupling solver.

In this context are being developed boundary conditions (like periodicity), the Baldwin-Lomax turbulence model, the Monte Carlo Method for Radiation Transfer .
The periodic boundary condition developed and implemented in parallel can be applied for both 2D and 3D case, for matching mesh, and for general shape boundary.

[1] PhD Candidate, Aeronautics and Aerospace Department, Chaussée de Waterloo 72, sanna@vki.ac.be
[2] Professor, Aeronautics and Aerospace Departmen, Chaussée de Waterloo 72, deconinck@vki.ac.be

The Baldwin-Lomax turbulence model is a strongly non local algebraic model. This has been implemented always in parallel, for both 2D and 3D case and for both structured and unstructured mesh. This was not at all an easy task, due to the strong non locality of this method that implied many communication between different processes. The non locality is especially due to the dependence of the turbulent viscosity in a point in the fluid domain to some fluid variables (like vorticity) along all the line connecting the point with its closest point on the wall.
The Monte Carlo Method for Radiative Transfer it is a general philosophy to compute the radiative heat source. It is made of different part: the random number generator, the particle tracking and the solution method. Different choice of the algorithm and/or implementation strategies of these three parts lead to different version of the Monte Carlo Methods. We chose to use an very elegant and fast method for the particle tracking, instead of use a tacking based on the shape function (as it is common). For the random number generator we implemented the Mersenne-Twister generator, that is the best one that nowadays exist. Finally for the solution methods we use the READ method that, without loose accuracy, is the faster.
Next steps are the development of the Conjugate Heat Transfer (CHT) module, the modeling of the Ablation and the moving boundaries.
In the context of CHT two main strategy exist to solve the problem. In fact we have two possibilities to take care of the continuity of temperature and heat flux on the common boundary between solid and fluid domain.
In the approach called *Conjugate Method* the entire set of equations, modeling both solid and fluid heat transfer, is solved as a single system. This require an unique mesh and a unique solution method for the global domain (solid and fluid). The continuity is obviously treated implicitly.
In the other approach called *Coupled Method* the equations of solid and fluid heat transfer are solved separately providing a suitable set of boundary conditions at the interface that preserve the continuity. In this method we can use (and normally it is) different mesh and different solution method for the solid and fluid domain. The continuity of temperature and heat flux is obtained thanks by an iterative procedure. The Coupled Method is than not only a competitive tool to solve CHT but also a framework for multi-physics analysis in a wide range of applications and complex geometries. This, perhaps, is the main reason why we are going to choose this method for implementing CHT. Many different algorithms have been developed to carry out concretely the iteration loop between the solid and fluid solvers. These strategies take into account different important aspect, among other we can cite that the characteristic time constant of the heat transfer in fluid is one order of magnitude smaller than for the solid.
In the context of ablation different aspects have to be considered. One is the retrocession of the solid surface, an other is the separation of solid particle from solid surface, then there could be also the evaporation of solid components. Obviously this solid processes strongly affect the fluid behavior, for example for what concern boundary stability, fluid forces distribution on the interface with solid and so on. In order to take into account all these phenomena the code should be able to simulate moving boundary, particle tracking, gas-solid interaction and many others. About moving boundary we are planning to implement the Arbitrary Lagrangian Eulerian (ALE) Method. Instead for the particle tracking we can use the same code developed for the ray tracing in the Monte Carlo Radiation Transfer Method and/or extend it to the general case of two phase flow.

Doctoral Project Summary

Experimental Study of Droplet Ejections from Wall Surfaces Due to an External Turbulent Flow Field – Application to Wiper System

Evangelos C. Bacharoudis[*]

Supervisors: Prof. Larbi Labraga[†]

Université de Valenciennes et du Hainaut Cambrésis

Prof. Jean-Marie Buchlin[‡]

von Karman for Fluid Dynamics, Rhode-Saint-Genèse, 1640, Belgium

Promoter: Dr. Bratec Hervé[§]

Robert Bosch Produktie N.V.

Overspray is known in the domain of wiper system as failure on the screen due to impact of small droplets ejected from certain regions on the wiper system. The main cause is an atomization of droplets flowing on the structure and entrained by the air flow. After the atomization process, the smaller droplets are entrained by the main turbulent air flow and either impact the windscreen or are flown away by the main air flow. The atomization process has been investigated. Experiments were conducted in the low speed wind tunnel L-1A in von Karman Institute using a real car model of scale 1:1 in order to investigate further the overspray phenomenon. The general behavior of the wiper blades and the overspray failure on the windscreen was assessed by simple video recording with a handy camera. The identification of the droplet ejection locations and the atomization processes involved in were captured by two high speed cameras. The developed air flow field on the wiper and on the windscreen surfaces was visualized conducting experiments using oil paint. Seven different locations on the wiper blade were identified to eject droplets in different rates while three droplet ejection positions seem to contribute to overspray failure on the windscreen. Finally, a short description of the atomization processes is given for each source of droplets and a correlation is proposed between the location of the droplet ejection and their impact on the windscreen.

[*] PhD Candidate, Turbomachinery and Propulsion Department, Chaussée de Waterloo 72, Belgium / LME Laboratoire de Mécanique et Energétique, Université de Valenciennes et du Hainaut Cambrésis, evangelos.bacharoudis@be.bosch.com,

[†] LME Laboratoire de Mécanique et Energétique, Université de Valenciennes et du Hainaut Cambrésis, llabraga@univ-valenciennes.fr

[‡] Environmental and Applied Fluid Dynamics Department, , Rhode-Saint-Genèse, 1640, Belgium, buchlin@vki.ac.be

[§] Herve.Bratec@be.bosch.com

Doctoral Project Summary
Simulation of rarefied gas flows for aerospace applications

Erik Torres*

Supervisor: Assistant Professor Thierry Magin†

von Karman Institute for Fluid Dynamics, Rhode-Saint-Genèse, 1640, Belgium

The focus of this project is on the application of the Direct Simulation Monte Carlo (DSMC) method to aerospace applications. The method is most useful in the rarefied gas flow regime, which occurs when space vehicles enter the outer regions of a planetary atmosphere. At these conditions, the assumptions of continuum flow are not valid and simulations using the Navier-Stokes equations are inaccurate regarding the calculated force coefficients and surface heat flux. While the peak heat flux, which is an important parameter for heat shield design, occurs at lower altitudes (inside the continuum flow regime), the accurate calculation of forces and moments acting on the vehicle in the rarefied regime is essential to predict the flight trajectory (and the landing site), but also the stability of the vehicle.

The DSMC method is based on a different philosophy than the traditional CFD methods. Instead of solving a set of equations (e.g. Euler, Navier-Stokes) that describe the flow field in terms of macroscopic variables (density, velocity components, temperature), it tracks the motion of a large number of molecules in the flow and models their interaction due to collisions applying conservation laws at the molecular level. By averaging quantities at the molecular level (number density, molecular momentum, molecular kinetic energy) over small regions of space (sampling cells), the familiar macroscopic quantities can then be calculated.

We propose to first perform DSMC simulations of reentry flows using the DSMC software (called RGDAS) available at the VKI. In a subsequent step, the coupling of the DSMC code with a continuum solver (e.g. the VKI's COOLFluiD) will be investigated. It may be necessary to rewrite parts of the DSMC code in the COOLFluiD framework to make the coupling possible. A first application of the work will be the prediction of the flow around future ESA reentry vehicle configurations in the rarefied flow regime. Another potential area of application would be to study the interaction of exhaust plumes coming from attitude control boosters with surfaces of space vehicles (e.g. exhaust deposits on solar panels of satellites). From the computational point of view, the use of GPU's with the DSMC method could be of interest. The strong parallel processing capabilities of GPU processors make them

* PhD Candidate, Aeronautics and Aerospace department, Chaussée de Waterloo 72, torres@vki.ac.be

† Assistant Professor, Aeronautics and Aerospace department, Chaussée de Waterloo 72, thierry.magin@vki.ac.be

ideal candidates to handle the large amount of relatively simple computing tasks inherent in the DSMC method.
From a physical point of view, the DSMC method is valid in all regimes of flow, from continuum to rarefied flow. However the large amount of particles necessary to adequately describe the flow make its use under conditions approaching continuum computationally expensive and the use of a Navier Stokes solver becomes a necessity. Most cases of practical interest exhibit a mixed behavior, where the flow field is composed both of regions of rarefied gas flow and of continuum flow. One such an example is the expansion of exhaust plumes emanating from attitude control boosters on satellites or reentry vehicles. Another example would be the compression of the freestream flow at the bow of the vehicle. The use of DSMC also becomes necessary, if one wishes to accurately describe the internal structure of a compression shock, because in this region the assumptions of near-equilibrium flow inherent in the Navier Stokes equations are not valid. It is thus of practical interest to couple the accuracy of the DSMC method in the rarefied flow regime with the computational efficiency of a standard CFD solver in the continuum regime.